České vysoké učení technické v Praze
Fakulta jaderná a fyzikálně inženýrská
Katedra fyziky

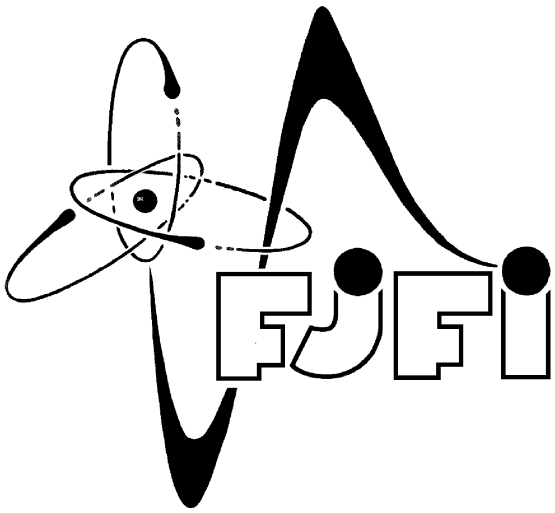

Dizertační práce

Interakce antikaonů s jaderným prostředím

Daniel Gazda

Praha 2012

Czech Technical University in Prague
Faculty of Nuclear Sciences and Physical Engineering
Department of Physics

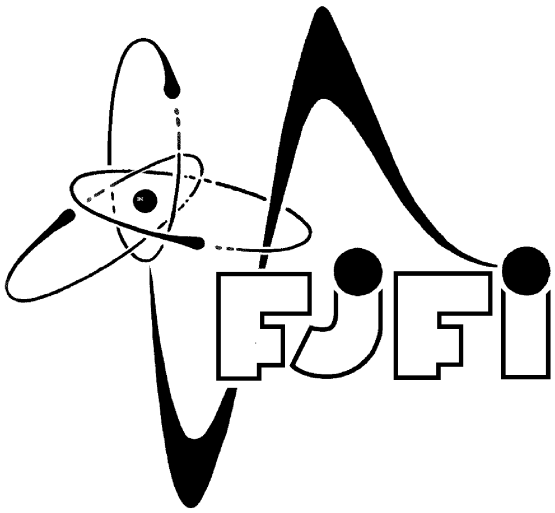

Ph.D. Thesis

Interaction of Antikaons with the Nuclear Medium

Daniel Gazda

Prague 2012

Interakce antikaonů s jaderným prostředím

Abstrakt

Předkládaná dizertační práce se věnuje studiu antikaonů v jaderném prostředí. Ve výpočtech v rámci relativistické teorie středního pole jsme se zaměřili na rozpadové šířky kvazivázaných stavů antikaonů v jádrech. Při zahrnutí všech relevantních absorpčních kanálů a zásadních dynamických procesů jsme nalezli značné šířky těchto stavů i pro vazbové energie antikaonu, pro něž se původně předpokládalo silné potlačení šířek v důsledku kinematického blokování hlavního rozpadového kanálu. Ukázali jsme, že v jaderných a hyperjaderných systémech dochází se zvyšováním počtu vázaných antikaonů k saturaci jejich vazbové energie. V důsledku toho v podivných hadronových systémech vázaných silnou interakcí nedochází ke kondenzaci antikaonů. K výpočtům kvazivázaných stavů $\bar{K}$–jádro jsme rovněž použili rozptylové amplitudy $\bar{K}$–nukleon, zkonstruované v rámci chirálního mnohokanálového přístupu. Silná energetická závislost chirálních amplitud vede k silně vázaným stavům antikaonů s rozpadovými šířkami, které jsou srovnatelné nebo i větší než odpovídající vazbové energie.

Interaction of Antikaons with the Nuclear Medium

Abstract

The present thesis deals with the study of antikaons in the nuclear medium. First, we focused on the decay widths of $\bar{K}$–nuclear quasi-bound states within the relativistic mean-field approach. When all relevant absorption channels and underlying dynamical processes were taken into account, the widths were found to be substantial even in the $\bar{K}$ binding energy range where they were anticipated to be strongly suppressed by kinematical blocking of the dominant decay channel. Calculations of nuclear and hypernuclear systems with a large number of antikaons revealed that the $\bar{K}$ binding energies saturate with the number of antikaons. As a consequence, it was argued that kaon condensation does not occur in strong-interaction self-bound strange hadronic matter. Finally, in-medium $\bar{K}$–nucleon scattering amplitudes developed within the chirally motivated coupled-channel model were applied in calculations of $\bar{K}$–nucleus quasi-bound states. The strong energy dependence of the chiral amplitudes was shown to imply deeply bound $\bar{K}$ states with decay widths comparable or even larger than the corresponding binding energies.

Acknowledgments

First and foremost I would like to thank my supervisor Jiří Mareš for all his contributions of time, ideas and efforts to make my Ph.D. experience both productive and enjoyable. I wish to express my sincere thanks to Eli Friedman, Avraham Gal and Aleš Cieplý for a very fruitful collaboration and number of illuminating discussions. My personal words of thanks belong especially to my parents, family and Aneta for their patience and love during the time of my Ph.D. pursuit.

Prohlášení

Dizertační práce obsahuje výsledky výzkumu provedeného v Ústavu jaderné fyziky Akademie věd České republiky, v. v. i. Pokud není uvedena explicitní reference, je dizertace založena pouze na originálních článcích, které jsou přiloženy na konci této práce. Výsledky byly získány ve spolupráci s autory uvedenými na příslušných publikacích.

Nemám závažný důvod proti užití této práce ve smyslu § 60 Zákona č.121/2000 Sb., o právu autorském, o právech souvisejících s právem autorským a o změně některých zákonů (autorský zákon).

Declaration of Originality

The thesis contains results of research conducted at the Nuclear Physics Institute of the Academy of Sciences of the Czech Republic. Unless an explicit reference is given, the thesis is based on the published articles attached at the end of this work. I declare that the presented results are original. They have been achieved in collaboration with the co-authors of the corresponding articles.

Prague, August 9, 2012 Daniel Gazda

Contents

Preface

This thesis is devoted to the study of antikaons in the nuclear medium. Antikaons serve as an impressive example of the growing interplay between various areas of contemporary nuclear physics. The issue of (anti)kaons spans a wide range of topics starting with their fundamental role in the theory of strong interactions at low-energies continuing over the exploration of hadron properties in dense nuclear matter in heavy ion collisions to physics of compact objects in astrophysics. Though the discovery of kaons took place more than six decades ago there still remain many open problems and challenging questions to be solved. In few years, hopefully, further progress in kaon and strangeness nuclear physics can be anticipated with new facilities in Frascati, Mainz, J-PARC in Japan and FAIR in Darmstadt.

The thesis is organized as follows: In Chapter 1, we briefly summarize the current state of knowledge of the interaction of antikaons with nucleons and the nuclear medium at low energies and discuss motivations for further studies. The theoretical frameworks used in our work are outlined in Chapter 2. In Chapter 3, we present selected results of our calculations. We first addressed the question of possible existence of deeply bound states of antikaons in nuclei within the relativistic mean-field methodology. We focused on a detailed study of the decay widths of $\bar{K}$–nuclear states, in particular, whether the widths are small enough to allow their experimental identification. Next we studied nuclear systems containing more than one antikaon embedded in the nuclear medium, as well as hadronic systems with extensive fraction of strangeness composed of large number of nucleons, hyperons, and antikaons. The principal question here was whether or not kaon condensation could occur in strong-interaction self-bound strange hadronic matter. In our most recent works, we revisited the domain of single-$\bar{K}$ nuclei and replaced the relativistic mean-field approach by a chirally motivated model. The in-medium $\bar{K}N$ scattering amplitudes, resulting from a chirally motivated coupled-channel model, were used to construct the $\bar{K}$–nucleus potential and calculate $\bar{K}$–nuclear quasi-bound states. Since all relevant results of our work have already been reported in various journals, in Chapter 3 we just highlight our main results. A comprehensive and detailed discussion of our calculations and their outcome can be found in selected publications in Appendix A. Finally, a summary with conclusions and outlook is given in Chapter 4.

Chapter 1

Introduction

Ever since their discovery in late forties kaons and antikaons have participated in many breakthrough advancements in particle physics. To explain slow decay of kaons but simultaneously their fast (and always in pairs) production in pion–proton reactions the 'strangeness' quantum number was introduced and its conservation in strong interactions postulated. Later this led to development of quark model and thus to establishing foundations of the standard model of particle physics. The violation of CP symmetry was discovered in the decays of neutral kaons.

The topical importance of kaons and antikaons emerged when kaons were identified with the pseudo-Nambu–Goldstone bosons of spontaneously broken (approximate) chiral $\mathrm{SU}(3)_L \times \mathrm{SU}(3)_R$ symmetry of strong interactions. Hence, the interaction of kaons and their properties in the nuclear medium encode important aspects of the nature of chiral symmetry of quantum chromodynamics (QCD), its breaking and restoration. The issue of antikaons in the nuclear medium has attracted considerable attention since the kaon condensation was proposed to possibly take place in dense nuclear matter, realized perhaps in the core of neutron stars. Recent theoretical and experimental interest has focused on the possible existence of deeply-bound $\bar{K}$–nuclear states.

In the following, we first discuss basic properties of interactions of antikaons with nucleons and elucidate their complexity that is reflected further in the attempts to understand many-body systems with antikaons. A separate section is devoted to antikaonic atoms as they represent a significant source of information on the antikaon–nucleus interaction and a strict test to be passed by any theoretical model. After that, the still unclear issue of the possible existence of $\bar{K}$–nuclear quasi-bound states is overviewed. Finally, in the last part of the introduction, the possible role of antikaons in dense nuclear matter is discussed.

1.1 Antikaon–Nucleon Interaction

While the kaon–nucleon interaction is weakly repulsive (see e.g. Ref. [1] for a review), the antikaon–nucleon interaction is strongly attractive (particularly in the isospin $I = 0$

channel). In addition to the attraction in the elastic $\bar{K}N$ channel the coupling to the $\pi\Sigma$ channel is almost equaly strong. The characteristic feature of the $\bar{K}N$ system that dominates the interaction at low energies is the existence of the $\Lambda(1405)$ resonance lying just 27 MeV below the $\bar{K}N$ threshold. The $\Lambda(1405)$ was predicted as a $\bar{K}N$ quasi-bound state first by Dalitz *et al.* within the vector-meson exchange model [2]. The $\bar{K}N$ interaction was demonstrated to be strong enough to bind $\Lambda(1405)$ also in the Jülich meson-exchange model [3]. Conventionally, $\Lambda(1405)$ is viewed as a meson–baryon quasi-bound state coupled to the $\pi\Sigma$ and $\bar{K}N$ channels [4]; but it can also be considered a standard 'qqq' baryon [5] or even a pentaquark state [6]. Recently, it was found that chiral models generate two poles in the complex energy plane that can be associated with the $\Lambda(1405)$ resonance [7,8]. The 'two-pole' structure is supported by the analysis of the $K^-p \to \pi^0\pi^0\Sigma^0$ measurement [9], however, it is still not clear if these experimental data are compatible with the shape of $\Lambda(1405)$ obtained in other experiments. The actual nature of the $\Lambda(1405)$ resonance thus still remains a puzzling problem.

The available experimental data near and above the $\bar{K}N$ threshold contain valuable information about the low-energy $\bar{K}N$ interaction. The data include precise measurements of the K^-p reaction branching ratios [10,11] as well as measurements of the K^-p scattering and reaction cross sections [12–14] that are unfortunately subject to large experimental errors, particularly near the K^-p threshold. Moreover, the data base was recently supplemented by new measurements of the strong interaction effects on the $1s$ atomic state in kaonic hydrogen [15–17].

Following the success in the SU(2) pion–nucleon sector (see e.g. Ref. [18] for a comprehensive overview), attempts have been made to consistently formulate chiral perturbation theory, the low-energy effective theory of QCD, also in the strangeness sector. However, the strangeness sector requires a special care – the antikaon–nucleon interaction is strongly influenced by the $\Lambda(1405)$ resonance rendering the standard chiral perturbation theory inapplicable. To deal with such nonperturbative nature of the $\bar{K}N$ interaction one has to resort to resummation techniques based on the Lippman–Schwinger [19,21] or Bethe–Salpeter equation [20,22–25]. The $\Lambda(1405)$ resonance is then generated dynamically as a $\bar{K}N$ quasi-bound state embedded in the $\pi\Sigma$ continuum.

Needless to say, consistent conclusions on the $\bar{K}N$ interaction are essential for reliable claims about the behavior of $\bar{K}$ mesons in more complex systems. Unfortunately, while chiral perturbation theory together with multichannel T-matrix resummation techniques provide satisfactory description of the $\bar{K}N$ data at and near above threshold, the

subthreshold extrapolations are still burdened by theoretical uncertainties.

1.2 Antikaonic Atoms

Hadronic atoms, in general, are important source of information on strong interactions of hadrons with the nuclear medium at low energies. Owing to much larger mass than the electron, the wavefunction of a hadron captured in an atomic state has a significant overlap with the nuclear density distribution ρ. This allows us to extract the in-medium hadron–nucleon t-matrix in a broad range of nuclear densities. In most cases, excluding very light hadronic atoms, the analysis of large data sets of atomic energy-level shifts, widths and yields is done by fitting optical potentials in a $V_K = t\rho$ form, where t is the hadron–nucleon scattering amplitude. So far, π^-, K^-, Σ^-, and $\bar{p}$ hadronic atoms have been observed and studied. For a comprehensive review see Ref. [1].

In case of K^- atoms, the data base consists of 65 energy-level shifts, widths, and transition yields that span a wide range of nuclei from ^{7}Li to ^{238}U (in addition to kaonic hydrogen [17], deuterium [26] and helium [27]). To analyze the data of kaonic atoms either phenomenological or chirally inspired approaches were used. Phenomenological approaches employ empirical density-independent amplitudes t as well as density-dependent amplitudes $t(\rho)$ for the construction of the optical potential. As shown in Ref. [28], reasonably good agreement with experimental data is achieved even for $t\rho$ optical potentials with depths $-\mathrm{Re}\, V_K \gtrsim 100$ MeV for medium-weight and heavy nuclei when extrapolated to the nuclear matter density. However, much improved description of the data is provided by density-dependent amplitudes or the relativistic mean-field methodology that results in very deep optical potentials of order $-\mathrm{Re}\, V_K \approx 150-200$ MeV with substantial absorptivity $-\mathrm{Im}\, V_K \approx 60-80$ MeV [1,29–31]. On the other hand, chirally motivated approaches start with a microscopically constructed energy- and density-dependent scattering amplitude $t(\sqrt{s},\rho)$ which is constrained by low-energy $\bar{K}N$ scattering data. Usually, the $\bar{K}N$ scattering amplitude was evaluated at the $\bar{K}N$ threshold energy and the potentials thus generated were considerably shallower $-V_K \approx 110-120$ MeV [32] than the phenomenological ones. Yet, even shallower potentials $-V_K \approx 50$ MeV were obtained when the K^- self-energy, taking into account medium effects, was self-consistently included in the construction of the K^- optical potential [33–35]. However, no chirally motivated model was able to reproduce deep K^- optical potentials and satisfactorily describe the data of kaonic atoms by now. We demonstrated in Ref. [36] that considerably deeper potentials are obtained when the

subthreshold $\bar{K}N$ energy domain is identified as the relevant region for the construction of the optical potential. Still, to achieve satisfactory agreement with the K^-–atom data, phenomenological terms had to be added to chirally motivated V_K. The phenomenological part was found to be heavily dominated by ρ^2 contributions that might correspond to multi-nucleonic processes not addressed by present chiral models. The idea that for kaonic atoms, with energies essentially at $\bar{K}$–nucleus threshold, the subthreshold $\Lambda(1405)$ resonance plays a dominant role in causing the in-medium $\bar{K}N$ scattering amplitude to become more attractive below the $\bar{K}N$ threshold was already proposed in Refs. [40–42]. The 'deep' vs. 'shallow' controversy of K^-–nuclear optical potentials is further discussed in the following section where additional estimates for V_K are considered.

1.3 Antikaon–Nucleus Interaction

As discussed in the previous section, the phenomenology of kaonic atoms clearly favors deep attractive K^-–nuclear potentials and thus supports the existence of deeply bound $\bar{K}$ nuclear states. However, this does not necessarily imply that such states would be sufficiently narrow to be resolved unambiguously in experiment. The depth of the $\bar{K}$–nucleus optical potential is decisive to answer whether the strong absorption of $\bar{K}$ mesons in the nuclear medium due to the $\bar{K}N \to \pi\Sigma, \pi\Lambda$ and $\bar{K}NN \to \Sigma N, \Lambda N$ processes could be suppressed by the $\bar{K}$–nucleus binding effects. Despite vigorous theoretical and experimental effort this issue still remains an unresolved problem. Various theoretical estimates for V_K are listed below:

- An order of magnitude estimate of the $\bar{K}$–nucleus interaction may be provided by the leading-order Tomozawa–Weinberg (TW) term of the chiral SU(3) effective Lagrangian that, when treated in Born approximation, leads already to a sizeable attraction at nuclear matter density:

$$V_K = -\frac{3}{8f_\pi^2}\,\rho \approx -55\,\frac{\rho}{\rho_0}\ \text{MeV},$$

  with $\rho_0 = 0.16$ fm^{-3} and the pseudoscalar decay constant $f_\pi \approx 93$ MeV. As already mentioned, this attraction is roughly doubled, $V_K \approx -100$ MeV, when the TW together with next-to-leading order terms are iterated in the $\bar{K}N - \pi\Sigma - \pi\Lambda$ coupled-channel in-medium Lippmann–Schwinger or Bethe-Salpeter equations [32]. However, potentials as shallow as $V_K \approx -50$ MeV are obtained, when the $\bar{K}$ self-energy in

the nuclear medium is taken into account self-consistently in the construction of V_K [34, 35]. When, in addition to hadron self-energies, the $\bar{K}$-nucleus kinematics is taken into account, the resulting potential depths become $V_K \approx -100$ MeV [36–38].

- The estimate based on the QCD sum-rules [39] leads to:

$$V_K \sim \frac{m_s}{m_N}\Sigma_N^{(s)} - \frac{1}{2}\Sigma_N^{(v)} \sim -130 \text{ MeV},$$

with the scalar and vector nucleon self-energies $\Sigma_N^{(s)}$, $\Sigma_N^{(v)}$; and the (current) strange quark and nucleon masses m_s, m_N.

- Similarly, the relativistic mean field estimate gives:

$$V_K \sim \frac{1}{3}\left(\Sigma_N^{(s)} - \Sigma_N^{(v)}\right) \sim -170 \text{ MeV},$$

where the factor 1/3 comes from the fact that, in the constituent quark model, the $\bar{K}$ meson contains one nonstrange antiquark compared to three nonstrange quarks in the nucleon [43, 44].

- An estimate of $V_K \approx -80$ MeV results from the analysis of the K^+/K^- production cross section ratios in the proton–proton and proton–nucleus collisions measured by the KaoS collaboration at GSI [45]. In the underlying transport calculations the two-nucleon absorption processes were apparently not considered, thus deeper potentials may arise once nonmesonic decay channels are included.

- In Ref. [46], it was shown that the capture rates of the (K^-_{stop}, π) reactions to specific Λ-hypernuclear states are sensitive to the strength of the $\bar{K}$–nuclear potentials. Although no conclusive results were obtained, deep $\bar{K}$ optical potentials are favored.

Current experimental interest in searching for deeply bound K^--nuclear states was triggered by suggestion to look for such states in the in-flight (K^-, p) reaction [47] and in the $\bar{K}NNN$ $I = 0$ system bound by $B_K \approx 100$ MeV when the dominant decay channel $\bar{K}N \to \pi\Sigma$ would be kinematically closed, resulting in a fairly narrow decay width [48] (as conjectured already in [49]). Subsequently, several candidates for deeply bound K^- states were reported:

- Controversial evidence of relatively narrow deeply bound states in the $(K^-_{\rm stop}, p(n))$ reactions on ^{4}He (KEK-PS E471) [50, 51] that has been revoked later (KEK-PS E549/570) [52].

- A possible explanation in terms of K^- bound states of few statistically weak irregularities of the neutron spectrum in the (K^-, n) in-flight reaction on ^{16}O (BNL-AGS, parasite E930) [53] not confirmed by the subsequent study of the $(K^-, p(n))$ reactions on ^{12}C (KEK-PS E548) [54].

- The FINUDA collaboration claimed evidence of the deeply bound K^-pp state in the $K^-_{\rm stop}$ reactions on ^{6}Li and ^{12}C by observing back-to-back Λp pairs coming from $K^-pp \to \Lambda p$ [55]. But these pairs could result from conventional absorption processes when final state interaction is taken into account as shown in Ref. [56]. The $K^-_{\rm stop}\, pn \to \Sigma^- p$ reaction on ^{6}Li was also studied [57].

- Observation of a very deeply bound and narrow ($B \sim 160$ MeV, $\Gamma \sim 30$ MeV) K^-pp state based on the analysis of Λp pairs in $\bar{p}$ annihilation on ^{4}He at the OBELIX spectrometer at LEAR, CERN [58]. However, in this experiment one can not rule out the possibility that the Λp pairs assigned to the K^-pp decay come from the mesonic decay of a different K^- cluster, like the $\bar{K}NNN$ $I = 0$ state. Moreover, the large value of the reported binding energy disagrees with all existing few-body calculations.

- Evidence of the $\bar{K}NNN$ $I = 0$ state with $B = 58 \pm 6$ MeV, $\Gamma = 37 \pm 14$ MeV has been presented by the FINUDA collaboration [59].

- Yamazaki *et al.* claimed evidence of the K^-pp state in the $pp \to K^+\Lambda p$ reaction in a reanalysis of the DISTO data [60].

The issue of deeply bound K^-–nuclear states is far from being settled and further dedicated systematic studies are necessary. Fortunately, fully exclusive study of the $K^- + {}^3$He $\to n+[\bar{K}[NN]_{I=1}]_{I=\frac{1}{2},I_3=+\frac{1}{2}}$ reaction is scheduled as day-one experiment at the J-PARC facility and further studies of the $\bar{K}$–nucleus interaction are part of the future scientific program at world laboratories.

Not only from the experimental point of view the issue of the possible existence of deeply-bound $\bar{K}$–nuclear states represents a challenging task. The complicated coupled-channel nonperturbative nature of the $\bar{K}N$ interaction poses a difficult problem for theoretical models. Few-body $\bar{K}NN$ and $\bar{K}NNN$ systems were studied using variational

techniques or Faddeev equations with phenomenological [48,61,62] as well as chiral potentials [63–68]. For heavier nuclei, where the mean-field concept is applicable, the $\bar{K}$–nuclear states were studied within the relativistic mean-field methodology [31,69] or, more recently, within models motivated by chiral effective field theory [37, 70]. All calculations agree on $\bar{K}$–nuclear configurations being bound, however, differ largely in the predicted binding energies and widths of such states.

The knowledge of the interaction of $\bar{K}$ mesons with a 'conventional' form of nuclear matter represents a pathway to understanding the peculiar role of strangeness in dense hadronic matter.

1.4 Antikaons in Dense Nuclear Matter

There is growing evidence that strangeness degrees of freedom might play an important role in dense hadronic matter. Besides hyperons that are likely to appear in dense baryonic matter [71], the possibility of kaon condensation was proposed by Kaplan and Nelson [72, 73]. Ever since, much attention was devoted to the question of antikaons in dense matter (see e.g. Refs. [74–79] for a comprehensive review).

Neutron stars, with densities extending several times normal nuclear density, offer the most natural dense systems where kaon condensation could be realized. In neutron stars, where weak interaction time-scales are operative, strangeness changing processes like $e^- \rightarrow \nu_e K^-$ allow for conversion of high-pressure electron gas into kaon condensate once the kaon effective mass drops below $m_K^* \lesssim 200$ MeV. Recalling that antikaons undergo attraction of approximately 100 MeV per density unit of ρ_0 [80], it was shown that the kaon condensation might occur at densities as low as $\rho \sim 3\rho_0$ or higher, depending on whether or not hyperons are taken into account [81]. On the other hand, in Ref. [80], the onset of kaon condensation does not emerge at all for a large range of densities examined. Once antikaons are considered relevant degrees of freedom of dense hadronic matter, the resulting equation of state becomes much softer. Still, for a long time this was in accordance with the limit of 1.5 solar masses $M_\odot$ for the mass of all observed neutron stars. However, the argument is no more valid due to the recent observation of the $M \approx 2M_\odot$ neutron star PSR J1614-2230 [82].

Under laboratory conditions, heavy ion collisions represent an ideal tool to study in-medium properties of antikaons in dense matter. However, in heavy ion collisions, where the processes of equilibration and hadronization subsequent to dense matter formation

occur over much shorter times, strong interactions govern the composition of matter. Still, if antikaons are strongly bound in nuclei, as argued in Ref. [83], $\bar{K}$ mesons could be the relevant degrees of freedom of self-bound strange hadronic matter, realized as multi-$\bar{K}$ nuclei. The $\bar{K}$ binding energy B_K is required to exceed $B_K \gtrsim m_K + m_N - m_\Lambda \approx 320$ MeV, thus allowing the $\Lambda \to \bar{K}N$ conversion in matter. The Λ and Ξ hyperons would no longer appear as constituents of a more conventional kaon-free form of strange matter [84]. However, the densities of $\rho \sim 3\rho_0$, required for the onset of $\bar{K}$ condensation, are unlikely to be encountered in these strange hadronic nuclei [69,104]. Yet, precursor phenomena to kaon condensation might be observed when the $\bar{K}$ binding energy reaches $B_K \gtrsim m_K + m_N - m_\Sigma \approx 240$ MeV. In this case the only available $\bar{K}$ absorption mechanism would be the fairly weak $\bar{K}NN \to \Lambda N$ process. The issue of multi-$\bar{K}$ nuclei and hypernuclei was studied by us in Ref. [104, 105] where the $\bar{K}$ binding energies, as well as the associated nuclear density distributions were found to saturate upon increasing the number of antikaons embedded in the medium. Since the calculated binding energies did not generally exceed 200 MeV it was deemed that kaon condensation is unlikely in self-bound strange hadronic matter. Similar results were obtained in Ref. [85–87] within the nuclear liquid drop model.

Chapter 2

Methodology

In our work we focused on the study of $\bar{K}$–nuclear states in heavier nuclear systems where the mean-field concept is applicable. We employed the relativistic mean-field theory (RMF) which has proven to be successful in calculations of various nuclear properties, as well as in studies of hypernuclei and allows straightforward inclusion of the $\bar{K}$ meson degrees of freedom.

Later in our calculations we replaced the RMF meson-exchange picture of the $\bar{K}$-nucleon interaction by a chirally motivated approach. In this approach, we constructed the $\bar{K}$ meson self-energy operator from the microscopic in-medium chiral $\bar{K}$-nucleon scattering amplitudes calculated within the nonperturbative coupled-channel formalism.

2.1 Relativistic Mean Field Model

The starting point of the relativistic mean filed theory is the meson-exchange picture of the strong nucleon–nucleon interactions. In RMF [88], the nucleus is described as a system of nucleons, represented by the Dirac field, interacting through the exchange of several intermediate-boson fields. The isoscalar-scalar σ-meson field is responsible for the attraction between nucleons, whereas the isoscalar-vector ω-meson field acts repulsively between nucleons. The isovector-vector ρ-meson field is introduced to tune the isospin interaction. Finally, the photon field (A) accounts for the electromagnetic interaction. The π and η mesons with unnatural parity are not included because we are working with nuclear states which have well-defined parity.

The model Lagrangian density then reads:

$$\begin{aligned}\mathcal{L}_{\mathrm{RMF}} &= \bar{\psi}[\mathrm{i}\not{\partial} - (m_N - g_{\sigma N}\sigma)]\psi \\ &+ \frac{1}{2}\partial_\mu\sigma\partial^\mu\sigma - \frac{1}{2}m_\sigma^2\sigma^2 + \frac{1}{3}g_2\sigma^3 - \frac{1}{4}g_3\sigma^4 \\ &- \frac{1}{4}(\partial_\mu\omega_\nu - \partial_\nu\omega_\mu)(\partial^\mu\omega^\nu - \partial^\nu\omega^\mu) + \frac{1}{2}m_\omega^2\omega_\mu\omega^\mu + \frac{1}{4}d(\omega_\mu\omega^\mu)^2 \\ &- \frac{1}{4}(\partial_\mu\vec{\rho}_\nu - \partial_\nu\vec{\rho}_\mu)(\partial^\mu\vec{\rho}^\nu - \partial^\nu\vec{\rho}^\mu) + \frac{1}{2}m_\rho^2\vec{\rho}_\mu\cdot\vec{\rho}^\mu \\ &- \frac{1}{4}(\partial_\mu A_\nu - \partial_\nu A_\mu)(\partial^\mu A^\nu - \partial^\nu A^\mu),\end{aligned} \tag{2.1}$$

with ψ denoting the nucleon iso-doublet:

$$\psi = \begin{pmatrix}\psi_p \\ \psi_n\end{pmatrix}, \tag{2.2}$$

and covariant derivative:

$$D_\mu = \partial_\mu + \mathrm{i}g_{\omega N}\omega + \mathrm{i}\vec{\rho_\mu}\cdot\vec{\tau} + \mathrm{i}e\tfrac{1}{2}(1+\tau_3)A_\mu. \tag{2.3}$$

The arrows indicate iso-vector quantities, the dot denotes inner product, and $\vec{\tau}$ stands for the triplet of Pauli matrices. The m_σ, m_ω, and m_ρ are the σ-, ω-, and ρ-meson masses, respectively. The $g_{\sigma N}$, $g_{\omega N}$, $g_{\rho N}$, and e are the σ-, ω-, ρ-meson and photon couplings to the nucleon, respectively. The g_2, g_3 and d represent the strengths of the scalar σ and vector ω field self-interaction. The meson coupling constants are specified by the RMF model parametrization. In our work we considered both the linear L-HS [89] and nonlinear NL-SH [90], NL-TM1(2) [91] RMF models.

Using the principle of stationary action:

$$\frac{\delta S[q_j]}{\delta q_j} = \frac{\delta}{\delta q_j}\int \mathrm{d}^4x\,\mathcal{L}\left[q_j(x), \partial_\mu q_j(x)\right] = 0, \tag{2.4}$$

where q_j is a generalized coordinate, $q_j = \psi, \bar{\psi}, \sigma, \omega_\mu, \vec{\rho}_\mu, A_\mu$, leads to field equations of motion:

$$\partial_\mu\left[\frac{\delta\mathcal{L}}{\delta(\partial_\mu q_j)}\right] - \frac{\delta\mathcal{L}}{\delta q_j} = 0. \tag{2.5}$$

The Lagrangian density (2.1) thus yields the Dirac equation for nucleon:

$$[\,\mathrm{i}\partial\!\!\!/ - (m_N - g_{\sigma N}\sigma) - g_{\omega N}\gamma_\mu\omega^\mu - g_{\rho N}\gamma_\mu\vec{\tau}\cdot\vec{\rho}^\mu - e\gamma_\mu\tfrac{1}{2}(1+\tau_3)A^\mu]\psi = 0 \tag{2.6}$$

and the Klein–Gordon, Proca, and Maxwell equations for the intermediate-boson fields:

$$\begin{aligned}
\left(\partial_\nu\partial^\nu + m_\sigma^2\right)\sigma &= g_{\sigma N}\bar{\psi}\psi + g_2\sigma^2 - g_3\sigma^3,\\
\partial_\mu(\partial^\mu\omega^\nu - \partial^\mu\omega^\nu) + m_\omega^2\omega^\nu &= g_{\omega N}\bar{\psi}\gamma^\nu\psi - d\,\omega^\nu(\omega_\mu\omega^\mu),\\
(\partial_\mu - g_{\rho N}\vec{\rho}_\mu\times)(\partial^\mu\vec{\rho}^\nu - \partial^\mu\vec{\rho}^\nu) + m_\rho^2\vec{\rho}^\nu &= g_{\rho N}\bar{\psi}\gamma^\nu\vec{\tau}\psi,\\
\partial_\mu(\partial^\mu A^\nu - \partial^\mu A^\nu) &= e\bar{\psi}\tfrac{1}{2}(1+\tau_3)\gamma^\nu\psi.
\end{aligned} \tag{2.7}$$

Equations (2.6)-(2.7) are coupled non-linear quantum field equations and their exact solution is enormously complicated. Moreover, since we expect the coupling constants (except e) to be large, perturbative approaches are not useful. Fortunately, there exists an approximative solution, which becomes more and more valid as the nuclear density increases [88]. Namely, as the source terms on the r.h.s. of eq. (2.7) increase, the meson field operators can be replaced by their vacuum expectation values, which are classical fields.

Furthermore, symmetries simplify the calculations considerably. We are looking for the nuclear ground states of doubly magic nuclei, and these are spherically symmetric. Rotational invariance implies that space-like components of the intermediate-boson fields vanish. In this case, the meson fields and also the source terms on the r.h.s. of the equations of motion (2.7) depend only on the radial coordinate r. The electromagnetic charge conservation prohibits the charged components of the ρ-meson from appearing as classical fields. Finally, since we are looking for stationary states, the time-derivatives of the boson fields vanish. Altogether, the meson fields are replaced by:

$$\begin{aligned}
\sigma(x) &\longrightarrow \langle\,\sigma(x)\,\rangle = \sigma(r),\\
\omega_\mu(x) &\longrightarrow \langle\,\omega_\mu(x)\,\rangle = \delta_{\mu 0}\,\omega(r),\\
\rho_\mu^i(x) &\longrightarrow \langle\,\rho_\mu^i(x)\,\rangle = \delta_{\mu 0}\,\delta^{i3}\,\rho(r),\\
A_\mu(x) &\longrightarrow \langle\,A_\mu(x)\,\rangle = \delta_{\mu 0}\,A(r)\,.
\end{aligned} \tag{2.8}$$

Moreover, in the traditional RMF approach, the contribution of antiparticles is not directly

considered. In this so called no-sea approximation the nucleon field is expanded as:

$$\psi(x) = \sum_{i \leq A} \psi_i(x) \hat{a}_i, \tag{2.9}$$

where the summation runs only over occupied positive-energy levels. The $\psi_i(x)$ now represents the wavefunction of a state i annihilated by the operator $\hat{a}_i$. With these assumptions we can rewrite the field equations (2.6)-(2.7) in the form:

$$\begin{aligned}
&[-\mathrm{i}\alpha \cdot \nabla + (m_N - g_{\sigma N}\sigma)\beta + g_{\omega N}\omega + g_{\rho N}\tau_3\rho + e\,\tfrac{1}{2}(1+\tau_3)A]\psi_i = E_i\,\psi_i,\\
&(-\nabla^2 + m_\sigma^2)\sigma = g_{\sigma N}\rho_s + g_2\sigma^2 - g_3\sigma^3,\\
&(-\nabla^2 + m_\omega^2)\omega = g_{\omega N}\rho_v - d\,\omega^4,\\
&(-\nabla^2 + m_\rho^2)\rho = g_{\rho N}\rho_3,\\
&\qquad -\nabla^2 A = e\,\rho_p,
\end{aligned} \tag{2.10}$$

where $E_i = \mathrm{i}\partial_t \psi_i$. At this stage, it is possible to solve the equations numerically.

The densities on the r.h.s. of (2.10) are defined as:

$$\begin{aligned}
\rho_s &= \langle 0| : \bar{\psi}\psi : |0\rangle &&= \sum_{i \leq A} \bar{\psi}_i \psi_i,\\
\rho_v &= \langle 0| : \psi^\dagger \psi : |0\rangle &&= \sum_{i \leq A} \psi_i^\dagger \psi_i,\\
\rho_3 &= \langle 0| : \psi^\dagger \tau_3 \psi : |0\rangle &&= \sum_{i \leq A} \psi_i^\dagger \vec{\tau} \psi_i,\\
\rho_p &= \langle 0| : \psi^\dagger \tfrac{1}{2}(1+\tau_3)\psi : |0\rangle &&= \sum_{i \leq A} \psi_i^\dagger \tfrac{1}{2}(1+\tau_3)\psi_i,
\end{aligned} \tag{2.11}$$

where the no-sea approximation allows simple evaluation of the vacuum ($\equiv$ nuclear ground state) expectation values of normal ordered quantum field operators ($\langle 0| : . : |0\rangle$). The vector densities are normalized accordingly to yield proper (conserved) charges:

$$\begin{aligned}
&\int \mathrm{d}^3x\, \rho_v = A,\\
&\int \mathrm{d}^3x\, \rho_3 = Z - N,\\
&\int \mathrm{d}^3x\, \rho_p = Z,
\end{aligned} \tag{2.12}$$

with the nucleon number A, proton number Z, and neutron number N.

The total energy of the system E is a vacuum expectation value of the Hamiltonian

obtained via the Legendre transform of the Lagrangian:

$$\begin{aligned} E = \langle : H : \rangle &= \langle : p_i \dot{q}_i - L : \rangle = \int \mathrm{d}^3x \; (E_i \psi_i^\dagger \psi_i - \langle : \mathcal{L} : \rangle) \\ &= \int \mathrm{d}^3x \, \big\{ \langle : \bar{\psi}[-\mathrm{i}\alpha \cdot \nabla + m_N - g_{\sigma N}\sigma + g_{\omega N}\omega + g_{\rho N}\tau_3\rho + e\tfrac{1}{2}(1+\tau_3)]\psi : \rangle \\ &+ \tfrac{1}{2}[(\nabla\sigma)^2 + m_\sigma^2\sigma^2] - \tfrac{1}{2}[(\nabla\omega)^2 + m_\omega^2\omega^2] - \tfrac{1}{2}[(\nabla\rho)^2 + m_\rho^2\rho^2] - \tfrac{1}{2}(\nabla A)^2 \\ &- \tfrac{1}{3}g_2\sigma^3 + \tfrac{1}{4}g_3\sigma^4 + \tfrac{1}{4}\, d\, \omega^4 \big\} \, . \end{aligned} \tag{2.13}$$

The vanishing of boson fields at large distances allows us to perform the following partial integration:

$$\begin{aligned} \frac{1}{2}\int \mathrm{d}^3x \; (\nabla\sigma)^2 + m_\sigma^2\sigma^2 &= \frac{1}{2}\int \mathrm{d}^3x \; \sigma(-\nabla^2 + m_\sigma^2)\sigma \\ &= \frac{1}{2}\int \mathrm{d}^3x \; \sigma(g_{\sigma N}\rho_s + g_2\sigma^2 - g_3\sigma^3). \end{aligned} \tag{2.14}$$

Similar manipulations for remaining fields, using normalization conditions (2.12) and Euler–Lagrange equations (2.10), lead to the final expression for the total energy:

$$\begin{aligned} E = \sum_{i\le A} E_i &+ \frac{1}{2}\int \mathrm{d}^3x \; (g_{\sigma N}\,\sigma\rho_s - g_{\omega N}\,\omega\rho_v - g_{\rho N}\,\rho\rho_3 - e\,A\rho_p) \\ &+ \frac{1}{2}\int \mathrm{d}^3x \; (\tfrac{1}{3}g_2\,\sigma^3 - \tfrac{1}{2}g_3\,\sigma^4 - \tfrac{1}{2}d\,\omega^4). \end{aligned} \tag{2.15}$$

2.1.1 RMF with Strangeness Degrees of Freedom

The RMF methodology introduced in the preceding section can be extended in a rather straightforward way to incorporate strangeness degrees of freedom. In the following we separately discuss the inclusion of antikaon and hyperon degrees of freedom together with the phenomenological input that was used to constrain the model.

2.1.1.1 Antikaons

To extend the RMF methodology in order to incorporate antikaons we introduced an isospin doublet of complex scalar fields:

$$K = \begin{pmatrix} K^+ \\ K^0 \end{pmatrix}, \quad K^\dagger = \begin{pmatrix} K^- & \bar{K}^0 \end{pmatrix}, \tag{2.16}$$

where K^0 and K^+ denote neutral and positively charged kaons and $\bar{K}^0$ and K^- their corresponding antiparticles. Subsequently, we added to the nuclear RMF Lagrangian (2.1) the Lagrangian $\mathcal{L}_K$:

$$\mathcal{L}_K = (D_\mu K)^\dagger (D^\mu K) - m_K^2 K^\dagger K + g_{\sigma K} m_K \sigma K^\dagger K + g_{\sigma^* K} m_K \sigma^* K^\dagger K, \tag{2.17}$$

where the covariant derivative D_μ involves the interaction of antikaons with vector ω, ρ, ϕ and photon fields:

$$\mathcal{D}_\mu \equiv \partial_\mu + \mathrm{i} g_{\omega K} \omega_\mu + \mathrm{i} g_{\rho K} \vec{I} \cdot \vec{\rho}_\mu + \mathrm{i} g_{\phi K} \phi_\mu + \mathrm{i} e (I_3 + 1/2\mathcal{Y}) A_\mu, \tag{2.18}$$

where I is the isospin operator, I_3 its third component, and $\mathcal{Y}$ stands for hypercharge. In Eq. (2.17), m_K, $g_{\sigma K}$, $g_{\sigma^* K}$, $g_{\omega K}$, $g_{\rho K}$, and $g_{\phi K}$ are the antikaon mass and coupling constants to the σ, σ^*, ω, ρ, and ϕ mesons, respectively. The 'hidden strangeness' scalar σ^* and vector ϕ fields that mediate the interaction exclusively between strange particles are introduced together with the corresponding free-field Lagrangian:

$$\begin{aligned} \mathcal{L}_{\sigma^*\phi} = & \frac{1}{2}\partial_\mu \sigma^* \partial^\mu \sigma^* - \frac{1}{2} m_{\sigma^*}^2 \sigma^{*2} \\ & - \frac{1}{4}(\partial_\mu \phi_\nu - \partial_\nu \phi_\mu)(\partial^\mu \phi^\nu - \partial^\nu \phi^\mu) + \frac{1}{2} m_\phi^2 \phi_\mu \phi^\mu, \end{aligned} \tag{2.19}$$

where m_{σ^*} and m_ϕ are the σ^*- and ϕ-meson masses, respectively. The full model Lagrangian thus reads:

$$\mathcal{L} = \mathcal{L}_{\mathrm{RMF}} + \mathcal{L}_{\sigma^*\phi} + \mathcal{L}_K. \tag{2.20}$$

Again, by minimizing the action, together with the RMF simplifications discussed previously for the purely nuclear case, $\mathcal{L}_K$ leads to the Klein–Gordon equation for antikaons:

$$(-\nabla^2 - \omega_K^2 + m_K^2 + \Pi_K) K^- = 0, \tag{2.21}$$

with $\omega_K = \mathrm{i}\partial_t K^-$ and the antikaon self-energy Π_K given by:

$$\begin{aligned} \Pi_K = & - g_{\sigma K} m_K \sigma - g_{\sigma^* K} m_K \sigma^* - 2\omega_K (g_{\omega K}\omega + g_{\rho K}\rho + g_{\phi K}\phi + eA) \\ & - (g_{\omega K}\omega + g_{\rho K}\rho - g_{\phi K}\phi + eA)^2. \end{aligned} \tag{2.22}$$

For the antikaon couplings to the vector meson fields we adopted a purely F-type,

vector SU(3) symmetry:

$$2g_{\omega K} = 2g_{\rho K} = \sqrt{2}g_{\phi K} = g_{\rho\pi} = 6.04, \tag{2.23}$$

where $g_{\rho\pi}$ is due to the $\rho \to 2\pi$ decay width [80]. However, SU(3) symmetry is not of much help when fixing the K^- coupling constants to the scalar σ field. Since there is still no consensus about the microscopic nature of the σ field and its coupling to the $\bar{K}$ mesons, we treated $g_{\sigma K}$ as a free parameter and adjusted it to several values of the K^- binding energy in the range 50–150 MeV. Finally, the coupling constant to the σ^* field is taken from the $f_0 \to K\bar{K}$ decay to be $g_{\sigma^* K} = 2.65$ [80].

The original set of field equations (2.10) is supplemented by Eq. (2.21) and equations for the σ^* and ϕ fields:

$$\begin{aligned} (-\nabla^2 + m_\sigma^{*2})\sigma^* &= g_{\sigma^* K} m_K \rho_s^{(K)}, \\ (-\nabla^2 + m_\phi^2)\phi &= -g_{\phi K}\rho_v^{(K)}, \end{aligned} \tag{2.24}$$

with source terms induced only by antikaons:

$$\begin{aligned} \rho_s^{(K)} &= K^- K^+, \\ \rho_v^{(K)} &= (\omega_K + g_{\omega K}\omega + g_{\rho K}\rho - g_{\phi K}\phi + eA)K^- K^+. \end{aligned} \tag{2.25}$$

The presence of antikaons also generates additional source terms:

$$\begin{aligned} &+ g_{\sigma K} m_K \rho_s^{(K)}, \\ &- g_{\omega K}\rho_v^{(K)}, \\ &- g_{\rho K}\rho_v^{(K)}, \\ &- e\rho_v^{(K)} \end{aligned} \tag{2.26}$$

in the field equations (2.7).

The particular choice of the interaction scheme (2.18) results in $\rho_v^{(K)}$ being the conserved Noether current. This allows us to normalize the current to the appropriate number κ of antikaons in the system:

$$\int \mathrm{d}^3 x \rho_v^{(K)} = \kappa. \tag{2.27}$$

Further, the presence of antikaons alters the expression for the total energy of the

system which is supplemented by:

$$\begin{aligned}\delta E^{(K)} = \kappa\,\omega_K - \frac{1}{2}\int \mathrm{d}^3x\ \big[&(g_{\sigma K}\sigma + g_{\sigma^* K}\sigma^*)m_K\rho_s^{(K)} \\ &+(g_{\omega K}\,\omega + g_{\rho K}\,\rho + g_{\phi K}\,\phi + e\,A)\rho_v^{(K)}\big]\,.\end{aligned} \tag{2.28}$$

Absorption of Antikaons in the Nuclear Medium

One drawback of the RMF methodology for antikaons is that it does not directly address the absorption of antikaons in the nuclear medium. In our approach, we employed the optical model phenomenology where the K^-–nuclear states acquire a width by allowing the antikaon self-energy Π_K to become complex and replacing

$$\omega_K \to \omega_K - \mathrm{i}\frac{\Gamma_K}{2}. \tag{2.29}$$

The imaginary part of the K^- self-energy $\mathrm{Im}\,\Pi_K$ was constructed phenomenologically in a $t\rho$ form. The amplitude t was constrained by fits to kaonic atom data [31] and the nuclear density ρ was taken from RMF calculations. It is to be noted that the nuclear density was treated as a dynamical quantity in our self-consistent calculations. When the antikaon is embedded in the nuclear medium, the attractive $\bar{K}$-nucleus interaction leads to nuclear core polarization (increased nuclear density) and thus to increased widths of the $\bar{K}$–nuclear states. On the other hand, the binding energy of the antikaon reduces the phase space available for the decay products of the $\bar{K}$–nuclear states. The amplitude t was made energy dependent by introducing suppression factors, explicitly considering the $\bar{K}$ binding energy for the initial decaying state and assuming two-body final state kinematics.

The first considered decay channel is the pionic conversion mode on a single nucleon:

$$\bar{K}N \to \pi\Sigma,\ \pi\Lambda \qquad (70\%,\ 10\%), \tag{2.30}$$

with thresholds about 100 MeV and 180 MeV, respectively, below the $\bar{K}N$ total mass. The K^- self-energy operator corresponding to these processes is:

$$\mathrm{Im}\,\Pi_K^{(1)} = (0.7 f_{1\Sigma} + 0.1 f_{1\Lambda})V_0^{(1)}\,\rho(r), \tag{2.31}$$

where the factors 0.7 and 0.1 represent the branching ratios measured in the CERN bubble chamber experiments [92], the value of $V_0^{(1)}$ is determined by the kaonic atom fits and the

suppression factors f_{1Y} ($Y = \Sigma, \Lambda$) are given by:

$$f_{1Y} = \frac{M_{01}^3}{M_1^3}\sqrt{\frac{[M_1^2-(m_\pi+m_Y)^2][M_1^2-(m_Y-m_\pi)^2]}{[M_{01}^2-(m_\pi+m_Y)^2][M_{01}^2-(m_Y-m_\pi)^2]}}, \tag{2.32}$$

with $M_{01} = m_K + m_N$, $M_1 = M_{01} - B_K$, where B_K is the K^- binding energy.

The second considered decay channel is the non-pionic conversion mode on two nucleons:

$$\bar{K}NN \to YN \qquad (20\%), \tag{2.33}$$

with thresholds about $m_\pi \simeq 140$ MeV lower than the single-nucleon thresholds. Since this channel is heavily dominated by the ΣN final state, the ΛN channel was not considered. The corresponding part of the K^- self-energy is given by:

$$\mathrm{Im}\,\Pi_K^{(2)} = 0.2\, f_{2\Sigma} V_0^{(2)} \rho^2(r)/\rho_0, \tag{2.34}$$

where the constant 0.2 represents the branching ratio, $\rho_0 = 0.16$ fm^{-3} appears from dimensional requirements and $V_0^{(2)}$ is again determined from the kaonic atom data. The quadratic density dependence of this part is a direct consequence of the double scattering character of the multi-nucleon absorption process. The suppression factor $f_{2\Sigma}$ has the form:

$$f_{2\Sigma} = \frac{M_{02}^3}{M_2^3}\sqrt{\frac{[M_2^2-(m_N+m_\Sigma)^2][M_2^2-(m_\Sigma-m_N)^2]}{[M_{02}^2-(m_N+m_\Sigma)^2][M_{02}^2-(m_\Sigma-m_N)^2]}}, \tag{2.35}$$

with $M_{02} = m_K + 2m_N$ and $M_2 = M_{02} - B_K$.

p-Wave Interaction

Even though the $\bar{K}N$ p-wave interaction, dominated by the $\Sigma(1385)$ resonance, plays only a minor role near threshold, it might become increasingly important for the $\bar{K}$ tightly bound in a nucleus [93]. In order to examine the possible role of p waves, we have extended the K^- self-energy Π_K to incorporate the p-wave interaction through the phenomenological Kisslinger-form term [94]:

$$\Pi_K^{(P)} = 4\pi\left(1+\frac{\omega_K}{m_N}\right)^{-1}[\nabla\rho(r)]\cdot c_{KN}\nabla, \tag{2.36}$$

where c_{KN} is the parameter of a particular model of the p-wave interaction (see Refs. [37,69] for details).

2.1.1.2 Hyperons

As a next step of our calculations we studied behavior of antikaons when submerged into strange baryonic matter. To achieve a baryonic environment with large fraction of strangeness we considered many-body systems of SU(3) octet baryons N, Λ, Σ, and Ξ that can be made particle stable against strong interactions [95, 96]. The energy-release (Q) values for various conversion reactions of the type $B_1B_2 \to B_3B_4$:

reaction	Q (MeV)
$\Sigma^- p \to \Lambda n$	81
$\Sigma^+ n \to \Lambda p$	75
$\Sigma^- \Lambda \to \Xi^- n$	52
$\Sigma^+ \Lambda \to \Xi^0 p$	52
$\Sigma^- \Sigma^+ \to \Lambda\Lambda$	156
$\Sigma^+ \Xi^- \to \Xi^0 \Lambda$	80
$\Sigma^- \Xi^0 \to \Xi^- \Lambda$	75
$\Xi^- p \to \Lambda\Lambda$	28
$\Xi^0 n \to \Lambda\Lambda$	23

together with phenomenological guidance on hyperon-nucleus interactions suggest that only the conversions $\Xi^- p \to \Lambda\Lambda$ and $\Xi^0 n \to \Lambda\Lambda$ can be overcome by binding effects. It becomes possible then to form particle-stable multi-$\{N, \Lambda, \Xi\}$ configurations for which the conversion $\Xi N \to \Lambda\Lambda$ is Pauli blocked owing to the Λ orbitals being filled up to the Fermi level. Composite configurations with Σ hyperons are unlikely to be particle stable since the energy release in the $\Sigma N \to \Lambda N$ conversion is too high ($Q \gtrsim 75$ MeV) and, moreover, the Σ–nuclear potential is repulsive [97].

To include hyperons in the RMF methodology we added $\mathcal{L}_Y$ to the nuclear RMF Lagrangian:

$$\mathcal{L}_Y = \bar{Y} \left[\mathrm{i}\partial\!\!\!/ - (m_Y - g_{\sigma Y}\sigma - g_{\sigma^* Y}\sigma^*) \right] Y. \tag{2.37}$$

The Dirac field Y stands for hyperonic degrees of freedom of mass m_Y, interacting through the exchange of scalar (σ and σ^*) and vector (ω, ρ, ϕ, A) fields introduced by the covariant

derivative:

$$D_\mu = \partial_\mu + \mathrm{i}g_{\omega Y}\omega_\mu + \mathrm{i}g_{\rho Y}\vec{I}\cdot\vec{\rho}_\mu + \mathrm{i}g_{\phi Y}\phi_\mu + \mathrm{i}e(I_3 + \frac{1}{2}\mathcal{Y})A_\mu, \tag{2.38}$$

where g_{iY} represents coupling constants of hyperons to the corresponding fields.

The couplings of the Λ hyperon to vector mesons were fixed by SU(6) symmetry relations:

$$g_{\omega\Lambda} = \frac{2}{3}g_{\omega N},\ g_{\rho\Lambda} = 0,\ g_{\phi\Lambda} = -\frac{\sqrt{2}}{3}g_{\omega N}. \tag{2.39}$$

The coupling to the scalar σ field was fixed to reproduce the Λ-hypernuclear binding energies [98]. The coupling of the Λ hyperon to the σ^* field was fitted to the measured binding energies of double-Λ hypernuclei [99]. For Ξ hyperons, the SU(6) symmetry gives:

$$g_{\omega\Xi} = \frac{1}{3}g_{\omega N},\ g_{\rho\Xi} = -g_{\rho N},\ g_{\phi\Xi} = -2\frac{\sqrt{2}}{3}g_{\omega N}. \tag{2.40}$$

Because there is no experimental information on $\Xi(\Lambda) - \Xi$ interactions, we put $g_{\phi\Xi} = g_{\sigma^*\Xi} = 0$ to avoid parameters that might lead to unphysical consequences and that are expected to play a marginal role. The coupling to the scalar σ field was then constrained to yield an optical potential $\mathrm{Re}\,V_{\Xi^-} = -14$ MeV in the center of ^{12}C [100].

The Lagrangian (2.37) leads to the Dirac equation for hyperons:

$$[-\mathrm{i}\alpha\cdot\nabla + \beta(m_Y - g_{\sigma Y}\sigma - g_{\sigma^* Y}\sigma^*)g_{\omega Y}\omega + g_{\rho Y}I_3\rho + g_{\phi Y}\phi + e(I_3 + 1/2\mathcal{Y})A]\,Y_i = E_i Y_i, \tag{2.41}$$

where Y_i now represents the wavefunction of the hyperon Y (Λ, Ξ) in a state of energy E_i. Further, the presence of hyperons modifies the equations of motion for the meson and Coulomb fields by additional source terms that are to be added to the right hand sides of equations (2.7) and (2.24):

$$\begin{aligned}
g_{\sigma Y}\rho_s^{(Y)} &= g_{\sigma Y}\bar{Y}_i Y_i,\\
g_{\omega Y}\rho_v^{(Y)} &= g_{\omega Y}Y_i^\dagger Y_i,\\
g_{\rho Y}\rho_3^{(Y)} &= g_{\rho Y}Y_i^\dagger I_3 Y_i,\\
e\rho_c^{(Y)} &= eY_i^\dagger\,(I_3 + 1/2\mathcal{Y})\,Y_i,\\
g_{\sigma^* Y}\rho_s^{(Y)} &= g_{\sigma^* Y}\bar{Y}_i Y_i,\\
g_{\phi Y}\rho_v^{(Y)} &= g_{\phi Y}Y_i^\dagger Y_i,
\end{aligned} \tag{2.42}$$

where summation runs over occupied energy levels (i) for all hyperon species (Y). Correspondingly, the expression for the total energy is modified by the additional terms:

$$\begin{aligned}\delta E^{(Y)} = \sum_{i\leq A,Y} E_i - \frac{1}{2}\int \mathrm{d}^3x(-g_{\sigma Y}\sigma\rho_s^{(Y)} - g_{\sigma^* Y}\sigma^*\rho_s^{(Y)} \\ + g_{\omega Y}\omega\rho_v^{(Y)} + g_{\rho Y}\rho\rho_3^{(Y)} + g_{\phi Y}\phi\rho_v^{(Y)} + eA\rho_c^{(Y)}).\end{aligned} \tag{2.43}$$

2.2 Model Based on Chiral Meson–Baryon Amplitudes

In this section, basic ingredients of the chirally motivated coupled-channel technique are presented. However, it is beyond the scope of the thesis to give full details of this approach. The model is thoroughly described in Refs. [21, 101].

2.2.1 Chirally Motivated Coupled-Channel Approach

A successful description of low-energy $\bar{K}N$ interactions is provided by a chiral model combined with a coupled-channel T-matrix resummation technique. In our approach [36, 37] we employed chirally motivated coupled channel s-wave potentials in a separable form:

$$V_{ij}(p,p') = \sqrt{\frac{1}{2\omega_i}\frac{M_i}{E_i}}g_i(p)\frac{C_{ij}(\sqrt{s})}{f_i f_j}g_j(p')\sqrt{\frac{1}{2\omega_j}\frac{M_j}{E_j}}, \tag{2.44}$$

where the indices i and j run over the meson–baryon coupled channels: $\pi\Lambda$, $\pi\Sigma$, $\bar{K}N$, $\eta\Lambda$, $\eta\Sigma$, and $K\Xi$, including all their charge states. The $\sqrt{s}$, p and p' stand for the total meson–baryon c.m. energy, initial and final state meson momenta, respectively. E_i, M_i and ω_i stand for the baryon energy, baryon mass, and meson energy in the c.m. system of channel i. The coupling matrix C_{ij} is determined directly from the chiral $SU(3)$ Lagrangian. The parameters f_i and f_j represent the pseudoscalar meson decay constants and the Yamaguchi-type form factors

$$g_i(p) = \frac{1}{1+(p/\alpha_i)^2} \tag{2.45}$$

are determined by the inverse-range parameters α_i. The potential (2.44) is then iterated to all orders in the Lippmann–Schwinger equation:

$$T_{ij} = V_{ij} + V_{ik}G_kT_{kj}, \tag{2.46}$$

where the meson–baryon propagator is given by:

$$G_i(\sqrt{s},\rho) = \frac{1}{f_i^2}\frac{M_i}{\sqrt{s}}\int_{\Omega_i(\rho)}\frac{\mathrm{d}^3p}{(2\pi)^3}\frac{g_i^2(p)}{p_i^2 - p^2 - \Pi_i(\omega_i, E_i, \vec{p}, \rho) + \mathrm{i}0}, \tag{2.47}$$

where p_i is the on-shell c.m. momentum in channel i. When the elementary $\bar{K}N$ system is submerged into the nuclear medium of density ρ one has to consider the effects of Pauli blocking in the $\bar{K}N$ channels as well as effects of the meson and baryon self-energies. The effect of Pauli blocking is accounted for by the integration domain $\Omega_i(\rho)$, and Π_i represents the sum of meson and baryon self-energies in channel i. Since the antikaon self-energy is constructed from the resulting $\bar{K}N$ amplitude, a self-consistent procedure is required. The baryon and pion self-energies were approximated by density-dependent potentials of the $V = V_0\ \rho/\rho_0$ form consistent with the mean-field potentials used in nuclear structure calculations.

The separable form of the potential (2.44) results in the scattering amplitude which is also of a separable form:

$$F_{ij}(p,p',\sqrt{s}) = -\frac{g_i(p)g_j(p')}{4\pi f_i f_j}\sqrt{\frac{M_iM_j}{s}}\left[1 - CG^{-1}C\right]_{ij}. \tag{2.48}$$

The multichannel form of the scattering amplitude (2.48) is not particularly suitable for nuclear bound state applications. We are interested in the dynamics of one single channel, $\bar{K}N$, while insisting on retaining the full coupled-channel nature of the underlying dynamics. For this purpose the effective interaction V_{eff} is constructed which incorporates the dynamics of N coupled channels into a single channel [102]:

$$T^{\mathrm{eff}} = V^{\mathrm{eff}} + V^{\mathrm{eff}}G_1T^{\mathrm{eff}} = T_{11}. \tag{2.49}$$

Consistency of Eq. (2.49) with Eq. (2.46) requires V_{eff} to be a sum of the bare interaction in channel 1 ($\bar{K}N$) and contributions from all other $N-1$ channels:

$$V_{\mathrm{eff}} = V_{11} + \sum_{2\le i\le N} V_{1i}G_iV_{i1} + \sum_{2\le i,j\le N} V_{1i}G_iT_{ij}^{(N-1)}G_jV_{j1}, \tag{2.50}$$

where $T_{ij}^{(N-1)}$ is a resummation of interactions in channels other than 1:

$$T_{ij}^{(N-1)} = V_{ij}^{(N-1)} + \sum_{1\le k\le N} V_{ik}^{(N-1)}G_k^{(N-1)}T_{kj}^{(N-1)}; \quad i,j = 2,\ldots,N. \tag{2.51}$$

2.2.2 $\bar{K}$–Nucleus Optical Potential

From the microscopic two-body $\bar{K}N$ amplitude, one should, in principle, be able to construct the full many-body $\bar{K}$–nucleus amplitude. This task is extremely difficult and for the nuclear mass region of our interest computationally intractable. We therefore employed the multiple scattering theory and constructed a $\bar{K}$–nucleus optical model potential. In the lowest approximation, the complicated many-body $\bar{K}$–nucleus scattering amplitude is decomposed as a sum of the two-body $\bar{K}N$ scattering amplitudes on each target nucleon. The self-energy operator Π_K (optical potential $V_{\rm opt}$) may be written as [103]:

$$\Pi_K = 2\omega\, V_{\rm opt} = -4\pi \frac{\sqrt{s}}{m_N} F_{\bar{K}N}\left(p, \sqrt{s}, \rho\right) \rho, \tag{2.52}$$

where $F_{\bar{K}N}$ is the $\bar{K}N$ forward scattering amplitude.

The self-energy operator (2.52) is then incorporated into the $\bar{K}$ meson Klein–Gordon equation:

$$\left[\nabla^2 + \omega_K^2 - m_K^2 - \Pi_K(p, \sqrt{s}, \rho)\right] K^- = 0, \tag{2.53}$$

where

$$\omega_K = m_K - B_K - V_{\rm C} - {\rm i}\frac{\Gamma_K}{2} \tag{2.54}$$

is the complex energy. The Coulomb interaction is introduced via the minimal substitution by adding $-V_{\rm C}$ to ω_K.

Before using the optical potential (2.52) in calculations we have to prescribe how to express the two-body $\bar{K}N$ c.m. energy $\sqrt{s} = \sqrt{(E_K + E_N)^2 - (\vec{p_k} + \vec{p_N})^2}$ and the relative momentum $\vec{p}$ in Eq. (2.52) via $\bar{K}$–nucleus kinematic variables. Near threshold, $E_{\rm th} = m_N + m_K$, we approximate:

$$\vec{p} \simeq \xi_N \vec{p}_K - \xi_N \vec{p}_N, \quad \xi_{N(K)} = m_{N(K)}/(m_N + m_K) \tag{2.55}$$

and after averaging over angles:

$$p^2 \simeq \xi_N \xi_K \left(2m_K \frac{p_N^2}{2m_N} + 2m_N \frac{p_K^2}{2m_K}\right). \tag{2.56}$$

Similarly, for $\sqrt{s}$, neglecting quadratic terms in the binding energies $B_N = m_N - E_N$ and

$B_K = m_K - E_K$, we write:

$$\sqrt{s} \simeq E_{\rm th} - B_N - B_K - \xi_N \frac{p_N^2}{2m_N} - \xi_K \frac{p_K^2}{2m_K}. \tag{2.57}$$

The nucleon kinetic energy $p_N^2/(2m_N)$ was approximated in the Fermi gas model and the K^- kinetic energy $p_K^2/(2m_K)$ is identified in the local density approximation:

$$\begin{aligned} p_N^2/(2m_N) &= T_N(\rho/\rho_0)^{2/3} \text{ with } T_N = 23 \text{ MeV}, \\ p_K^2/(2m_K) &= -B_K - \mathrm{Re}\, V_{\rm opt} - V_{\rm C}. \end{aligned} \tag{2.58}$$

We note that all the terms on the r.h.s. of Eq. (2.57) are negative, thus resulting in the anticipated negative energy shift into the $\bar{K}N$ subthreshold region.

It is to be stressed that the optical potential (2.52), entering the K.–G. equation (2.53), depends on the binding energy B_K. This interconnection introduces additional self-consistency requirement in the solution of the K.–G. equation (2.53).

The chiral $\bar{K}N$ scattering amplitude incorporates only the s-wave two-body scattering. As discussed in section 2.1.1, the p-wave interaction and two-body absorption mechanisms can contribute significantly to the properties of $\bar{K}$–nuclear states. To estimate the p-wave contribution, we added into the K^- self-energy a phenomenological term $\Pi_K^{(p)}$ identical to that of Eq. (2.36), where the parametrization of the p-wave amplitude c_{KN} was taken from Ref. [70]. To include two-nucleon processes we proceeded in exactly the same way as in the RMF calculations. We added the phenomenological term in the form of Eq. (2.34) that is constrained by kaonic atom data fits together with the phenomenological energy dependence given by the phase-space reduction for K^- bound states.

Chapter 3

Results

In this section we present selected results of our calculations. First we focused on the strong-interaction decay widths of K^-–nuclear quasi-bound states within the RMF approach. Then, we explored nuclear and hypernuclear configurations containing several antikaons. Finally, chirally motivated $\bar{K}N$ scattering amplitudes were used to construct the K^- self-energy operator and calculate K^-–nuclear states. We highlight here our key results, while more detailed discussion of the results can be found in the selected articles in Appendix A.

It is complicated to evaluate the author's contribution to particular publications, since each article is a result of collective efforts. However, the collection of selected publications represents the author's original calculations. Ref. [37] is an exception as it covers a broad range of topics. The author contributed there by calculations of $\bar{K}$–nuclear states.

3.1 Dynamical RMF Calculations of $\bar{K}$–Nuclear States

We performed dynamical relativistic mean field calculations of $\bar{K}$–nuclear states for nuclei across the periodic table. Our aim was to study in detail the interplay between underlying dynamical processes and $\bar{K}$ absorption thresholds that determine the decay widths of the $\bar{K}$–nuclear quasi-bound states. Since there is still no definite consensus about the $\bar{K}$–nucleus interaction, we scaled its strength in our calculations to cover a wide range of $\bar{K}$ binding energies, $B_K \lesssim 200$ MeV. Antikaons in the nuclear medium are subject to strong-interaction absorption processes. Thus, for antikaonic nuclei, the principal question is whether the decay widths Γ_K of $\bar{K}$ states are small enough to allow their experimental identification. If antikaons bound strongly to nuclei, $B_K \gtrsim 90$ MeV, the dominant decay channel $\bar{K}N \rightarrow \pi\Sigma + 90$ MeV ($\approx 70\%$) would be kinematically blocked and the decay widths would be governed by weaker absorption processes. As argued in Ref. [48], the widths Γ_K of $\bar{K}$ states could be as small as $\Gamma_K \approx 20$ MeV.

However, in our calculations [69] we demonstrated that the widths of $\bar{K}$–nuclear states

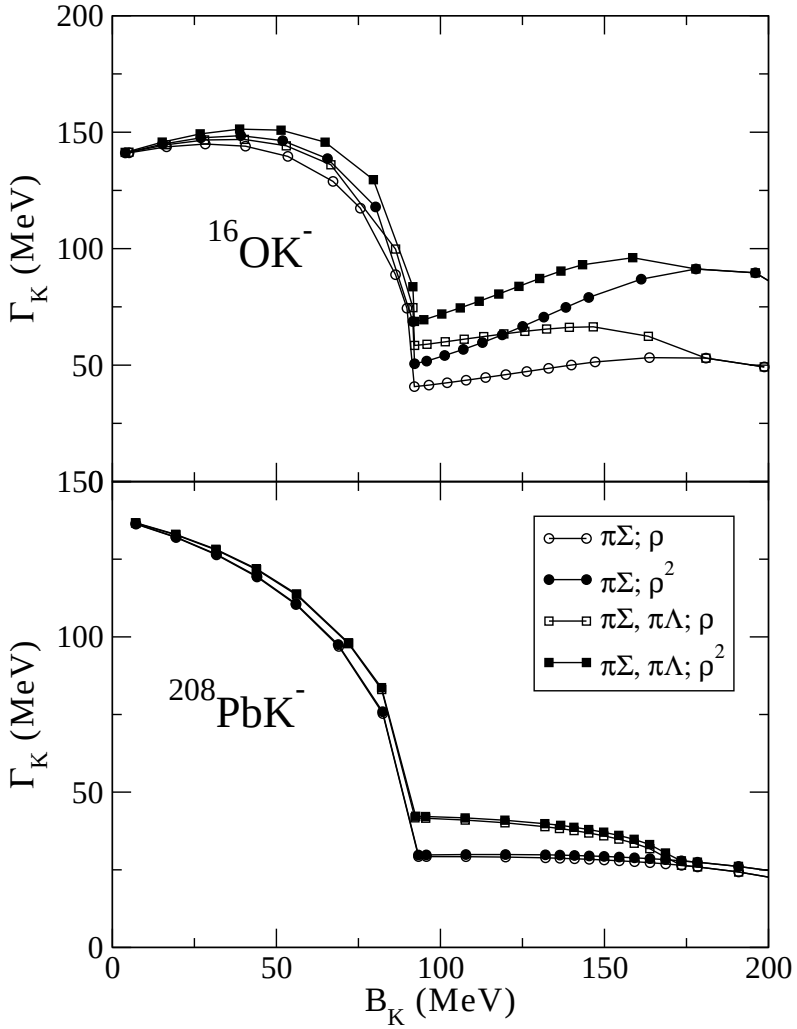

Figure 3.1: The $1s$ K^- decay width Γ_K calculated in ${}^{16}_{K^-}$O using the NL-SH RMF model (top panel) and in ${}^{208}_{K^-}$Pb using the L-HS RMF model (bottom panel) as a function of the K^- binding energy B_K, for absorption through $\bar{K}N \to \pi\Sigma$, with and without $\bar{K}N \to \pi\Lambda$, and assuming ρ or ρ^2 dependence for $\bar{K}NN \to \Sigma N$.

are substantial, $\Gamma_K \gtrsim 50$ MeV, even for deeply-bound $\bar{K}$ mesons, $B_K \approx 100$ MeV, once the dynamical processes and all absorption channels are considered. Significant contributions to the widths were found from the nonmesonic absorption modes $\bar{K}NN \to \Sigma N + 240$ MeV ($\approx 20\%$) on two nucleons and $\bar{K}N \to \pi\Lambda + 160$ MeV ($\approx 10\%$) processes with higher thresholds.

In Fig. 3.1, the calculated decay width Γ_K as a function of the $\bar{K}$ binding energy B_K is shown for the $1s$ K^-–nuclear states in ^{16}O and ^{208}Pb using the NL-SH and L-HS RMF model parametrizations, respectively, for various assumptions on the K^- absorption modes.

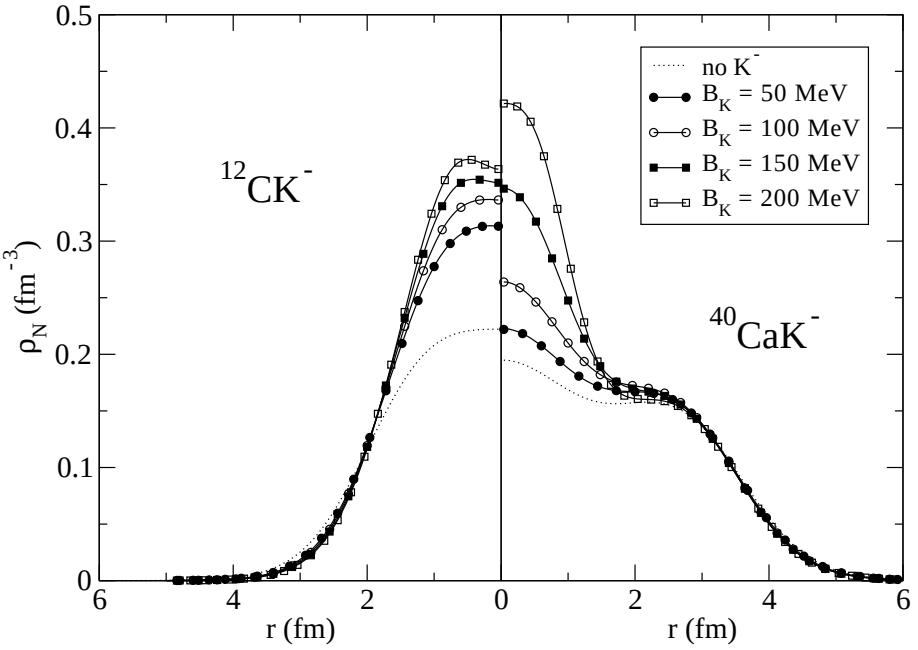

Figure 3.2: Nuclear density ρ_N of ${}^{12}_{K^-}$C (left panel) and ${}^{40}_{K^-}$Ca (right panel) for several $1s$ K^-–nuclear states with the specified binding energy, using the NL-SH RMF model. The dotted curves stand for the corresponding nuclear density in the absence of the K^- meson.

The shape of the $\Gamma_K = \Gamma_K(B_K)$ follows the binding energy dependence of the suppression factors of Eqs. (2.32) and (2.34). The widths fall off rapidly until $B_K \approx 90$ MeV, reflecting the presence of the $\bar{K}N \to \pi\Sigma$ reaction threshold. For $B_K \gtrsim 90$ MeV, the widths are dominated by the two-nucleon absorption processes $\bar{K}NN \to YN$. The curves denoted by empty circles correspond to the K^- decay widths calculated with only the $\bar{K}N \to \pi\Sigma$ (80%) and $\bar{K}NN \to \Sigma N$ (20%) absorption modes included. Significant contributions to the decay widths were found when the $\bar{K}N \to \pi\Lambda$ conversion mode was explicitly considered (empty squares), adding approximately 20 MeV to the widths for the K^- binding energies in range $B_K \approx 100-160$ MeV. Further enhancement of the $\bar{K}$ absorption widths (full circles and full squares) is obtained when the linear density dependence of the multi-nucleon conversion channels $\bar{K}NN \to YN$ is replaced by the quadratic one which is more appropriate for two-nucleon absorption processes. The enhancement is particularly pronounced in light nuclear systems for high values of the $\bar{K}$ binding energy. It results from strong nuclear core polarization effects due to the presence of the $\bar{K}$ meson. The nuclear core polarization is illustrated in Fig. 3.2 where the nucleon density distributions ρ_N in ${}^{12}_{K^-}$C and ${}^{40}_{K^-}$Ca calculated in the NL-SH RMF model are shown for several values of the K^- binding energy

B_K. In case of larger nuclear systems, antikaons affect the nuclear density distributions only in the vicinity of the center of the nucleus which corresponds to the density distribution of the K^- meson.

We also verified that the inclusion of the ρ-meson exchange modifies the results only slightly. It reduces the $\bar{K}$ binding energy B_K by less than about 5 MeV, compared with the minimal $\sigma\omega$ model of Ref. [31]. The effect of the p-wave interaction was also studied since it could play an important role for tightly bound $\bar{K}$ mesons in light nuclear systems. Although the inclusion of p-waves was found to play a marginal role in heavier $\bar{K}$–nuclear systems, the contribution of ~ 10 MeV to the total $\bar{K}$ binding in light nuclear systems (such as ${}^{12}_{K^-}$C) is certainly nonnegligible. For details see Appendix A.1.

Finally, we also performed first calculations of nuclear systems containing more than one antikaon. These systems are discussed in the following section.

3.2 Nuclear Configurations with Multiple Strangeness

We explored in detail baryonic configurations with large fraction of strangeness. Antikaons were embedded into the nuclear [104], and lately also into the hypernuclear [105] medium in order to search for kaon condensation precursor phenomena in self-bound strange hadronic matter. For a sufficiently attractive $\bar{K}$–nucleus interaction the strong nuclear core polarization induced by the presence of $\bar{K}$ mesons could lead to sizeable enhancement of the $\bar{K}$ meson binding energy upon increasing the number of antikaons in the nuclear medium. This might result in substantially bound configurations stable against strong interactions once the $\bar{K}$ binding energy exceeds $B_K \gtrsim 320$ MeV, or narrow $\bar{K}$ states for $B_K \gtrsim 240$ MeV where only the $\bar{K}NN \to \Lambda N$ absorption mechanism would contribute to the widths.

In our calculations, by contrast, we observed that the $\bar{K}$ binding energies B_K saturate with the number of antikaons submerged in the nuclear medium. The saturation pattern is found to be robust feature of the multi-$\bar{K}$ strangeness nuclear configurations, appearing for all RMF models considered and a wide range of variations of the $\bar{K}$–nucleus interaction. In Fig. 3.3, the $1s$ K^- binding energy B_K in multi-K^- nuclei ^{16}O+κK^- is plotted as a function of the number κ of antikaons for several compositions of the K^- self-energy of Eq. (2.22). In the lower (upper) group of curves, the $g_{\sigma K}$ coupling constant was fixed to yield $B_K = 50$ (100) MeV in ^{16}O+$1K^-$. The primary reason behind the saturation is the repulsive interaction between antikaons mediated by the vector ω-meson field. No

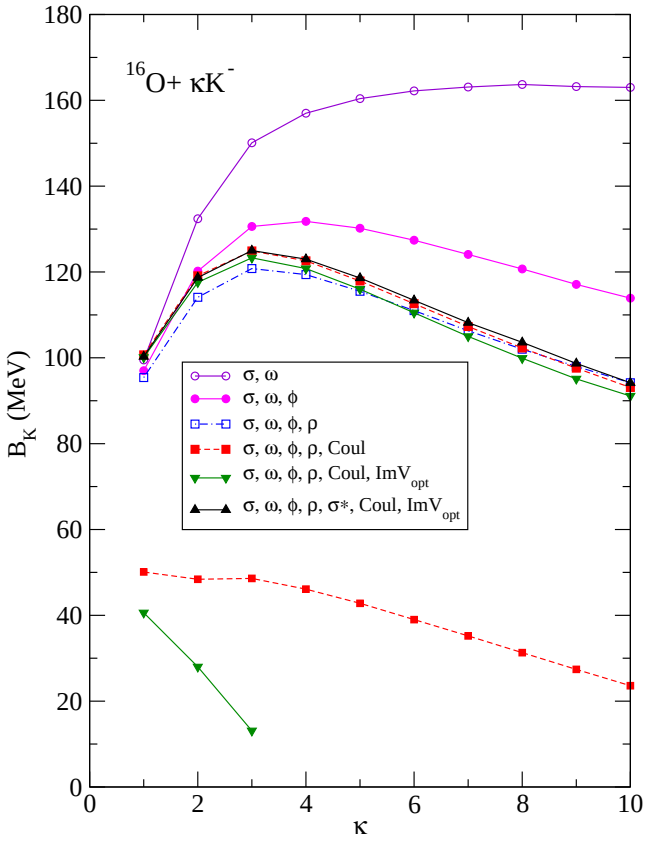

Figure 3.3: The $1s$ K^- binding energy B_K in ^{16}O+κK^- as a function of the number κ of antikaons for various mean-field compositions calculated in the NL-SH RMF model.

saturation was observed for purely scalar σ-meson exchange. With respect to the minimal $\sigma\omega$ model, main contributions originate from the ϕ- and ρ-meson vector fields which act repulsively between antikaons. On the other hand, the Coulomb and σ^* fields make only a small difference. The effect of $\bar{K}$ absorption, denoted by $\mathrm{Im}\,V_{\mathrm{opt}}$, is substantial for $B_K \lesssim 100$ MeV.

The saturation of $\bar{K}$ binding energies is reflected also in the behavior of the associated nuclear and antikaon density distributions. In Fig. 3.4, the nuclear ρ_N and antikaon ρ_K density distributions are shown for several numbers κ of antikaons embedded in ^{208}Pb+κK^-. The K^- coupling constants were chosen such that $B_K = 100$ MeV in the single-K^- configuration. The density distributions behave quite regularly and the initial increase of the central densities slows down with κ. Generally, for all nuclei considered, nuclear densities saturate at $2-3$ times the nuclear-matter density. We are aware of the fact that the nuclear densities reached in these multi-$\bar{K}$ nuclear configurations are quite higher than

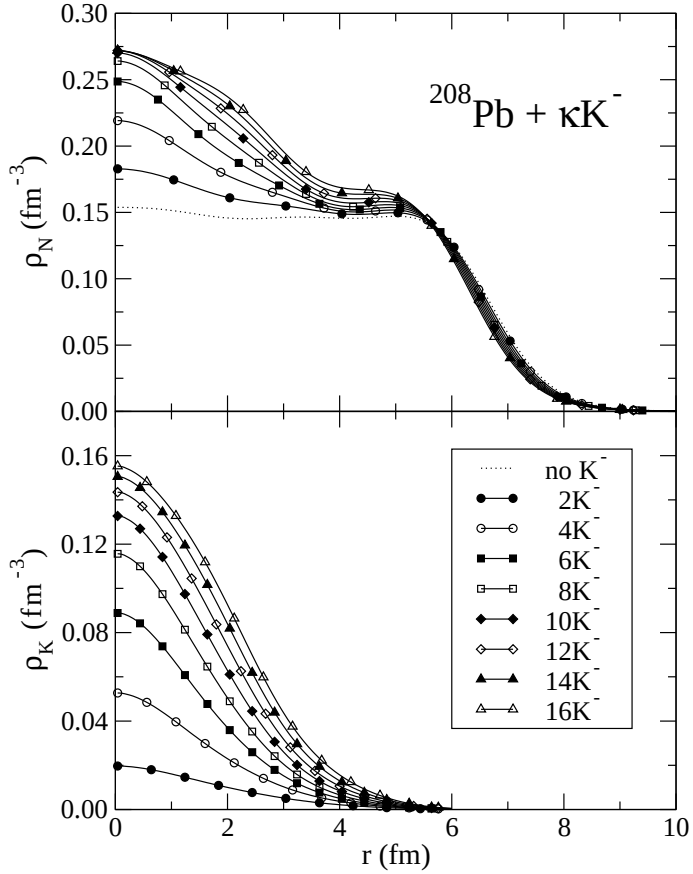

Figure 3.4: Nuclear density ρ_N (top panel) and $1s$ K^- density ρ_K (bottom panel) distributions in ^{16}O+κK^- calculated in the NL-SH RMF model.

the typical values of nuclear densities for which the RMF methodology was constrained. However, qualitatively identical results [106] were obtained for RMF models with density-dependent coupling constants constrained to reproduce Dirac–Brueckner calculations of nuclear matter [107–109].

The saturation of the $\bar{K}$ binding energies occurs also in the presence of large number of hyperons. This is illustrated in Fig. 3.5 where $\bar{K}$ mesons were embedded into particle-stable configurations of nucleons and Λ and Ξ hyperons. The initial values of the antikaon coupling constants were again fixed such that $B_K = 100$ MeV for $\kappa = 1$ and no hyperons ($\eta = \mu = 0$). The figure demonstrates that the heavier the system is the more antikaons is required to reach saturation of B_K. We note that adding hyperons lowers B_K with respect to multi-$\bar{K}$ nuclear configurations and that B_K does not exceed 120 MeV.

Further, we studied systems composed solely of $\bar{K}^0$ mesons and neutrons or K^- mesons and protons, as well as the possibility to bind K^+ mesons in multi-strangeness configura-

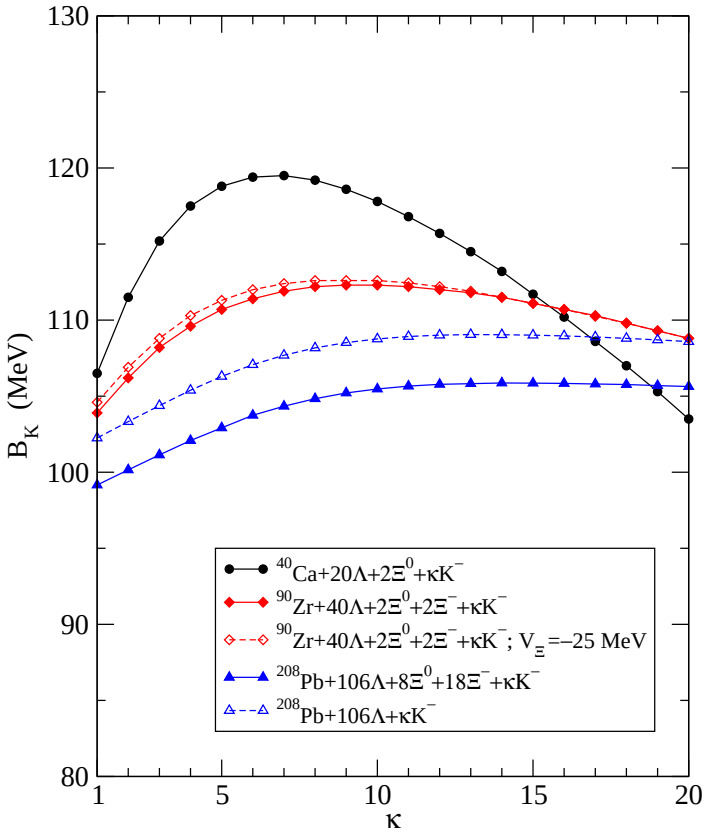

Figure 3.5: The $1s$ K^- binding energy B_K in ^{40}Ca, ^{90}Zr, and ^{208}Pb with $\eta\Lambda+\mu\Xi+\kappa K^-$ calculated in the NL-TM1 RMF model.

tions. For results of these calculations, as well as full details of the results briefly discussed above, we refer to A.2 and A.3 in Appendix.

3.3 Chirally Motivated Approach for Kaonic Nuclei

In our recent works [36–38], a self-consistent procedure to construct the self-energy operator Π_K of $\bar{K}$ mesons in the nuclear medium from the underlying $\bar{K}N$ scattering amplitudes was developed. The $\bar{K}N$ scattering amplitudes were generated within a chirally motivated in-medium coupled-channel model of meson–baryon interactions. It was shown how to incorporate strong energy and density dependencies of the chiral $\bar{K}N$ scattering amplitudes into the self-consistent evaluation of Π_K. The $\bar{K}$ meson self-energy operator was then used to confront the data of kaonic atoms and to calculate $\bar{K}$–nuclear quasi-bound states. Our calculations [36] provided for the first time a microscopic link between shallow chiral $\bar{K}$–

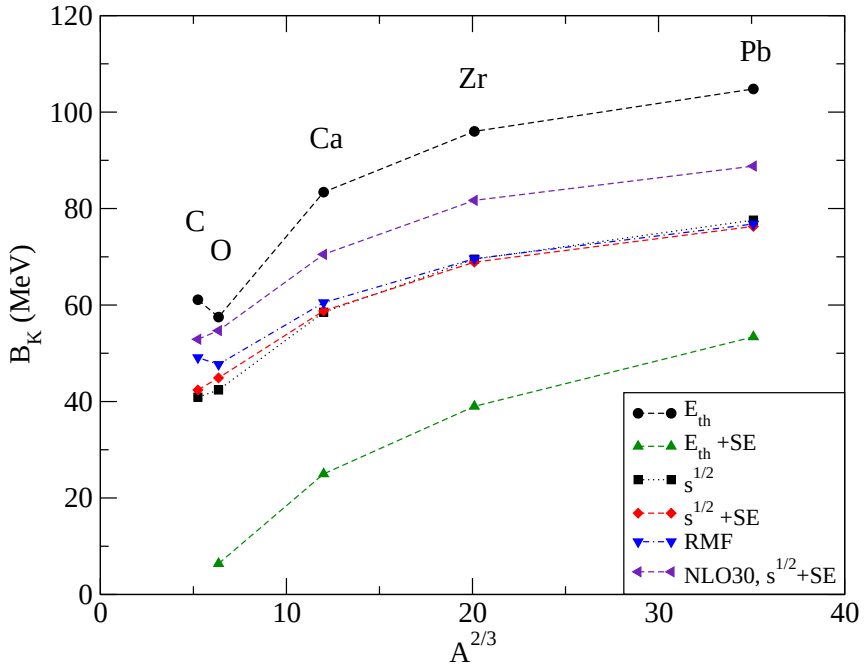

Figure 3.6: Binding energies B_K of $1s$ K^- nuclear quasi-bound states in several nuclei, calculated using static RMF nuclear densities and TW1 chiral amplitudes at threshold ('$E_{\rm th}$') and with $\sqrt{s}$ (2.57), in both in-medium versions: only Pauli blocking ('no SE') and including also hadron self-energies ('+SE'). Results of static RMF calculations, with a K^- nuclear interaction mediated by vector mesons only, as well as for NLO30 chiral '+ SE' amplitudes are shown for comparison.

nuclear potentials evaluated at threshold and deep phenomenological potentials obtained by the K^--atom data analysis.

The calculations of $\bar{K}$–nuclear states revealed that chirally motivated potentials are sufficiently attractive to bind $\bar{K}$ mesons in nuclei. The $\bar{K}$ binding energies in range of 50–90 MeV for nuclei spanning from ^{6}Li to ^{208}Pb were obtained. In Fig. 3.6, the K^- separation energies B_K of the $1s$ K^-–nuclear states are shown for several nuclei and various constructions of the self-energy operator Π_K. The values of B_K obtained using the $\bar{K}N$ leading order TW1 in-medium amplitudes evaluated at threshold energy ('$E_{\rm th}$', $\sqrt{s} = E_{\rm th} = m_K + m_N$) without and with ('+SE') hadron self-energies are compared with those ('$s^{1/2}$') calculated self-consistently using the subthreshold extrapolation of $\sqrt{s}$ from Eq. (2.57). The K^- separation energies resulting from the next-to-leading order chiral amplitudes ('NLO30') are also shown for comparison. It is worth noting that the binding energies calculated using the leading-order sub-threshold extrapolated TW1 amplitudes are remarkably close to those calculated within the RMF approach where the interaction

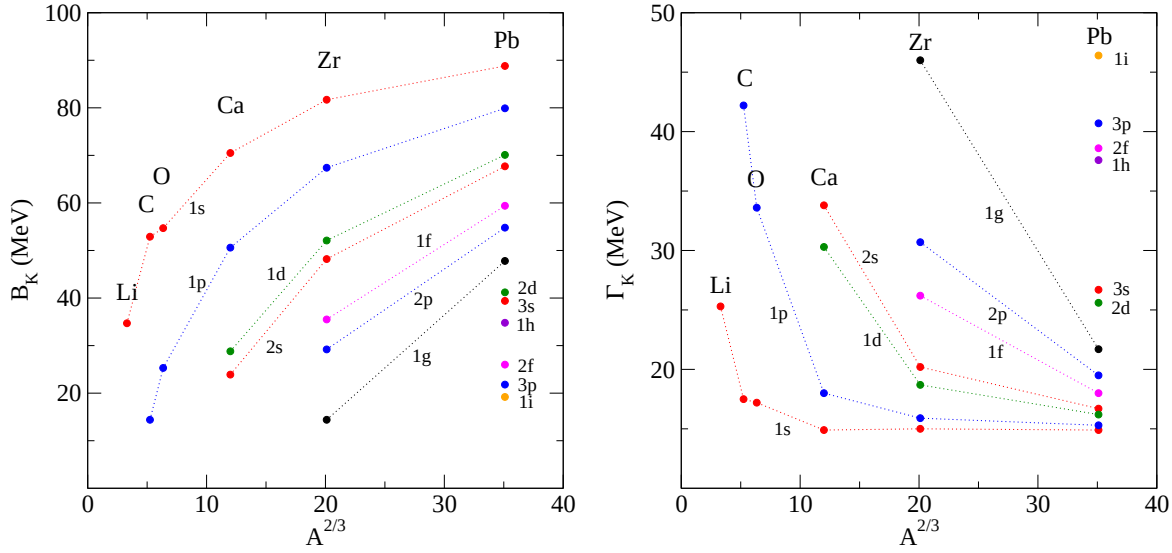

Figure 3.7: Binding energies B_K (left panel) and widths Γ_K (right panel) of K^- quasi-bound states in selected nuclei, calculated self-consistently with static RMF densities and the NLO30 scattering amplitudes with hadron self-energies ('+SE'). $\bar{K}NN \to YN$ decay modes are not included.

of antikaons is mediated exclusively by vector mesons with purely SU(3) F-type couplings.

The results for all $\bar{K}$–nuclear quasi-bound states, including excited states, are shown in Fig. 3.7 where the K^- separation energies B_K (left panel) and decay widths Γ_K (right panel) are calculated using the static RMF densities and the NLO30 amplitudes with hadron self-energies. The present two-body chiral amplitudes when evaluated self-consistently below the $\bar{K}N$ threshold yield fairly narrow low-lying $1s$ $\bar{K}$–nuclear states with decay widths $\Gamma_K \sim 15$ MeV, due to the proximity of the $\bar{K}N \to \pi\Sigma$ reaction threshold. On the other hand, the widths of the excited states are quite large especially for light nuclei. Moreover, contributions from the $\bar{K}NN \to YN$ absorption processes are estimated to yield additional ~ 40 MeV to the total widths in this energy range, as demonstrated in the last block of Table 3.1 ('+2N abs.'). When the $\bar{K}NN \to YN$ processes are taken into account, the resulting decay widths are comparable or even larger than the corresponding $\bar{K}$ binding energies, exceeding considerably the energy level spacings. In Table 3.1, we present the K^- binding energies B_K and decay widths Γ_K of the K^- quasi-bound states in ^{40}Ca calculated self-consistently in the NLO30 chiral model with hadron self-energies. The results of calculations which take into account dynamical nuclear core polarization by the strongly bound K^- meson are compared with calculations using the static RMF densities in the first two blocks. As anticipated, dynamical calculations give generally

Table 3.1: Binding energies B_K and widths Γ_K (in MeV) of the K^- nuclear quasi-bound states in Ca, calculated self-consistently using the NLO30 amplitudes with hadron self-energies. Calculations with dynamical and static RMF densities are compared in the first two blocks. Results with static RMF densities including p-wave amplitudes are shown in the third block, and $\bar{K}NN \to YN$ decay modes are included in the last block.

	dynamical		static		stat. + p wave		stat. + $2N$ abs.	
	B_K	Γ_K	B_K	Γ_K	B_K	Γ_K	B_K	Γ_K
$1s$	72.3	14.8	70.5	14.9	73.0	14.8	68.9	58.9
$1p$	52.8	17.7	50.6	18.0	53.1	17.9	49.2	53.6
$1d$	30.5	29.2	28.8	30.3	32.1	29.3	27.7	59.7
$2s$	24.6	30.9	23.9	33.8	26.3	34.2	21.6	67.1

higher binding energies and smaller widths. Also shown in Table 3.1, using the static RMF densities, is the effect of adding the p-wave $\bar{K}N$ interaction assigned to the $\Sigma(1385)$ resonance. Consistently with the kaonic atoms phenomenology p-waves play a secondary role for deeply-bound K^- states.

For a detailed discussion of the obtained results we refer to A.4 and A.5 in Appendix.

Chapter 4

Summary

In this work we performed a comprehensive study of the interaction of $\bar{K}$ mesons with nuclei. Using various theoretical models we analysed available sources of experimental data and carried out for the first time complex, fully self-consistent calculations of $\bar{K}$–nuclear states.

Altogether, the results of our dynamical calculations suggest the decay widths of K^-–nuclear states to be substantial, $\Gamma_K \gtrsim 50$ MeV, even if the dominant decay mode $\bar{K}N \to \pi\Sigma$ is kinematically closed. Within a chirally motivated model we demonstrated that the strong energy dependence of the underlying $\bar{K}N$ interaction results in deeply bound states of $\bar{K}$ mesons in nuclei. When the $\bar{K}NN \to YN$ processes are considered the total decay widths are comparable or even higher than the corresponding binding energies, exceeding considerably the energy level spacings. The large widths resulting from our calculations should discourage the searches for narrow $\bar{K}$–nuclear quasi-bound states in any but very light nuclei.

In nuclear and hypernuclear systems containing several antikaons, the $\bar{K}$ binding energies were found to saturate with increasing the number of antikaons embedded in the medium. The primary reason responsible for the saturation of binding energies and associated density distributions is the repulsion between antikaons due to the vector-meson exchange. The saturation of $\bar{K}$ binding energies manifests itself also in the behavior of baryon densities that do not exhibit any abrupt or substantial increase and behave quite regularly with the number of antikaons. Since the $\bar{K}$ binding energy B_K was found to be bounded from above, $B_K \lesssim 200$ MeV, we conclude that kaon condensation or its precursor phenomena do not occur in these strange hadronic configurations. Nevertheless, this does not rule out kaon condensation in neutron stars where different conditions govern the composition of matter.

To progress further, it is necessary yet to account for the two-nucleon absorption processes, as well as their possible dispersive contributions, on the basis of a fully microscopic model. Moreover, very little is known about the $\bar{K}\bar{K}$ interaction and this subject also requires further studies.

References

[1] E. Friedmam, A. Gal, Phys. Rep. 452 (2007) 89.

[2] R. H. Dalitz, T. C. Wong, G. Rajasekaran, Phys. Rev. 153 (1967) 1617.

[3] A. Müller-Groeling, K. Holinde, J. Speth, Nucl. Phys. A 513 (1990) 557.

[4] M. Jones, R. H. Dalitz, R. R. Horgan, Nucl. Phys. B 129 (1977) 45.

[5] N. Isgur and G. Karl, Phys. Rev. D 18 (1978) 4187.

[6] T. Inonue, Nucl. Phys. A 790 (2007) 530.

[7] J. A. Oller and U.-G. Meissner, Phys. Lett. B 500 (2001) 263.

[8] D. Jido, J. A. Oller, E. Oset, A. Ramos, U.-G. Meissner, Nucl. Phys. A 725 (2003) 181.

[9] V. K. Magas, E. Oset, A. Ramos, Phys. Rev. Lett. 95 (2005) 052301.

[10] D. N. Tovee *et al.*, Nucl. Phys. B 33 (1971) 493.

[11] R. J. Nowak *et al.*, Nucl. Phys. B 139 (1978) 61.

[12] A. D. Martin, Nucl. Phys. B 179 (1981) 33; and references therein.

[13] J. Ciborowski *et al.*, J. Phys. G 8 (1982) 13.

[14] D. Evans *et al.*, J. Phys. G 9 (1983) 885.

[15] M. Iwasaki *et al.*, Phys. Rev. Lett. 78 (1997) 3067;
T. M. Ito *et al.*, Phys. Rev. C 58 (1998) 2366.

[16] G. Beer *et al.* (DEAR collaboration), Phys. Rev. Lett. 94 (2005) 212302.

[17] M. Bazzi *et al.* (SIDDHARTA collaboration), Phys. Lett. B 704 (2011) 113, and references therein to previous experiments.

[18] S. Scherer, Adv. Nucl. Phys. 27 (2003) 277.

[19] N. Kaiser, P. B. Siegel, W. Weise, Nucl. Phys. A 594 (1995) 325.

[20] Y. Ikeda, T. Hyodo, W. Weise, Nucl. Phys. A 881 (2012) 98.

[21] A. Cieplý and J. Smejkal, Nucl. Phys. A 881 (2012) 115.

[22] E. Oset and A. Ramos, Nucl. Phys. A 635 (1998) 99.

[23] B. Borasoy, R. Nissler, W. Weise, Eur. Phys. J. A 25 (2005) 79.

[24] B. Borasoy, U.-G. Meissner, and R. Nissler, Phys. Rev. C 74 (2006) 055201.

[25] J. A. Oller, Eur. Phys. J. A 28 (2006) 63.

[26] Talk by C. Curceanu (SIDDHARTA collaboration) at LEANNIS Meeting, Prague, May 2012.

[27] M. Bazzi *et al.* (SIDDHARTA collaboration), Phys. Lett. B 697 (2011) 199; *ibid.* 681 (1009) 310.

[28] C. J. Batty, Phys. Rep. 287 (1997) 385.

[29] E. Friedman, A. Gal, C. J. Batty, Phys. Lett. B 308 (1993) 6; Nucl. Phys. A 579 (1994) 518.

[30] E. Friedman, A. Gal, J. Mareš, A. Cieplý , Phys. Rev. C 60 (1999) 024314.

[31] J. Mareš, E. Friedman, A. Gal, Nucl. Phys. A 770 (2006) 84.

[32] T. Waas, N. Kaiser, W. Weise, Phys. Lett. B 365 (1996) 12.

[33] M. Lutz, Phys. Lett. B 426 (1998) 12.

[34] A. Ramos and E. Oset, Nucl. Phys. A 671 (2000) 481.

[35] A. Cieplý , E. Friedman, A. Gal, J. Mareš, Nucl. Phys. A 696 (2001) 173.

[36] A. Cieplý, E. Friedman, A. Gal, D. Gazda, J. Mareš, Phys. Lett. B 702 (2011) 402.

[37] A. Cieplý, E. Friedman, A. Gal, D. Gazda, J. Mareš, Phys. Rev. C 84 (2011) 045206.

[38] D. Gazda and J. Mareš, Nucl. Phys. A 881 (2012) 159.

[39] Adopted from [1], based on private communication with E. G. Drukarev.

[40] S. Wycech, Nucl. Phys. B 28 (1971) 541.

[41] W. A. Bardeen and E. W. Torigoe, Phys. Lett. B 38 (1972) 135.

[42] J. R. Rook, Nucl. Phys. A 249 (1975) 466.

[43] J. Schaffner, A. Gal, I. N. Mishustin, H. Stöcker, W. Greiner, Phys. Lett. B 334 (1994) 268.

[44] G. E. Brown and M. Rho, Nucl. Phys. A 596 (1996) 503.

[45] W. Scheinast *et al.*, Phys. Rev. Lett. 96 (2006) 072301, and references therein.

[46] A. Cieplý, E. Friedman, A. Gal, J. Mareš, Nucl. Phys. A 696 (2001) 173.

[47] T. Kishimoto, Phys. Rev. Lett. 83 (1999) 4701.

[48] Y. Akaishi and T. Yamazaki, Phys. Rev. C 65 (2002) 044005; T. Yamazaki and Y. Akaishi, Phys. Lett. B 535 (2002) 70.

[49] S. Wycech, Nucl. Phys. A 450 (1986) 399.

[50] T. Suzuki *et al.*, Phys. Lett. B 597 (2004) 263.

[51] T. Suzuki *et al.*, Nucl. Phys. A 754 (2005) 375.

[52] M. Iwasaki *et al.*, arXiv:0706.0297 [nucl-ex], plenary talk by M. Iwasaki at HYP06, Mainz, October 2006.

[53] T. Kishimoto *et al.*, Nucl. Phys. A 754 (2005) 383.

[54] T. Kishimoto *et al.* (KEK E548 collaboration), Prog. Theor. Phys. 118 (2007) 181.

[55] M. Agnello *et al.*, Phys. Rev. Lett. 94 (2005) 212303.

[56] V. K. Magas, E. Oset, A. Ramos, H. Toki, Phys. Rev. C 74 (2006) 025206.

[57] M. Agnello *et al.*, Nucl. Phys. A 775 (2006) 35.

[58] G. Bendiscioli *et al.*, Nucl. Phys. A 789 (2007) 222.

[59] M. Agnello *et al.*, Phys. Lett. B (2007) 65480.

[60] T. Yamazaki *et al.*, arXiv:0810.5182v1 [nucl-ex].

[61] T. Yamazaki and Y. Akaishi, Phys. Rev. C 76 (2007) 045201.

[62] N. V. Shevchenko, A. Gal, J. Mareš, J. Révai, Phys. Rev. C 76 (2007) 044004.

[63] Y. Ikeda and T. Sato, Phys. Rev. C 76 (2007) 035203.

[64] A. Doté and W. Weise, Prog. Theor. Phys. Suppl. 168 (2007) 593.

[65] A. Doté, T. Hyodo, W. Weise, Nucl. Phys. A 804 (2008) 197; Phys. Rev. C 79 (2009) 014003.

[66] Y. Ikeda and T. Sato, Phys. Rev. C 79 (2009) 035201.

[67] N. Barnea, A. Gal, E. Z. Liverts, Phys. Lett. B 712 (2012) 132.

[68] Y. Ikeda, H. Kamano, T. Sato, Prog. Theor. Phys. 124 (2010) 533.

[69] D. Gazda, E. Friedman, A. Gal, J. Mareš, Phys. Rev. C 76 (2007) 055204.

[70] W. Weise and R. Härtle, Nucl. Phys. A 804 (2008) 173.

[71] S. Weissenborn, D. Chatterjee, J. Schaffner-Bielich, Phys. Rev. C 85 (2012) 065802; and references therein.

[72] D. B. Kaplan and A. E. Nelson, Phys. Lett. B 175 (1986) 57; *ibid.* 179 (1986) 409.

[73] A. E. Nelson and D. B. Kaplan, Phys. Lett. B 192 (1987) 193.

[74] C.-H. Lee, Phys. Rep. 275 (1996) 255.

[75] M. Prakash, I. Bombaci, M. Prakash, P. J. Ellis, J. M. Lattimer, R. Knorren, Phys. Rep. 280 (1997) 1.

[76] H. Heiselberg and M. Hjorth-Jensen, Phys. Rep. 328 (2000) 237.

[77] H. Heiselberg and V.R. Pandharipande, Ann. Rev. Nucl. Part. Sci. 50 (2000) 481.

[78] N. K. Glendenning, Phys. Rep. 342 (2001) 393.

[79] A. Ramos, J. Schaffner-Bielich, J. Wambach, Lect. Notes Phys. 578 (2001) 175.

[80] J. Schaffner and I. N. Mishustin, Phys. Rev. C 53 (1996) 1416.

[81] P. J. Ellis, R. Knorren, M. Prakash, Phys. Lett. B 349 (1995) 11.

[82] P. B. Demorest, T. Pennucci, S. M. Ransom, M. S. E. Roberts, J. W. T. Hessels, Nature 467 (2010) 1081.

[83] T. Yamazaki, A. Doté, Y. Akaishi, Phys. Lett. B 587 (2004) 167.

[84] J. Schaffner-Bielich and A. Gal, Phys. Rev. C 62 (2000) 034311; and references therein.

[85] T. Muto, Nucl. Phys. A 804 (2008) 322.

[86] T. Muto, Phys. Rev. C 77 (2008) 015810.

[87] T. Muto, T. Maruyama, T. Tatsumi, Phys. Rev. C 79 (2009) 035207.

[88] B. D. Serot and J. D. Walecka, Adv. Nucl. Phys. 16 (1986) 1.

[89] C. J. Horowitz and B. D. Serot, Nucl. Phys. A 368 (1981) 503.

[90] M. M. Sharma, M. A. Nagarajan, P. Ring, Phys. Lett. B 312 (1993) 377.

[91] Y. Sugahara and H. Toki, Nucl. Phys. A 579 (1994) 557.

[92] C. Vander Velde-Wilquet, J. Sacton, J. H. Wickens, D. N. Tovee, D. H. Davis, Nuovo Cimento A 39 (1977) 538.

[93] S. Wycech and A. M. Green, arXiv:nucl-th/0501019v1.

[94] L. S. Kisslinger, Phys. Rev. 98 (1955) 761.

[95] J. Schaffner, C. B. Dover, A. Gal, C. Greiner, H. Stöcker, Phys. Rev. Lett. 71 (1993) 1328.

[96] J. Schaffner, C. B. Dover, A. Gal, C. Greiner, D. J. Millener, H. Stöcker, Ann. Phys. 235 (1994) 35.

[97] J. Mareš, E. Friedman, A. Gal, B. K. Jennings, Nucl. Phys. A 594 (1995) 311.

[98] O. Hashimoto and H. Tamura, Prog. Part. Nucl. Phys. 57 (2006) 564.

[99] H. Takahashi *et al.*, Phys. Rev. Lett. 87 (2001) 212502.

[100] P. Khaustov *et al.*, Phys. Rev. 61 (2000) 054603.

[101] A. Cieplý, J. Smejkal, Eur. Phys. J. A 43 (2010) 191.

[102] T. Hyodo and W. Weise, Phys. Rev. C 77 (2008) 035204.

[103] M. L. Goldberger and K. M. Watson, *Collision theory* (John Wiley & Sons, Inc., New York, 1964).

[104] D. Gazda, E. Friedman, A. Gal, J. Mareš, Phys. Rev. C 77 (2008) 045206.

[105] D. Gazda, E. Friedman, A. Gal, J. Mareš, Phys. Rev. C 80 (2009) 035205.

[106] D. Gazda, E. Friedman, A. Gal, J. Mareš, Int. J. Mod. Phys. A 26 (2011) 567.

[107] S. Typel and H. H. Wolter, Nucl. Phys. A 656 (1999) 331.

[108] T. Nikšić, D. Vretenar, P. Finelli, P. Ring, Phys. Rev. C 66 (2002) 024306.

[109] W. Long, J. Meng, N. V. Giai, S.-G. Zhou, Phys. Rev. C 69 (2004) 034319

List of Author's Publications

Total impact factor 25.24, h-index 5, 97 citations (according to WOS, including autocitations).

Articles

1. D. Gazda and J. Mareš,
   Calculations of K^- nuclear quasi-bound states based on chiral meson–baryon amplitudes,
   Nucl. Phys. A 881 (2012) 159.

2. J. Mareš, A. Cieplý, D. Gazda, E. Friedman, A. Gal,
   $\bar{K}$–nuclear potentials based on chiral meson–baryon amplitudes,
   AIP Conf. Proc. 1441 (2012) 353.

3. A. Cieplý, E. Friedman, A. Gal, D. Gazda, J. Mareš,
   $\bar{K}$–nuclear potentials from in-medium chirally motivated models,
   Phys. Rev. C 84 (2011) 045206.

4. A. Cieplý, E. Friedman, A. Gal, D. Gazda, J. Mareš,
   Chirally motivated $\bar{K}$–nuclear potentials,
   Phys. Lett. B 702 (2011) 402.

5. D. Gazda, E. Friedman, A. Gal, J. Mareš,
   Strange baryonic matter and kaon condensation,
   Int. J. Mod. Phys. A 26 (2011) 567.

6. D. Gazda, E. Friedman, A. Gal, J. Mareš,
   Multi-kaonic hypernuclei and kaon condensation,
   J. Phys.: Conf. Series 312 (2011) 22013.

7. D. Gazda, E. Friedman, A. Gal, J. Mareš,
   Kaon condensation and multistrange matter,
   Nucl. Phys. A 835 (2010) 287.

8. D. Gazda, E. Friedman, A. Gal, J. Mareš,
Multi-$\bar{K}$ (hyper)nuclei,
Proc. Strangeness in Nuclei, Oct. 4–8, 2010, Trento, Italy,
arXiv:1104.1926 [nucl-ex].

9. D. Gazda, E. Friedman, A. Gal, J. Mareš,
Multi-$\bar{K}$ (hyper)nuclei,
Proc. Hadronic Atoms and Kaonic Nuclei, Oct. 12–16, 2009, Trento, Italy,
arXiv:1003.2328 [nucl-ex].

10. D. Gazda, E. Friedman, A. Gal, J. Mareš,
Multi-$\bar{K}$ (hyper)nuclei and kaon condensation,
Proc. Int. Symp. Strangeness in Nuclear and Hadronic Systems, Dec. 14–18, 2008,
Sendai, Japan, (Eds. K. Maeda, S. N. Nakamura, H. Tamura, O. Hashimoto), World Sci.,
New Jersey (2010) 63.

11. D. Gazda, E. Friedman, A. Gal, J. Mareš,
Multi-$\bar{K}$ (hyper)nuclei and kaon condensation,
Int. J. Mod. Phys. E 19 (2010) 2594.

12. D. Gazda, E. Friedman, A. Gal, J. Mareš,
Multi-$\bar{K}$ hypernuclei,
Phys. Rev. C 80 (2009) 035205.

13. D. Gazda, E. Friedman, A. Gal, J. Mareš,
Dynamical calculations of $\bar{K}$ and multi-$\bar{K}$ nuclei,
Int. J. Mod. Phys. A 24 (2009) 438.

14. D. Gazda, E. Friedman, A. Gal, J. Mareš,
Multi-$\bar{K}$ nuclei and kaon condensation,
Phys. Rev. C 77 (2008) 045206.

15. D. Gazda, E. Friedman, A. Gal, J. Mareš,
Dynamics of $\bar{K}$ and multi-$\bar{K}$ nuclei,
Proc. Int. Conf. on Meson–Nucleon Physics and the Structure of the Nucleon,
Sep. 10–14, 2007, Jülich, Germany.

16. D. Gazda, E. Friedman, A. Gal, J. Mareš,
Dynamics of $\bar{K}$ and multi-$\bar{K}$ nuclei,
Phys. Rev. C 76 (2007) 055204.

Conference Presentations

1. Strange Baryonic Matter, ECT* Trento, Italy, Sep. 26–30, 2011.
   (oral presentation)
2. Conference of Slovak and Czech Physicists, Žilina, Slovakia, Sep. 5–8, 2011.
   (poster)
3. Strangeness in Nuclei, ECT* Trento, Italy, Oct. 4–8, 2010.
   (oral presentation)
4. International Nuclear Physics Conference, Vancouver, Canada, Jul. 4–9, 2010.
   (poster)
5. Meson Production, Properties, and Interaction, Cracow, Poland, Jun. 10–15, 2010.
   (oral presentation)
6. Hadronic Atoms and Kaonic Nuclei, ECT* Trento, Italy, Oct. 12–16, 2009.
   (oral presentation)
7. European Nuclear Physics Conference, Bochum, Germany, Mar. 16–20, 2009.
   (oral presentation)
8. Particles and Nuclei International Conference, Eilat, Israel, Nov. 9–14, 2008.
   (poster)
9. Meson Production, Properties, and Interaction, Cracow, Poland, Jun. 6–10, 2008.
   (oral presentation)
10. Conference of Czech and Slovak Physicists, Hradec Králové, Sep. 8–12, 2008.
    (oral presentation)
11. Meson–Nucleon Physics and the Structure of the Nucleon, Jülich, Germany,
    Sep. 10–14, 2007.
    (oral presentation)
12. Hypernuclear and Strange Particle Physics, Mainz, Germany, Oct. 10–14, 2006.
    (poster)

Appendix A

Selected Publications

Published in Physical Review C 76 (2007) 05520402

Dynamics of $\bar{K}$ and multi-$\bar{K}$ nuclei

D. Gazda[1], E. Friedman[2], A. Gal[2], J. Mareš[1]

[1]*Nuclear Physics Institute, 25068 Řež, Czech Republic*
[2]*Racah Institute of Physics, The Hebrew University, Jerusalem 91904, Israel*

Abstract

We report on self-consistent calculations of single-K^- nuclear states and multi-$\bar{K}$ nuclear states in ^{12}C, ^{16}O, ^{40}Ca and ^{208}Pb within the relativistic mean-field (RMF) approach. Gradient terms motivated by the p–wave resonance $\Sigma(1385)$ are found to play a secondary role for single-K^- nuclear systems where the mean-field concept is acceptable. Significant contributions from the $\bar{K}N \to \pi\Lambda$ conversion mode, and from the nonmesonic $\bar{K}NN \to YN$ conversion modes which are assumed to follow a ρ^2 density dependence, are evaluated for the deep binding-energy range of over 100 MeV where the decay channel $\bar{K}N \to \pi\Sigma$ is closed. Altogether we obtain K^- total decay widths of 50–100 MeV for binding energies exceeding 100 MeV in single-K^- nuclei. Multi-$\bar{K}$ nuclear calculations indicate that the binding energy per $\bar{K}$ meson saturates upon increasing the number of $\bar{K}$ mesons embedded in the nuclear medium. The nuclear and $\bar{K}$ densities increase only moderately and are close to saturation, with no indication of any kaon-condensation precursor.

1 Introduction

The subject of the present work is the study of $\bar{K}$ meson interactions with the nuclear medium. It is closely related to one of the most important, so far unresolved problems in hadronic physics, of how hadron masses and interactions change within the nuclear medium. The in-medium properties of antikaons in dense nuclear matter have attracted considerable attention since the pioneering work of Kaplan and Nelson on the possibility of kaon condensation in dense matter [1, 2] and subsequent works offering related scenarios in nuclear matter [3, 4].

The existence of $\Lambda(1405)$, a $\bar{K}N$ quasi-bound state lying about 27 MeV below the K^-p threshold, suggests that the $\bar{K}N$ interaction is strongly attractive, as demonstrated first in a vector-meson exchange model due to Dalitz *et al.* [5]. This is consistent with low-energy $\bar{K}N$ scattering data [6] as well as with the measured level shift of the $1s$ state

in the kaonic hydrogen atom [7, 8]. The $\Lambda(1405)$, as a K^-p quasi-bound state, was also corroborated in the Jülich meson exchange model [9], where the scalar σ and vector ω mesons act jointly to give strong attraction. Subsequent chiral SU(3) calculations showed that the $I = 0$ coupled-channel $\bar{K}N - \pi\Sigma$ interaction is sufficiently attractive to bind the $\Lambda(1405)$ [10, 11]. For an update on such calculations see Refs. [12, 13, 14].

The $\bar{K}$–nucleus interaction, too, is strongly attractive, as deduced from analyses of strong-interaction level shifts and widths in kaonic atoms [15, 16, 17, 18, 19, 20]. These fits to kaonic-atom data are based on phenomenological density dependent optical potentials [15, 16, 17, 19, 20] or on a relativistic mean-field (RMF) approach [18], yielding strongly attractive K^-–nucleus potentials of depths 150–200 MeV. For an update see Ref. [21]. In contrast, coupled-channel calculations using $\bar{K}N$ interactions constrained by chiral models and fitted to the low-energy $\bar{K}N$ scattering and reaction data result in shallower $\bar{K}$–nucleus potentials of depth in the range of 100–150 MeV [22]. Imposing a self-consistency requirement on the evaluation of the in-medium $\bar{K}$–nucleus potential, yields much shallower potentials of depth about 50 MeV [23, 24, 25, 26]. Similar results are obtained when the Jülich meson-exchange model is used within a self-consistent coupled-channel calculation [27]. A depth of about 80 MeV is indicated by analyzing the enhanced near-threshold production of K^- mesons in proton–nucleus collisions, in recent experiments by the KaoS Collaboration at GSI [28] (and references cited therein to earlier nucleus-nucleus experiments).

The $\bar{K}$–nuclear interaction is also strongly absorptive, due dominantly to the one-nucleon absorption reactions $\bar{K}N \to \pi Y$ with approximately 100 MeV ($Y = \Sigma$) and 180 MeV ($Y = \Lambda$) energy release for the final hyperon Y. The strong absorptivity is confirmed by fits to kaonic-atom data [17].

Considerable interest in this field in recent years has focused on the question of possible existence of deeply bound $\bar{K}$–nuclear states, and whether such states are sufficiently narrow to allow unique experimental identification. Kishimoto [29], and Akaishi and Yamazaki [30, 31], suggested to look for $\bar{K}$–nuclear states bound by over 100 MeV, for which the dominant $\bar{K}N \to \pi\Sigma$ decay channel would become kinematically forbidden. Furthermore, it was suggested that multi-$\bar{K}$ high-density nuclear clusters should also exist, providing perhaps a precursor stage to kaon condensation [32]. Several searches for $\bar{K}$ deeply bound states have been subsequently made in KEK [33, 34, 35, 36], by the FINUDA collaboration in DAΦNE, Frascati [37] and at the AGS, Brookhaven [38]. However, the interpretation of the observed spectra is ambiguous, as demonstrated by an alternative explanation of the

(allegedly K^-pp) peak observed in the back-to-back Λp invariant mass distribution of $K^-_{\rm stop}$ reactions on ^{6,7}Li and on ^{12}C [37] in terms of quasi-free K^-NN absorption and final-state interaction [39].

The theoretical calculations of $\bar{K}$–nuclear bound states may be divided into two classes: (i) few-body calculations using a single-channel G-matrix or AMD methodology [31, 40, 41, 42], and coupled-channel $\bar{K}NN - \pi\Sigma N$ Faddeev equations [43, 44] which agree with Refs. [31, 42] on K^-pp being bound, although differing widely on the binding energy and width calculated for this lightest possible system; (ii) dynamical RMF calculations [45, 46] which take into account the polarization of the nucleus owing to the strongly interacting $\bar{K}$ meson, as well as the reduction of phase space available for the decay of the deeply bound $\bar{K}$ meson. The calculations of Ref. [19] provide a lower limit of $\Gamma_{K^-} \simeq 50$ MeV on the width of nuclear bound states for K^- binding energy in the range $B_{K^-} \sim 100 - 200$ MeV.

The purpose of the present paper is twofold. In the first part we report on dynamical calculations of single-K^- nuclear states within the relativistic mean field (RMF) approach. This part of the work deals with three items:

- Effects due to the vector-meson ρ and ϕ mean fields which were not included in our previous calculations [45] are studied. The introduction of the ρ-meson mean field allows for a departure from $N = Z$ nuclear cores for $\bar{K}$–nuclear states, and the introduction of the ϕ-meson mean field allows for studying multi-strange $\bar{K}$–nuclear states.

- The effect of p-wave gradient terms motivated by the $I = 1$ $\Sigma(1385)$ resonance is studied by extending the RMF coupled equations in the simplest form. Although the role of the $\bar{K}N$ p-wave interaction is marginal near threshold [47], it might become more important for deeply bound antikaons, owing to local variations in the nuclear densities induced by the antikaon [48].

- Following our previous work [45], we explore in more detail and rigor the absorptive part of the optical potential in the energy region where the dominant decay channel $\bar{K}N \to \pi\Sigma$ is closed. This is done by incorporating for the first time the $\bar{K}N \to \pi\Lambda$ channel, with threshold some 80 MeV below the $\pi\Sigma$ threshold, and by considering a ρ^2 density dependence for the two-nucleon absorption modes $\bar{K}NN \to YN$. The ρ^2 dependence is more appropriate for the description of the two-nucleon nature of these absorption modes.

In the second part of this work we explore within the RMF methodology deeply bound multi-$\bar{K}$ nuclear states, in order to study the behavior of the nuclear medium under the influence of increasing strangeness. The issue here is whether or not the binding energy per $\bar{K}$ meson of multi-$\bar{K}$ nuclear states increases significantly upon adding a large number of $\bar{K}$ mesons, so that $\bar{K}$ mesons provide the physical degrees of freedom for self-bound strange hadronic systems. Kaon condensation in nuclear matter would occur beyond some threshold value of strangeness, if the binding energy per $\bar{K}$ meson exceeds the combination $m_K + \mu_N - m_\Lambda \gtrsim 320$ MeV (in this paper we use $\hbar = c = 1$), where μ_N is the nucleon chemical potential. In such a case, Λ, Σ and Ξ hyperons would no longer combine macroscopically with nucleons to compose the more conventional kaon-free form of strange hadronic matter [49]. In neutron stars, the binding energy per $\bar{K}$ meson necessary for the onset of kaon condensation is given by $m_K - \mu_{e^-}$, where μ_{e^-} is the electron chemical potential (generally accepted to assume values of $\mu_{e^-} \lesssim 200$ MeV). The RMF approach was first applied to the study of kaon condensation in the mid 1990s, originally without considering a possible interplay with hyperons [50, 51] and then with hyperons included [52, 53]. This approach was also used in Ref. [54] to consider $\bar{K}^0$ condensation in addition to K^- condensation in neutron stars. Recent calculations offer a wide range of interesting precursor phenomena to kaon condensation in both hadronic and quark sectors (see Refs. [55, 56, 57, 58, 59] and previous work cited therein). The present calculations may shed some light on the likelihood of a kaon-condensation scenario in nuclear matter.

The RMF methodology, including the extension to absorptive processes and p-wave gradient interaction terms, and to multi-$\bar{K}$ nuclear states is discussed in Sec. 2. Results of calculations for a representative set of nuclear cores across the periodic table are presented and discussed in Sec. 3. Section 4 summarizes the new results of the present work, along with conclusions and outlook.

2 Model

In the present work, $\bar{K}$-nuclear states are studied within the theoretical framework of the relativistic mean field (RMF) approach applied to a system of nucleons and one or more $\bar{K}$ mesons. The interaction among hadrons is mediated by the exchange of scalar and vector meson fields. The standard RMF Lagrangian density $\mathcal{L}_N$ describing the nucleonic sector is specified in Sec. 3. The (anti)kaonic sector is incorporated by adding to $\mathcal{L}_N$ the Lagrangian

density $\mathcal{L}_K$:

$$\mathcal{L}_K = (\mathcal{D}_\mu K)^\dagger \, (\mathcal{D}^\mu K) - m_K^2 K^\dagger K + g_{\sigma K} m_K K^\dagger K \, \sigma \, , \tag{1}$$

with

$$K = \begin{pmatrix} K^+ \\ K^0 \end{pmatrix} \qquad K^\dagger = \begin{pmatrix} K^-, & \bar{K}^0 \end{pmatrix} \tag{2}$$

and the covariant derivative $\mathcal{D}_\mu$ given by:

$$\mathcal{D}_\mu \equiv \partial_\mu + \mathrm{i}\, g_{\omega K}\, \omega_\mu + \mathrm{i}\, g_{\rho K}\, \vec{\tau} \cdot \vec{\rho}_\mu + \mathrm{i}\, g_{\phi K}\, \phi_\mu + \mathrm{i}\, e\, \tfrac{1}{2}(1+\tau_3) A_\mu \, . \tag{3}$$

This particular choice of interaction scheme leads to the coupling of the vector meson fields to conserved currents. The conserved (Noether) current associated with the kaonic field is obtained from the invariance of $\mathcal{L}_K$ under global phase transformation. Using

$$K \to e^{\mathrm{i}\lambda} K \quad \Rightarrow \quad \delta \mathcal{L}_K = 0 \quad \Rightarrow \quad \partial_\mu \, j_K^\mu = \partial_\mu \left[\frac{\delta \mathcal{L}_K}{\delta \, (\partial_\mu K)} \, \delta K + \delta K^\dagger \frac{\delta \mathcal{L}_K}{\delta \, (\partial_\mu K^\dagger)} \right] = 0 \, , \tag{4}$$

one obtains a conserved vector current whose vacuum (represented by filled shells of nucleons and κ $\bar{K}$ mesons) expectation value transforms to the expression for ρ_{K^-} given in Eq. (6) below. The standard variational principle yields equations of motion for all field operators. The meson field operators and source terms are then replaced by their expectation values, according to the mean-field approximation. For simplicity, we limit discussion in this section to nuclear systems with K^- mesons. The generalization to nuclear systems with $\bar{K}^0$ mesons is straightforward.

Whereas the Dirac equation for nucleons is not explicitly affected by the addition of $\mathcal{L}_K$, the presence of K^- mesons induces additional source terms in the equations of motion for the meson (mean) fields:

$$\begin{aligned}
(-\nabla^2 + m_\sigma^2)\sigma_0 &= +g_{\sigma N}\rho_s + g_2\sigma_0^2 - g_3\sigma_0^3 + g_{\sigma K} m_K K^- K^+ \\
(-\nabla^2 + m_\omega^2)\omega_0 &= +g_{\omega N}\rho_v - g_{\omega K}\rho_{K^-} \\
(-\nabla^2 + m_\rho^2)\rho_0 &= +g_{\rho N}\rho_3 - g_{\rho K}\rho_{K^-} \\
(-\nabla^2 + m_\phi^2)\phi_0 &= -g_{\phi K}\rho_{K^-} \\
-\nabla^2 A_0 &= +e\,\rho_p - e\,\rho_{K^-} \, ,
\end{aligned} \tag{5}$$

with ρ_s, ρ_v and ρ_3 denoting the scalar, vector and isovector nuclear densities, respectively,

and with ρ_p denoting the proton density. The K^- density ρ_{K^-} is given by:

$$\rho_{K^-} = 2(E_{K^-} + g_{\omega K}\,\omega_0 + g_{\rho K}\,\rho_0 + g_{\phi K}\,\phi_0 + e\,A_0)K^-K^+\,, \qquad \int \mathrm{d}^3x\,\rho_{K^-} = \kappa\,, \quad (6)$$

where $E_{K^-} = \mathrm{i}\,\partial_t K^-$. The density ρ_{K^-} is normalized to the number of antikaons κ in a multi-K^- system.

The Klein–Gordon (KG) equation of motion for the K^- meson obtained from the RMF model acquires the form:

$$[-\nabla^2 - E_{K^-}^2 + m_K^2 + \mathrm{Re}\,\Pi_{K^-}\,]K^- = 0\,, \quad (7)$$

where the K^- self-energy term is given by:

$$\begin{aligned} \mathrm{Re}\,\Pi_{K^-} = \; & - \; g_{\sigma K} m_K \sigma_0 - 2E_{K^-}(g_{\omega K}\omega_0 + g_{\rho K}\rho_0 + g_{\phi K}\phi_0 + eA_0) \\ & - \; (g_{\omega K}\omega_0 + g_{\rho K}\rho_0 + g_{\phi K}\phi_0 + eA_0)^2\,. \end{aligned} \quad (8)$$

This implies a K^- effective mass m_K^* of the form $m_K^{*2} = m_K^2 - g_{\sigma K} m_K \sigma_0$, in contrast to another possible choice [54] $m_K^* = m_K - g_{\sigma K}\sigma_0$. Qualitatively, our results are insensitive to this difference and the conclusions of the present study hold also for the other choice.

Assuming that all the K^- mesons occupy the same energy level, the total binding energy of the combined κK^-–nuclear system $B(A, Z, \kappa K^-)$ has the form:

$$\begin{aligned} B(A, Z, \kappa K^-) \; = \; & \textstyle\sum_{i=1}^{A} B_i^{\mathrm{sp}} + \kappa\, B_{K^-}^{\mathrm{sp}} \\ & - \; \frac{1}{2}\int \mathrm{d}^3\,x(-g_{\sigma N}\,\sigma_0\rho_s + g_{\omega N}\,\omega_0\rho_v + g_{\rho N}\,\rho_0\rho_3 + e\,A_0\rho_p) \\ & - \; \frac{1}{2}\int \mathrm{d}^3\,x(-\tfrac{1}{3}g_2\,\sigma_0^3 - \tfrac{1}{2}g_3\,\sigma_0^4) \\ & + \; \frac{1}{2}\int \mathrm{d}^3\,x[(g_{\omega K}\,\omega_0 + g_{\rho K}\,\rho_0 + g_{\phi K}\,\phi_0 + e\,A_0)\rho_{K^-} + g_{\sigma K} m_K \sigma_0 K^-K^+]\,, \end{aligned} \quad (9)$$

with $B_i^{\mathrm{sp}} = m_N - E_i$ and $B_{K^-}^{\mathrm{sp}} = m_K - E_{K^-}$, where E_i and E_{K^-} are the nucleon and K^- single particle energies, respectively. From this expression, it is evident that the K^- binding energy $B_{K^-} = B[A, Z, \kappa K^-] - B[A, Z, (\kappa - 1)K^-]$ contains, in addition to $B_{K^-}^{\mathrm{sp}}$, mean field contributions representing part of the rearrangement energy of the nuclear core.

2.1 P-wave contributions

To study the role of p waves in the $\bar{K}N$ interaction, we have extended the K^- self energy Π_{K^-} by adding a phenomenological isoscalar p–wave potential:

$$\Pi_{K^-}^{(P)} = 4\pi \left(1 + \frac{E_{K^-}}{m_N}\right)^{-1} c_0(\nabla\rho_v)\cdot\nabla \,, \tag{10}$$

where $c_0 = (c_p + c_n)/2 \approx 3c_p/2$ is an energy-dependent strength parameter dominated by the contribution of the $\Sigma(1385)$ p-wave resonance [60]. Calculations were done for K^-–nuclear states bound by about 100 MeV, corresponding roughly to $\sqrt{s_{\bar{K}N}} = 1330$ MeV, namely about 55 MeV below the $\Sigma(1385)$ resonance, where c_0 is positive (attractive) and nearly real:

$$c_0(1330\ \text{MeV}) = \frac{3}{2}\, c_p(1330\ \text{MeV}) = 0.186\ \text{fm}^3 \,, \tag{11}$$

in agreement with the plot of c_p in Fig. 2 of Ref. [42].

2.2 Absorptive contributions

Having dealt with the nuclear binding energy of K^- mesons, in the next step we consider $\bar{K}$ absorption in the nuclear medium, in order to evaluate the K^- decay width Γ_{K^-}. In our model, this is done by allowing the self energy Π_{K^-} to become complex and replacing $E_{K^-} \to E_{K^-} - \mathrm{i}\Gamma_{K^-}/2$. Since the imaginary part of the self energy is not addressed by the traditional RMF approach, $\mathrm{Im}\,\Pi_{K^-}$ was taken from optical model phenomenology. We follow Ref. [45] taking the optical potential imaginary-part depth from fits to K^- atomic data, while the nuclear density is treated as a dynamical quantity in these self-consistent calculations. Once the antikaon is embedded in the nuclear medium, the attractive $\bar{K}N$ interaction compresses the nuclear core, thus increasing the nuclear density which leads to an increased $\bar{K}$ width. On the other hand, the phase space available for decay products is reduced due to the binding energy of the $\bar{K}$ meson, particularly in the case of $\bar{K}$ deeply bound states. To accomplish this reduction, suppression factors multiplying $\mathrm{Im}\,\Pi_{K^-}$ were introduced, explicitly considering $\bar{K}$ binding energy for the initial decaying state and assuming two-body final state kinematics.

We first consider absorption on a single nucleon, leading to the following pionic decay modes:

$$\bar{K}N \to \pi\Sigma,\ \pi\Lambda \quad (70\%,\ 10\%) \,, \tag{12}$$

with thresholds about 100 MeV and 180 MeV, respectively, below the $\bar{K}N$ total mass. The numbers in parentheses give approximately the branching ratios known from bubble chamber and emulsion experiments [61]. The corresponding single-nucleon absorptive contribution to the optical potential is given in leading approximation by:

$$\mathrm{Im}\,\Pi^{(1)}_{K^-} = (0.7 f_{1\Sigma} + 0.1 f_{1\Lambda})\, W_0\, \rho_v(r)\,, \tag{13}$$

where W_0 is taken from kaonic atom fits and the phase-space suppression factors f_{1Y} ($Y = \Sigma, \Lambda$) are given by:

$$f_{1Y} = \frac{M_{01}^3}{M_1^3} \sqrt{\frac{[M_1^2 - (m_\pi + m_Y)^2][M_1^2 - (m_Y - m_\pi)^2]}{[M_{01}^2 - (m_\pi + m_Y)^2][M_{01}^2 - (m_Y - m_\pi)^2]}}\, \Theta(M_1 - m_\pi - m_Y)\,, \tag{14}$$

with $M_{01} = m_K + m_N$ and $M_1 = M_{01} - B_{K^-}$.

Absorption on two nucleons leads to non-pionic decay modes

$$\bar{K}NN \to YN \quad (20\%)\,, \tag{15}$$

with thresholds about $m_\pi \simeq 140$ MeV lower than the corresponding pionic decay mode thresholds. Since the non-pionic modes are heavily dominated by the ΣN final state, the ΛN channel was not considered in the present work and we focused attention primarily on a quadratic density dependence of the ΣN final-state contribution to the absorptive part of the optical potential. A quadratic density dependence for two-nucleon absorption processes has been successfully used in studies of pionic atoms [17, 21]. The $\bar{K}$ two-nucleon absorptive part of the optical potential is given by:

$$\mathrm{Im}\,\Pi^{(2)}_{K^-} = 0.2\, f_{2\Sigma}\, W_0\, \rho_v^2(r)/\rho_0\,, \tag{16}$$

where the factor 0.2 represents the approximately 20% branching ratio for two-nucleon absorption from rest [61] and $\rho_0 \sim 0.16$ fm^{-3} is an A-dependent central nuclear density used for properly normalizing the two-nucleon absorption strength with respect to the one-nucleon absorption strength. The phase-space suppression factor $f_{2\Sigma}$ has the form:

$$f_{2\Sigma} = \frac{M_{02}^3}{M_2^3} \sqrt{\frac{[M_2^2 - (m_N + m_\Sigma)^2][M_2^2 - (m_\Sigma - m_N)^2]}{[M_{02}^2 - (m_N + m_\Sigma)^2][M_{02}^2 - (m_\Sigma - m_N)^2]}}\, \Theta(M_2 - m_\Sigma - m_N)\,, \tag{17}$$

with $M_{02} = m_K + 2m_N$ and $M_2 = M_{02} - B_{K^-}$.

The set of coupled equations containing the Dirac equation for nucleons, the KG equations (5) and (7) for the meson mean fields and for antikaons, respectively, was solved self-consistently using an iterative procedure.

3 Results and discussion

Calculations of $\bar{K}$-nuclear states in ^{12}C, ^{16}O, ^{40}Ca, and ^{208}Pb were performed, using both the linear (HS) [62] and non-linear (NL-SH) [63] parameterizations of the nucleonic Lagrangian density $\mathcal{L}_N$. These RMF parameterizations give quite different estimates of nuclear properties. In particular, the non-linear models yield generally lower values of the nuclear incompressibility. Therefore, stronger polarization effects in these models owing to the presence of $\bar{K}$ meson(s) are anticipated, in comparison with the linear models.

The (anti)kaon coupling constants to the meson fields were chosen as follows: The coupling constant $g_{\omega K}$ was given a reference value $g^0_{\omega K} = (1/3)g_{\omega N}$ following the simple quark model. The reference value for $g_{\sigma K}$ was taken then from fits to kaonic atom data, which yielded $g^0_{\sigma K} = 0.2\, g_{\sigma N}$ for the linear and $g^0_{\sigma K} = 0.233\, g_{\sigma N}$ for the non-linear parameterizations of $\mathcal{L}_N$ [18]. Finally, the coupling constants $g_{\rho K}$ and $g_{\phi K}$ were adopted from the $SU(3)$ relations: $\sqrt{2}\, g_{\phi K} = 2\, g_{\rho K} = g_{\rho\pi} = 6.04$ [53].

The $SU(3)$ relation $2g_{\omega K} = g_{\rho\pi}$ was not imposed on $g_{\omega K}$ since its value was varied in the calculations, along with varying $g_{\sigma K}$, in order to scan over different values of $\bar{K}$ binding energies. Thus a particular way of varying these coupling constants away from their 'reference' values was used. Starting from $g_{iK} \equiv \alpha_i\, g^0_{iK} = 0 \quad (i = \sigma, \omega)$, we first scaled up α_ω from the value required for the onset of binding all the way to $\alpha_\omega = 1$, corresponding to $g_{\omega K} = g^0_{\omega K}$. Then, for $\alpha_\omega = 1$, we scaled up α_σ from 0 to 1 corresponding to $g_{\sigma K} = g^0_{\sigma K}$, and finally we again scaled α_ω from 1 upwards until the binding energy value of $B_{\bar{K}} \simeq 200$ MeV was reached. Generally, similar results and conclusions are reached if different scanning procedures are applied. We comment below, for multi-$\bar{K}$ nuclei, when this is no longer the case.

3.1 Single-K^- nuclei

In the first part of this work, single-K^- nuclear states were studied. We verified that the interaction generated by the ρ-meson mean field has a small effect on the K^- binding energy B_{K^-} and on the width Γ_{K^-}, for $B_{K^-} \lesssim 200$ MeV and for all the RMF parameterizations considered in the present work. This interaction acts repulsively on a K^- meson, producing

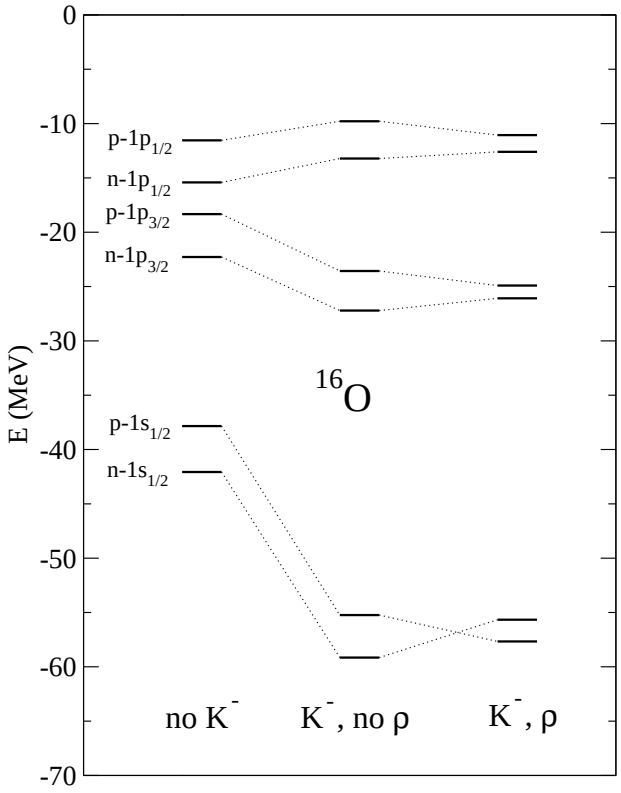

Figure 1: Nucleon single-particle energies with respect to the nucleon mass in ^{16}O (left spectrum) and in $^{16}_{K^-}$O (middle and right spectra) for $B_{K^-} = 100$ MeV, with and without coupling the K^- meson to the ρ-meson mean field, using the NL-SH RMF model.

a small decrease of B_{K^-}, less than 5 MeV in the case of ^{208}Pb where the most significant effect is anticipated due to the large excess of neutrons. The effect of the ρ meson field on the K^- decay width is even smaller, except in the region 60 MeV $\lesssim B_{K^-} \lesssim$ 100 MeV where the phase-space suppression factor $f_{1\Sigma}$ varies rapidly and, hence, Γ_{K^-} increases by approximately 10 MeV.

Figure 1 shows the effect of the ρK^- coupling on the nucleon single-particle energies in ^{16}O. The left-hand spectrum shows the nucleon single-particle energies in the absence of K^- mesons, using the NL-SH model. The middle spectrum displays the rearrangement of these single-particle energies caused by a K^- meson bound by 100 MeV, with no ρK^- coupling. The most pronounced effect is observed for the $1s_{1/2}$ nucleon states, which become significantly more bound in the presence of a $1s$ K^- meson. The right-hand spectrum displays further modification of the nucleon single-particle energies due to the ρK^- coupling. It is seen that the isovector ρK^- interaction reverses the order of the $1s_{1/2}$ proton and neutron energy levels, determined in the absence of ρK^- coupling by the

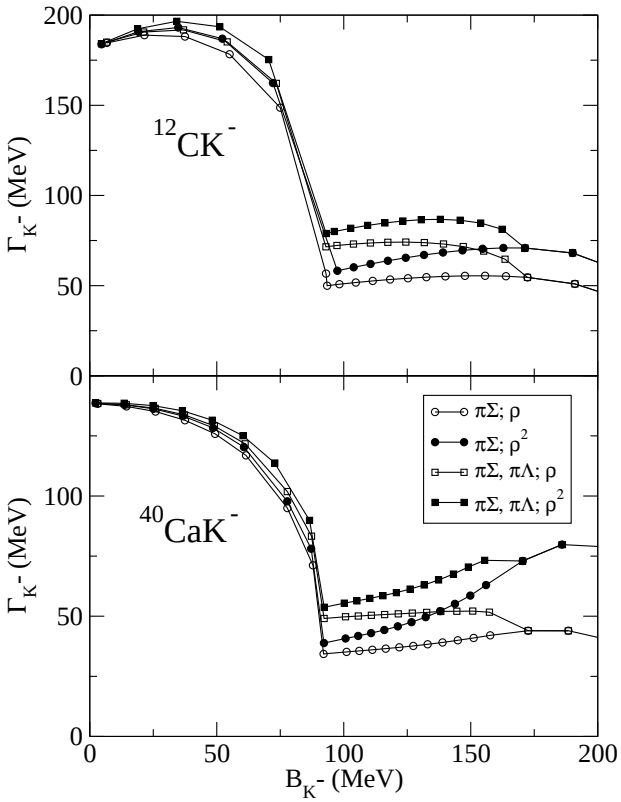

Figure 2: Widths of the $1s$ K^--nuclear state in $^{12}_{K^-}$C (top panel) and in $^{40}_{K^-}$Ca (bottom panel) as a function of the K^- binding energy, for absorption through $\bar{K}N \to \pi\Sigma$, with and without $\bar{K}N \to \pi\Lambda$, and assuming ρ or ρ^2 dependence for $\bar{K}NN \to \Sigma N$ (using the NL-SH RMF model).

Coulomb interaction. This reversal is due to the ρK^- coupling acting against the Coulomb interaction.

The interaction generated by the ϕ-meson mean field reduces the K^- binding energy in systems with more than one K^- meson, as it mediates repulsive interaction exclusively among strange particles. Generally, for the parameterizations and nuclei studied, the effect of the ϕ-meson repulsion increases with B_{K^-}, owing to the increased central K^- density. It amounts to several MeV for binding energies $B_{K^-} \lesssim 200$ MeV.

In the next step, considering the K^- decay modes discussed in the previous section, we calculated the corresponding widths of K^--nuclear bound states. In particular, we considered the one-nucleon absorption mode $\bar{K}N \to \pi\Lambda$, in addition to the dominant $\bar{K}N \to \pi\Sigma$ mode studied in our recent work [45], and also both ρ and ρ^2 density dependencies of the two-nucleon absorption mode $\bar{K}NN \to \Sigma N$.

Figure 2 shows the calculated width Γ_{K^-} as a function of the binding energy B_{K^-}

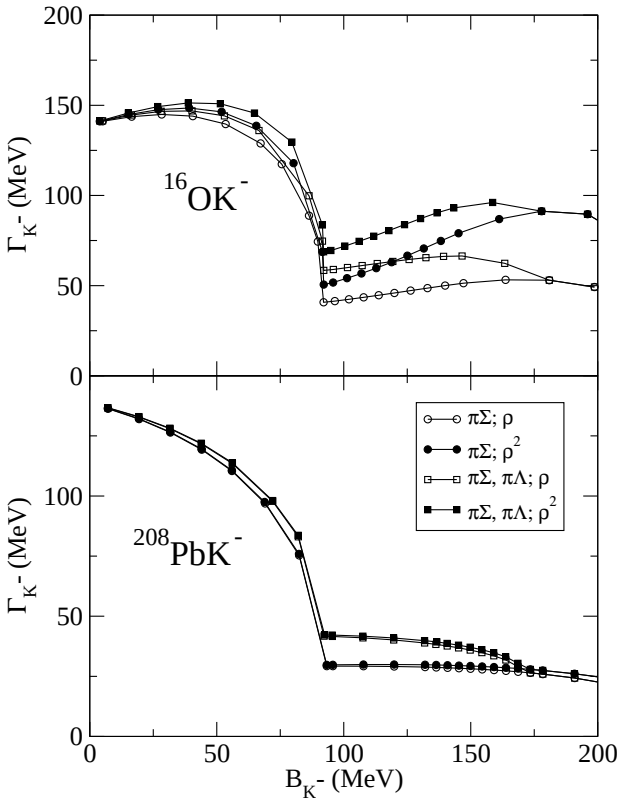

Figure 3: Widths of the $1s$ K^--nuclear state in ${}^{16}_{K^-}$O using the NL-SH RMF model (top panel), and in ${}^{208}_{K^-}$Pb using the HS RMF model (bottom panel), as a function of the K^- binding energy for various combinations of and assumptions on the K^- absorption modes as in Fig. 2.

for the K^- $1s$ state in ${}^{12}_{K^-}$C (top) and in ${}^{40}_{K^-}$Ca (bottom), using the nonlinear model NL-SH. The effect of allowing the $\pi\Lambda$ decay mode (10%) to share alongside with $\pi\Sigma$ (70%) the one-nucleon absorption strength is shown by squares, compared to circles for the $\pi\Sigma$ mode alone (80%). In each of the two groups of curves shown (one for ρ and the other one for ρ^2 density dependence of the two-nucleon mode) the inclusion of the secondary $\pi\Lambda$ decay mode contributes approximately 20 MeV in ${}^{12}_{K^-}$C and 15 MeV in ${}^{40}_{K^-}$Ca to the width in the region of binding energies B_{K^-} between 100 and 160 MeV. As for the density dependence of the two-nucleon absorption mode, the widths calculated assuming ρ and ρ^2 density dependence are denoted by open and solid symbols, respectively. Assuming ρ^2 instead of ρ density dependence, it leads to increased widths of the $1s$ K^--nuclear states, as demonstrated for ${}^{12}_{K^-}$C and ${}^{40}_{K^-}$Ca in Fig. 2, and for ${}^{16}_{K^-}$O in Fig. 3. The effect of the ρ^2 dependence of the $2N$-absorption mode clearly grows with B_{K^-} as a consequence of the enhanced central nuclear density ρ_N. While for $B_{K^-} \lesssim 100$ MeV it is less than 10 MeV,

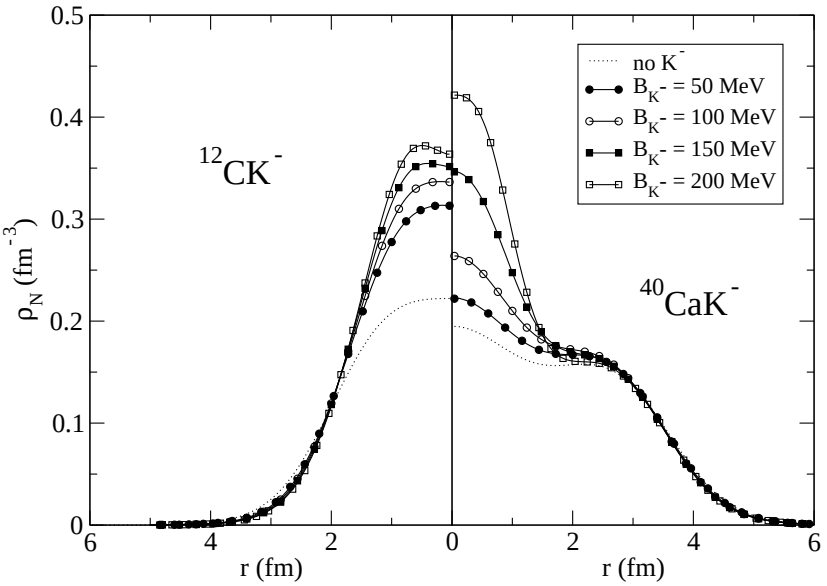

Figure 4: Nuclear density ρ_N of ${}^{12}_{K^-}$C (left panel) and ${}^{40}_{K^-}$Ca (right panel) for several $1s$ K^--nuclear states with specified binding energy, using the NL-SH RMF model. The dotted curves denote the corresponding nuclear density in the absence of the K^- meson.

for $B_{K^-} \gtrsim 150$ MeV it amounts to about 20 MeV in C and as much as about 30 MeV in Ca.

Figure 3 shows the widths Γ_{K^-} in ${}^{16}_{K^-}$O for the nonlinear model NL-SH (top) and in ${}^{208}_{K^-}$Pb for the linear model HS (bottom). As in the previous figure, switching on the $\pi\Lambda$ decay channel adds further conversion width to K^--nuclear states. In the range $B_{K^-} \simeq 100-160$ MeV the width Γ_{K^-} increases by about 20 MeV. The $\pi\Lambda$ conversion mode disappears at $B_{K^-} \simeq 175$ MeV. The effect of the $\pi\Lambda$ absorption channel is almost uniform for both nonlinear (NL-SH in Fig. 2 and Fig. 3, top) and linear (HS in Fig. 3, bottom) parameterizations in all nuclei under consideration. On the other hand, the widths calculated assuming ρ^2 dependence for the two-nucleon absorption mode exhibit strong sensitivity to the type of RMF model applied and to the nucleus considered (via the nuclear density ρ_N). In ${}^{208}_{K^-}$Pb, there is almost no difference between the widths Γ_{K^-} calculated using ρ or ρ^2 dependence. It was found that nonlinear parameterizations, represented here by NL-SH, produce larger increase of the width Γ_{K^-} owing to a ρ^2 density dependence of the $2N$ K^- absorption than linear models do, as could be anticipated from the considerably lower incompressibilities predicted by nonlinear models. It is to be noted that the particularly large widths Γ_{K^-} in ${}^{40}_{K^-}$Ca for $B_{K^-} \gtrsim 150$ MeV are due to a more significant increase of the central nuclear density in ${}^{40}_{K^-}$Ca than in ${}^{12}_{K^-}$C within the NL-SH model, see Fig. 4.

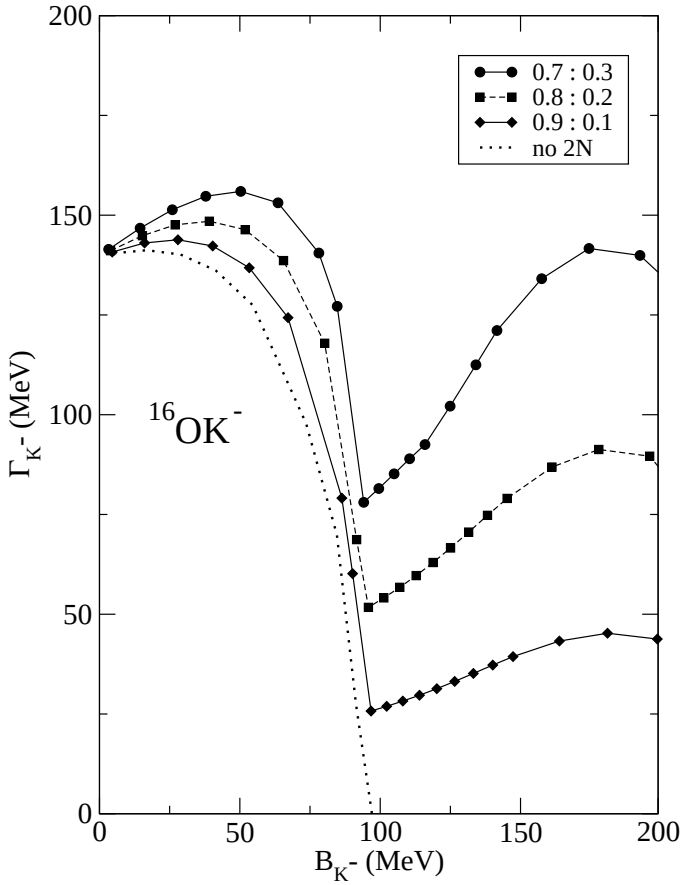

Figure 5: Widths of the $1s$ K^--nuclear state in $^{16}_{K^-}$O for various absorption branching ratios $\bar{K}N \to \pi\Sigma : \bar{K}NN \to \Sigma N$, using the NL-SH RMF model and ρ^2 dependence for the $2N$-absorption channel. The dotted curve stands for the decay widths in the absence of $2N$-absorption.

Figure 4 demonstrates that the effect of nuclear compression, as evidenced by the increase of the nuclear density ρ_N upon increasing the binding energy B_{K^-} of the $1s$ state, is limited to relatively small radii, $r \lesssim 1.5$ fm. Whereas in as light a nucleus as C this region constitutes most of the nucleus, it is only a fraction of the nuclear volume in medium-weight nuclei such as Ca and in heavier nuclei (not shown in the figure).

We also studied another possible source of uncertainty for the calculated K^- decay width, namely the dependence on the branching ratios assumed for the various conversion modes. Figure 5 shows the K^- decay width Γ_{K^-} as a function of the K^- binding energy B_{K^-} in $^{16}_{K^-}$O for the NL-SH model, assuming a ρ^2 dependence of the $2N$-conversion mode. The branching ratios of the decay modes, $\bar{K}N \to \pi\Sigma : \bar{K}NN \to \Sigma N$, are varied from 0.7 : 0.3 (circles) to 0.8 : 0.2 (squares) and to 0.9 : 0.1 (diamonds). The dotted curve represents

the decay widths calculated when the $2N$-absorption modes are neglected altogether. It is shown that varying the K^- absorption branching ratios by ± 0.1 away from the commonly used value $0.8 : 0.2$ alters the K^- decay width Γ_{K^-} by less than 10 MeV for binding energies $B_{K^-} \lesssim 90$ MeV. More remarkable is the effect in the region of $B_{K^-} \gtrsim 90$ MeV, where the dispersion reaches values of approximately 50 MeV. These results further point out to the delicacy of the estimates for the K^- decay widths in that region of binding energies. It is worth noting that the $0.8 : 0.2$ 'canonical' ratio is used here in a rather conservative way, implicitly assuming that it is effective for capture in the nuclear central-density region [see Eq. (16) for Im $\Pi^{(2)}_{K^-}$], whereas capture from rest in bubble-chamber and emulsion experiments [61] is likely to occur in lower-density regions. Therefore, the contribution to the K^- decay widths due to Im $\Pi^{(2)}_{K^-}$ could be larger than estimated by adopting the $0.8 : 0.2$ 'canonical' ratio. The ambiguities involved in evaluating the contribution of Im $\Pi^{(2)}_{K^-}$ have been recently discussed by Yamagata and Hirenzaki [64].

The last item studied for single-K^- nuclear states was the effect of a p-wave K^--nucleus interaction $\Pi^{(P)}_{K^-}$ [Eq. (10)]. Table 1 demonstrates the effects of this interaction, with a strength parameter c_0 given by Eq. (11) for a nominal value of $B_{K^-} = 100$ MeV. Shown are the K^- binding energy B_{K^-}, the single-particle binding energy $B^{\rm sp}_{K^-}$ and the decay width Γ_{K^-}, calculated for $1s$ K^-–nuclear states using the NL-SH parameterization. The results using the linear HS model are almost the same. The calculations excluding the p-wave K^- interaction are denoted by S, while those including the p-wave interaction are denoted by S+P. It is seen that the introduction of the p-wave interaction leads to an increase of the binding energy by approximately 13 MeV in ${}^{12}_{K^-}$C and by approximately 6 MeV in ${}^{40}_{K^-}$Ca. The decay width is then enhanced by about 6 MeV for carbon and by about 3 MeV for calcium. This enhancement of the decay width is a consequence of the K^- binding energy dependence of Γ_{K^-} in the relevant region of B_{K^-} (see Fig. 2) and also

Table 1: p-wave interaction contributions to the K^- binding energy B_{K^-}, to the single-particle binding energy $B^{\rm sp}_{K^-}$ and to the width Γ_{K^-}, for the $1s$ K^-–nuclear states in ${}^{12}_{K^-}$C and in ${}^{40}_{K^-}$Ca, using the NL-SH parameterization. Results for s-wave interactions exclusively are denoted by S and results including the p-wave interaction Eqs. (10) and (11) are denoted by S+P.

	^{12}C			^{40}Ca		
	B_{K^-} (MeV)	$B^{\rm sp}_{K^-}$ (MeV)	Γ_{K^-} (MeV)	B_{K^-} (MeV)	$B^{\rm sp}_{K^-}$ (MeV)	Γ_{K^-} (MeV)
S	100.0	109.8	51.1	100.0	104.4	35.0
S+P	112.8	123.3	56.9	105.6	111.8	38.3

of the moderate increase of the nuclear density distributions when compared to the case of purely s-wave interactions.

3.2 Multi-$\bar{K}$ nuclei

In the second part of this work, we embedded several ($\kappa \geq 2$) antikaons in the nuclear medium and studied the nuclear response, as well as the energies and widths of bound states in such multi-$\bar{K}$ nuclear systems. We studied nuclear systems containing only K^- mesons or only $\bar{K}^0$ mesons.

Figure 6 shows the calculated binding energies and widths of $1s$ K^- states in ^{16}O with two bound antikaons, using the NL-SH model, in comparison to similar calculations for a single antikaon bound in ^{16}O. The K^- binding energy B_{K^-} of the second K^- in the double-K^- nucleus ${}^{16}_{2K^-}$O is lower than the K^- binding energy in ${}^{16}_{1K^-}$O for binding energies $B_{K^-} \lesssim 90$ MeV. Primarily, this is a consequence of the dominance of the mutual repulsion induced by the vector-meson mean fields between the two K^- mesons over the extra polarization of the nuclear core evoked by the presence of the second K^- meson. It

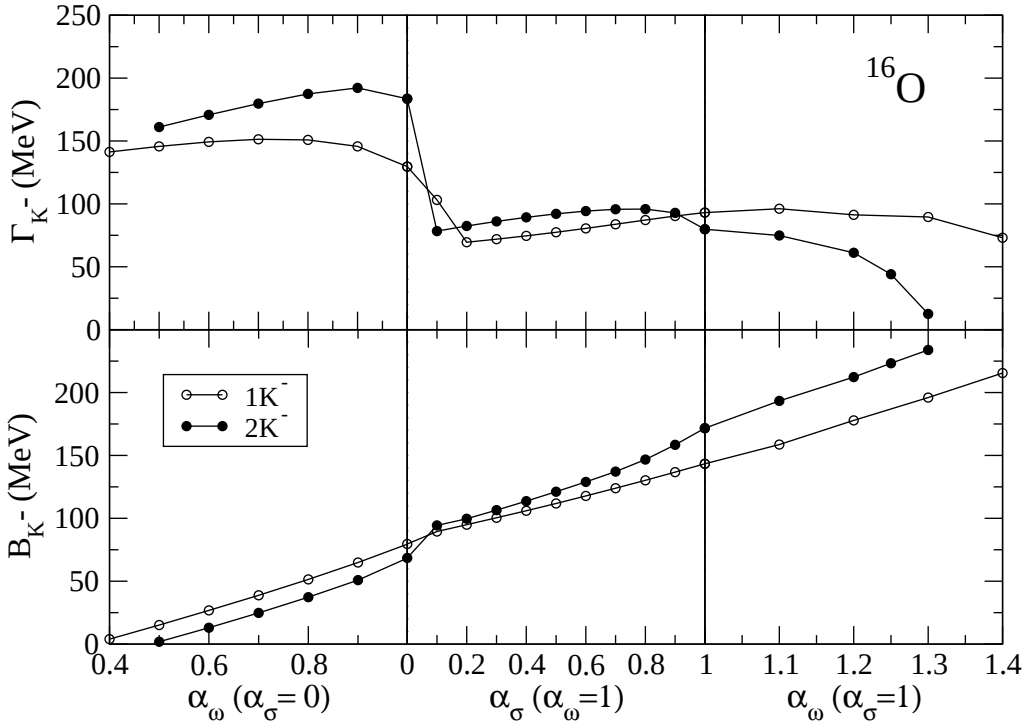

Figure 6: $1s$ K^- binding energy (bottom panels) and width (top panels) in ^{16}O with one and two antikaon(s) as a function of the coupling strengths α_ω and α_σ (see text), using the NL-SH RMF model.

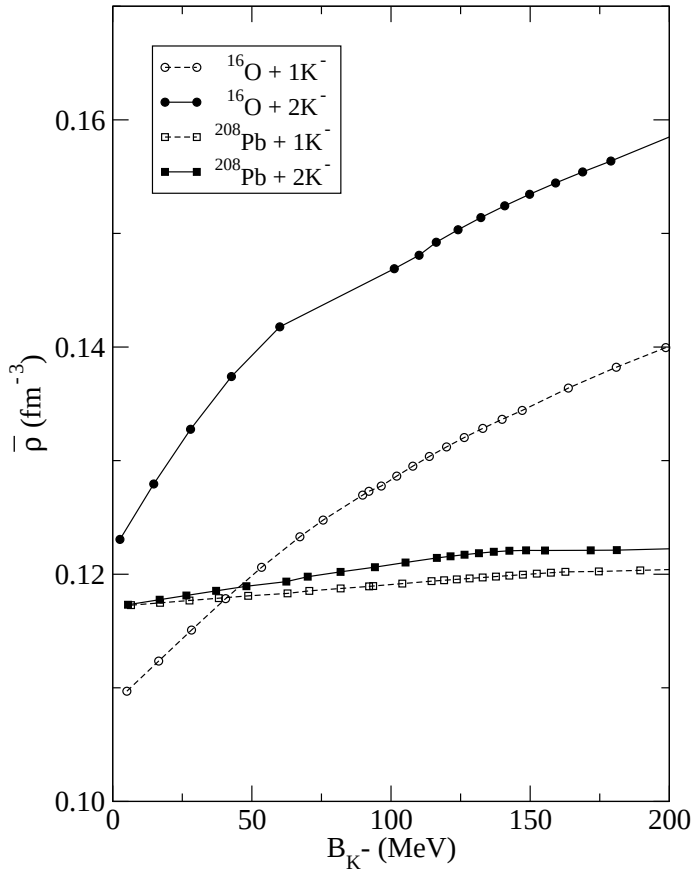

Figure 7: Average nuclear density $\bar{\rho}$ for ^{16}O and ^{208}Pb with one and two antikaon(s) as a function of the $1s$ K^- binding energy, using the NL-SH RMF model.

is worth noting that this result is amplified by the larger width Γ_{K^-} in the case of two antikaons, which acts repulsively, and by setting $\alpha_\sigma = 0$, for the attractive interaction generated by the scalar mean field, at the low B_{K^-} region of the left-hand panels in the figure. (If the coupling of the K^- meson to *all* the vector-meson mean fields is switched off, so that B_{K^-} is generated solely via the scalar σ-meson mean field, and furthermore the imaginary potential is switched off, the binding energy B_{K^-} of the second K^- in ${}^{16}_{2K^-}$O is *always* larger than B_{K^-} in ${}^{16}_{1K^-}$O.) This hierarchy is reversed at $B_{K^-} \simeq 90$ MeV when the K^- binding energy in ${}^{16}_{2K^-}$O becomes larger than in ${}^{16}_{1K^-}$O, reflecting a strong polarization of the nuclear core (see Figs. 7 and 10). The enhancement of the binding energy B_{K^-} in the double K^- nucleus is then responsible for the crossings of the curves for the K^- decay widths Γ_{K^-}, at $B_{K^-} \simeq 90$ and 170 MeV, caused by the binding energy dependence of the suppression factors. Finally, the sharp decrease of the width Γ_{K^-} in ${}^{16}_{2K^-}$O, at $B_{K^-} \simeq 230$ MeV, is due to the disappearance of the $2N$-absorption channel $\bar{K}NN \to \Sigma N$.

Figure 7 shows the average nuclear density $\bar{\rho}$ in ^{16}O and in ^{208}Pb with one and with two K^- mesons as a function of the K^- binding energy. Adding the second K^- to the nuclear system leads to further polarization of the nuclear core. The enhancement of the average nuclear density is quite pronounced in light nuclei (^{16}O) while in heavy nuclei (^{208}Pb) it is rather weak.

Figure 8 presents the 1s $\bar{K}$ binding energy $B_{\bar{K}}$ in the multi-$\bar{K}$ nuclei $^{16}\mathrm{O} + \kappa\bar{K}$, where $\kappa\bar{K} = \kappa K^-$ or $\kappa\bar{K}^0$, as a function of the number of antikaons κ, calculated within the NL-SH RMF parameterization. The figure demonstrates that increasing the number of antikaons in the nuclear medium does not necessarily lead to a sizable increase of the binding energy $B_{\bar{K}}$. Just on the contrary, for relatively small values of $B_{\bar{K}}$ (the curve starting with 50 MeV for $\kappa = 1$ in the figure), $B_{\bar{K}}$ decreases as a function of κ. This is consistent with the trend shown in Fig. 6 for one and two K^- mesons. (Had we replaced

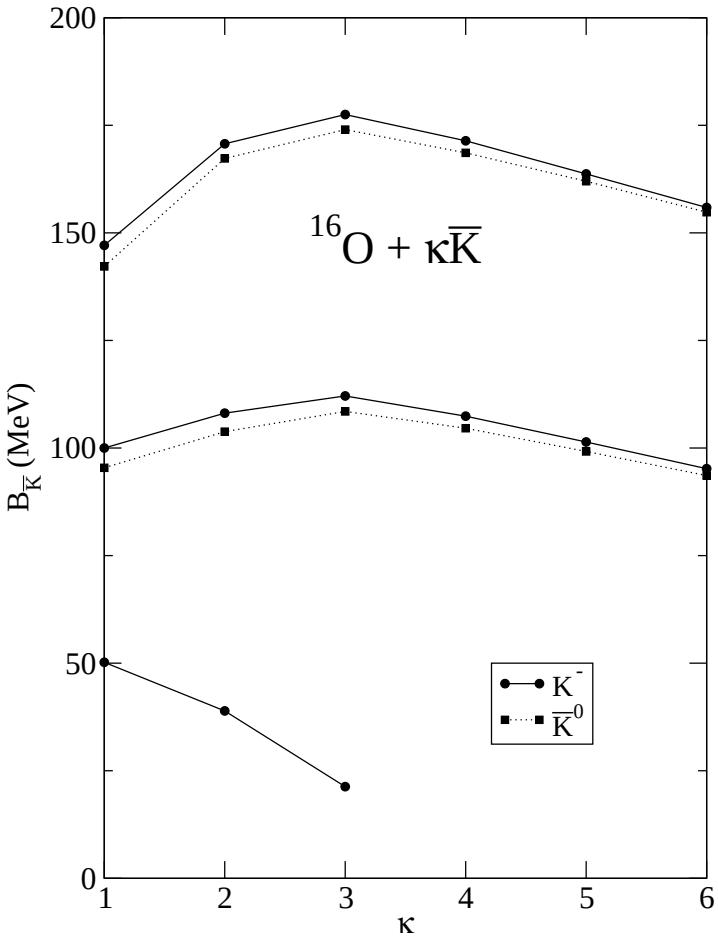

Figure 8: 1s $\bar{K}$ binding energy $B_{\bar{K}}$ in $^{16}\mathrm{O} + \kappa\bar{K}$, where $\bar{K} = K^-$ (circles) or $\bar{K}^0$ (squares), as a function of the number κ of antikaons, using the NL-SH RMF model.

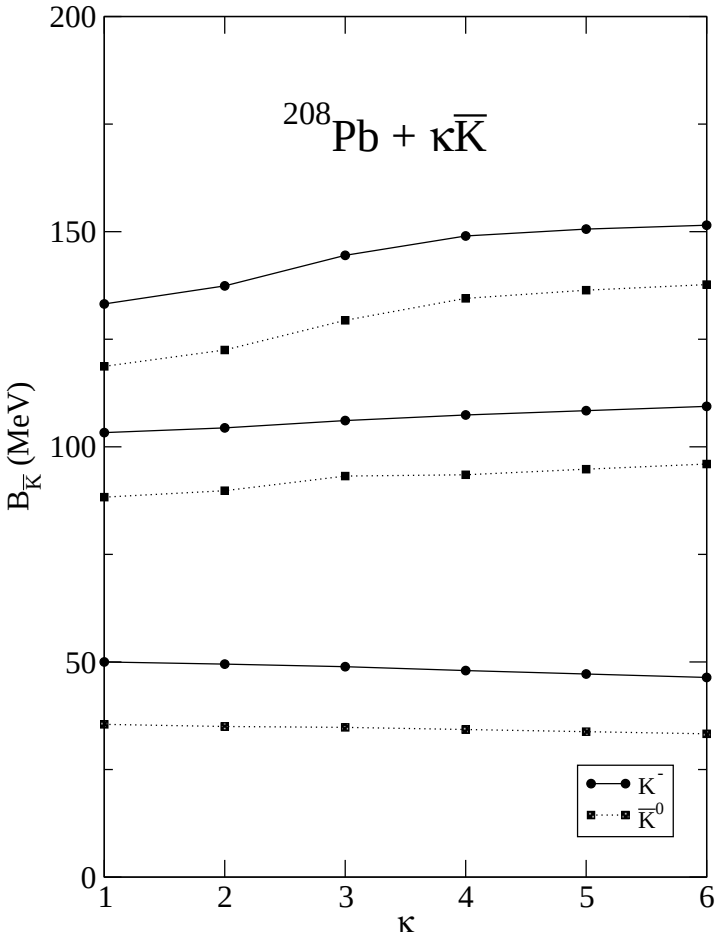

Figure 9: Same as Fig. 8, but for $^{208}\mathrm{Pb} + \kappa\bar{K}$, where $\bar{K} = K^-$ (circles) and $\bar{K}^0$ (squares).

the vector-meson mean-field couplings by an equivalent purely scalar-meson mean-field coupling to yield the same starting value of $B_{\bar{K}}$, setting also Im $\Pi_{\bar{K}} = 0$, $B_{\bar{K}}$ would rather increase as a function of κ.) For the higher starting values for $B_{\bar{K}}$ in the figure, a moderate decrease of $B_{\bar{K}}$ as a function of κ occurs for $\kappa > 3$, indicating that the $\bar{K}$ binding energies have reached saturation. We note that the difference between the K^- and $\bar{K}^0$ curves is relatively small, a few MeV at most, decreasing with κ owing to the increased role of the Coulomb repulsion among the K^- mesons.

Figure 9 shows the 1s $\bar{K}$ binding energy in the multi-$\bar{K}$ nuclei $^{208}\mathrm{Pb} + \kappa\bar{K}$, where $\kappa\bar{K} = \kappa K^-$ or $\kappa\bar{K}^0$, calculated using the NL-SH model. It is found that the attractive Coulomb interaction of a K^- meson with the large number of protons ($Z = 82$ for ^{208}Pb) outweighs the repulsion due to the $\rho\bar{K}$ coupling, so that the lowest-energy configuration is provided by a purely K^- charge configuration. The K^- curves are displaced by about 15

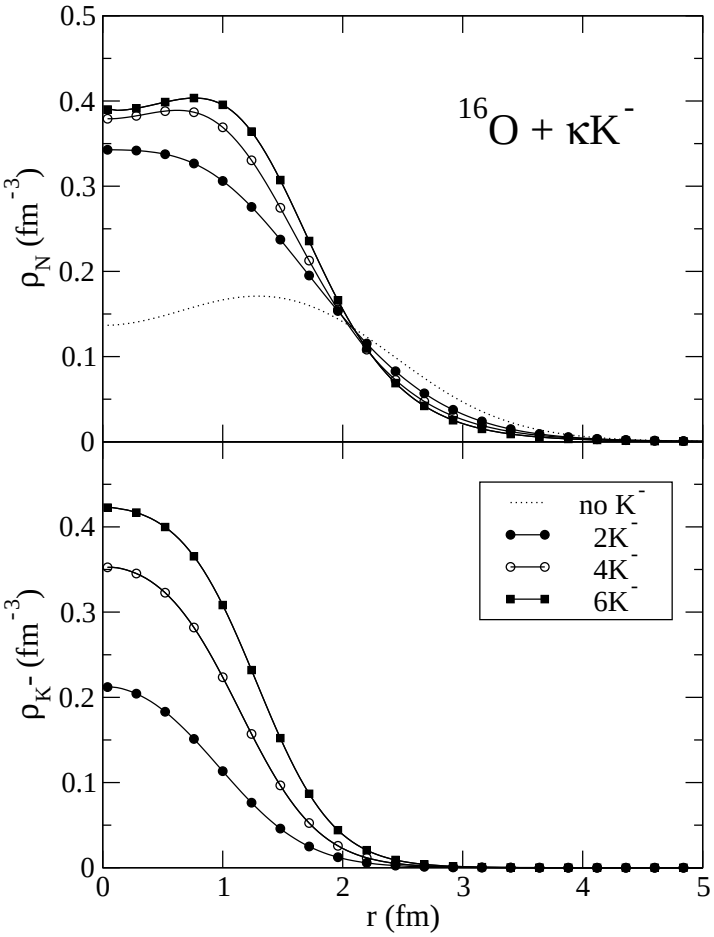

Figure 10: Nuclear density ρ_N (top panel) and $1s$ K^- density ρ_{K^-} (bottom panel) in $^{16}\mathrm{O} + \kappa K^-$, using the NL-SH RMF model with $\alpha_\sigma = 0.26$ and $\alpha_\omega = 1$, yielding $B_{K^-} = 100$ MeV in $^{16}\mathrm{O} + 1K^-$. The dotted curve stands for the ^{16}O density in the absence of K^- mesons.

MeV to higher values of binding energies than the respective $\bar{K}^0$ curves. Here and in the previous figure, the $\bar{K}^0$ couplings to the isoscalar-meson mean fields were taken identical to the corresponding K^- couplings, while differing in sign for the isovector ρ-meson mean field. Furthermore, Im $\Pi_{\bar{K}}$ was assumed to be the same for $\bar{K}^0$ mesons as for K^- mesons. For the lowest starting value of $B_{\bar{K}}$ in Fig. 9, as for ^{16}O in the previous figure, $B_{\bar{K}}$ decreases as a function of κ, although at a slower rate. For higher starting values of $B_{\bar{K}}$, a moderate increase of $B_{\bar{K}}(\kappa)$ is observed, which gradually slows down with increasing the number of antikaons κ. We checked that saturation of $B_{\bar{K}}(\kappa)$ is actually reached for a higher value of κ than shown in the figure ($\kappa \geq 10$).

The dependence of the nuclear density $\rho_N(r)$ and the K^- density $\rho_{K^-}(r)$ on the number

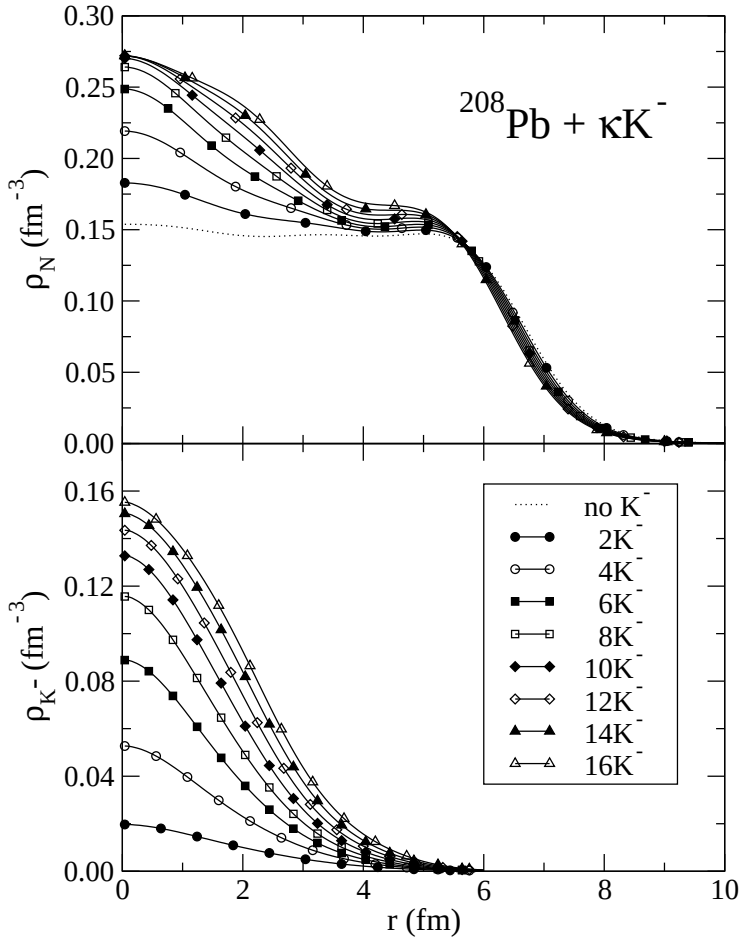

Figure 11: Same as in Fig. 10, but for $^{208}\mathrm{Pb} + \kappa K^-$ with $\alpha_\sigma = 0$ and $\alpha_\omega = 0.86$, yielding $B_{K^-} = 100$ MeV in $^{208}\mathrm{Pb} + 1K^-$.

of K^- mesons embedded in the nuclear medium is shown in Fig. 10 for ($^{16}\mathrm{O} + \kappa K^-$) and in Fig. 11 for ($^{208}\mathrm{Pb} + \kappa K^-$). Shown also for comparison, in dotted lines, are the density distributions ρ_N for $\kappa = 0$. The K^- couplings were chosen such that the $1K^-$ configuration was bound by 100 MeV. The density distributions behave quite regularly as a function of κ. In $^{16}\mathrm{O}+\kappa K^-$, for $\kappa \geq 4$, the nuclear density distribution recovers the saddle it had without antikaons at $r \approx 0$. The increase of the nuclear density resulting from the $1s$ antikaons is limited to the vicinity of the nuclear center where the density ρ_{K^-} is substantial, much the same as for single-K^- nuclei (see Fig. 4) upon increasing B_{K^-}. The gradual increase of ρ_{K^-} as well as of ρ_N slows down with κ, leading to saturation as demonstrated for $\rho_N(0)$ in Figs. 10 and 11. The saturation is also apparent when the K^- densities ρ_{K^-} (normalized to κ) are shown as $\rho_{K^-}(0)/\kappa$ in Table 2.

Table 2: Values of $\rho_{K^-}(0)/\kappa$ (in fm^{-3}) as a function of the number of K^- mesons κ in ^{16}O and ^{208}Pb, using the NL-SH RMF parameterization. The K^- density ρ_{K^-} is normalized to κ. The K^- coupling constants for each core nucleus give rise to $B_{K^-} = 100$ MeV for a single K^- meson.

	κ	1	2	4	6	8	10
$\rho_{K^-}(0)/\kappa$	$^{16}\mathrm{O} + \kappa K^-$	0.098	0.106	0.088	0.070		
$\rho_{K^-}(0)/\kappa$	$^{208}\mathrm{Pb} + \kappa K^-$	0.009	0.010	0.013	0.014	0.015	0.013

4 Conclusions

In the present work, we studied in detail the interplay between the underlying dynamical processes and the relevant kinematical conditions which determine the decay width of deeply bound $\bar{K}$–nuclear states in the nuclear medium. We performed fully self-consistent dynamical calculations of $\bar{K}$–nuclear states for nuclear systems with one and several $\bar{K}$ mesons within the RMF approach.

We verified that the interaction of a $1s$ K^- meson with the ρ-meson mean field affects negligibly the K^- binding energy. Its main effect on the nucleon single particle energies is to partly cancel, and for the $1s$ nucleon level even reverse the $p - n$ Coulomb energy difference. For all nuclei and RMF parameterizations considered in the present work, the ρ-meson contribution slightly decreases the K^- binding energy B_{K^-} by less than about 5 MeV for $B_{K^-} \lesssim 200$ MeV. Similarly, the ϕ-meson contribution in systems with several K^- mesons reduces the K^- binding energy by a few MeV in this range of B_{K^-} values.

The calculations involving the p-wave interaction of the K^- meson with a nucleus indicate that the p-wave interaction plays a secondary role for deeply bound K^-–nuclear systems where the mean-field concept is acceptable. Although the p-wave interaction by itself is too weak to cause nuclear binding, its contribution in the lightest (carbon) nucleus considered in the present work amounts to more than 10 MeV and is certainly nonnegligible. Since the effect of the p-wave interaction appears to increase upon decreasing the atomic number, it could play a primary role in deeply and tightly bound few-body K^- systems.

We found that the implementation of the $\pi\Lambda$ decay channel in the single-nucleon absorption mode enhances the K^- conversion width for K^- binding energies $B_{K^-} \lesssim 170$ MeV. This enhancement is almost uniform for both linear and nonlinear parameterizations in all nuclei considered. The most remarkable contribution occurs for K^- binding energies in the range $B_{K^-} \approx 100 - 160$ MeV where it reaches values of approximately 20 MeV. The assumption of a ρ^2 density dependence for the $2N$-absorption mode adds further conversion

width especially to the deeply bound K^-–nuclear states. The increase is particularly large for nonlinear parameterizations owing to the strong polarization effects affordable through the moderate value of nuclear incompressibility, as opposed to the highly unrealistic values in linear parameterizations. Altogether, the results of these comprehensive calculations suggest that K^- total decay widths for deeply bound K^- nuclear states ($B_{K^-} > 100$ MeV) are substantial, $\Gamma_{K^-} \sim 50 - 100$ MeV.

We also studied nuclear systems containing several antikaons. The nuclear and $\bar{K}$ densities were found to behave quite regularly upon increasing the number of antikaons embedded in the nuclear medium. The calculations do not indicate any abrupt or substantial increase of the densities. The central nuclear densities in multi-K^- ^{16}O nuclei and in multi-K^- ^{208}Pb nuclei appear to saturate at about only 50% and 60%, respectively, higher values than the central nuclear densities in the corresponding systems with one antikaon. Furthermore, the $\bar{K}$ binding energy saturates upon increasing the number of $\bar{K}$ mesons embedded in the nuclear medium. The heavier the nucleus is, the more antikaons it takes to saturate the binding energies, but even for ^{208}Pb the number required does not exceed approximately 10. The saturated values of $\bar{K}$ binding energies do not exceed the range of values 100–200 MeV considered normally as providing deep binding for one antikaon. This range of binding energies leaves antikaons in multi-$\bar{K}$ nuclei comfortably above the range of energies where hyperons might be relevant. It is therefore unlikely that multi-$\bar{K}$ nuclei may offer precursor phenomena in nuclear matter towards kaon condensation. This does not rule out that kaon condensation occurs in neutron stars where different constraints hold for the composition of matter. Although we presented results for one particular choice of RMF model, the NL-SH model [63], the use of other realistic mean-field models supports these conclusions.

Acknowledgments

One of us (AG) acknowledges and thanks Wolfram Weise for stimulating discussions, particularly on the $\bar{K}$–nuclear p-wave interaction. This work was supported in part by the GA AVCR grant IAA100480617 and by the Israel Science Foundation grant 757/05.

References

[1] B.D. Kaplan, A.E. Nelson, Phys. Lett. B **175**, 57 (1986).

[2] A.E. Nelson, B.D. Kaplan, Phys. Lett. B **192**, 193 (1987).

[3] G.E. Brown, C.-H. Lee, M. Rho, V. Thorsson, Nucl. Phys. A **567**, 937 (1994).

[4] C.-H. Lee, G.E. Brown, D.-P. Min, M. Rho, Nucl. Phys. A **585**, 401 (1995).

[5] R.H. Dalitz, T.C. Wong, G. Rajasekaran, Phys. Rev. **153**, 1617 (1967).

[6] A.D. Martin, Nucl. Phys. B **179**, 33 (1981).

[7] M. Iwasaki *et al.*, Phys. Rev. Lett. **78**, 3067 (1997); T.M. Ito *et al.*, Phys. Rev. C **58**, 2366 (1998).

[8] G. Beer *et al.*, Phys. Rev. Lett. **94**, 212302 (2005).

[9] A. Müller-Groeling, K. Holinde, J. Speth, Nucl. Phys. A **513**, 557 (1990).

[10] V. Koch, Phys. Lett. B **337**, 7 (1994).

[11] N. Kaiser, P.B. Siegel, W. Weise, Nucl. Phys. A **594**, 325 (1995).

[12] B. Borasoy, R. Nißler, W. Weise, Phys. Rev. Lett. **94**, 213401 (2005); *ibid.* **96**, 199201 (2006); Eur. Phys. J. A **25**, 79 (2005).

[13] J.A. Oller, J. Prades, M. Verbeni, Phys. Rev. Lett. **95**, 172502 (2005); *ibid.* **96**, 199202 (2006); J.A. Oller, Eur. Phys. J. A **28**, 63 (2006); J.A. Oller, J. Prades, M. Verbeni, Eur. Phys. J. A **31**, 527 (2007).

[14] B. Borasoy, U.-G. Meißner, R. Nißler, Phys. Rev. C **74**, 055201 (2006).

[15] E. Friedman, A. Gal, C.J. Batty, Phys. Lett. B **308**, 6 (1993).

[16] E. Friedman, A. Gal, C.J. Batty, Nucl. Phys. A **579**, 518 (1994).

[17] C.J. Batty, E. Friedman, A. Gal, Phys. Rep. **287**, 385 (1997).

[18] E. Friedman, A. Gal, J. Mareš, A. Cieplý, Phys. Rev. C **60**, 024314 (1999).

[19] J. Mareš, E. Friedman, A. Gal, Nucl. Phys. A **770**, 84 (2006).

[20] N. Barnea, E. Friedman, Phys. Rev. C **75**, 022202(R) (2007).

[21] E. Friedman, A. Gal, Phys. Rep. **452**, 89 (2007).

[22] T. Waas, N. Kaiser, W. Weise, Phys. Lett. B **365**, 12 (1996); *ibid.* **379**, 34 (1996).

[23] J. Schaffner-Bielich, V. Koch, M. Effenberger, Nucl. Phys. A **669**, 153 (2000).

[24] A. Ramos, E. Oset, Nucl. Phys. A **671**, 481 (2000).

[25] A. Baca, C. García-Recio, J. Nieves, Nucl. Phys. A **673**, 335 (2000).

[26] A. Cieplý, E. Friedman, A. Gal, J. Mareš, Nucl. Phys. A **696**, 173 (2001).

[27] L. Tolos, A. Ramos, A. Polls, T.T.S. Kuo, Nucl. Phys. A **690**, 547 (2001).

[28] W. Scheinast *et al.*, Phys. Rev. Lett. **96**, 072301 (2006).

[29] T. Kishimoto, Phys. Rev. Lett. **83**, 4701 (1999).

[30] Y. Akaishi, T. Yamazaki, in *Proc. III Int. Workshop on Physics and Detectors for DAΦNE*, edited by S. Bianconi *et al.*, Frascati Physics Series XVI (LNF, Frascati, 1999), p. 59.

[31] Y. Akaishi, T. Yamazaki, Phys. Rev. C **65**, 044005 (2002).

[32] T. Yamazaki, A. Doté, Y. Akaishi, Phys. Lett. B **587**, 167 (2004).

[33] T. Suzuki *et al.*, Phys. Lett. B **597**, 263 (2004).

[34] T. Suzuki *et al.*, Nucl. Phys. A **754**, 375c (2005).

[35] M. Iwasaki *et al.*, arXiv:0706.0297 [nucl-ex].

[36] T. Kishimoto *et al.*, Prog. Theor. Phys. **118**, 181 (2007).

[37] M. Agnello *et al.*, Phys. Rev. Lett. **94**, 212303 (2005).

[38] T. Kishimoto *et al.*, Nucl. Phys. A **754**, 383c (2005).

[39] V.K. Magas, E. Oset, A. Ramos, H. Toki, Phys. Rev. C **74**, 025206 (2006).

[40] T. Yamazaki, Y. Akaishi, Phys. Lett. B **535**, 70 (2002).

[41] A. Doté, H. Horiuchi, Y. Akaishi, T. Yamazaki, Phys. Lett. B **590**, 51 (2004); Phys. Rev. C **70**, 044313 (2004); Y. Akaishi, A. Doté, T. Yamazaki, Phys. Lett. B **613**, 140 (2005).

[42] A. Doté, W. Weise, arXiv:nucl-th/0701050.

[43] N.V. Shevchenko, A. Gal, J. Mareš, Phys. Rev. Lett. **98**, 082301 (2007); Phys. Rev. C **76** 044004 (2007).

[44] Y. Ikeda, T. Sato, Phys. Rev. C **76**, 035203 (2007).

[45] J. Mareš, E. Friedman, A. Gal, Phys. Lett. B **606**, 295 (2005); Nucl. Phys. A **770**, 84 (2006).

[46] X.H. Zhong, G.X. Peng, L. Li, P.Z. Ning, Phys. Rev. C **74**, 034321 (2006).

[47] C. García-Recio, J. Nieves, E. Oset, A. Ramos, Nucl. Phys. A **703**, 271 (2002).

[48] S. Wycech, A.M. Green, arXiv:nucl-th/0501019.

[49] J. Schaffner-Bielich, A. Gal, Phys. Rev. C **62**, 034311 (2000).

[50] J. Schaffner, A. Gal, I.N. Mishustin, H. Stöcker, W. Greiner, Phys. Lett. B **334**, 268 (1994).

[51] G.E. Brown, M. Rho, Nucl. Phys. A **596**, 503 (1996).

[52] R. Knorren, M. Prakash, P.J. Ellis, Phys. Rev. C **52**, 3470 (1995).

[53] J. Schaffner, I.N. Mishustin, Phys. Rev. C **53**, 1416 (1996).

[54] S. Pal, D. Bandyopadhyay, W. Greiner, Nucl. Phys. A **674**, 553 (2000).

[55] T. Maruyama, T. Muto, T. Tatsumi, K. Tsushima, A.W. Thomas, Nucl. Phys. A **760**, 319 (2005).

[56] G.E. Brown, C.-H. Lee, H.-J. Park, M. Rho, Phys. Rev. Lett. **96**, 062303 (2006).

[57] C.Y. Ryu, C.H. Hyun, S.W. Hong, B.T. Kim, Phys. Rev. C **75**, 055804 (2007).

[58] Y. Kim, K. Kubodera, D.-P. Min, F. Myhrer, M. Rho, Nucl. Phys. A **792**, 249 (2007).

[59] T. Muto, arXiv:nucl-th/0702027.

[60] W. Weise, arXiv:nucl-th/0701035.

[61] C. Vander Velde-Wilquet, J. Sacton, J.H. Wickens, D.N. Tovee, D.H. Davis, Nuovo Cimento A **39**, 538 (1977).

[62] C.J. Horowitz, B.D. Serot, Nucl. Phys. A **368**, 503 (1981).

[63] M.M. Sharma, M.A. Nagarajan, P. Ring, Phys. Lett. B **312**, 377 (1993).

[64] J. Yamagata, S. Hirenzaki, Eur. Phys. J. A **31**, 255 (2007).

Published in Physical Review C 77 (2008) 045206

Multi-$\bar{K}$ nuclei and kaon condensation

D. Gazda[1], E. Friedman[2], A. Gal[2], J. Mareš[1]

[1]*Nuclear Physics Institute, 25068 Řež, Czech Republic*
[2]*Racah Institute of Physics, The Hebrew University, Jerusalem 91904, Israel*

Abstract

We extend previous relativistic mean-field (RMF) calculations of multi-$\bar{K}$ nuclei, using vector boson fields with SU(3) PPV coupling constants and scalar boson fields constrained phenomenologically. For a given core nucleus, the resulting $\bar{K}$ separation energy $B_{\bar{K}}$, as well as the associated nuclear and $\bar{K}$-meson densities, saturate with the number κ of $\bar{K}$ mesons for $\kappa > \kappa_{\rm sat} \sim 10$. Saturation appears robust against a wide range of variations, including the RMF nuclear model used and the type of boson fields mediating the strong interactions. Because $B_{\bar{K}}$ generally does not exceed 200 MeV, it is argued that multi-$\bar{K}$ nuclei do not compete with multihyperonic nuclei in providing the ground state of strange hadronic configurations, and that kaon condensation is unlikely to occur in strong-interaction self-bound strange hadronic matter. Last, we explore possibly self-bound strange systems made of neutrons and $\bar{K}^0$ mesons, or protons and K^- mesons, and study their properties.

1 Introduction and Overview

Kaon condensation in dense matter was proposed over 20 years ago by Kaplan and Nelson [1, 2]. It is necessary to distinguish in this context between K mesons and $\bar{K}$ mesons which interact quite differently with matter. The empirical evidence from K^- atoms is that the $\bar{K}$-nuclear interaction is strongly attractive, and absorptive as well, with typical values of $150 - 200$ MeV attraction at nuclear-matter density ρ_0, as reviewed recently by Friedman and Gal [3]. A strong nuclear attraction of somewhat less than 100 MeV at ρ_0 for K^- mesons, compared to a weak repulsion of order 25 MeV for K^+ mesons, follows from observations of enhanced near-threshold production of K^- mesons in proton-nucleus collisions at GSI [4]. This weakly repulsive nature of the K^+-nuclear interactions was quantified a long time ago, starting with Dover and Moffa [5], and is also reviewed in Ref. [3]. Given the distinction between the nuclear interactions of K mesons and $\bar{K}$ mesons, the term *kaon condensation* is used loosely here and elsewhere to mean $\bar{K}$ condensation.

Neutron stars, with a density range extending over several times ρ_0, offer the most natural dense systems where kaon condensation could be realized; see Refs. [6, 7, 8, 9, 10, 11] for comprehensive reviews of past work. We note that in *Heaven*, for neutron stars, weak-interaction time scales of order 10^{-8} s and longer are operative, enabling strangeness-changing processes such as $e^- \rightarrow K^- + \nu_e$ to transform high-pressure dense electrons to K^- mesons once the effective mass of K^- mesons drops down below approximately 200 MeV. Under some optimal conditions, recalling that $\bar{K}$ mesons undergo attraction of order 100 MeV per density unit of ρ_0 [12], kaon condensation could occur at densities about $3\rho_0$, depending on the way hyperons enter the constituency of neutron stars as first recognised by Ellis, Knorren and Prakash [13]. However, on *Earth* under laboratory conditions, strong-interaction time scales of order 10^{-23} s are operative; processes of equilibration and hadronization subsequent to dense-matter formation in heavy-ion collisions occur over much shorter times than those controlling the composition of neutron stars. If antikaons bind strongly to nuclei, according to a scenario spelled out recently by Yamazaki *et al.* [14], then $\bar{K}$ mesons might provide the relevant physical degrees of freedom for self-bound strange hadronic matter that would then be realized as multi-$\bar{K}$ nuclei. It requires that the $\bar{K}$ separation energy $B_{\bar{K}}$ beyond some threshold value of strangeness exceeds $m_K c^2 + \mu_N - m_\Lambda c^2 \gtrsim 320$ MeV, where μ_N is the nucleon chemical potential, thus allowing for the conversion $\Lambda \rightarrow \bar{K} + N$ in matter. For this strong binding, Λ and Ξ hyperons would no longer combine macroscopically with nucleons to compose the more conventional kaon-free form of strange hadronic matter [15]. $\bar{K}$ mesons will then condense macroscopically. However, the nuclear densities encountered in these strange hadronic nuclei are somewhat less than the typical $3\rho_0$ threshold required to lower sufficiently the $\bar{K}$ energy in matter to reach condensation. Yet, precursor phenomena to kaon condensation in nuclear matter could occur at lower densities as soon as $B_{\bar{K}}$ exceeds the combination $m_K c^2 + \mu_N - m_\Sigma c^2 \gtrsim 240$ MeV. In this case, the only mechanism underlying the widths of multi-$\bar{K}$ states is the fairly weak conversion $\bar{K}NN \rightarrow \Lambda N$.

Recently we have reported on preliminary calculations of multi-$\bar{K}$ nuclear configurations [16] using the relativistic mean-field (RMF) methodology, constrained by $\bar{K}$-nucleus phenomenology. It was found that the nuclear and $\bar{K}$ densities behave regularly on increasing the number of antikaons embedded in the nuclear medium, without any indication for abrupt or substantial increase, and that the $\bar{K}$ separation energy saturates. Roughly speaking, the heavier the nucleus is, the more antikaons it takes to saturate the separation energies, but even for ^{208}Pb the number required does not exceed approximately 10.

Because the calculated $\bar{K}$ separation energies $B_{\bar{K}}$ do not generally exceed 200 MeV, for input binding in the accepted "deep-binding" range $B_{\bar{K}} \sim 100 - 150$ MeV for a single $\bar{K}$ meson [17, 18, 19], it was deemed unlikely that kaon condensation occurs in nuclear matter. This leaves antikaons in multi-$\bar{K}$ nuclei comfortably above the range of energies appropriate to (hyperonic) strange hadronic matter [15]. In the present article we discuss the full scope of these calculations demonstrating the robustness of this saturation property. In particular we study the sensitivity of the results to the nuclear equation of state used, through the nonlinear RMF version employed, and the role of "hidden strangeness" isoscalar meson fields beyond the standard isoscalar, scalar (σ), and vector (ω) meson fields. Although both σ- and ω-meson fields mediate attraction between $\bar{K}$ mesons and nucleons, they play different roles for the interactions within $\bar{K}$ mesons, similarly to the pattern well known for nucleons. The σ meson induces attraction, whereas the ω meson induces repulsion. If the $\bar{K}$-meson couplings were exclusively limited to scalar-meson fields, the resulting $\bar{K}$-meson separation energies would not have saturated. However, chiral model studies of $\bar{K}N$ low-energy phenomenology give a clear evidence in favor of the lowest-order Tomozawa-Weinberg *vector* interaction, which in terms of meson exchanges is equivalent to vector-meson exchanges with purely F-type SU(3) pseudoscalar-pseudoscalar-vector (PPV) vertices [19]. Our philosophy in this work is to use these vector-meson fields coupling constants as they are, augmenting the $\bar{K}$-nucleus vector interaction by additional *scalar* couplings such that $B_{\bar{K}} \sim 100 - 150$ MeV holds for single-$\bar{K}$ nuclei. We find no precursor behavior to kaon condensation for $\bar{K}$ mesons in self-bound nuclear matter.

We also explore in this work exotic strange self-bound configurations where $\bar{K}$ mesons are bound to either neutrons or protons. The simple example of a quasibound K^-pp system (and thus also its charge-symmetric partner $\bar{K}^0nn$) recently calculated solving Faddeev coupled-channel equations [20, 21, 22], clearly demonstrates that $\bar{K}$ mesons can bind together nuclear clusters that are otherwise unbound. The point here is that the underlying K^-p and $\bar{K}^0n$ interactions (each with equally mixed $I = 0$ and $I = 1$ components) provide considerably more attraction than the purely $I = 1$ K^-n and $\bar{K}^0p$ interactions. The RMF calculations reported here start with eight neutrons, showing that a finite number of neutrons can be made self bound by adding together a few $\bar{K}^0$ mesons, with $\bar{K}$ separation energies of order $B_{\bar{K}} \sim 50 - 100$ MeV. We study the role of the isovector ρ meson in stabilizing these exotic configurations, owing to its role in distinguishing between the underlying $I = 0$ and $I = 1$ $\bar{K}N$ interactions. We find that the emergent stable neutron configurations are more tightly bound than in the corresponding ordinary nuclei with $N \approx Z$ along the

stability valley, and the neutron single-particle spectra display substantial rearrangement. However, these exotic configurations are found to be unstable against charge-exchange $\bar{K}^0 + n \rightarrow K^- + p$ reactions.

In Sec. 2 we briefly outline the RMF methodology and discuss the $\bar{K}$ coupling constants to the meson fields used in the present calculations. Results are shown and discussed in Sec. 3 for $\bar{K}$ separation energies and density distributions, also displaying the dependence on the type of nonlinear RMF model used and the contribution of specific meson fields to the energy systematics and particularly to maintaining saturation in a robust way. A separate subsection is devoted to the study of exotic multi-$\bar{K}$ "nuclei" with neutrons only. Again, binding energies and densities are discussed, plus rearrangement features of the neutrons in the $\bar{K}$-extended mean field. We conclude with a brief summary in Sec. 4.

2 Methodology

2.1 RMF equations of motion

Bound nuclear systems of nucleons and several $\bar{K}$ mesons are treated in this work within the RMF framework, where the interactions among hadrons are mediated by the exchange of scalar- and vector-meson fields. The model Lagrangian consists of a standard nuclear part $\mathcal{L}_N$ and the Lagrangian density $\mathcal{L}_K$ describing the kaonic sector:

$$\mathcal{L}_K = (\mathcal{D}_\mu K)^\dagger (\mathcal{D}^\mu K) - m_K^2 K^\dagger K + g_{\sigma K} m_K K^\dagger K \, \sigma + g_{\sigma^* K} m_K K^\dagger K \, \sigma^* \, . \tag{1}$$

Here,

$$\mathcal{D}_\mu \equiv \partial_\mu + \mathrm{i}\, g_{\omega K}\, \omega_\mu + \mathrm{i}\, g_{\rho K}\, \vec{\tau} \cdot \vec{\rho}_\mu + \mathrm{i}\, g_{\phi K}\, \phi_\mu + \mathrm{i}\, e\, \tfrac{1}{2}(1+\tau_3) A_\mu \, , \tag{2}$$

and K ($K^\dagger$) denotes the kaon (antikaon) doublet. To be specific, we discuss K^--nuclear systems. Similar expressions hold for $\bar{K}^0$ mesons. In addition to a scalar-meson field σ and to vector-meson fields ω and ρ normally used in purely nuclear RMF calculations, we also considered meson fields that couple exclusively to strangeness degrees of freedom, a scalar σ^*, and a vector ϕ. Standard techniques yield a coupled system of equations of motion for nucleons and all meson mean fields involved; we refer the reader to our earlier work [16] for details. Here it suffices to recall that the presence of $\bar{K}$ meson(s) induces additional source terms in the Klein-Gordon (KG) equations for the meson (mean) fields. In the case

of K^- mesons, the source terms contain the K^- density

$$\rho_{K^-} = 2(E_{K^-} + g_{\omega K}\,\omega_0 + g_{\rho K}\,\rho_0 + g_{\phi K}\,\phi_0 + e\,A_0)K^-K^+\,, \qquad \int \mathrm{d}^3x\,\rho_{K^-} = \kappa\,, \quad (3)$$

where $E_{K^-} = \mathrm{i}\,\partial_t K^-$. Hence, the $\bar{K}$ mesons modify the scalar and vector potentials that enter the Dirac equation for nucleons, thus leading to rearrangement of the nuclear core. The polarized nucleons, in turn, modify the $\bar{K}$-nucleus interaction. This calls for a self-consistent procedure for solving the equations of motion.

In our model, the KG equation of motion for the K^- meson acquires the form

$$[-\nabla^2 - E_{K^-}^2 + m_K^2 + \mathrm{Re}\,\Pi_{K^-}\,]K^- = 0\,, \quad (4)$$

with the K^- self-energy given by

$$\begin{aligned} \mathrm{Re}\,\Pi_{K^-} = \; & - \; (g_{\sigma K} m_K \sigma_0 + g_{\sigma^* K} m_K \sigma_0^*) - 2E_{K^-}(g_{\omega K}\omega_0 + g_{\rho K}\rho_0 + g_{\phi K}\phi_0 + eA_0) \\ & - \; (g_{\omega K}\omega_0 + g_{\rho K}\rho_0 + g_{\phi K}\phi_0 + eA_0)^2\,. \end{aligned} \quad (5)$$

Of the three terms on the right-hand side (rhs) of Eq. (5), the first one is a scalar-meson contribution, whereas the other two terms are vector-meson contributions. The scalar contribution is sometimes lumped together with the kaon mass m_K to form a density-dependent effective kaon mass m_K^* via

$$m_K^{*\,2} \;=\; m_K{}^2 \;-\; g_{\sigma K} m_K \sigma_0 \;-\; g_{\sigma^* K} m_K \sigma_0^*\,. \quad (6)$$

Finally, to account for K^- absorption in the nuclear medium, the self-energy $\Pi_{K^-} = 2E_{K^-}V_{\mathrm{RMF}}^{K^-}$ in Eq. (4) was made complex by adding $\mathrm{Im}\,\Pi_{K^-}$ and the real energy E_{K^-} was replaced by $E_{K^-} - \mathrm{i}\Gamma_{K^-}/2$. The imaginary part of the self-energy, $\mathrm{Im}\,\Pi_{K^-}$, was taken from optical model phenomenology, with a strength fitted to K^- atomic data [23] and with energy dependence that follows the reduced phase space for the decaying initial state. We assumed two-body final-state kinematics for the decay products in the absorption channels $\bar{K}N \to \pi Y$ ($Y = \Sigma,\ \Lambda$) (80%) and $\bar{K}NN \to YN$ (20%) with branching ratios indicated in parentheses [17, 18].

The set of coupled equations containing the Dirac equation for nucleons, the KG equations for the meson mean fields and for antikaons was solved fully self-consistently using an iterative procedure. This appeared crucial for the proper evaluation of the dynamical

effects in nuclei with κ ($\kappa = 1, 2, 3, \cdots$) $\bar{K}$ mesons. The $\bar{K}$ separation energy

$$B_{\bar{K}} = B[A, Z, \kappa\bar{K}] - B[A, Z, (\kappa - 1)\bar{K}] \,, \tag{7}$$

where $B(A, Z, \kappa\bar{K})$ is the binding energy of the $\kappa\bar{K}$-nuclear system, contains mean-field contributions due to rearrangement of the nuclear core.

2.2 Choice of parameters

For the nucleonic Lagrangian density $\mathcal{L}_N$ we used the RMF parameter sets NL-SH [24] and NL-TM1(2) [25] which have been successfully used in numerous calculations of various nuclear systems. For the (anti-)kaon coupling constants to the vector-meson fields, we used a purely F-type SU(3) symmetry, $\alpha_{\rm V} \equiv F/(F + D) = 1$:

$$2g_{\omega K} = \sqrt{2}\, g_{\phi K} = 2\, g_{\rho K} = \, g_{\rho\pi} = 6.04 \,, \tag{8}$$

where the value of $g_{\rho\pi}$ is due to the $\rho \to 2\pi$ decay width. As mentioned in Sec. 1, this choice corresponds to the underlying Tomozawa-Weinberg lowest-order term in chiral perturbation theory [19]. The value of $g_{\omega K}^{\rm SU(3)} = 3.02$ adopted here is considerably lower than the quark-model (QM) value applied to NL-SH, $g_{\omega K} = \frac{1}{3} g_{\omega N}^{\rm NL-SH} = 4.32$, which was used in our previous work [16], and we consider it to be the minimal value suggested by theory. The $\bar{K}$ RMF *vector* potential at threshold in nuclear matter is then given, in the static approximation, by using the last two terms on the rhs of Eq. (5):

$$V_{\rm RMF-vector}^{K^-} = -\frac{g_{\omega K}^{\rm SU(3)} g_{\omega N}^{\rm NL-SH} \rho_0}{m_\omega^2} - \frac{1}{2m_K} \left(\frac{g_{\omega K}^{\rm SU(3)} g_{\omega N}^{\rm NL-SH} \rho_0}{m_\omega^2} \right)^2 = -76.7 \text{ MeV} \,, \tag{9}$$

with $m_\omega = 783$ MeV and $\rho_0^{\rm NL-SH} = 0.146$ fm^{-3}. We point out that the value $g_{\omega N}^{\rm NL-SH} = 12.95$ is not far away from the value $g_{\omega N}^{\rm ESC04} = 11.06$ from the latest NN-potential fit by the Nijmegen group [26]. This latter value was obtained in that NN analysis after allowing for part of the isoscalar vector-meson field strength to result from a combined ρ-π exchange. We also studied the role of isovector $\bar{K}$ nucleus interactions by comparing the results of using the present SU(3) choice $g_{\rho K}^{\rm SU(3)} = 3.02$ with results applying a QM *universal* isospin coupling to NL-SH: $g_{\rho K} = g_{\rho N}^{\rm NL-SH} = 4.38$. This value is substantially higher than the Nijmegen potential fit value $g_{\rho N}^{\rm ESC04} = 2.77$, apparently to compensate for disregarding the almost four times higher value of the tensor coupling constant $f_{\rho N}^{\rm ESC04}$.

SU(3) symmetry is not much of help in fixing the (anti-)kaon coupling to the scalar-meson field σ, simply because the microscopic origin of the σ field and its various couplings are not unambiguous. It has been shown recently that interpreting the σ field in terms of a $(J^\pi, I) = (0^+, 0)$ resonance in the $\pi\pi$-$K\bar{K}$ coupled-channel system leads to a vanishing $\bar{K}N$ forward-scattering amplitude at threshold, thus suggesting a vanishing contribution to the corresponding $\bar{K}$-nucleus optical potential [27]. However, even for the empirically large value of $g_{\sigma N}$ obtained in the NN case ($g_{\sigma N}^{\rm ESC04} = 10.17$) and also within the RMF description of nuclei, there is no consensus on its microscopic origin, except that QCD sum-rules do produce strong scalar condensates. Modern NN potentials using chiral perturbation theory guidelines obtain a rather strong isoscalar-scalar two-pion exchange contribution involving excitation of $\Delta(1232)$ in intermediate states [28]. A similar two-pion exchange contribution for $\bar{K}N$, involving the excitation of $K^*(892)$, cannot be excluded at present. In the absence of QCD sum-rule determinations of $g_{\sigma K}$, one relies for an order of magnitude estimate on simplified models such as the QM, giving rise to $g_{\sigma K}^{\rm QM} = \frac{1}{3}\, g_{\sigma N}$, which for the NL-SH model gives $g_{\sigma K}^{\rm QM} = 3.48$. The associated RMF K^- nuclear *scalar* potential, in the static approximation, is given by:

$$V_{\rm RMF-scalar}^{K^-} = -\frac{g_{\sigma K}^{\rm QM}\, g_{\sigma N}^{\rm NL-SH}\, \rho_0^s}{2\, m_\sigma^2} = -66.3 \text{ MeV}\,, \tag{10}$$

using the values $m_\sigma = 526.1$ MeV from NL-SH and $\rho_0^s \approx 0.9\rho_0$, where ρ_0^s is the scalar density. Our choice of $g_{\sigma K}$ is conceptually different, fitting $g_{\sigma K}$ to several selected values of $\bar{K}$ separation energy $B_{\bar{K}}$ in nuclear systems with a single $\bar{K}$ meson. These fitted values, all of which were considerably lower than the QM value, are specified in the next section. Thus, our scalar potentials are viewed as a supplement to the minimal vector potentials discussed above to scan over $\bar{K}$ nuclear binding energies in a given energy range, without imparting any microscopic meaning to these scalar potentials. We also tested the effect of adding another scalar-meson field that couples exclusively to strangeness, "hidden strangeness" σ^* meson with mass $m_{\sigma^*} = 980$ MeV, and coupling constant $g_{\sigma^* K} = 2.65$ determined from $f_0(980) \to K^+K^-$ decay [12].

3 Results and discussion

3.1 Saturation of $\bar{K}$ binding energies and hadronic densities

Following the observation made in Ref. [16] that $\bar{K}$ binding energies, as well as nuclear and $\bar{K}$ densities, saturate on increasing the number κ of $\bar{K}$ mesons, we have explored how robust this saturation is. In particular we studied, for several selected nuclei across the periodic table, the role of various components of the $\bar{K}$-nucleus interaction in establishing saturation and the sensitivity to the choice of the RMF model. Representative examples are shown in Figs. 1 and 2.

Figure 1 presents the $1s$ K^- separation energy B_{K^-} in multi-K^- nuclei $^{16}\mathrm{O} + \kappa K^-$ as a function of the number κ of K^- mesons, using the NL-SH RMF parametrization, for several mean-field compositions of the K^- self-energy Eq. (5) with K^- vector-meson couplings given by Eq. (8). The upper group of curves is based on a value of $g_{\sigma K} = 2.433$ ensuring $B_{K^-} = 100$ MeV for $\kappa = 1$. The ϕ, ρ, σ^* meson fields do not practically contribute in this case, whereas the Coulomb field adds a few MeV attraction and $\mathrm{Im}V_{\mathrm{opt}}$ adds a few MeV repulsion. For $\kappa > 1$, the various curves of the upper group diverge from each other: with respect to a "minimal" σ+ω model (open circles), the main contributors are the repulsive ϕ and ρ *vector* mesons, as judged by the curves marked by solid circles and open squares, respectively. Given their contributions, which get larger with κ, the inclusion of the Coulomb field, the σ^* meson field and $\mathrm{Im}V_{\mathrm{opt}}$ makes a small difference. However, the K^- absorptivity $\mathrm{Im}V_{\mathrm{opt}}$ makes a big difference for the lower group of curves consisting of only two choices, both with $g_{\sigma K} = 1.703$ fitted to $B_{K^-} \approx 40 - 50$ MeV for $\kappa = 1$. The energy dependence of $\mathrm{Im}V_{\mathrm{opt}}$ magnifies its effect for relatively low values of B_{K^-} in the region $B_{\bar{K}} \leq 100$ MeV, adding significant repulsion the lesser the value of B_{K^-} is. This added repulsion (lowest curve in Fig. 1) leads to a rapid fall-off of B_{K^-}, terminating the binding at $\kappa = 3$, because the system ^{16}O+$4K^-$ is found to be unbound for this particular choice of $\kappa = 1$ parameters. The lesson from Fig. 1 is that saturation of the K^- binding energy in nuclear systems with κ K^-mesons is a robust phenomenon, which remains valid regardless of the type of meson fields mediating the strong interaction among antikaons and nucleons, provided a *minimal* isoscalar vector-meson field (ω) is included. For a sufficiently large number κ of K^- mesons, the combined repulsive K^-K^- interaction generated by the vector meson fields ω, ϕ, ρ wins over the attractive interaction generated by the isoscalar scalar-meson fields (dominated by σ). The effect of adding the σ^* scalar field is found to be insignificant. These conclusions hold also for a Lagrangian in which scalar fields are

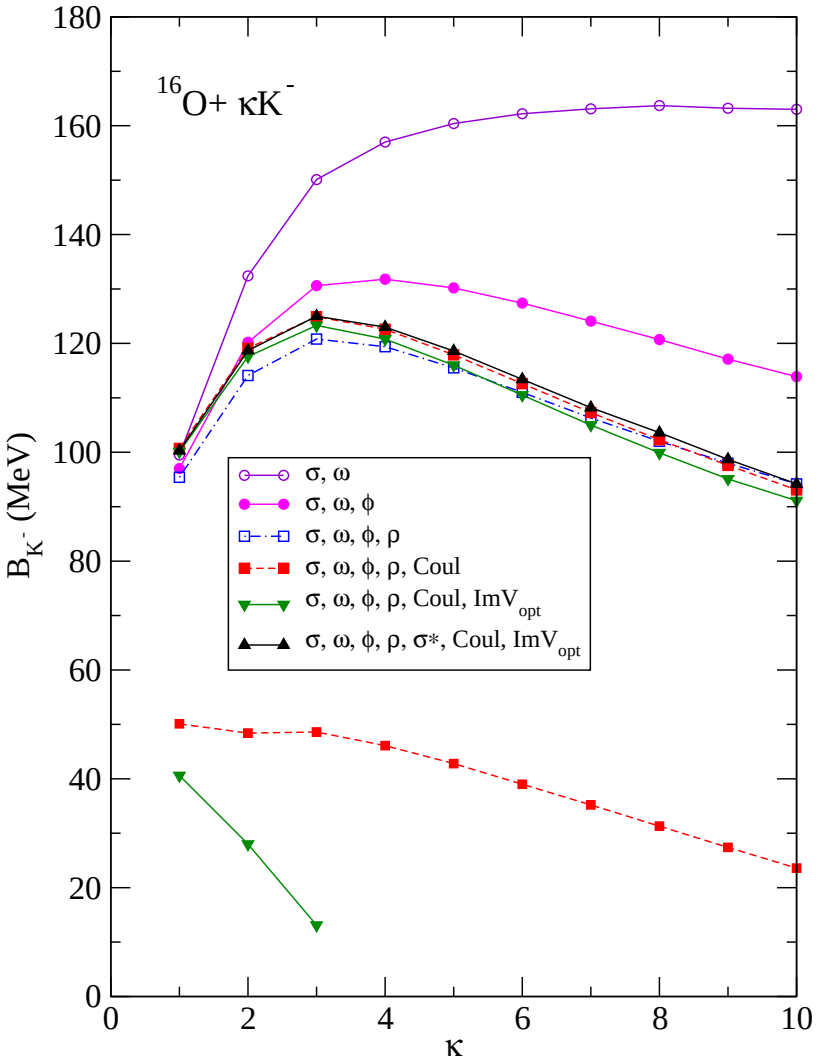

Figure 1: $1s$ K^- separation energy B_{K^-} in ^{16}O+κK^- as a function of the number κ of antikaons in several calculations detailed in the text, as listed in the inset, using the NL-SH RMF nuclear model with $g_{\sigma K} = 2.433$ for the upper group of curves and $g_{\sigma K} = 1.703$ for the lower group.

introduced differently than in Eq. (1), resulting in a correspondingly different definition of effective masses, $m^*_K = m_K - g_{\sigma K}\sigma_0 - g_{\sigma^* K}\sigma^*_0$ [29], than in Eq. (6).

Figure 2 shows the $1s$ K^- separation energy B_{K^-} in multi-K^- nuclei ^{40}Ca + κK^- as a function of the number κ of K^- mesons, calculated in the NL-SH, NL-TM1, and NL-TM2 RMF models for two choices of $g_{\sigma K}$ designed, within each model, to produce $B_{K^-} = 100$ and 130 MeV for $\kappa = 1$. The values of $g_{\sigma K}$ for NL-SH were 1.703 and 2.993, respectively. The difference between the various curves, for a given starting value of B_{K^-}, originates from the

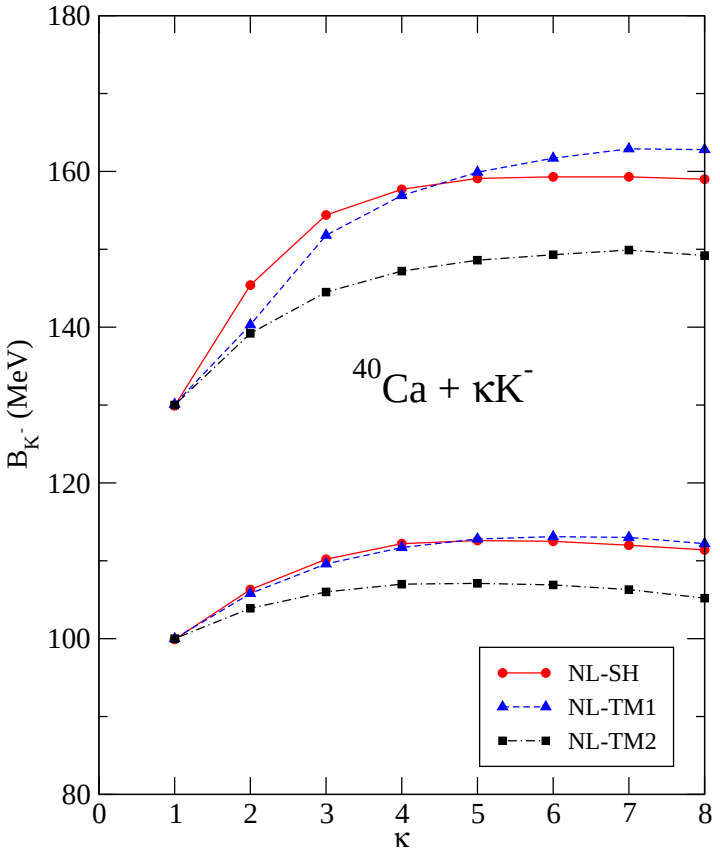

Figure 2: $1s$ K^- separation energy B_{K^-} in ^{40}Ca+κK^-, as a function of the number κ of K^- mesons, calculated in the NL-SH (circles, solid lines), NL-TM1 (triangles, dashed lines), and NL-TM2 (squares, dot-dashed lines) RMF models. The lower (upper) group of curves was constrained to produce $B_{K^-} = 100$ (130) MeV for $\kappa = 1$.

specific balance in each one of these RMF models between the vector fields and the scalar field. The figure illustrates that the saturation of the $\bar{K}$ binding energy in nuclear systems with several antikaons is not limited to a particular choice of RMF parametrization but is a general feature independent of the applied RMF model. Without loss of generality, we therefore specialize in the subsequent discussion to a specific RMF model, namely NL-SH.

The dependence of the nuclear density $\rho_N(r)$ and the K^- density $\rho_{K^-}(r)$ on the number κ of K^- mesons in multi-K^- nuclei $^{40}\mathrm{Ca} + \kappa K^-$ is shown in Fig. 3. The coupling constant $g_{\sigma K} = 1.703$ was chosen such that the single-K^- configuration was bound by 100 MeV, the same as for the NL-SH lower curve in Fig. 2. The density distribution ρ_N for ^{40}Ca is also shown, for comparison, by the dotted curve in the upper panel. It is clear from this figure that the central nuclear density ρ_N saturates for $\kappa = 8$ at a value about twice larger than that for ρ_N in ^{40}Ca. In the lower panel, it is seen that the gradual increase of ρ_{K^-}

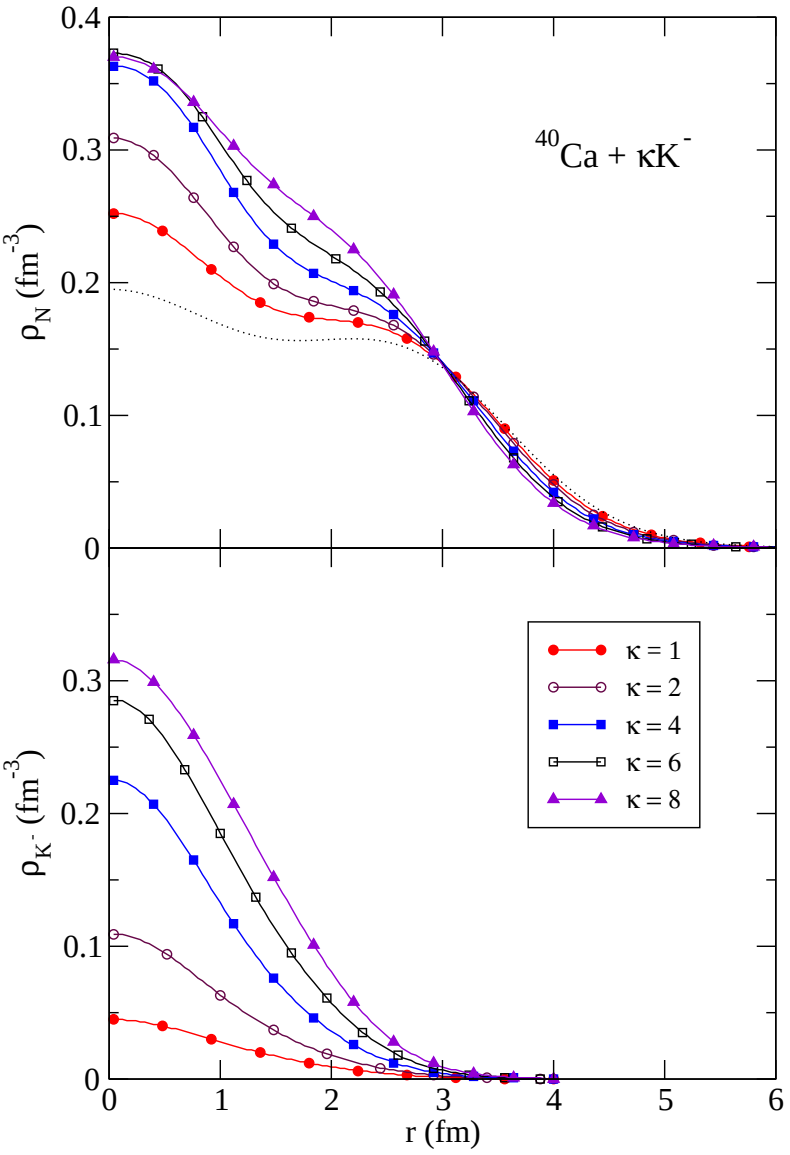

Figure 3: Nuclear density ρ_N (top panel) and $1s$ K^- density ρ_{K^-} (bottom panel) in ^{40}Ca+κK^-, calculated in the NL-SH RMF model, with $g_{\sigma K} = 1.703$ chosen to yield $B_{K^-} =$ 100 MeV in ^{40}Ca+$1K^-$. The dotted curve stands for the ^{40}Ca density in the absence of K^- mesons.

with κ slows down with increasing κ.

The saturation of the nuclear density in multi-$\bar{K}$ nuclei manifests itself also in the behavior of the $\bar{K}$ effective mass in the nuclear medium, Eq. (6), as a function of the number κ of antikaons. This is illustrated for ^{208}Pb + κK^- in Fig. 4. Note that the calculated effective mass distribution $m^*_{K^-}(r)$ remains almost independent of the number

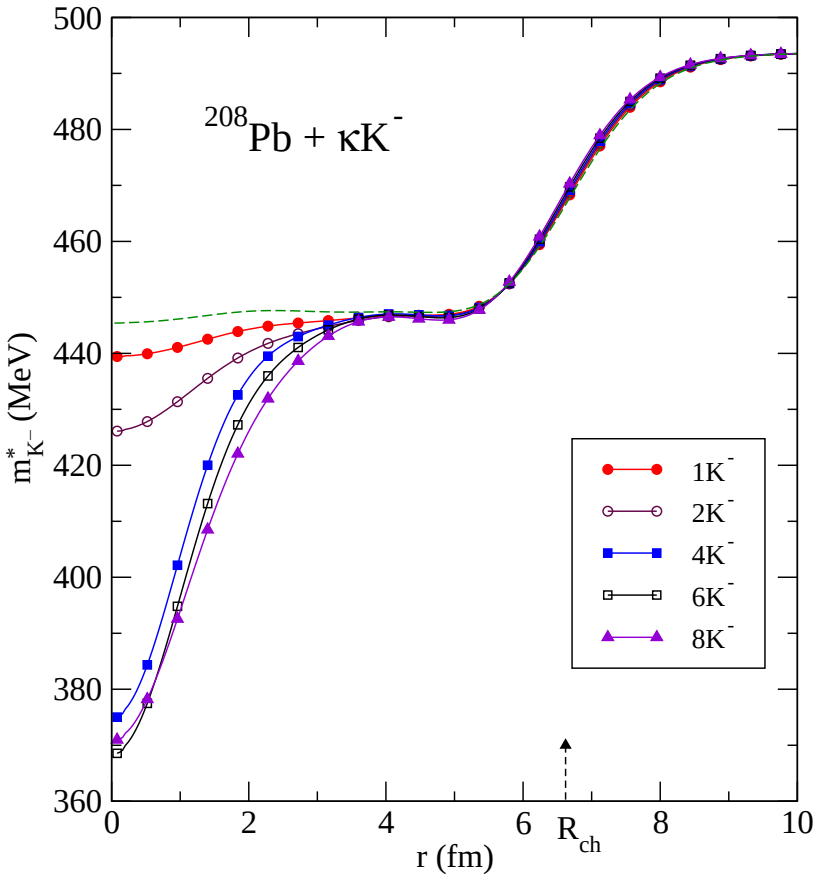

Figure 4: $1s$ K^- effective mass $m^*_{K^-}$ in multi-K^- nuclei ^{208}Pb+κK^-, calculated in the NL-SH model with $g_{\sigma K} = 2.433$ chosen to yield $B_{K^-} = 100$ MeV in ^{208}Pb+$1K^-$. The dashed curve stands for the "static" case where the ^{208}Pb σ field in a purely nuclear RMF calculation was used in Eq. (6) for $m^*_{K^-}$. The dashed arrow indicates the charge half-density radius $R_{\rm ch}$ in ^{208}Pb.

of K^- mesons over a large volume of the nucleus, for $r \geq 3$–4 fm, reflecting a similar κ independence of the scalar σ field through the underlying nuclear density. In fact, the σ field in this region is almost unaffected by the presence of K^- mesons, as demonstrated by the dashed curve which uses the "static" ^{208}Pb σ field from a purely nuclear RMF calculation. It is only within a relatively small region near the nuclear center, typically $r \leq 2$–3 fm, that the variation of $m^*_{K^-}(r)$ with κ gets to be more pronounced. However, $m^*_{K^-}(r = 0)$ quickly saturates, already for $\kappa \approx 8$. The figure demonstrates clearly that the concept of "nuclear matter" is far from being realized, even for a nucleus as large as ^{208}Pb and that conclusions made on $\bar{K}$ binding and kaon condensation in finite nuclei, using nuclear-matter arguments, should be taken with a grain of salt.

3.2 Exotic $\bar{K}$ nuclear configurations

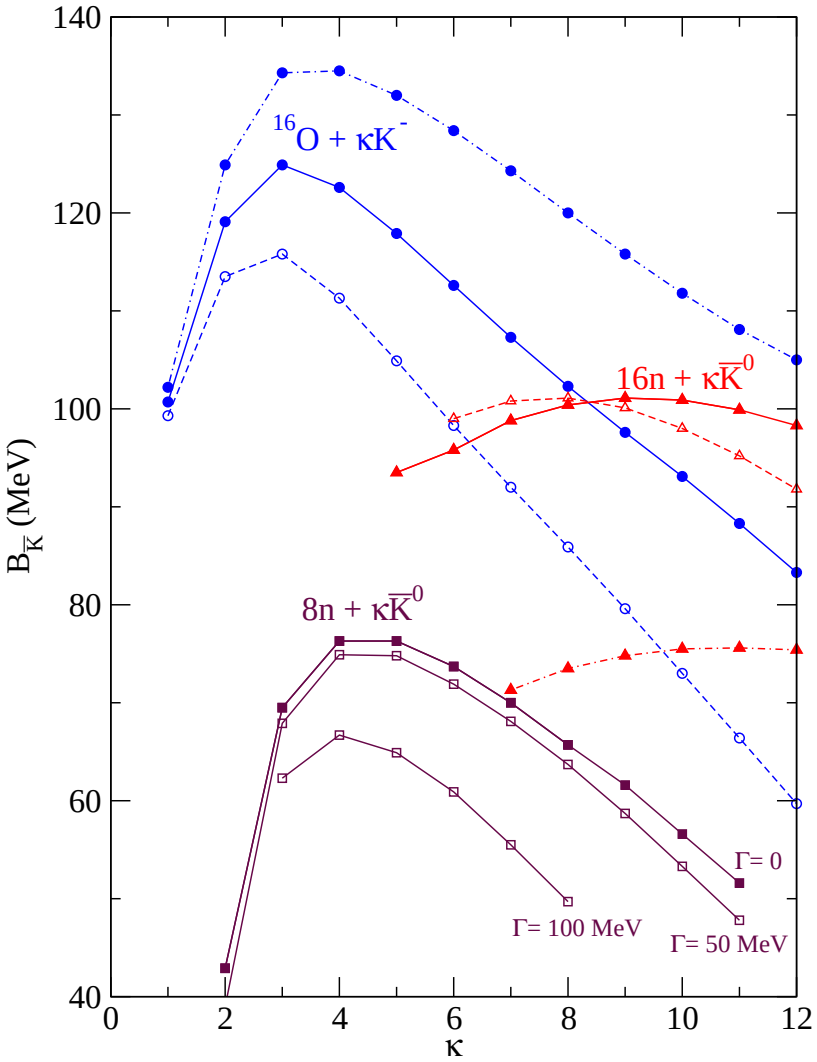

Figure 5: $1s$ $\bar{K}$ separation energy $B_{\bar{K}}$ in ^{16}O+κK^-, $16n$+$\kappa\bar{K}^0$, and $8n$+$\kappa\bar{K}^0$, as a function of κ, calculated in the NL-SH RMF model, with $g_{\rho K} = 0$ (dot-dashed curves), $g_{\rho K}^{\rm SU(3)} = 3.02$ (solid curves) and $g_{\rho K} = g_{\rho N} = 4.38$ (dashed curves). Im$V_{\rm opt} = 0$ is assumed everywhere except for the two lowest solid curves (open squares) in $8n$+$\kappa\bar{K}^0$ where Im$V_{\rm opt} \neq 0$, such that the value of width $\Gamma_{\bar{K}^0}$ is held fixed at 50 and 100 MeV, respectively, see text.

Because in the underlying $\bar{K}N$ dynamics the $I = 0$ interaction is considerably more attractive than the $I = 1$ interaction, we have looked for ways to maximize the role of the $\bar{K}N$ $I = 0$ channel in multi-$\bar{K}$ nuclei. For a nuclear core with $N = Z$, no matter which charge states are assigned to the $\bar{K}$ mesons, the average $\bar{K}N$ interaction is given by a $(2I + 1)$-average which disfavors the $I = 0$ channel. This disadvantage is partly removed

by considering $n\bar{K}^0$ (or pK^-) multi-$\bar{K}$ nuclei, where both isospin channels assume equal weight, so that the stronger $I = 0$ component may provide sufficient attraction to overcome the insufficient attraction in purely neutron matter. We therefore studied exotic configurations consisting solely of $\bar{K}^0$ mesons bound to neutrons. Our calculations confirmed that $\bar{K}$ mesons can bind together systems of nucleons that otherwise are unbound.

In Fig. 5, we compare the separation energies $B_{\bar{K}}$ in $16n{+}\kappa\bar{K}^0$ and in $8n{+}\kappa\bar{K}^0$ exotic multi-$\bar{K}$ configurations with $B_{\bar{K}}$ in ^{16}O$+\kappa K^-$ multi-$\bar{K}$ nuclei, most of which were calculated in the NL-SH RMF model with the "canonical" g_{vK} coupling constants of Eq. (8) and $g_{\sigma K} = 2.433$ chosen to yield $B_{K^-} = 100$ MeV in ^{16}O$+1K^-$ as in Fig. 1, and for $\mathrm{ImV_{opt}} = 0$. For each sequence of multi-$\bar{K}$ nuclei, $B_{\bar{K}}$ increases as a function of κ to a maximum value and then starts to decrease. Whereas the sequence consisting of 8 neutrons plus $\bar{K}^0$ mesons starts with $\kappa = 1$ (not shown in the figure), a larger number of neutrons generally requires a threshold value for κ as shown for the sequences consisting of 16 neutrons plus $\bar{K}^0$ mesons. Exceptions to the use of the canonical g_{vK} set of Eq. (8), or to $\mathrm{ImV_{opt}} = 0$, are as follows:

- $g_{\rho K}^{\mathrm{SU(3)}} = 3.02$ was used everywhere except for $g_{\rho K} = 0$ in the dot-dashed curves and except for $g_{\rho K} = g_{\rho N} = 4.38$ (universal isospin coupling) in the dashed curves to study the role of the ρ meson in "nonexotic" multi-$\bar{K}$ nuclei ($^{16}\mathrm{O} + \kappa K^-$) and in "exotic" ones ($16n{+}\kappa\bar{K}^0$). In ^{16}O$+\kappa K^-$, the values of B_{K^-} for a given value of $\kappa > 1$ decrease as $g_{\rho K}$ is increased, as expected from the *repulsive* K^-K^- isovector interaction. In contrast, the larger the value of $g_{\rho K}$ is, the larger is the value of $B_{\bar{K}^0}$ expected in $16n{+}\kappa\bar{K}^0$, because it is the ρ isovector interaction that distinguishes the more attractive $I = 0$ component of the $\bar{K}^0 n$ interaction from the less attractive $I = 1$ component. Indeed, this holds for $\kappa \leq 8$ in the figure. However, for $\kappa > 8$, the contribution of the repulsive $\bar{K}^0\bar{K}^0$ isovector interaction becomes substantial for the values of $g_{\rho K} \neq 0$ used here; the $B_{\bar{K}^0}$ dashed curve for the universal ρ coupling heads down, crossing the $B_{\bar{K}^0}$ solid curve corresponding to SU(3) ρ coupling. All in all, substantial binding in $16n{+}\kappa\bar{K}^0$ multi-$\bar{K}$ nuclei is reached for these values of $g_{\rho K} \neq 0$.

- The effect of $\mathrm{ImV_{opt}}$ on $B_{\bar{K}}$ is relatively unimportant for $B_{\bar{K}} \geq 100$ MeV, where the dominant $\bar{K}N \to \pi\Sigma$ decay channel is closed. The inclusion of $\mathrm{ImV_{opt}}$ is found then to induce repulsion of less than 5 MeV. However, in $8n{+}\kappa\bar{K}^0$ multi-$\bar{K}$ nuclei, where $B_{\bar{K}^0} \leq 80$ MeV, the effect of $\mathrm{ImV_{opt}}$ becomes significant. An estimate of this effect is given by comparing the $B_{\bar{K}^0}$ curve for $\Gamma = 0$ (solid squares) with the $B_{\bar{K}^0}$ curves using $\mathrm{ImV_{opt}} \neq 0$ (open squares) such that the value of $\Gamma_{\bar{K}^0}$ is *held fixed* at 50 and 100

MeV. As expected, the larger input widths induce a stronger repulsion that lowers the calculated $B_{\bar{K}^0}$ values. Yet considerably lower values of $B_{\bar{K}^0}$ are obtained once the $\bar{K}^0$ widths are included self-consistently in these dynamical calculations.

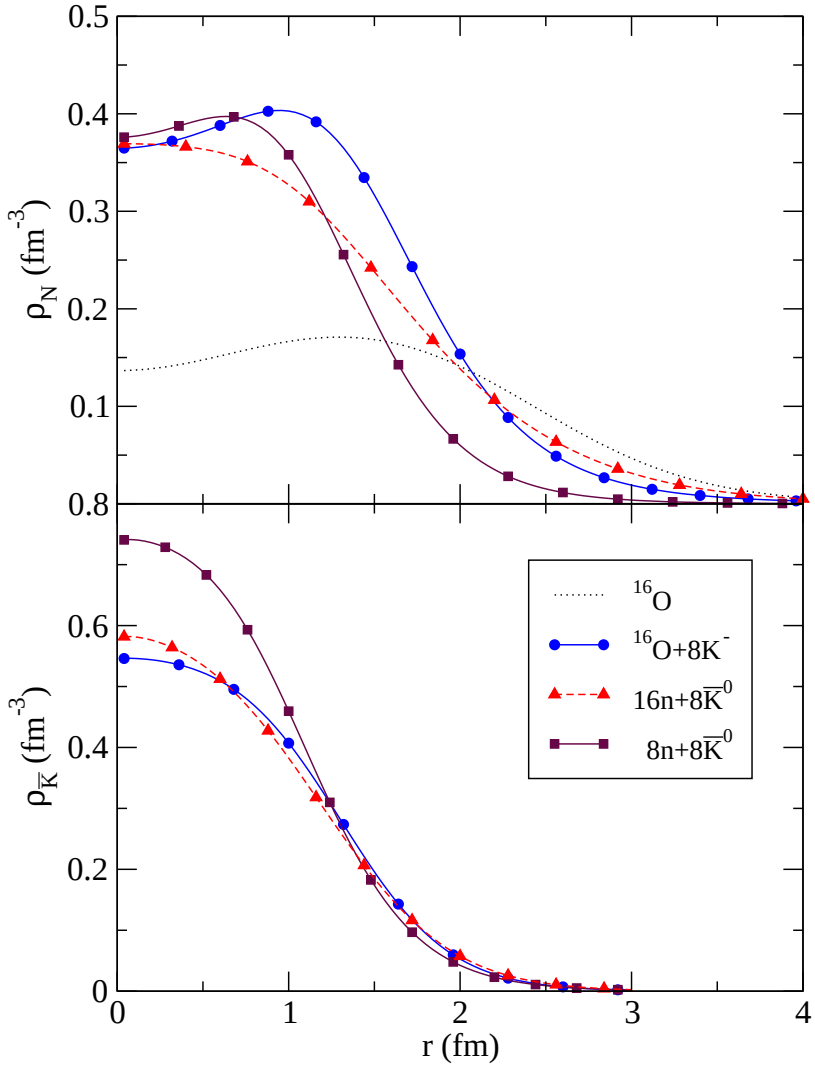

Figure 6: Nuclear density ρ_N (top panel) and $1s$ $\bar{K}$ density $\rho_{\bar{K}}$ (bottom panel) in ^{16}O+$8K^-$, $16n$+$8\bar{K}^0$ and $8n$+$8\bar{K}^0$, calculated in the NL-SH RMF model, with the "canonical" g_{vK} coupling constants of Eq. (8) and with $g_{\sigma K} = 2.433$ to yield $B_{K^-} = 100$ MeV in ^{16}O+$1K^-$ as in Fig. 5. The dotted curve stands for the ^{16}O density in the absence of $\bar{K}$ mesons.

The nucleon-density distribution $\rho_N(r)$ and the $\bar{K}$-density distribution $\rho_{\bar{K}}(r)$ are shown in Fig. 6 for ^{16}O+$8K^-$, $16n$+$8\bar{K}^0$, and $8n$+$8\bar{K}^0$. We note that ρ_N and $\rho_{\bar{K}}$ are normalized to the number of nucleons and number of antikaons, respectively. The $\bar{K}$ couplings were chosen such that the $1K^-$ configuration in ^{16}O is bound by 100 MeV, as in Fig. 5. For

comparison, we also present the density distribution ρ_N for ^{16}O without $\bar{K}$ mesons. Owing to the substantial $\bar{K}$ density $\rho_{\bar{K}}$ in the nuclear center, the central nuclear density $\rho_N(0)$ in all three systems with 8 $\bar{K}$ mesons is about 2-3 times larger than the central nuclear density ρ_0 in ^{16}O for $\kappa = 0$. The situation is particularly pronounced in $8n{+}8\bar{K}^0$, with the same central density $\rho_N(0)$ as in the systems with 16 nucleons + $8\bar{K}$. Furthermore, the $8n{+}8\bar{K}^0$ system is compressed substantially in comparison with the other multi-$\bar{K}$ systems, judging by the radial extension of ρ_N and $\rho_{\bar{K}}$ in both panels of Fig. 6. The relatively high value $\rho_{\bar{K}}(0) \sim 5\rho_0$ for this system does not introduce complications due to possible overlap between antikaons, because the mean-square radius of K^- is less than half of the corresponding quantity for the proton [30, 31].

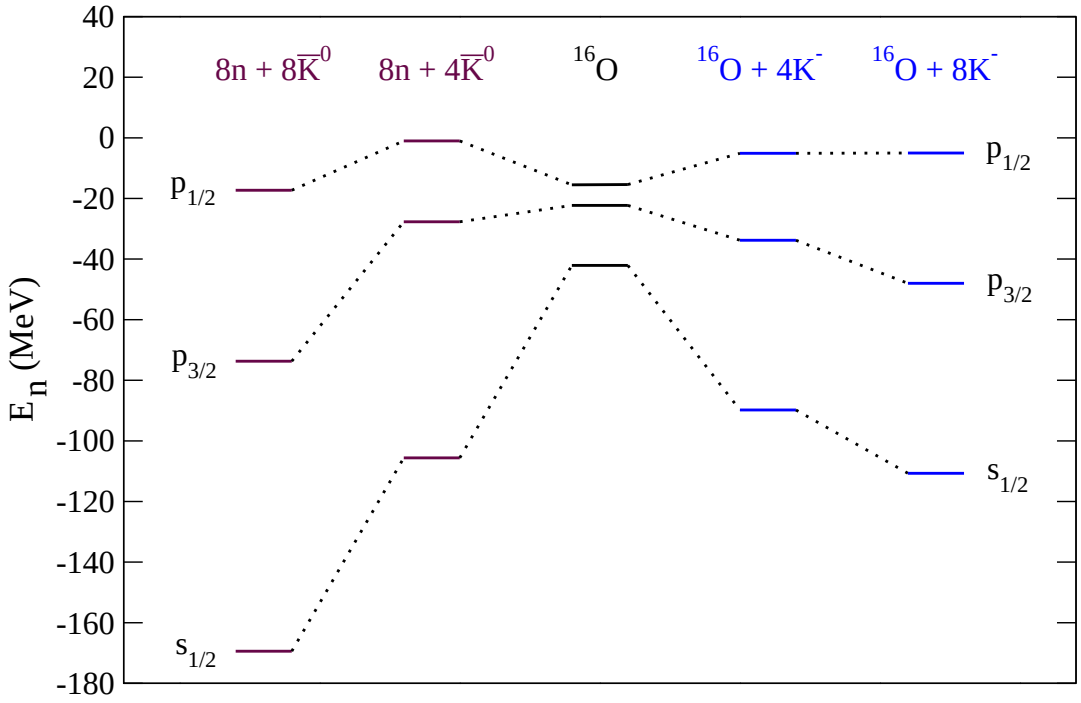

Figure 7: Neutron single-particle spectra in ^{16}O (center) ^{16}O+4(8)K^- (right) and $8n{+}4(8)\bar{K}^0$ (left), calculated in the NL-SH RMF model with $g_{\sigma K} = 2.433$ chosen to yield $B_{K^-} = 100$ MeV in ^{16}O+1K^-.

Given the compressed nuclear densities plotted in Fig. 6, we show in Fig. 7 the calculated neutron single-particle energy levels in ^{16}O, in ^{16}O+κK^- and in $8n{+}\kappa\bar{K}^0$ multi-$\bar{K}$ nuclei for $\kappa = 4,\ 8$. The $\bar{K}$ couplings are the same as in Figs. 5 and 6, again chosen to ensure $B_{K^-} = 100$ MeV in ^{16}O+1K^-. The $1s_{1/2}$ and $1p_{3/2}$ levels undergo increasingly attractive shifts on varying κ in these multi-$\bar{K}$ systems. Particularly strong is the downward shift of the $1s_{1/2}$ level, by about 70 MeV in ^{16}O+8K^- and by about 130 MeV in $8n{+}8\bar{K}^0$. In

contrast, the $1p_{1/2}$ neutron level is pushed up by about 10 MeV in the ^{16}O+κK^- systems as a result of a gradually increasing spin-orbit splitting which reaches 43 MeV for $\kappa = 8$ (recall that it is 7 MeV for $\kappa = 0$ using NL-SH). The $1p_{1/2}$ neutron level is weakly bound in the exotic $8n$+$\kappa\bar{K}^0$ systems for $1 < \kappa < 6$, getting more bound with κ as shown in the figure for these systems. The $1p$ spin-orbit splitting becomes as large as 56 MeV in the exotic $8n + 8\bar{K}^0$ system which exhibits the largest single-particle level splittings in this figure. Here the $1p_{1/2}$ neutron level, too, undergoes attraction.

It is worth mentioning that exotic multi-$\bar{K}^0$ configurations that contain no protons lie high in the continuum of "nonexotic" multi-$\bar{K}$ nuclei that are based on nuclear cores with protons and neutrons. Figure 8 shows the calculated *total* binding energy $B[A, Z, \kappa\bar{K}]$, Eq. (7), assuming for simplicity $g_{\rho K} = 0$, for three sequences of multi-$\bar{K}$ nuclei. To illustrate the relationship between "exotic" and "nonexotic" configurations, we take the $16n$+$8\bar{K}^0$ configuration, specifically in its lowest isospin $I = 4$ state, and replace successively $\bar{K}^0$+n pairs by K^-+p pairs until ^{16}O+$8K^-$ is reached. This is demonstrated by the empty triangles along the vertical dotted line that connects the initial and final configurations. Both initial and final configurations have identical quantum numbers $B = 8$, $Q = 0$, $I = 4$, so they are commensurate. Therefore, although $\bar{K}$ mesons are capable of stabilizing purely neutron configurations, these exotic configurations do not compete energetically with multi-$\bar{K}$ nuclei based on nuclear cores along the nuclear valley of stability.

4 Summary

In the main part of this work, we studied several dynamical aspects of multi-$\bar{K}$ nuclear states within RMF methodology. In particular, we discussed in detail the saturation pattern of $\bar{K}$ separation energies and nuclear densities on increasing the number of antikaons embedded in the nuclear medium. Saturation was demonstrated to be a robust feature of multi-$\bar{K}$ nuclei. The saturated values of $B_{\bar{K}}$, for "natural" values of meson-field coupling constants were found generally to be below 200 MeV, considerably short of the threshold value ≈320 MeV needed for the onset of kaon condensation under laboratory conditions. We conclude, consistently with our earlier conjecture [16], that $\bar{K}$ mesons do not provide the physical "strangeness" degrees of freedom for self-bound strange dense matter.

We first explored contributions of specific meson mean fields to the $\bar{K}$ separation energy $B_{\bar{K}}$. Saturation of $B_{\bar{K}}$ emerged for any boson-field composition that includes the dominant vector ω-meson field, using the "minimal" SU(3) value suggested by the leading-order

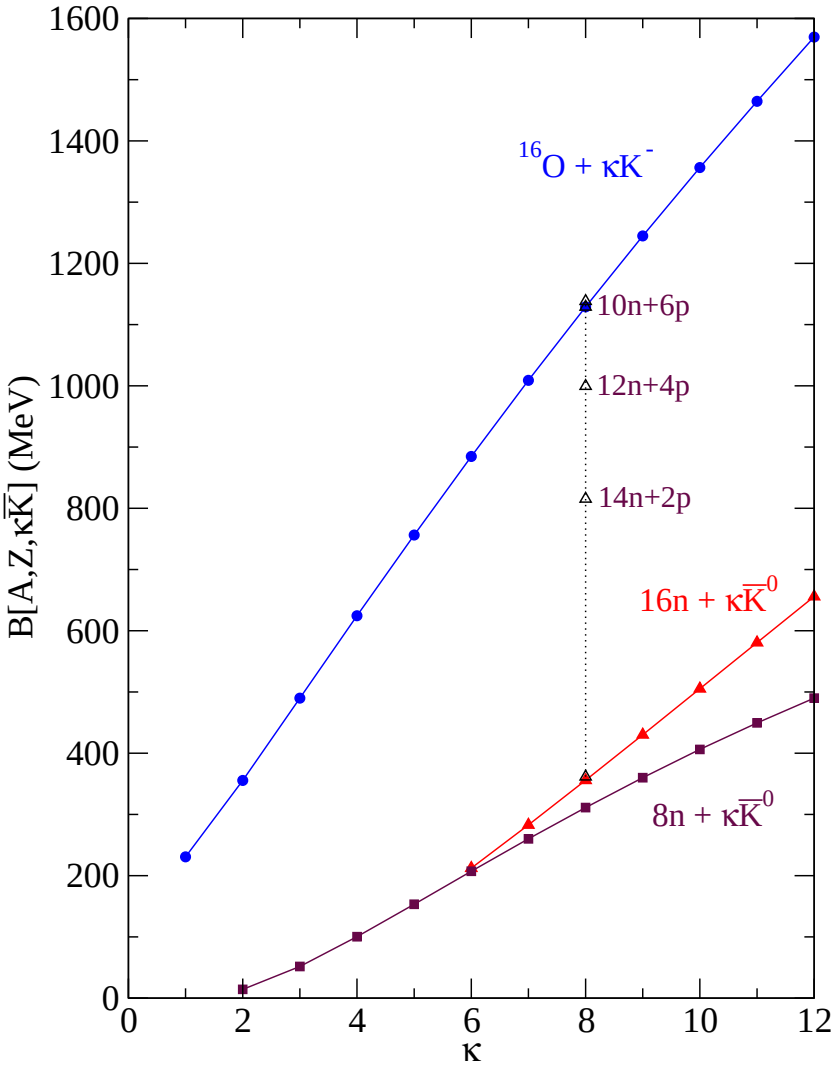

Figure 8: Total binding energy $B[A, Z, \kappa\bar{K}]$ of ^{16}O+κK^- (circles), $16n$+$\kappa\bar{K}^0$ (solid triangles) and $8n+\kappa\bar{K}^0$ (squares) multi-$\bar{K}$ systems, as a function of κ, calculated in the NL-SH RMF model with $g_{\sigma K} = 2.433$ chosen to yield $B_{K^-} = 100$ MeV in ^{16}O+$1K^-$, and with $g_{\rho K} = 0$. For $\kappa = 8$, total binding energy values for configurations that are intermediate between ^{16}O+$8K^-$ and $16n$+$8\bar{K}^0$ are shown in open triangles along the dashed line.

Tomozawa-Weinberg term of the meson-baryon effective Lagrangian. Moreover, the contribution of each one of the vector ϕ-meson and ρ-meson fields was found to be substantially repulsive for systems with a large number of antikaons, reducing the $\bar{K}$ separation energy as well as lowering the threshold value of number of antikaons required for saturation to occur. In contrast, the Coulomb interaction and the addition of a hidden-strangeness scalar σ^*-meson field have little effect on the binding energy balance and on the pattern of

saturation.

We also verified that the saturation behavior of $B_{\bar{K}}$ is qualitatively independent of the RMF model applied to the nucleonic sector. The onset of saturation was found to depend on the atomic number. Generally, the heavier the nucleus is, the more antikaons it takes to saturate their separation energies.

The saturation phenomenon found for the $\bar{K}$ separation energy is also reflected in the nucleon and antikaon density distributions, with the assertions made above remaining valid. The saturation of the nuclear density in multi-$\bar{K}$ nuclei manifests itself in the behavior of the $\bar{K}$ effective mass distribution in the nuclear medium. We stress that in the case of antikaons the concept of nuclear matter is far from being realized even in such a heavy nucleus as ^{208}Pb. Specifically, the reduction of $m^*_{\bar{K}}(r)$ on adding $\bar{K}$ mesons is pronounced only within a small region around the nuclear center.

In the second part of this work, we studied exotic configurations consisting exclusively of neutrons and $\bar{K}^0$ mesons. We demonstrated that a finite number of neutrons can be made self-bound by adding few $\bar{K}^0$ mesons, with the resulting nuclear configurations more tightly bound than ordinary nuclei. Saturation of $B_{\bar{K}^0}$ was found for these exotic configurations too. Yet, these exotic configurations consisting exclusively of neutrons and $\bar{K}^0$ mesons lie high in the continuum of the less exotic multi-$\bar{K}$ configurations based on nuclear cores along the nuclear valley of stability.

In conclusion, over a wide range of variations our calculations do not indicate any precursor phenomena to kaon condensation in self-bound strange nuclear systems.

Acknowledgments

This work was supported in part by the GA AVCR grant IAA100480617 and by the Israel Science Foundation grant 757/05.

References

[1] D.B. Kaplan, A.E. Nelson, Phys. Lett. B **175**, 57 (1986); *ibid* **B179**, 409 (1986).

[2] A.E. Nelson, D.B. Kaplan, Phys. Lett. B **192**, 193 (1987).

[3] E. Friedman, A. Gal, Phys. Rep. **452**, 89 (2007); and earlier references cited therein.

[4] W. Scheinast *et al.*, Phys. Rev. Lett. **96**, 072301 (2006); and earlier references to nucleus-nucleus experiments cited therein.

[5] C.B. Dover, P.J. Moffa, Phys. Rev. C **16**, 1087 (1977).

[6] C.-H. Lee, Phys. Rep. **275**, 255 (1996).

[7] M. Prakash, I. Bombaci, M. Prakash, P.J. Ellis, J.M. Lattimer, R. Knorren, Phys. Rep. **280**, 1 (1997).

[8] H. Heiselberg, M. Hjorth-Jensen, Phys. Rep. **328**, 237 (2000).

[9] H. Heiselberg, V.R. Pandharipande, Annu. Rev. Nucl. Part. Sci. **50**, 481 (2000).

[10] N.K. Glendenning, Phys. Rep. **342**, 393 (2001).

[11] A. Ramos, J. Schaffner-Bielich, J. Wambach, Lect. Notes Phys. **578**, 175 (2001).

[12] J. Schaffner, I.N. Mishustin, Phys. Rev. C **53**, 1416 (1996).

[13] P.J. Ellis, R. Knorren, M. Prakash, Phys. Lett. B **349**, 11 (1995).

[14] T. Yamazaki, A. Doté, Y. Akaishi, Phys. Lett. B **587**, 167 (2004).

[15] J. Schaffner-Bielich, A. Gal, Phys. Rev. C **62**, 034311 (2000); and references cited therein.

[16] D. Gazda, E. Friedman, A. Gal, J. Mareš, Phys. Rev. C **76**, 055204 (2007).

[17] J. Mareš, E. Friedman, A. Gal, Phys. Lett. B **606**, 295 (2005).

[18] J. Mareš, E. Friedman, A. Gal, Nucl. Phys. A **770**, 84 (2006).

[19] W. Weise, *Proc. IX Int. Conf. Hypernuclear and Strange Particle Physics*, Eds. J. Pochodzalla and Th. Walcher (SIF and Springer-Verlag, Berlin Heidelberg, 2007) p. 243 [arXiv:nucl-th/0701035]; W. Weise, R. Härtle, Nucl. Phys. A **804**, 173 (2008).

[20] N.V. Shevchenko, A. Gal, J. Mareš, Phys. Rev. Lett. **98**, 082301 (2007).

[21] N.V. Shevchenko, A. Gal, J. Mareš, J. Révai, Phys. Rev. C **76**, 044004 (2007).

[22] Y. Ikeda, T. Sato, Phys. Rev. C **76**, 035203 (2007).

[23] E. Friedman, A. Gal, J. Mareš, A. Cieplý, Phys. Rev. C **60**, 024314 (1999).

[24] M.M. Sharma, M.A. Nagarajan, P. Ring, Phys. Lett. B **312**, 377 (1993).

[25] Y. Sugahara, H. Toki, Nucl. Phys. A **579**, 557 (1994).

[26] Th.A. Rijken, Phys. Rev. C **73**, 044007 (2006).

[27] A. Martinez Torres, K.P. Khemchandani, E. Oset, submitted to Eur. Phys. J. A, arXiv:0712.1938 [nucl-th].

[28] P. Finelli, N. Kaiser, D. Vretenar, W. Weise, Nucl. Phys. A **770**, 1 (2006).

[29] N.K. Glendenning, J. Schaffner-Bielich, Phys. Rev. Lett. **81**, 4564 (1998).

[30] S.R. Amendolia *et al.*, Phys. Lett. B **178**, 435 (1986).

[31] G. Simon, C. Schmitt, F. Borkowski, V. Walther, Nucl. Phys. A **333**, 381 (1980).

Published in Physical Review C 80 (2009) 035205

Multi-$\bar{K}$ hypernuclei

D. Gazda[1], E. Friedman[2], A. Gal[2], J. Mareš[1]

[1]*Nuclear Physics Institute, 25068 Řež, Czech Republic*
[2]*Racah Institute of Physics, The Hebrew University, Jerusalem 91904, Israel*

Abstract

Relativistic mean-field calculations of multi-$\bar{K}$ *hypernuclei* are performed by adding K^- mesons to particle-stable configurations of nucleons, Λ and Ξ hyperons. For a given hypernuclear core, the calculated $\bar{K}$ separation energy $B_{\bar{K}}$ saturates with the number of $\bar{K}$ mesons for more than roughly 10 mesons, with $B_{\bar{K}}$ bounded from above by 200 MeV. The associated baryonic densities saturate at values $2-3$ times nuclear-matter density within a small region where the $\bar{K}$-meson densities peak, similarly to what was found for multi-$\bar{K}$ nuclei. The calculations demonstrate that particle-stable multistrange $\{N, \Lambda, \Xi\}$ configurations are stable against strong-interaction conversions $\Lambda \to N\bar{K}$ and $\Xi \to N\bar{K}\bar{K}$, confirming and strengthening the conclusion that kaon condensation is unlikely to occur in strong-interaction self-bound strange hadronic matter.

1 Introduction

Quasibound nuclear states of $\bar{K}$ mesons have been studied by us recently in a series of articles [1, 2, 3, 4], using a self-consistent extension of nuclear relativistic mean-field (RMF) models. References [1, 2, 3] focused on the widths expected for $\bar{K}$ quasibound states, particularly in the range of $\bar{K}$ separation energy $B_{\bar{K}} \sim 100-150$ MeV deemed relevant from K^--atom phenomenology [2, 5] and from the KEK-PS E548 ^{12}C(K^-, N) missing-mass spectra [6] that suggest values of Re $V_{\bar{K}}(\rho_0) \sim -(150-200)$ MeV. Such deep potentials are not reproduced at present by chirally based approaches that yield values of Re $V_{\bar{K}}(\rho_0)$ of order -100 MeV or less attractive, as summarized recently in Ref. [7]. For a recent overview of $\bar{K}N$ and $\bar{K}$-nucleus dynamics, see Ref. [8].

The subject of multi-$\bar{K}$ nuclei was studied in Refs. [3, 4], where the focal question considered was whether or not kaon condensation could occur in strong-interaction self-bound nuclear matter. Yamazaki *et al.* [9] argued that $\bar{K}$ mesons might provide the relevant physical degrees of freedom for reaching high-density self-bound strange matter that could

then be realized as multi-$\bar{K}$ nuclear matter. This scenario requires that $B_{\bar{K}}$ beyond some threshold value of strangeness exceeds $m_K c^2 + \mu_N - m_\Lambda c^2 \gtrsim 320$ MeV, where μ_N is the nucleon chemical potential, thus allowing for the conversion $\Lambda \rightarrow \bar{K} + N$ in matter. For this strong $\bar{K}$ binding, Λ and Ξ hyperons would no longer combine with nucleons to compose the more conventional kaon-free form of strange hadronic matter, which is made out of $\{N, \Lambda, \Xi\}$ particle-stable configurations [10, 11] (see Ref. [12] for an update), and $\bar{K}$ mesons would condense then macroscopically. However, our detailed calculations in Ref. [4] demonstrated a robust pattern of saturation for $B_{\bar{K}}$ and for nuclear densities upon increasing the number of $\bar{K}$ mesons embedded in the nuclear medium. For a wide range of phenomenologically allowed values of meson-field coupling constants compatible with assuming a deep $\bar{K}$-nucleus potential, the saturation values of $B_{\bar{K}}$ were found generally to be below 200 MeV, considerably short of the threshold value of ≈ 320 MeV required for the onset of kaon condensation under laboratory conditions. Similar results were subsequently published by Muto *et al.* [13]. Our discussion here concerns kaon condensation in self-bound systems, constrained by the strong interactions. It differs from discussions of kaon condensation in neutron stars where weak-interaction constraints are operative for any given value of density. For very recent works on kaon condensation in neutron-star matter, see Ref. [14], where hyperon degrees of freedom were disregarded, and Ref. [15], where the interplay between kaon condensation and hyperons was studied, and references to earlier relevant work cited therein.

In our calculations of multi-$\bar{K}$ nuclei [4], the saturation of $B_{\bar{K}}$ emerged for any boson-field composition that included the dominant vector ω-meson field, using the F-type SU(3) value $g_{\omega KK} \approx 3$ associated with the leading-order Tomozawa-Weinberg term of the meson-baryon effective Lagrangian. This value is smaller than in any of the other commonly used models [4]. Moreover, the contribution of each one of the vector ϕ-meson and ρ-meson fields was found to be substantially repulsive for systems with a large number of antikaons, reducing $B_{\bar{K}}$ as well as lowering the threshold value of the number of antikaons required for saturation to occur. We also verified that the saturation behavior of $B_{\bar{K}}$ is qualitatively independent of the RMF model applied to the nucleonic sector. The onset of saturation was found to depend on the atomic number. Generally, the heavier the nucleus is, the more antikaons it takes to saturate their separation energies. We concluded that $\bar{K}$ mesons do not provide a constituent degree of freedom for self-bound strange dense matter.

In the present work we extend our previous RMF calculations of multi-$\bar{K}$ nuclei into the domain of multi-$\bar{K}$ *hypernuclei*, to check whether a joint consideration of $\bar{K}$ mesons

together with hyperons could bring new features or change our previous conclusions. This is the first RMF calculation that considers both $\bar{K}$ mesons and hyperons together within *finite self-bound* hadronic configurations. The effect of hyperonic strangeness in bulk on the dispersion of kaons and antikaons was considered by Schaffner and Mishustin [16]. More recently, kaon-condensed hypernuclei as highly dense self-bound objects have been studied by Muto [17], using liquid-drop estimates.

The plan of the article is as follows. In Sec. 2 we briefly outline the RMF methodology for multi-$\bar{K}$ hypernuclei and discuss the hyperon and $\bar{K}$ couplings to the meson fields used in the present work. Results of these RMF calculations for multi-$\bar{K}$ hypernuclei are shown and discussed in Sec. 3. We conclude with a brief summary and outlook in Sec. 4.

2 Model

2.1 RMF formalism

In the present work, our interest is primarily aimed at multiply strange baryonic systems containing (anti)kaons. We employed the relativistic mean-field approach where the strong interactions among pointlike hadrons are mediated by *effective* mesonic degrees of freedom. In the following calculations we started from the Lagrangian density

$$\begin{aligned}\mathcal{L} &= \bar{B}\left[\mathrm{i}\gamma^{\mu}D_{\mu} - (M_B - g_{\sigma B}\sigma - g_{\sigma^* B}\sigma^*)\right] B \\ &+ (D_{\mu}K)^{\dagger}\,(D^{\mu}K) - (m_K^2 - g_{\sigma K}\,m_K\sigma - g_{\sigma^* K}\,m_K\sigma^*)K^{\dagger}K \\ &+ (\sigma, \sigma^*, \omega_{\mu}, \vec{\rho}_{\mu}, \phi_{\mu}, A_{\mu}\,\text{free-field terms}) - U(\sigma) - V(\omega),\end{aligned} \tag{1}$$

which includes, in addition to the common isoscalar scalar (σ), isoscalar vector (ω), isovector vector (ρ), electromagnetic (A) fields, and nonlinear self-couplings $U(\sigma)$ and $V(\omega)$, also *hidden strangeness* isoscalar σ^* and ϕ fields that couple exclusively to strangeness degrees of freedom. Vector fields are coupled to baryons B (nucleons, hyperons) and K mesons via the covariant derivative

$$D_{\mu} = \partial_{\mu} + \mathrm{i}\,g_{\omega\Phi}\,\omega_{\mu} + \mathrm{i}\,g_{\rho\Phi}\,\vec{I}\cdot\vec{\rho}_{\mu} + \mathrm{i}\,g_{\phi\Phi}\,\phi_{\mu} + \mathrm{i}\,e\,(I_3 + \tfrac{1}{2}Y)A_{\mu}\,, \tag{2}$$

where $\Phi = B$ and K, with $\vec{I}$ denoting the isospin operator, I_3 being its z component, and Y standing for hypercharge. This particular choice of the coupling scheme for K^- mesons ensures the existence of a conserved Noether current, the timelike component of which can

then be normalized to the number of K^- mesons in the medium,

$$\rho_{K^-} = 2(E_{K^-} + g_{\omega K}\,\omega + g_{\rho K}\,\rho + g_{\phi K}\,\phi + e\,A)K^+K^-, \qquad \int \mathrm{d}^3x\,\rho_{K^-} = \kappa, \tag{3}$$

and serves as a dynamical source in the equations of motion for the boson fields in matter:

$$\begin{aligned}
(-\nabla^2 + m_\sigma^2)\sigma &= g_{\sigma B}\bar{B}B + g_{\sigma K}m_K K^+K^- - \frac{\partial}{\partial\sigma}U(\sigma)\\
(-\nabla^2 + m_\sigma^{*2})\sigma^* &= g_{\sigma^* B}\bar{B}B + g_{\sigma^* K}m_K K^+K^-\\
(-\nabla^2 + m_\omega^2)\omega &= g_{\omega B}B^\dagger B - g_{\omega K}\rho_{K^-} + \frac{\partial}{\partial\omega}V(\omega)\\
(-\nabla^2 + m_\rho^2)\rho &= g_{\rho B}B^\dagger I_3 B - g_{\rho K}\rho_{K^-}\\
(-\nabla^2 + m_\phi^2)\phi &= g_{\phi B}B^\dagger B - g_{\phi K}\rho_{K^-}\\
-\nabla^2 A &= e\,B^\dagger(I_3 + \tfrac{1}{2}Y)B - e\,\rho_{K^-}.
\end{aligned} \tag{4}$$

These *dynamically* generated intermediate fields then enter the Dirac equation for baryons,

$$\left[-\mathrm{i}\boldsymbol{\alpha}\cdot\boldsymbol{\nabla} + \beta\,(M_B - g_{\sigma B}\sigma - g_{\sigma^* B}\sigma^*) + g_{\omega B}\omega + g_{\rho B}I_3\rho + g_{\phi B}\phi + e\left(I_3 + \tfrac{1}{2}Y\right)A\right]B = \epsilon B \tag{5}$$

and the Klein-Gordon equation for K^- mesons,

$$[-\boldsymbol{\nabla}^2 - E_{K^-}^2 + m_K^2 + \Pi_{K^-}]K^- = 0, \tag{6}$$

with the in-medium K^- self-energy,

$$\begin{aligned}
\Pi_{K^-} = &- g_{\sigma K}m_K\sigma - g_{\sigma^* K}m_K\sigma^* - 2E_{K^-}(g_{\omega K}\omega + g_{\rho K}\rho + g_{\phi K}\phi + eA)\\
&- (g_{\omega K}\omega + g_{\rho K}\rho + g_{\phi K}\phi + eA)^2.
\end{aligned} \tag{7}$$

Hence, the presence of the $\bar{K}$ mesons modifies the scalar and vector mean fields entering the Dirac equation, consequently leading to a *dynamical* rearrangement of the baryon configurations and densities that, in turn, modify the $\bar{K}$ quasibound states in the medium. This requires a self-consistent solution of these coupled wave equations, a procedure followed numerically in the present as well as in our previous works. In the present work, for the sake of simplicity, we have suppressed the imaginary part of Π_{K^-} arising from in-medium K^- absorption processes except for demonstrating its effect in one example. Note that, for the range of values $B_{K^-} \gtrsim 100$ MeV mostly considered here, the effect of Im Π_{K^-} was

Table 1: $\bar{K}$ and K^- separation energies, $B_{\bar{K}}$ and B_{K^-}, respectively, calculated statically (in MeV) for a single antikaon 1s state in several nuclei, using the NL-TM nuclear RMF parametrizations (TM2 for ^{12}C and ^{16}O, TM1 for ^{40}Ca and above) and vector SU(3) coupling constants, Eq. (10). The difference $B_{K^-} - B_{\bar{K}}$ is due to the K^- finite-size Coulomb potential.

	^{12}C	^{16}O	^{40}Ca	^{90}Zr	^{208}Pb
$B_{\bar{K}}$	44.8	42.7	49.8	54.5	53.6
B_{K^-}	49.0	47.6	59.2	69.4	76.6

found to be negligible (see Fig. 1 of Ref. [4]).

2.2 Choice of the model parameters

To parametrize the nucleonic part of the Lagrangian density (1) we considered the standard RMF parameter sets NL-SH [18] and NL-TM1(2) [19], which have been successfully used in numerous calculations of various nuclear systems.

In the case of hyperons the coupling constants to the vector fields were fixed using SU(6) symmetry. For Λ hyperons this leads to

$$g_{\omega\Lambda} = \frac{2}{3} g_{\omega N},\ g_{\rho\Lambda} = 0,\ g_{\phi\Lambda} = \frac{-\sqrt{2}}{3} g_{\omega N}. \tag{8}$$

The coupling to the scalar σ field, $g_{\sigma\Lambda}/g_{\sigma N} = 0.6184\,(0.623)$ for the NL-SH (NL-TM) RMF model, was then estimated by fitting to measured Λ-hypernuclear binding energies [20]. This essentially ensures the well depth of 28 MeV for Λ in nuclear matter. The coupling of the Λ hyperon to the scalar σ^* field was fixed by fitting to the measured value $\Delta B_{\Lambda\Lambda} \approx$ 1 MeV of the uniquely identified hypernucleus ${}^{\ 6}_{\Lambda\Lambda}$He [21]. For Ξ hyperons, SU(6) symmetry gives

$$g_{\omega\Xi} = \frac{1}{3} g_{\omega N},\ g_{\rho\Xi} = -g_{\rho N},\ g_{\phi\Xi} = -2\frac{\sqrt{2}}{3} g_{\omega N}. \tag{9}$$

Because there are no experimental data for $\Xi(\Lambda)$-Ξ interactions, we set $g_{\phi\Xi} = g_{\sigma^*\Xi} = 0$ to avoid parameters that might lead to unphysical consequences and that, in addition, are expected to play a minor role (in analogy to the small effect, of order 1 MeV for B_{K^-}, found upon putting $g_{\phi\Lambda}$ and $g_{\sigma^*\Lambda}$ to zero, and as is demonstrated below in Fig. 7 within a different context). The coupling to the scalar σ field was then constrained to yield an optical potential Re $V_{\Xi^-} = -14$ MeV in the center of ^{12}C [22]. This corresponds to $g_{\sigma\Xi} = 0.299 g_{\sigma N}$ for the NL-TM2 RMF model.

Finally, for the antikaon couplings to the vector meson fields we adopted a purely F-type, vector SU(3) symmetry:

$$2g_{\omega K} = 2g_{\rho K} = \sqrt{2}g_{\phi K} = g_{\rho\pi} = 6.04, \tag{10}$$

where $g_{\rho\pi}$ is due to the $\rho \to 2\pi$ decay width [7]. (Here we denoted by g_{VP} the VPP electric coupling constant g_{VPP}.) Using this "minimal" set of coupling constants to establish correspondence with chirally based approaches, we calculate the single antikaon $1s$ separation energies $B_{\bar{K}}$ and B_{K^-} listed in Table 1. These separation energies are lower roughly by 25 MeV than those anticipated from $\bar{K}N - \Sigma\pi$ coupled-channel chiral approaches [7], most likely because the $K^\star$ vector-meson off-diagonal coupling is not included in the standard RMF formulation. The missing attraction, and beyond it, is incorporated here by coupling the antikaon to scalar fields σ and σ^*. SU(3) symmetry is not of much help when fixing the coupling constants of scalar fields. Because there still is no consensus about the microscopic origin of the scalar σ field and the strength of its coupling to $\bar{K}$ mesons [23, 24], in this work we fitted $g_{\sigma K}$ to several assumed K^- separation energies B_{K^-} in the range of $100 - 150$ MeV for a single K^- meson in selected nuclei across the periodic table, as implied by the deep K^--nucleus potential phenomenology of Refs. [2, 6]. Furthermore, for use in multistrange configurations, the coupling constant to the σ^* field is taken from $f_0(980) \to K\bar{K}$ decay to be $g_{\sigma^* K} = 2.65$ [16]. The effect of the σ^* field was found generally to be minor. For a more comprehensive discussion of the issue of scalar couplings, see our previous work [4].

2.3 Inclusion of the SU(3) baryon octet

We considered many-body systems consisting of the SU(3) octet N, Λ, Σ, and Ξ baryons that can be made particle stable against strong interactions [10, 11]. The energy release Q values for various conversion reactions of the type $B_1 B_2 \to B_3 B_4$ together with phenomenological guidance on hyperon-nucleus interactions suggest that only the conversions $\Xi^- p \to \Lambda\Lambda$ and $\Xi^0 n \to \Lambda\Lambda$ (for which $Q \simeq 20$ MeV) can be overcome by binding effects. It becomes possible then to form particle-stable multi-$\{N, \Lambda, \Xi\}$ configurations for which the conversion $\Xi N \to \Lambda\Lambda$ is Pauli blocked owing to the Λ orbitals being filled up to the Fermi level. For composite configurations with Σ hyperons the energy release in the $\Sigma N \to \Lambda N$ conversion is too high ($Q \gtrsim 75$ MeV) and, hence, it is unlikely for hypernuclear systems with Σ hyperons to be particle stable.

3 Results and discussion

In Refs. [3, 4] we studied multi-$\bar{K}$ nuclei, observing that the calculated K^- separation energies as well as the nuclear densities saturate upon increasing the number of K^- mesons embedded dynamically in the nuclear medium. This saturation phenomenon, which is qualitatively independent of the applied RMF model, emerged for any boson-field composition containing the dominant vector ω-meson field which acts repulsively between $\bar{K}$ mesons. Because the calculated K^- separation energies did not exceed 200 MeV, for coupling-constant combinations designed to bind a single K^- meson in the range $B_{K^-} \sim 100 - 150$ MeV, it was argued that kaon condensation is unlikely to occur in strong-interaction self-bound hadronic matter. In this section we demonstrate that these conclusions hold also when adding, within particle-stable multistrange configurations, large numbers of hyperons to nuclei across the periodic table.

3.1 Multi-$\{N, \Lambda, K^-\}$ configurations

Figure 1 presents $1s$ K^- separation energies B_{K^-} in ^{16}O+$\eta\Lambda$+κK^- multi-$K^-\Lambda$ hypernuclei as a function of the number κ of K^- mesons for $\eta = 0, 2, 4, 6$, and 8 Λ hyperons, calculated in the NL-SH model for two values of $g_{\sigma K}$ ($g_{\sigma K} = 0.233 g_{\sigma N}$ and $0.391 g_{\sigma N}$) chosen to produce $B_{K^-} = 100$ and 150 MeV, respectively, for $\eta = 0$, $\kappa = 1$. In addition, the lower group of curves with $B_{K^-} < 60$ MeV corresponds to $g_{\sigma K} = 0$. The figure illustrates saturation of B_{K^-} with the number of antikaons in multi-Λ hypernuclei. There is an apparent increase of B_{K^-} (up to 15%) when the first two Λ hyperons fill the $1s$ shell. Further Λ hyperons, placed in the p shell, cause only insignificant variation of B_{K^-} for small values of κ. However, the effect of the $1p_{3/2}$-shell hyperons increases with the number of antikaons, and for $\kappa = 8$ it adds another $5 - 10$ MeV to B_{K^-}. The separation energy B_{K^-} remains almost unaffected (or even decreases) by the next two Λ hyperons placed in the $1p_{1/2}$ shell. The figure thus suggests saturation of the K^- separation energy also with the number η of Λ hyperons in the nuclear medium. When the K^- coupling to the σ field is switched off, $g_{\sigma K} = 0$, the K^- separation energy assumes relatively low values, $B_{K^-} \lesssim 50$ MeV, and decreases as a function of κ when Im Π_{K^-} is considered (solid lines). In this case, the effect of K^- absorption is not negligible as illustrated by the dot-dashed line showing B_{K^-} for Im $\Pi_{K^-} = 0$. The effect of Im $\Pi_{K^-} \neq 0$ for $B_{K^-} > 100$ MeV in the upper groups of curves is negligible and is not shown here or in all subsequent figures.

It is worth noting that $\eta = 8$ is the maximum number of Λ hyperons in our calculation

that can be bound in the ^{16}O nuclear core. In some of the $^{16}\mathrm{O} + \eta\Lambda + \kappa K^-$ allowed configurtions, $1p_{1/2}$ neutrons became less bound than $1d_{5/2}$ neutrons because of the strong spin-orbit interaction. (This occurs, e.g., for $\eta = 0$ when $\kappa \geq 5$ or for $\eta = 8$ when $\kappa \geq 3$.) However, the total binding energy of the system was found always to be higher for configurations with $1p_{1/2}$ neutrons. Consequently, the standard shell configurations of oxygen are more bound and are thus energetically favorable.

The saturation of B_{K^-} upon increasing the number of Λ hyperons in multi-$K^-\Lambda$ hypernuclei based on a ^{16}O nuclear core holds also when going over to heavier core nuclei. Figure 2 shows the $1s$ K^- separation energy B_{K^-} in $^{208}\mathrm{Pb} + \eta\Lambda + \kappa K^-$ multi-$K^-\Lambda$ hypernuclei as a function of both the number κ of K^- mesons and η of Λ hyperons, calculated in the NL-TM1 model for $g_{\sigma K} = 0.133 g_{\sigma N}$ such that $B_{K^-} = 100$ MeV for $\eta = 0$, $\kappa = 1$. For

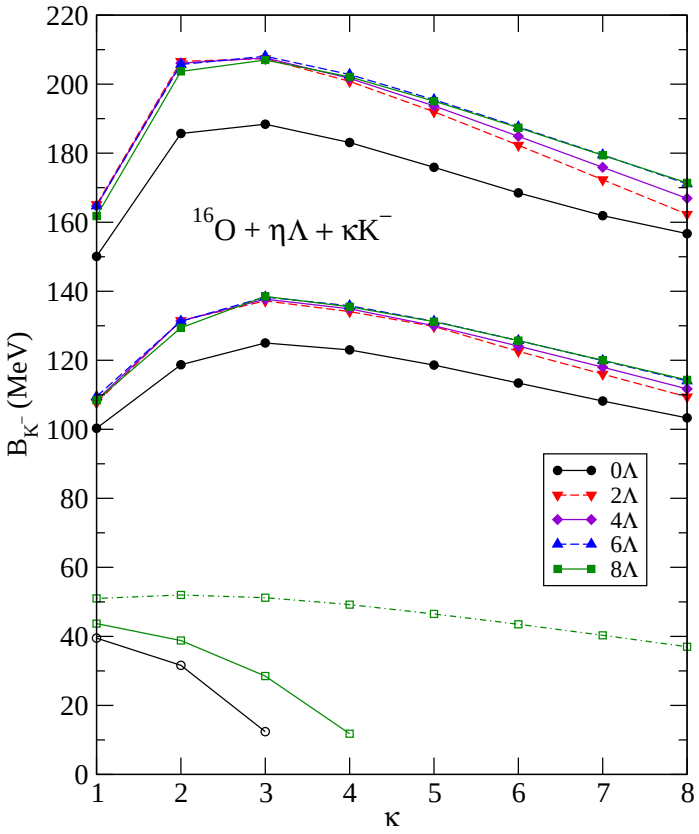

Figure 1: (Color online) The $1s$ K^- separation energy B_{K^-} in $^{16}\mathrm{O} + \eta\Lambda + \kappa K^-$ as a function of the number κ of antikaons for several values of the number η of Λ hyperons, with initial values $B_{K^-} = 100$ and 150 MeV for $\eta = 0$, $\kappa = 1$, calculated in the NL-SH RMF model. The solid (dot-dashed) lines with open symbols correspond to $g_{\sigma K} = 0$ including (excluding) Im Π_{K^-}.

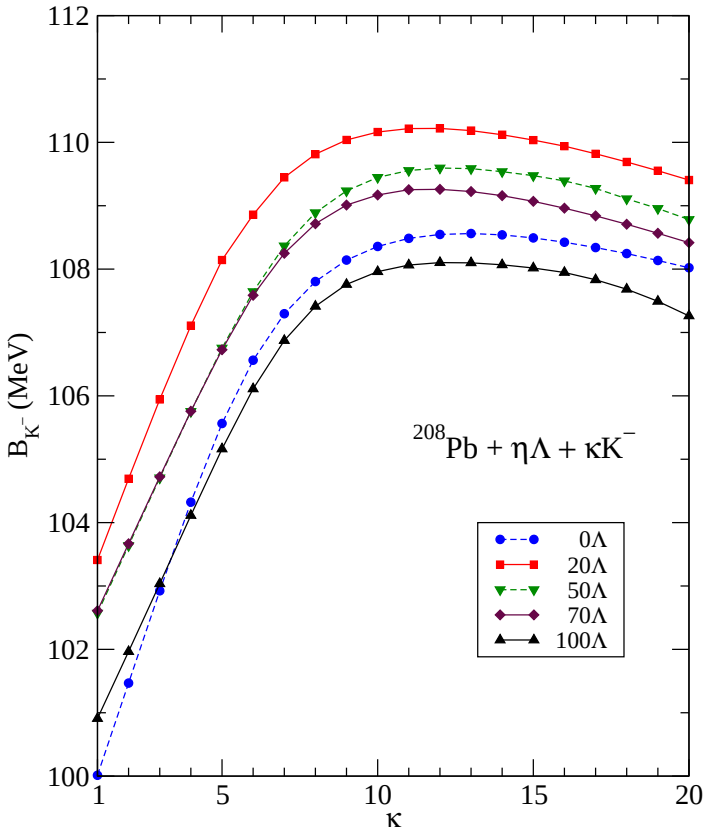

Figure 2: (Color online) The $1s$ K^- separation energy B_{K^-} in $^{208}\mathrm{Pb} + \eta\Lambda + \kappa K^-$ as a function of the number κ of antikaons for several values of the number η of Λ hyperons, with initial value $B_{K^-} = 100$ MeV for $\eta = 0$, $\kappa = 1$, calculated in the NL-TM1 RMF model.

any given number η of Λ hyperons, B_{K^-} saturates with the number κ of K^- mesons, reaching its maximum value for $\kappa = 12$. Morever, B_{K^-} increases with the number of hyperons up to $\eta = 20$, when it reaches its maximum value $B_{K^-} \approx 110$ MeV for $\kappa = 12$, and then starts to decrease with η. Consequently, in the Pb configurations with 100 Λ hyperons and more than 5 K^- mesons, K^- mesons are even less bound than in configurations with no Λ hyperons. The decrease of B_{K^-} with η beyond $\eta = 20$ is apparently related to a depletion of the central nuclear density in the presence of a massive number of hyperons in outer shells, as confirmed by some of the subsequent figures, because B_{K^-} is greatly affected by the central nuclear density.

3.2 Multi-$\{N, \Lambda, \Xi, K^-\}$ configurations

When building up baryonic multi-$\{N, \Lambda, \Xi\}$ configurations with maximum strangeness for selected core nuclei, we first started by filling up Λ hyperon single-particle states in a given nuclear core up to the Λ Fermi level. Subsequently, we added Ξ^0 and Ξ^- hyperons as long as the reaction $[AN, \eta\Lambda, \mu\Xi] \rightarrow [(A-1)N, \eta\Lambda, (\mu-1)\Xi] + 2\Lambda$ was energetically forbidden (here, [...] denotes a bound configuration). Finally, we checked that the inverse reaction $[AN, \eta\Lambda, \mu\Xi] \rightarrow [(A+1)N, (\eta-2)\Lambda, (\mu+1)\Xi]$ is kinematically blocked as well. These conditions guarantee that such $\{N, \Lambda, \Xi\}$ multistrange configurations are particle stable against strong interactions, decaying only via weak interactions.

Clearly, the amount of Ξ hyperons bound in a given system depends on the depth $-V_\Xi$ of the Ξ-nucleus potential. We adopted a value for $g_{\sigma\Xi}$ that gives $V_\Xi^{\rm Dirac} = V_{\rm S} + V_{\rm V} = -18$ MeV, corresponding to a depth of $-V_\Xi^{\rm Schr.} \simeq 14$ MeV for use in the Schroedinger equation [22]. For comparison, in some cases we also considered $V_\Xi^{\rm Dirac} = -25$ MeV.

The ^{16}O core can accommodate up to $\eta = 8$ Λ hyperons in particle-stable configurations, and the $^{16}{\rm O} + 8\Lambda$ system admits many more, of order 40 K^- mesons. However, we have not found any energetically favorable conversion $\Lambda\Lambda \rightarrow \Xi N$ in $^{16}{\rm O} + \eta\Lambda + \kappa K^-$ systems. Therefore, Ξ hyperons are not part of any particle-stable multistrange configurations built upon the ^{16}O core. While checking the energy balance in heavier systems with ^{40}Ca, ^{90}Zr, and ^{208}Pb nuclear cores, we found particle-stable configurations: $^{40}{\rm Ca} + 20\Lambda + 2\Xi^0$, $^{90}{\rm Zr} + 40\Lambda + 2\Xi^0 + 2\Xi^-$, and $^{208}{\rm Pb} + 106\Lambda + 8\Xi^0 + 18\Xi^-$. We then embedded several K^- mesons in these configurations and studied density distributions and binding energies in such multi-K^- hypernuclear systems. Figure 3 demonstrates the calculated $1s$ K^- separation energy B_{K^-} in $^{40}{\rm Ca} + 20\Lambda + 2\Xi^0 + \kappa K^-$, $^{90}{\rm Zr} + 40\Lambda + 2\Xi^0 + 2\Xi^- + \kappa K^-$, and $^{208}{\rm Pb} + 106\Lambda + 8\Xi^0 + 18\Xi^- + \kappa K^-$ as a function of the number κ of K^- mesons. For comparison, in the case of the ^{208}Pb core, we also present calculations done excluding Ξ hyperons but keeping the same number, $\eta = 106$, of Λ hyperons. A decrease of B_{K^-} upon adding hyperons (Ξ in this case) is noted, in line with the trend observed and discussed for Fig. 2 above.

The calculations shown in Fig. 3 were performed within the NL-TM1 nuclear RMF scheme using values of $g_{\sigma K} = 0.211 g_{\sigma N}$ (^{40}Ca) and $0.163 g_{\sigma N}$ (^{90}Zr), which yield $B_{K^-} = 100$ MeV for a single K^- nuclear configuration with $\eta = \mu = 0$, where μ denotes the number of Ξ hyperons. The figure demonstrates that the saturation of K^- separation energies, observed for multi-Λ hypernuclei in Figs. 1 and 2, holds also when Ξ hyperons are added dynamically within particle-stable configurations and that the heavier the system is, the larger number

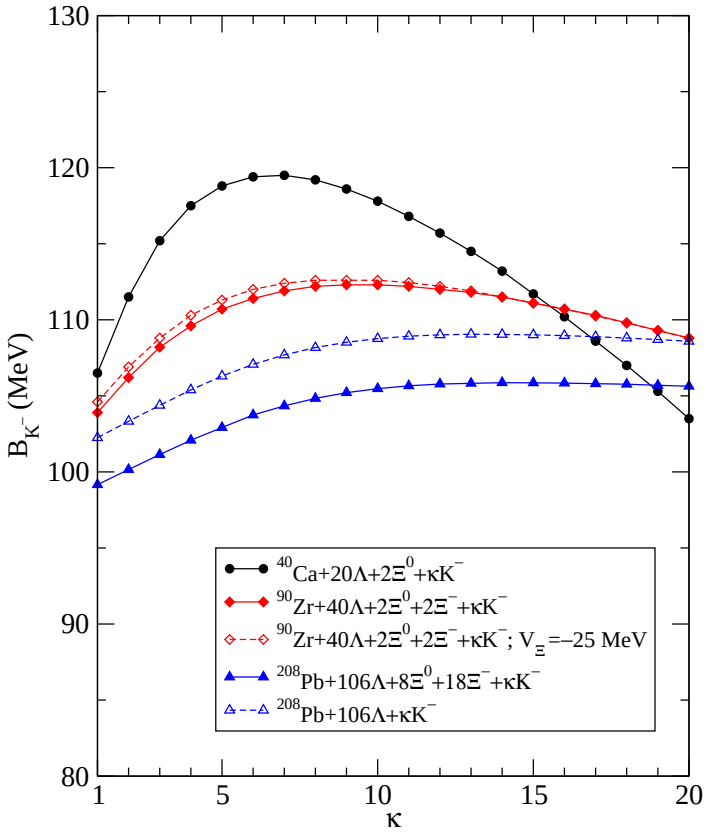

Figure 3: (Color online) The $1s$ K^- separation energy B_{K^-} in ^{40}Ca, ^{90}Zr, and ^{208}Pb with $\eta\Lambda + \mu\Xi + \kappa K^-$ as a function of the number κ of antikaons, with initial value $B_{K^-} = 100$ MeV for $\eta = \mu = 0$, $\kappa = 1$, calculated in the NL-TM1 RMF model.

κ of antikaons it takes to saturate B_{K^-}. It is worth noting that in all cases B_{K^-} does not exceed 120 MeV. Finally, the two curves for a ^{90}Zr nuclear core in Fig. 3 (using diamond symbols) show the sensitivity to the value assumed for the Ξ hyperon potential depth, the standard $-V_\Xi^{\rm Dirac} = 18$ MeV, and a somewhat increased depth $-V_\Xi^{\rm Dirac} = 25$ MeV, illustrating the tiny effect it exercises on B_{K^-} that is noticeable only for $\kappa < 12$.

A deeper Ξ potential supports binding of more Ξ hyperons in a given multi-Λ hypernucleus. For $V_\Xi^{\rm Dirac} = -18$ MeV, only $2\Xi^0$ and $2\Xi^0 + 2\Xi^-$ hyperons were found to be bound in $^{40}{\rm Ca} + 20\Lambda$ and $^{90}{\rm Zr} + 40\Lambda$, respectively. However, for $V_\Xi^{\rm Dirac} = -25$ MeV it is possible to accommodate up to $8\Xi^0 + 2\Xi^-$ hyperons in $^{40}{\rm Ca} + 20\Lambda$ and $8\Xi^0 + 8\Xi^-$ hyperons in $^{90}{\rm Zr} + 40\Lambda$. Figure 4 presents the $1s$ K^- separation energy B_{K^-} in multi-K^- hypernuclei $^{40}{\rm Ca} + 20\Lambda + 8\Xi^0 + 2\Xi^- + \kappa K^-$ and $^{90}{\rm Zr} + 40\Lambda + 8\Xi^0 + 8\Xi^- + \kappa K^-$ as a function of the number κ of K^- mesons, calculated in the NL-TM1 model for $V_\Xi^{\rm Dirac} = -25$ MeV, using values for $g_{\sigma K}$ such that $B_{K^-} = 100$ MeV in $^{40}{\rm Ca} + 1K^-$ and in $^{90}{\rm Zr} + 1K^-$. The figure

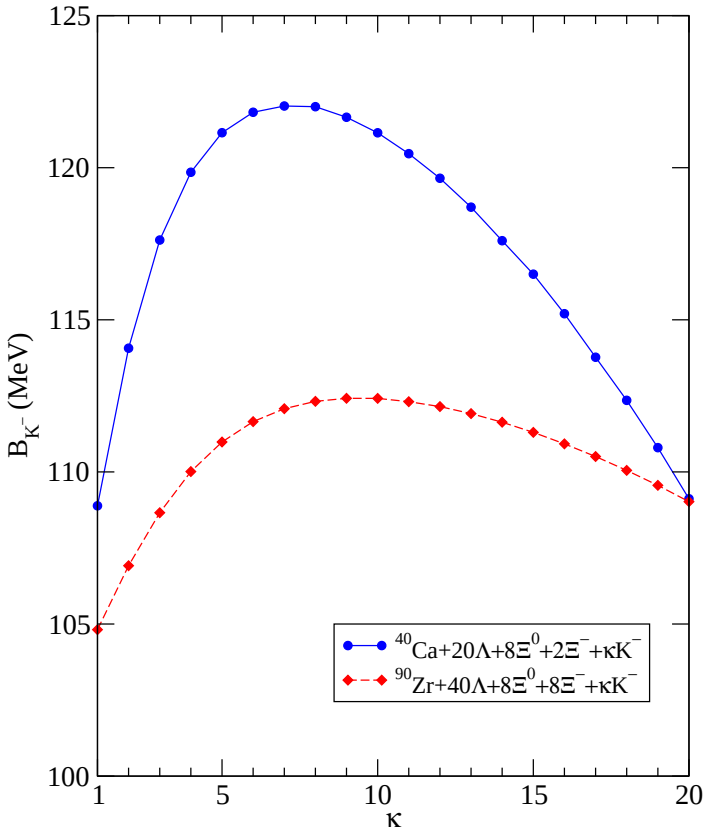

Figure 4: (Color online) The $1s$ K^- separation energy B_{K^-} in ^{40}Ca and ^{90}Zr with $\eta\Lambda + \mu\Xi + \kappa K^-$, for $V_\Xi^{\rm Dirac} = -25$ MeV, as a function of the number κ of antikaons, with initial value $B_{K^-} = 100$ MeV for $\eta = \mu = 0$, $\kappa = 1$, calculated in the NL-TM1 RMF model.

illustrates that the saturation of the K^- separation energy occurs also in baryonic systems with three species of hyperons, Λ, Ξ^0, and Ξ^-, reaching quite large fractions of strangeness [$|S|/B = 0.57(0.8)$ for a Ca(Zr) core]. We note that the separation energy B_{K^-} barely exceeds 120 MeV in these cases too.

We also studied the rearangement of nuclear systems induced by embedding hyperons and K^- mesons. Figure 5 presents the evolution of the density distributions in Zr after first adding 40Λ+4Ξ hyperons (top panel) and then 10 K^- mesons (bottom panel). The nucleon density ρ_N in ^{90}Zr is denoted by a dotted line. The relatively weakly bound hyperons with extended density distributions (dashed line, solid diamonds) attract nucleons, thus depleting the central nucleon density ρ_N (dashed line, circles). Adding extra 10 K^- mesons to the hypernuclear system induces large rearrangement of the baryons. The K^- mesons, which pile up near the origin (solid line, squares), attract the surrounding nucleons and hyperons. Consequently, the densities ρ_N and ρ_Y (solid lines, solid circles and diamonds,

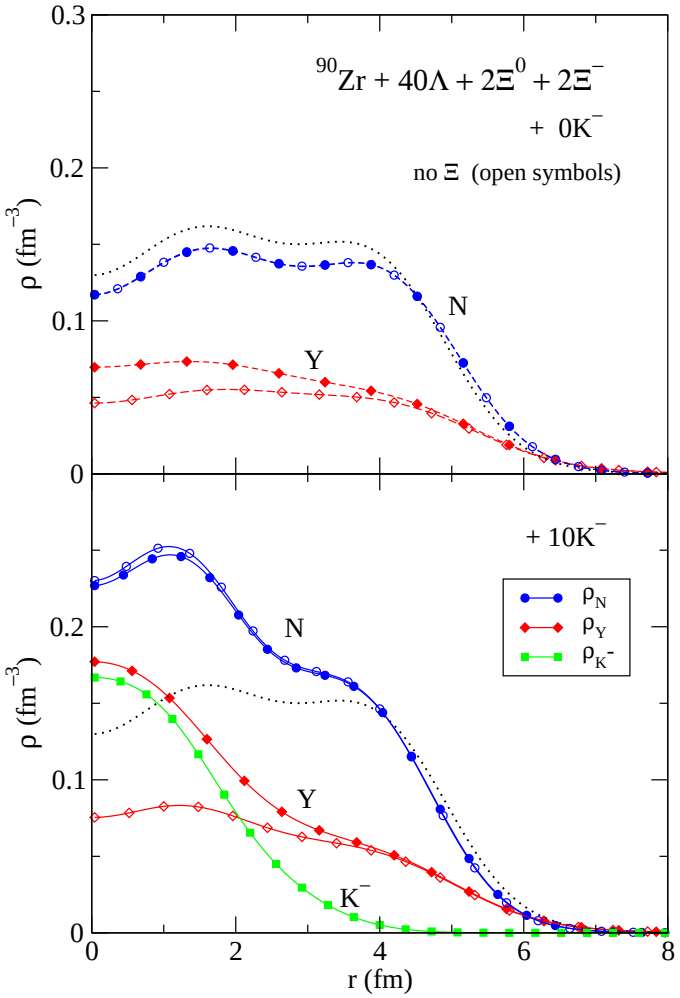

Figure 5: (Color online) Density distributions in ^{90}Zr + 40Λ + 2Ξ^0 + 2Ξ$^-$ + κK^-, for $\kappa = 0$ (top panel) and $\kappa = 10$ (bottom panel), with $B_{K^-} = 100$ MeV for $\eta = \mu = 0$, $\kappa = 1$, calculated in the NL-TM1 RMF model. The dotted line corresponds to the nucleon density ρ_N in ^{90}Zr. The densities ρ_Λ (open diamonds) and ρ_N (open circles) in ^{90}Zr + 40Λ + κK^- are shown for comparison.

respectively) increase considerably in the central region. The resulting configuration ^{90}Zr + 40Λ + 2Ξ^0 + 2Ξ$^-$ + 10K^- is thus significantly compressed, with central baryon density ρ_B exceeding the nuclear density in ^{90}Zr by a factor of roughly 3.

For comparison we present in Fig. 5 also the Λ hyperon (ρ_Λ, open diamonds) and nucleon (ρ_N, open circles) density distributions calculated in ^{90}Zr + 40Λ + κK^- for $\kappa = 0$ and 10 K^- mesons. The removal of the 1s-state Ξ hyperons from the primary baryonic configuration ^{90}Zr + 40Λ + 2Ξ^0 + 2Ξ$^-$ affects considerably the hyperon density distribution ρ_Y in the central region of the nucleus, this effect being magnified by the presence of

K^- mesons. In contrast, the nucleon density ρ_N remains almost intact. For $\kappa = 10$, Ξ hyperons appear to repel nucleons from the center of the multi-$\{N, Y, \bar{K}\}$ system, much like Λ hyperons do.

3.3 Multi-$\{N, \Lambda, \Xi, K^+\}$ configurations

The K^+-nucleus potential is known to be repulsive, with $V_{K^+} \approx 30$ MeV at central nuclear density [5]. Schaffner and Mishustin [16] suggested that the presence of hyperons could lead eventually to a decrease of the repulsion that K^+ mesons undergo in nuclear matter so that the K^+ potential might even become attractive. Here we studied the possibility of binding K^+ mesons in hypernuclear matter, neglecting for simplicity dynamical effects arising from coupling K^+ mesons to the hypernuclear system. The K^+-nucleus potential was constructed simply by applying a G-parity transformation to the corresponding K^- potential, choosing $g_{\sigma K}$ such that it produces $B_{K^-} = 100$ MeV in the given core nucleus.

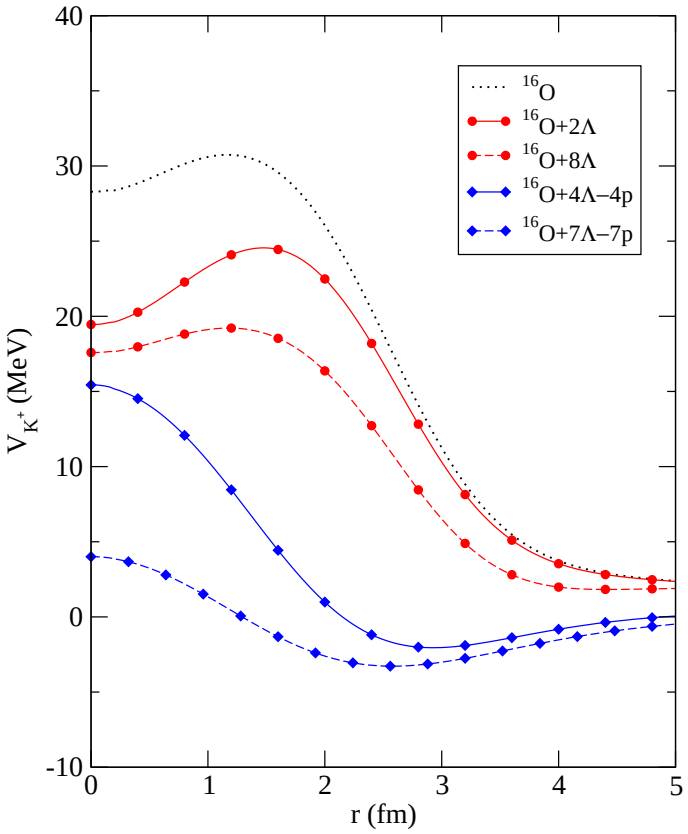

Figure 6: (Color online)The K^+ static potential in $^{16}\mathrm{O} + \eta\Lambda - \nu p$, calculated in the NL-SH RMF model.

Figure 6 shows the radial dependence of the real part of the static K^+ potential in various hypernuclear systems connected with ^{16}O. The dotted line shows the repulsive K^+ potential in ^{16}O for comparison. The figure indeed shows that the repulsion decreases, from roughly 30 MeV down to roughly 20 MeV with the number of Λ hyperons added to the nuclear core, but the K^+ potential remains always repulsive in ^{16}O+$\eta\Lambda$ systems. Searching for a K^+ bound state in hadronic systems we also calculated the K^+ potential in more exotic multistrange hypernuclei $^{A}\mathrm{Z}+\eta\Lambda-\nu p$, where several protons are removed from the nuclear core in an attempt to increase the $|S|/B$ ratio and to reduce Coulomb repulsion. Figure 6 indicates that such removal of protons from ^{16}O has a sizable effect on the shape of the K^+ potential, which may result in a shallow attractive pocket. However, the attraction is insufficient to bind a K^+ meson in these hadronic systems. Our calculations confirmed that the above conclusion holds also in heavier hypernuclear configurations based on Ca, Zr, and Pb cores.

In heavier nuclei, where it becomes possible to accommodate also Ξ hyperons in addition

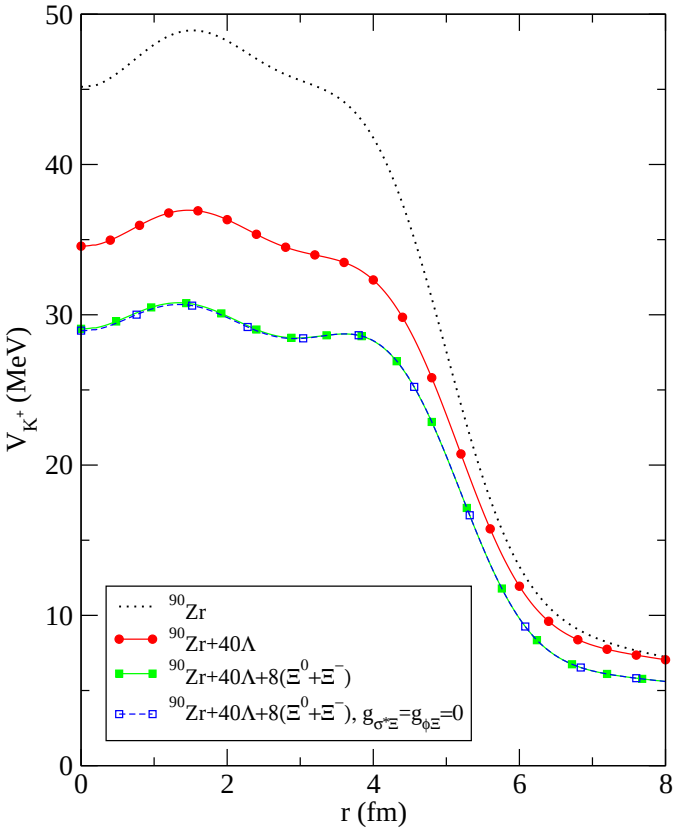

Figure 7: (Color online) The K^+ static potential in $^{90}\mathrm{Zr}+\eta\Lambda+\mu(\Xi^0+\Xi^-)$, calculated in the NL-TM1 RMF model.

to Λ hyperons, the K^+ repulsion may be further reduced. This is demonstrated in Fig. 7 for a ^{90}Zr nuclear core. However, this reduction is insufficient to reverse the repulsion into attraction. The figure also shows that the *hidden strangeness* couplings (chosen to be $g_{i\Xi} = 2g_{i\Lambda},\ i = \sigma^*,\ \phi$) have no effect whatsoever on the reduction accomplished by the presence of Ξ hyperons.

Finally, we searched for K^+ bound states in nuclei sustained by K^- mesons. The presence of deeply bound K^- mesons makes the K^+ potential immensely deep (more than 100 MeV in $^{16}\mathrm{O} + 8\mathrm{K}^-$). Hovever, because the K^- mesons are concentrated at the very center of the nucleus, the K^+ potential is of a rather short range of about 1 fm. As a result, we found only very weakly bound K^+ states (by 1 MeV) in multi-$\{N, Y, K^-\}$ configurations. A more careful treatment of K^+K^- dynamics near threshold is necessary before coming to further conclusions, but our conclusion is not at odds with recent studies of the $I = 1/2, J^\pi = 1/2^+$ $K\bar{K}N$ system [25, 26].

4 Summary and conclusions

In this work, the RMF equations of motion for multi-$\bar{K}$ hypernuclei were formulated and solved for self-bound finite multistrange configurations. The choice of coupling constants of the constituents – nucleons, hyperons, and $\bar{K}$ mesons – to the vector and scalar meson fields was guided by a combination of accepted models and by phenomenology. The sensitivity to particular chosen values was studied. The results of the RMF calculations show a robust pattern of binding-energy saturation for $\bar{K}$ mesons as a function of their number κ. Compared to our previous RMF results for multi-$\bar{K}$ nuclei [4], the added hyperons do not bring about any quantitative change in the $B_{K^-}(\kappa)$ saturating curve. The main reason for saturation remains the repulsion induced by the vector meson fields, primarily ω, between $\bar{K}$ mesons. The SU(3)$_V$ values adopted here for g_{vK}, Eq. (10), provide the "minimal" strength for $g_{\omega K}$ out of several other choices made in the literature, implying that the saturation of $B_{K^-}(\kappa)$ persists also for other choices of coupling-constant sets, as discussed in Ref. [4]. The repulsion between $\bar{K}$ mesons was also the primary reason for saturation in multi-$\bar{K}$ nuclei, both in our previous work [4] and in Ref. [13].

The saturation of B_{K^-} with typical values below 200 MeV, considerably short of what it takes to replace a Λ hyperon by a nucleon and a $\bar{K}$ meson, means that $\bar{K}$ mesons do not compete favorably and thus cannot replace hyperons as constituents of strange hadronic matter. In other words, $\bar{K}$ mesons do not condense in self-bound hadronic matter. The

baryon densities of multi-$\bar{K}$ hypernuclei are between $(2-3)\rho_0$, where ρ_0 is nuclear-matter density. This is somewhat above the values obtained without $\bar{K}$ mesons, but still within the density range where hadronic models are likely to be applicable.

Our conclusion of no "kaon condensation" is specific to self-bound finite hadronic systems run under strong-interaction constraints. It is not directly related to the Kaplan-Nelson conjecture of macroscopic kaon condensation [27], nor to hadronic systems evolving subject to weak-interaction constraints, such as neutron stars. Yet, this conclusion has been challenged recently by Muto [17] who uses the liquid-drop approach to claim that multi-$\bar{K}$ hypernuclei (termed by him "kaon-condensed hypernuclei") may provide the ground-state configuration of finite strange hadronic systems at densities about $9\rho_0$. Of course this high value of density for kaon-condensed hypernuclei is beyond the range of applicability of hadronic models, because quark-gluon degrees of freedom must enter in this density range. His calculation also reveals an isomeric multistrange hypernuclear state, without $\bar{K}$ mesons, at density about $2\rho_0$ which is close to what we find here within a RMF bound-state calculation. The appearance of a high-density kaon-condensed hypernuclear bound state in Muto's calculation might be just an artifact of the applied liquid-drop methodology, which does not provide an accurate substitute for a more microscopically oriented bound-state calculation.

The role of K^- strong decays in hadronic matter was played down in the present calculation of multi-K^- hypernuclei because our aim, primarily, was to discuss and compare (real) binding energies of strange hadronic matter with and without K^- mesons. The width of deeply bound K^- nuclear configurations was explored by us in Refs. [1, 2, 3], concluding that residual widths of order $\Gamma_{K^-} \sim 50$ MeV due to $K^-NN \to \Lambda N, \Sigma N$ pionless conversion reactions are expected in the relevant range of binding energy $B_{K^-} \sim 100 - 200$ MeV. This estimate should hold also in multi-K^- hypernuclei where added conversion channels are allowed: $K^-NY \to \Lambda Y, \Sigma Y$, $K^-N\Lambda \to N\Xi$, and $K^-\Lambda Y \to \Xi Y$. We know of no physical mechanism capable of reducing substantially these widths, and therefore we do not anticipate multi-K^- nuclei or multi-K^- hypernuclei to exist as relatively long-lived isomeric states of strange hadronic matter which consists of multi-$\{N, \Lambda, \Xi\}$ configurations.

Acknowledgments

This work was supported in part by GACR grant 202/09/1441 and by SPHERE within the FP7 research grant system. AG acknowledges instructive discussions with Wolfram

Weise and the support extended by the DFG Cluster of Excellence, Origin and Structure of the Universe, during a visit to the Technische Universität München.

References

[1] J. Mareš, E. Friedman, A. Gal, Phys. Lett. B **606**, 295 (2005).

[2] J. Mareš, E. Friedman, A. Gal, Nucl. Phys. A **770**, 84 (2006).

[3] D. Gazda, E. Friedman, A. Gal, J. Mareš, Phys. Rev. C **76**, 055204 (2007).

[4] D. Gazda, E. Friedman, A. Gal, J. Mareš, Phys. Rev. C **77**, 045206 (2008).

[5] E. Friedman, A. Gal, Phys. Rep. **452**, 89 (2007); and references to earlier work cited therein.

[6] T. Kishimoto *et al.*, Prog. Theor. Phys. **118**, 181 (2007); T. Kishimoto *et al.*, Nucl. Phys. A **827**, 321c (2009).

[7] W. Weise, R. Härtle, Nucl. Phys. A **804**, 173 (2008); and references to earlier work cited therein.

[8] A. Gal, Hyperfine Interact. (in press), arXiv:0812.0144 [nucl-th].

[9] T. Yamazaki, A. Doté, Y. Akaishi, Phys. Lett. B **587**, 167 (2004).

[10] J. Schaffner, C.B. Dover, A. Gal, C. Greiner, H. Stöcker, Phys. Rev. Lett. **71**, 1328 (1993).

[11] J. Schaffner, C.B. Dover, A. Gal, C. Greiner, D.J. Millener, H. Stöcker, Ann. Phys. **235**, 35 (1994).

[12] J. Schaffner-Bielich, A. Gal, Phys. Rev. C **62**, 034311 (2000).

[13] T. Muto, T. Maruyama, T. Tatsumi, Phys. Rev. C **79**, 035207 (2009).

[14] S. Banik, W. Greiner, D. Bandyopadhyay, Phys. Rev. C **78**, 065804 (2008).

[15] T. Muto, Phys. Rev. C **77**, 015810 (2008).

[16] J. Schaffner, I.N. Mishustin, Phys. Rev. C **53**, 1416 (1996).

[17] T. Muto, Nucl. Phys. A **804**, 322 (2008).

[18] M.M. Sharma, M.A. Nagarajan, P. Ring, Phys. Lett. B **312**, 377 (1993).

[19] Y. Sugahara, H. Toki, Nucl. Phys. A **579**, 557 (1994).

[20] O. Hashimoto, H. Tamura, Prog. Part. Nucl. Phys. **57**, 564 (2006).

[21] H. Takahashi *et al.*, Phys. Rev. Lett. **87**, 212502 (2001).

[22] P. Khaustov *et al.*, Phys. Rev. **61**, 054603 (2000).

[23] A. Martinez Torres, K.P. Khemchandani, E. Oset, Eur. Phys. J. A **36**, 211 (2008).

[24] R. Kamiński, G. Mennessier, S. Narison, Phys. Lett. B (in press), arXiv:0904.2555 [hep-ph].

[25] D. Jido, Y. Kanada-En'yo, Phys. Rev. C **78**, 035203 (2008).

[26] A. Martinez Torres, K.P. Khemchandani, E. Oset, Phys. Rev. C **79**, 065207 (2009); A. Martinez Torres, K.P. Khemchandani, U.-G. Meißner, E. Oset, arXiv:0902.3633 [nucl-th].

[27] B.D. Kaplan, A.E. Nelson, Phys. Lett. B **175**, 57 (1986); **B179**, 409 (1986).

Published in Physical Review C 84 (2011) 045206

K^- nuclear potentials from in-medium chirally motivated models

A. Cieplý[1], D. Gazda[1], E. Friedman[2], A. Gal[2], J. Mareš[1]

[1]*Nuclear Physics Institute, 25068 Řež, Czech Republic*

[2]*Racah Institute of Physics, The Hebrew University, Jerusalem 91904, Israel*

Abstract

A self consistent scheme for constructing K^- nuclear optical potentials from subthreshold in-medium $\bar{K}N$ s-wave scattering amplitudes is presented and applied to analysis of kaonic atoms data and to calculations of K^- quasibound nuclear states. The amplitudes are taken from a chirally motivated meson-baryon coupled-channel model, both at the Tomozawa-Weinberg leading order and at the next to leading order. Typical kaonic atoms potentials are characterized by a real part $-\mathrm{Re}\,V_{K^-}^{\mathrm{chiral}} = 85 \pm 5$ MeV at nuclear matter density, in contrast to half this depth obtained in some derivations based on in-medium $\bar{K}N$ threshold amplitudes. The moderate agreement with data is much improved by adding complex ρ- and ρ^2–dependent phenomenological terms, found to be dominated by ρ^2 contributions that could represent $\bar{K}NN \to YN$ absorption and dispersion, outside the scope of meson-baryon chiral models. Depths of the real potentials are then near 180 MeV. The effects of p-wave interactions are studied and found secondary to those of the dominant s-wave contributions. The in-medium dynamics of the coupled-channel model is discussed and systematic studies of K^- quasibound nuclear states are presented.

1 Introduction

A key issue in studying in-medium K^- meson interactions concerns the strength of the attractive K^- nuclear potential [1]. Related topical questions involve (i) the underlying free-space $\bar{K}N$ interaction and whether or not it can realistically support K^- nuclear clusters (see Ref. [2] for a recent review), and (ii) the role of K^- mesons in multistrange self-bound matter [3] and in compact stars [4]. An order of magnitude estimate of the nuclear potential V_{K^-} is provided by the leading-order (LO) Tomozawa-Weinberg (TW) vector term of the chiral effective meson-baryon Lagrangian [5] which in the Born approximation gives

$$V_{K^-} = -\frac{3}{8f_\pi^2}\,\rho \approx -57\,\frac{\rho}{\rho_0} \quad \text{(in MeV)}, \tag{1}$$

where ρ is the nuclear density, $\rho_0 = 0.17$ fm^{-3}, and $f_\pi \approx 93$ MeV is the pion decay constant. This attraction is doubled, roughly, within chirally based coupled-channel $\bar{K}N$–$\pi\Sigma$–$\pi\Lambda$ calculations that produce dynamically a $\bar{K}N$ quasibound state loosely identified with the $\Lambda(1405)$ resonance [6]. Deeper potentials, in the range Re $V_{K^-}(\rho_0) \sim -(150\text{–}200)$ MeV are obtained in comprehensive global fits to K^--atom strong-interaction shifts and widths by introducing empirical density dependent effective K^-N amplitudes [7, 8, 9, 10]. Such strongly attractive potentials are expected to generate K^- nuclear quasibound states which could prove relatively narrow once the strong transition $\bar{K}N \to \pi\Sigma$ becomes kinematically forbidden for binding energies exceeding about 100 MeV, as conjectured by Akaishi and Yamazaki [11]. Experimentally, we mention the K^- quasibound signals claimed for K^-pp [12, 13] at and below the $\pi\Sigma N$ threshold. However, these reported signals are quite broad, at variance with the underlying physics. In contrast to the indications of a deep K^- potential, considerably shallower potentials, Re$V_{K^-}(\rho_0) \sim -(40\text{–}60)$ MeV, are obtained for zero kinetic-energy kaons by introducing self energy (SE) contributions to the in-medium K^-N threshold scattering amplitude, within a self-consistent procedure that includes in particular the potential V_{K^-} thus generated [14, 15].

In a recent Letter [16] we reported on new, self consistent calculations of K^- quasibound states that lead to deep K^- nuclear potentials, considerably deeper than the 'shallow' potentials deduced in Refs. [14, 15]. The basic idea is to identify the K^-N *subthreshold* energy domain required for the construction of V_{K^-}. For kaonic atoms, essentially at the K^- nuclear threshold, this was explored during the 1970s by Wycech [17], Bardeen and Torigoe [18] and Rook [19] who noted the dominance of the subthreshold $\bar{K}N$ quasibound state $\Lambda(1405)$ in causing the in-medium $\bar{K}N$ scattering amplitude to become more attractive as one goes to subthreshold K^-N energies. In our Letter [16] we applied this idea, introducing a new self consistency requirement, to a comprehensive study of kaonic atoms that uses scattering amplitudes derived from a chirally motivated coupled channel meson-baryon Lagrangian [20]. Here we expand on these recent calculations to provide more details on derivation, systematics and results. In addition to the next to leading-order (NLO) model CS30 used in the Letter, in the present work we report on a new LO model TW1 fitted to the new SIDDHARTA values of shift and width of the $1s$ state in the K^- hydrogen atom [21]. The paper is organized as follows: in Sec. 2 we describe a self consistent scheme of handling in-medium subthreshold K^-N scattering amplitudes used in the construction of V_{K^-}. In Sec. 3 we discuss the derivation of in-medium scattering amplitudes in both models TW1 and CS30. Some details are relegated to an Appendix.

In Sec. 4 we discuss kaonic atom calculations, and in Sec. 5 we discuss calculations of K^- nuclear quasibound states. Sec. 6 concludes the work with a brief summary of the main results.

2 Handling K^-N subthreshold amplitudes

In the single-nucleon approximation, the K^- potential in nuclear matter of density ρ is given in terms of the in-medium K^-N scattering amplitude F_{K^-N},

$$V_{K^-} = -\frac{2\pi}{\omega_K}\,(1+\frac{\omega_K}{m_N})\,F_{K^-N}(\vec{p},\sqrt{s};\rho)\,\rho, \tag{2}$$

where $F_{K^-N}(\vec{p},\sqrt{s};\rho\to 0)$ reduces to the free-space two-body K^-N c.m. forward scattering amplitude $F_{K^-N}(\vec{p},\sqrt{s})$ and the nucleon energy E_N is approximated by its mass m_N in the kinematical factor in front of F_{K^-N}. Here, $\vec{p}$ is the relative K^-N momentum and $s=(E_K+E_N)^2-(\vec{p}_K+\vec{p}_N)^2$ is the Lorentz invariant Mandelstam variable s which reduces to the square of the total K^-N energy in the two-body c.m. frame. In the laboratory frame, $E_K=\omega_K$. Before constructing V_{K^-} for use in actual calculations, we need to prescribe how to interpret in Eq. (2) the two-body arguments $\vec{p}$ and $\sqrt{s}$ of the in-medium scattering amplitude. For s-wave amplitudes, the momentum dependence arises through the magnitude p of the relative momentum $\vec{p}$ which near threshold is approximated by

$$\vec{p}=\xi_N\vec{p}_K-\xi_K\vec{p}_N,\quad \xi_{N(K)}=m_{N(K)}/(m_N+m_K). \tag{3}$$

Averaging over angles, the square of $\vec{p}$ assumes the form

$$p^2\to\xi_N\xi_K(2m_K\frac{p_N^2}{2m_N}+2m_N\frac{p_K^2}{2m_K}). \tag{4}$$

For $\sqrt{s}$ we note that $\vec{p}_K+\vec{p}_N=0$ in the two-body c.m. system, but $\vec{p}_K+\vec{p}_N\neq 0$ in the nuclear laboratory system which nearly coincides with the K^-–nucleus c.m. system. Averaging over angles yields $(\vec{p}_K+\vec{p}_N)^2\to(p_K^2+p_N^2)$. Near threshold, neglecting quadratic terms in the binding energies $B_K=m_K-E_K$, $B_N=m_N-E_N$, we have

$$\sqrt{s}\approx E_{\rm th}-B_N-B_K-\xi_N\frac{p_N^2}{2m_N}-\xi_K\frac{p_K^2}{2m_K}, \tag{5}$$

where $E_{\rm th} = m_N + m_K$. To transform the momentum dependence into density dependence, the nucleon kinetic energy $p_N^2/(2m_N)$ is approximated in the Fermi gas model by $T_N(\rho/\rho_0)^{2/3}$, with $T_N = 23.0$ MeV, and the K^- kinetic energy $p_K^2/(2m_K)$ is identified in the local density approximation with $-B_K - {\rm Re}\,\mathcal{V}_{K^-}(\rho)$, where $\mathcal{V}_{K^-} = V_{K^-} + V_c$ and V_c is the K^- finite-size Coulomb potential. Under these approximations, Eqs. (4) and (5) become

$$p^2 \approx \xi_N \xi_K [2m_K T_N (\rho/\rho_0)^{2/3} - 2m_N (B_K + {\rm Re}\,\mathcal{V}_{K^-}(\rho))], \tag{6}$$

where both terms on the r.h.s. are positive for attractive V_{K^-}, and

$$\sqrt{s} \approx E_{\rm th} - B_N - \xi_N B_K - 15.1(\frac{\rho}{\rho_0})^{2/3} + \xi_K {\rm Re}\,\mathcal{V}_{K^-}(\rho) \tag{7}$$

(in MeV), where *all* the terms following $E_{\rm th}$ on the r.h.s. are negative, thus implementing the anticipated downward energy shift into the K^-N subthreshold energy region. Eq. (7) is used in most of the bound state applications below as is, although we also checked the effect of implementing gauge invariance through the substitution $\sqrt{s} \to \sqrt{s} - V_c$. Gauge invariance often is not implemented in the solution of the free-space Lippmann-Schwinger equations of underlying chiral models simply because its effects on the two-body meson-baryon system are negligible.

We note that the K^- nuclear potential V_{K^-} appears as an argument in expressions (6) and (7) for p^2 and $\sqrt{s}$, respectively, which in turn serve as arguments in expression (2) for this same V_{K^-}. This suggests to calculate V_{K^-} self consistently within a scheme in which the downward energy shift into the K^-N subthreshold energy region is density dependent and is controlled by the outcome self-consistent $V_{K^-}(\rho)$. In the corresponding sections below we elaborate on the self consistency scheme which is applied to the solution of the wave equation satisfied by in-medium K^- mesons.

3 In-medium $\bar{K}N$ amplitudes

The synergy of chiral perturbation theory and coupled channel T-matrix resummation techniques provides successful description of $\bar{K}N$ interactions at low energies [2]. In our approach we employ chirally motivated coupled-channel s-wave potentials that are taken

in a separable form,

$$V_{ij}(p,p';\sqrt{s}) = \sqrt{\frac{1}{2\omega_i}\frac{M_i}{E_i}}\, g_i(p)\, \frac{C_{ij}(\sqrt{s})}{f_\pi^2}\, g_j(p') \sqrt{\frac{1}{2\omega_j}\frac{M_j}{E_j}} \ , \qquad g_j(p) = \frac{1}{1+(p/\alpha_j)^2} \ , \quad (8)$$

with E_i, M_i and ω_i denoting baryon energy, baryon mass and meson energy in the c.m. system of channel i. The coupling matrix C_{ij} is determined by chiral SU(3) symmetry. The parameter $f_\pi \sim 100$ MeV represents the pseudoscalar-meson decay constant in the chiral limit, and the inverse range parameters α_i are fitted to the low energy $\bar{K}N$ data. The indices i and j run over the meson-baryon coupled channels $\pi\Lambda$, $\pi\Sigma$, $\bar{K}N$, $\eta\Lambda$, $\eta\Sigma$ and $K\Xi$, including all their appropriate charge states. Details of the free-space version of this model are given in Ref. [20]. Here we summarize its essential points with emphasis on in-medium modifications.

The chiral symmetry of meson-baryon interactions is reflected in the structure of the C_{ij} coefficients derived directly from the Lagrangian. The exact content of the matrix elements up to second order in the meson c.m. kinetic energies was specified already in Ref. [22]. In practice, one often considers only the leading order TW interaction [5] with energy dependence given by

$$C_{ij}(\sqrt{s}) = -C_{ij}^{\rm TW}(2\sqrt{s} - M_i - M_j)/4. \quad (9)$$

The structure constants $C_{ij}^{\rm TW}$ are listed in Ref. [23]. We note that this relativistic prescription differs from the one adopted in models derived from a chiral Lagrangian formulation for static baryons [20, 22] and expanded strictly only to second order in meson energies and quark masses. There, the energy dependence form $(2\sqrt{s} - M_i - M_j)$ is replaced by $(\omega_i' + \omega_j')$ where the primed meson energies ω_j' include a relativistic correction: $\omega_j' = \omega_j + (\omega_j^2 - m_j^2)/(2M_0)$, with m_j denoting the meson mass in channel j and where M_0 is the baryon mass in the chiral limit. In principle, approaches based on different formulations of the chiral Lagrangian should give identical results for physical observables. However, this is true only when one sums up an infinite series of relevant Feynman diagrams to all orders in q, and need not hold at a given perturbative order. In other words, models based on different Lagrangian formulations, or models that differ from each other in prescribing how to treat terms beyond leading order, may give within reasonable limits different predictions for physical observables.

The scattering amplitudes corresponding to the separable potentials (8) are also of a

separable form

$$F_{ij}(p,p';\sqrt{s}) = g_i(p) f_{ij}(\sqrt{s}) g_j(p'), \tag{10}$$

with the same form factors $g_i(p)$ and $g_j(p')$, and where the *reduced* scattering amplitude f_{ij} is given explicitly by

$$f_{ij}(\sqrt{s}) = -\frac{1}{4\pi f_\pi^2}\sqrt{\frac{M_i M_j}{s}}\left[(1 - C(\sqrt{s})\cdot G(\sqrt{s}))^{-1}\cdot C(\sqrt{s})\right]_{ij} \ . \tag{11}$$

Here the meson-baryon propagator $G(\sqrt{s})$ is diagonal in the channel indices i and j. When the elementary $\bar{K}N$ system is submerged in the nuclear medium one has to consider Pauli blocking and self energies (SE) generated by the interactions of mesons and baryons with the medium. Thus, the propagator $G(\sqrt{s})$ and the reduced amplitudes $f_{ij}(\sqrt{s})$ become dependent on the nuclear density ρ. The intermediate state Green's function is calculated as

$$G_i(\sqrt{s};\rho) = \frac{1}{f_\pi^2}\frac{M_i}{\sqrt{s}}\int_{\Omega_i(\rho)}\frac{d^3\vec{p}}{(2\pi)^3}\frac{g_i^2(p)}{p_i^2 - p^2 - \Pi_i(\omega_i, E_i, \vec{p};\rho) + \mathrm{i}0} \ . \tag{12}$$

Here $\vec{p_i}$ is the on-shell c.m. momentum in channel i and the integration domain $\Omega_i(\rho)$ is limited by the Pauli principle in the $\bar{K}N$ channels. Included in the denominator of the Green's function (12) is the sum Π_i of meson and baryon self energies in channel i. In particular the kaon SE $\Pi_K = 2\omega_K V_{K^-}$, which serves as input in Eq. (12) and therefore also in Eq. (11) for the output reduced amplitude f_{K^-N}, requires by Eq. (2) the knowledge of this same output f_{K^-N}. This calls for a *self consistent* solution of the in-medium reduced scattering amplitudes $f_{ij}(\sqrt{s},\rho)$ as was first suggested by Lutz [24]. In the present calculation, following Ref. [15], the baryon and pion self energies were approximated by momentum independent potentials $V = V_0\,\rho/\rho_0$ with real and imaginary parts of V_0 chosen consistently from mean-field potentials used in nuclear structure calculations and in scattering calculations, respectively. Specifically, we adopted $V_0^\pi = (30 - \mathrm{i}10)$ MeV, $V_0^\Lambda = (-30 - \mathrm{i}10)$ MeV, $V_0^\Sigma = (30 - \mathrm{i}10)$ MeV and $V_0^N = (-60 - \mathrm{i}10)$ MeV.

The free parameters of the separable-interaction chiral models considered in Ref. [20] and in the present work were fitted to the available experimental data on low energy $\bar{K}N$ interactions, consisting of K^-p low-energy cross sections for elastic scattering and reactions to the $\bar{K^0}n$, $\pi^+\Sigma^-$, $\pi^-\Sigma^+$, $\pi^0\Lambda$ and $\pi^0\Sigma^0$ channels (as listed in Ref. [22]). In addition, the accurately determined K^-p threshold branching ratios γ, R_c, R_n [25] provide a rather strict test for any quantitative model. Another stringent test is provided by the recent SIDDHARTA measured values ΔE_{1s} and Γ_{1s} of the K^-–hydrogen atom $1s$ level shift and

Table 1: K^-p threshold observables calculated in several free-space LO coupled-channel chiral models. The K^-–hydrogen atom $1s$ shift ΔE_{1s} and width Γ_{1s} (in eV) marked by asterisks were obtained from the calculated K^-p scattering length by means of a modified Deser-Trueman relation [26] and are compared to the SIDDHARTA measured values [21]. The K^-p threshold branching ratios γ, R_c, R_n are from Ref. [25]. The last two columns list the calculated $I = 0$ S-matrix pole positions z_1, z_2 (in MeV) on the $[-,+]$ second Riemann sheet of the complex energy plane.

	ΔE_{1s}	Γ_{1s}	γ	R_c	R_n	z_1	z_2
TW1	323	659	2.36	0.636	0.183	(1371,−54)	(1433,−25)
JOORM [27]	275*	586*	2.30	0.618	0.257	(1389,−64)	(1427,−17)
HW [28]	270*	570*	1.80	0.624	0.225	(1400,−76)	(1428,−17)
exp.	283	541	2.36	0.664	0.189	–	–
error (±)	42	111	0.04	0.011	0.015	–	–

width [21].

In the present work we focus on a separable-interaction LO chiral model marked TW1, constructed by fitting just two parameters to the data, $f_\pi = 113 \pm 2$ MeV for the PS meson decay constant and $\alpha = 701 \pm 20$ MeV for the common inverse range parameter, both within one's theoretical expectations. Some characteristics of the TW1 model in comparison to other LO models are listed in Table 1. These LO models include only the leading TW interaction [5], with interchannel couplings given by Eq. (9). Also listed in the table are the positions z_1, z_2 of the two $I = 0$ S-matrix poles that reside on the second Riemann sheet $[-,+]$ of the complex energy manifold, where the signs are those of the imaginary parts of the c.m. momenta in the $\pi\Sigma$ and $\bar{K}N$ channels, respectively. Their origin may be traced to poles in decoupled $I = 0$ channels, a $\pi\Sigma$ resonance pole $z_1^{(0)}$ and a $\bar{K}N$ quasibound state pole $z_2^{(0)}$. The $\pi\Sigma$–$\bar{K}N$ interchannel coupling moves the poles away from their zero-coupling position, the precise full-coupling position exhibiting some model dependence. It is remarkable that all the LO TW models listed in the table are in close agreement on the position of the upper pole z_2. This agreement is spoiled when NLO corrections that require additional low energy constants to be fitted to the experimental data are included in the interchannel couplings. In contrast, the position of the lower pole z_1 exhibits model dependence already in TW models. Generally, it is located much further away from the real axis than the pole z_2. The pole z_2 is usually relegated to the subthreshold behavior of the K^-p amplitude and to the $\Lambda(1405)$ resonance observed in the $\pi\Sigma$ mass spectrum in $\bar{K}N$ initiated reactions. Nuclear medium effects on the poles z_1, z_2 are discussed in the Appendix.

In Fig. 1 we show the energy dependence of the reduced elastic scattering amplitudes f_{K^-p} and f_{K^-n} in model TW1 in free space and for two versions of in-medium modifications (marked 'with' and 'without' SE). Recall that $f_{K^-p} = \frac{1}{2}(f_{\bar{K}N}^{I=0} + f_{\bar{K}N}^{I=1})$ is affected by the subthreshold $I = 0$ $\Lambda(1405)$ resonance, whereas $f_{K^-n} = f_{\bar{K}N}^{I=1}$ is not affected. Indeed, the free-space amplitudes, in dashed lines, exhibit a marked difference between K^-p and K^-n, with the former amplitude showing a typical resonance structure. The pronounced peak in Im f_{K^-p} and the change of sign in Re f_{K^-p} point to the existence of a quasibound state generated by the $I = 0$ $\bar{K}N$ interaction closely below the K^-p threshold. In contrast, the pure $I = 1$ K^-n amplitude displays hardly any energy dependence besides a smooth and slow decrease of the imaginary part upon going to subthreshold energies where phase space cuts it down. The free-space K^-n interaction is weakly attractive and its in-medium renormalization, given by the other curves on the right-hand panels, is rather weak and exhibits little density dependence, in clear distinction to the in-medium effect on the K^-p amplitudes shown on the left-hand panels. Here, in-medium Pauli blocking moves the K^-p free-space resonance structure to higher energies, as demonstrated by the dot-dashed lines (marked 'without SE') in the left panels of the figure which correspond to nuclear matter density $\rho_0 = 0.17$ fm^{-3}. The TW1 results obtained here with Pauli blocking fully agree with those obtained long ago by Waas, Kaiser, Weise [6] and which are recoverable upon switching on their parameter set in our chiral formulation. In contrast, a very different pattern was presented by Ramos and Oset [14], most likely due to their on-shell treatment of the intermediate state propagator and the inclusion of a "nucleon hole" term.

The effect of combined Pauli blocking and hadron SE on the K^-p amplitude is shown by the solid lines (marked 'with SE') in Fig. 1. The real part of the amplitude remains positive (attractive) in the whole energy range, in agreement with phenomenological analyses of kaonic atoms [7], while the peak of the imaginary part moves back to approximately where it was in the free-space amplitude. The most striking feature of the model is the sharp increase in the real part of the amplitude when going to subthreshold energies, caused mainly by the introduction of kaon self energy in the propagator (12) which is responsible for moving the resonant structure related to the $\Lambda(1405)$ back below the $\bar{K}N$ threshold. Consequently, the K^-p interaction becomes much stronger at energies about 30 MeV below the K^-p threshold with respect to its strength at threshold. This feature is missing in the in-medium calculations of Ref. [14] which get substantially different results than ours already when only Pauli blocking is accounted for.

Although the simple LO TW1 model was used to demonstrate the nuclear medium

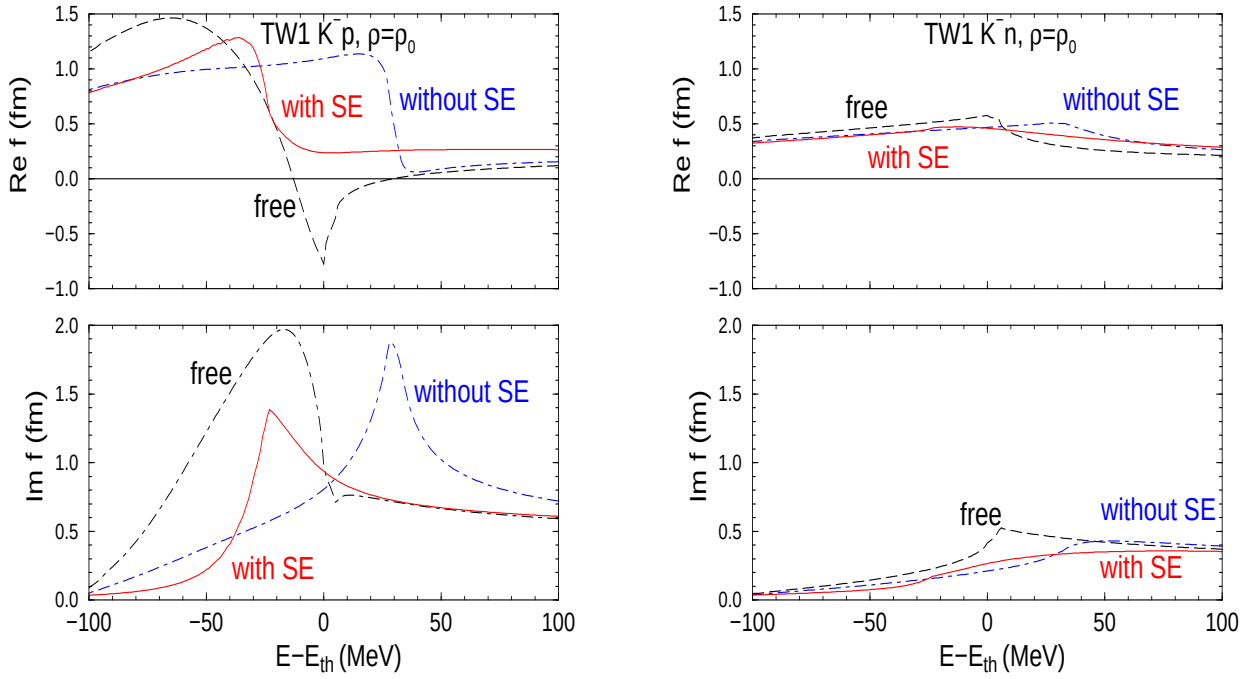

Figure 1: (Color online) Energy dependence of the c.m. reduced amplitudes f_{K^-p} (left panels) and f_{K^-n} (right panels) in model TW1. The upper and lower panels refer to the real and imaginary parts of f, respectively. Dashed curves: free space, dot-dashed: Pauli blocked amplitude (without SE) at $\rho = \rho_0$, solid curves: including meson and baryon self energies (with SE) at $\rho = \rho_0$.

effect on the K^-p interaction in Fig. 1, the same pattern is obtained within the NLO CS30 model of Ref. [20]. This is demonstrated in Fig. 2 where in-medium 'with SE' K^-p reduced scattering amplitudes generated in these two models are compared to each other at $\rho = \rho_0$. The differences between the two sets of curves are seen to be minute.

To end this section we show in Fig. 3, for model TW1, the reduced scattering amplitude corresponding to the interaction of K^- mesons with symmetric nuclear matter,

$$f_{K^-N}(\sqrt{s},\rho) = \frac{1}{2}[\, f_{K^-p}(\sqrt{s},\rho) + f_{K^-n}(\sqrt{s},\rho)\,], \tag{13}$$

where $f_{K^-N}(\sqrt{s},\rho=0) \equiv f_{K^-N}(\sqrt{s})$. The free-space amplitude $f_{K^-N}(\sqrt{s})$, for $\rho = 0$, is marked by dashed lines. Its imaginary part peaks about 15 MeV below the $\bar{K}N$ threshold, and its real part rapidly varies there from weak attraction above to strong attraction below threshold. While $f_{K^-N}(\sqrt{s})$ at and near threshold is constrained by data that serve to determine the parameters of the chiral model, the extrapolation to the subthreshold region may suffer from ambiguities depending on the applied model [2]. Also shown in Fig. 3

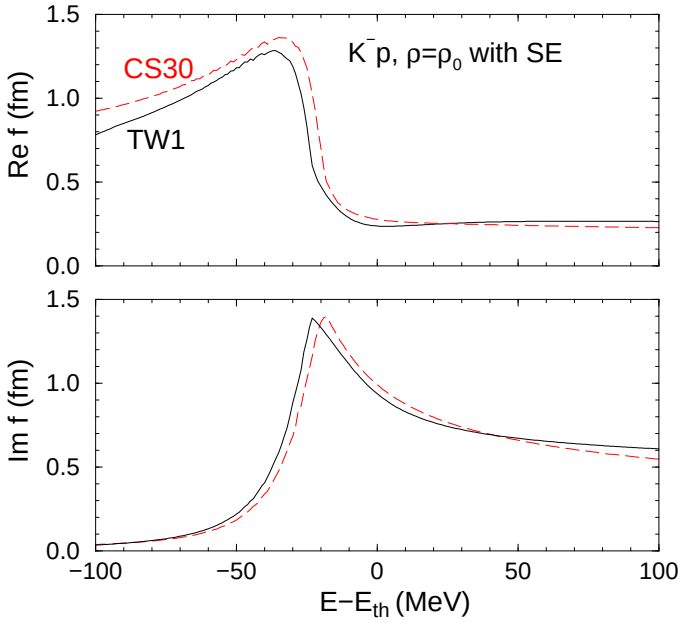

Figure 2: (Color online) Energy dependence of the in-medium c.m. reduced amplitude f_{K^-p} at nuclear matter density ρ_0 in models TW1 (solid lines) and CS30 (dashed lines). The calculations include Pauli blocking and self energies.

are two versions of in-medium reduced amplitudes $f_{K^-N}(\sqrt{s}, \rho = 0.5\rho_0)$. One version, in dot-dashed lines (marked 'without SE'), implements Pauli blocking in the intermediate $\bar{K}N$ states for $\rho \neq 0$. The resulting f_{K^-N} exhibits a resonance-like behavior about 20 MeV above threshold, in agreement with Ref. [6]. The other in-medium version, in solid lines (marked 'with SE'), adds self consistently meson and baryon self energies in intermediate states, as explained earlier. The resulting in-medium f_{K^-N} is strongly energy dependent, with a resonance-like behavior about 35 MeV below threshold. Similar results are obtained at full nuclear matter density $\rho_0 = 0.17$ fm^{-3}. We note that whereas the two in-medium reduced amplitudes shown in the figure are close to each other far below and far above threshold, they differ substantially at and near threshold. This applies also to the full amplitudes F_{K^-N}, Eq. (10), since the form factors $g(p)$ remain the same in the transition from free-space to in-medium separable amplitudes. At threshold, in particular, the real part of the 'with SE' amplitude is about half of that 'without SE', corresponding to a depth $-\mathrm{Re}\, V_{K^-}(\rho_0) \approx 40$ MeV, in rough agreement with Ref. [14].

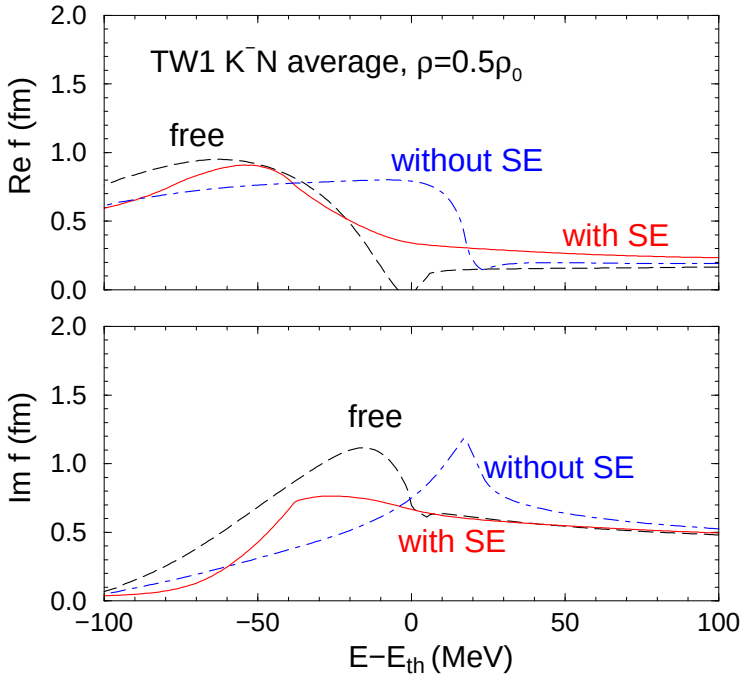

Figure 3: (Color online) Energy dependence of the c.m. reduced amplitude f_{K^-N} (13) in model TW1 below and above threshold. Dashed curves: in free-space; dot-dashed curves: Pauli blocked amplitude at $0.5\rho_0$; solid curves: including meson and baryon self energies at $0.5\rho_0$.

4 K^- atom calculations

Strong interaction level shifts and widths in kaonic atoms have been for decades a source of precise data on the K^- nuclear interaction near threshold. Particularly instructive are so-called 'global' analyses when data for many nuclei across the periodic table are being analyzed together, usually with the help of optical potentials which are related to the nuclear densities [10]. This type of analyses could reveal characteristic features of the interaction which, in turn, reflect on the underlying K^-N interaction in the medium, for example, its energy and density dependence. It was shown already in 1993 [7] that with density-dependent empirical amplitudes within a '$t\rho$' approach to the optical potential, very good fits to the data were possible. Depths of the real potential were close to 180 MeV whereas fixed-t models achieved inferior fits and the resulting potentials were half as deep. Later predictions of in-medium chiral models *at threshold* [14] presented depths of only 50 MeV for the real potential at full nuclear density. This wide span of values has been termed the 'deep *vs.* shallow' controversy in kaonic atoms [29]. While attention has been

focused on depths of the potentials, little attention was paid to the other empirical finding [7], namely, that the best-fit real potentials were not only deep but also *'compressed'* relative to the corresponding nuclear densities, with r.m.s. radii smaller than the nuclear r.m.s. radii. This feature means that the real part of the underlying K^--bound nucleon interaction increases with density, and it is shown below to be in line with the density dependence of the chiral model in-medium amplitudes employed in the present work.

4.1 Wave equation

The choice of K^- wave equation follows naturally from the in-medium dispersion relation

$$\omega_K^2 - \vec{p}_K^{\,2} - m_K^2 - \Pi_K(\vec{p}_K, \omega_K, \rho) = 0, \tag{14}$$

where $\Pi_K(\vec{p}_K, \omega_K, \rho) = 2(\mathrm{Re}\,\omega_K)V_{K^-}$ is the self energy (SE) operator for a K^- meson with momentum $\vec{p}_K$ and energy ω_K [30]. The Klein-Gordon (KG) dispersion relation (14) leads in hadronic atoms applications to a KG equation satisfied by the K^- wavefunction [10]:

$$[\,\nabla^2 - 2\mu(\mathcal{B}_K + V_c) + (V_c + \mathcal{B}_K)^2 + 4\pi(1 + \frac{A-1}{A}\frac{\mu}{m_N})F_{K^-N}(\vec{p}, \sqrt{s}; \rho)\,\rho\,]\,\psi = 0. \tag{15}$$

Here, μ is the K^--nucleus reduced mass, $\mathcal{B}_K = B_K + \mathrm{i}\Gamma_K/2$ is a complex binding energy, including a strong interaction width Γ_K, and V_c is the K^- Coulomb potential generated by the finite-size nuclear charge distribution, including vacuum-polarization terms.

4.2 s waves

The first application of the scheme presented in Sec. 2 for handling K^-N amplitudes below threshold was to global analyses of strong-interaction effects in kaonic atoms. The data base was the same as in Ref. [7] with 65 data points for targets from ^{7}Li to ^{238}U. In solving the KG equation (15), the $\vec{p}_K$ momentum dependence of F_{K^-N} was transformed into density and energy dependence according to Eq. (6). Furthermore, proton and neutron densities were handled separately, replacing $F_{K^-N}(\sqrt{s}, \rho)\rho(r)$ by an effective amplitude

$$\mathcal{F}^{\mathrm{eff}}_{K^-N}(\sqrt{s}, \rho)\rho(r) = F_{K^-p}(\sqrt{s}, \rho)\rho_p(r) + F_{K^-n}(\sqrt{s}, \rho)\rho_n(r), \tag{16}$$

with ρ_p and ρ_n normalized to Z and N, respectively, and $Z+N = A$. Two-parameter Fermi distributions (2pF) were used for both densities, with ρ_p obtained from the known charge

distribution by unfolding the finite size of the charge of the proton. For ρ_n averages of the 'skin' and 'halo' forms of Ref. [31] were chosen with the difference between r.m.s. radii given by $r_n - r_p = (N-Z)/A - 0.035$ fm. The reduced amplitudes f_{K^-p} and f_{K^-n} were evaluated at $\sqrt{s}$ given by Eq. (7), where the atomic binding energy B_K was neglected with respect to $B_N \approx 8.5$ MeV. A similar approximation was made in Eq. (6) for p^2 when using the form factors $g(p)$ of Eq. (10). The K^--nucleus potentials were calculated by requiring self consistency in solving Eq. (7) with respect to Re V_{K^-}, i.e., the value of Re $V_{K^-}(\rho)$ in the expression for $\sqrt{s}$ and in the form factors g had to agree with the resulting Re $V_{K^-}(\rho)$. That was done at each radial point and for every target nucleus in the data base.

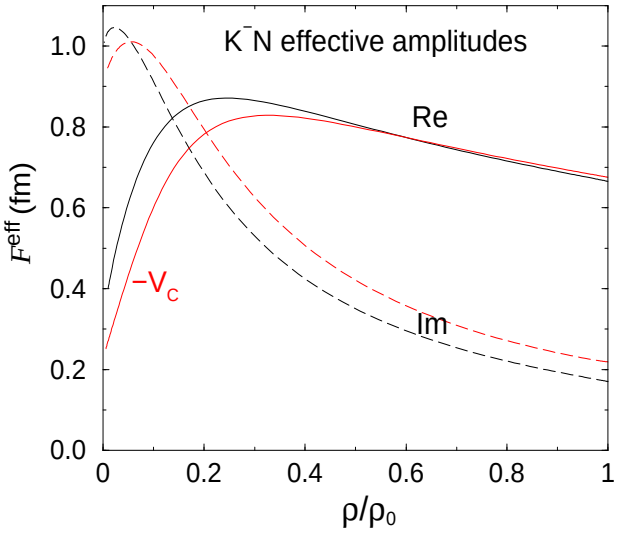

Figure 4: (Color online) Density dependence of the in-medium 'without SE' CS30 self consistent subthreshold amplitude $\mathcal{F}^{\rm eff}_{K^-N}$ for Ni.

It is instructive to start by inspecting the effective amplitudes Eq. (16) obtained in the above self consistent procedure. Figure 4 shows effective amplitudes for K^- on Ni, calculated from the CS30 'without SE' K^-N amplitudes, with and without the $\sqrt{s} \to \sqrt{s} - V_c$ substitution discussed in Sec. 2. The increase of Re $\mathcal{F}^{\rm eff}_{K^-N}(\rho)$ with density over the nuclear surface region combined with the decrease of Im $\mathcal{F}^{\rm eff}_{K^-N}(\rho)$ are the underlying mechanisms behind the compression of the real part and inflation of the imaginary part of best-fit density-dependent phenomenological potentials [7]. Similar results for CS30 amplitudes that include SE were shown in Ref. [16]. Although there are differences in details between the various models, the geometrical implications are robust. The decrease of Im$\mathcal{F}^{\rm eff}_{K^-N}$ with increasing density is unreasonably rapid, originating from the one-nucleon

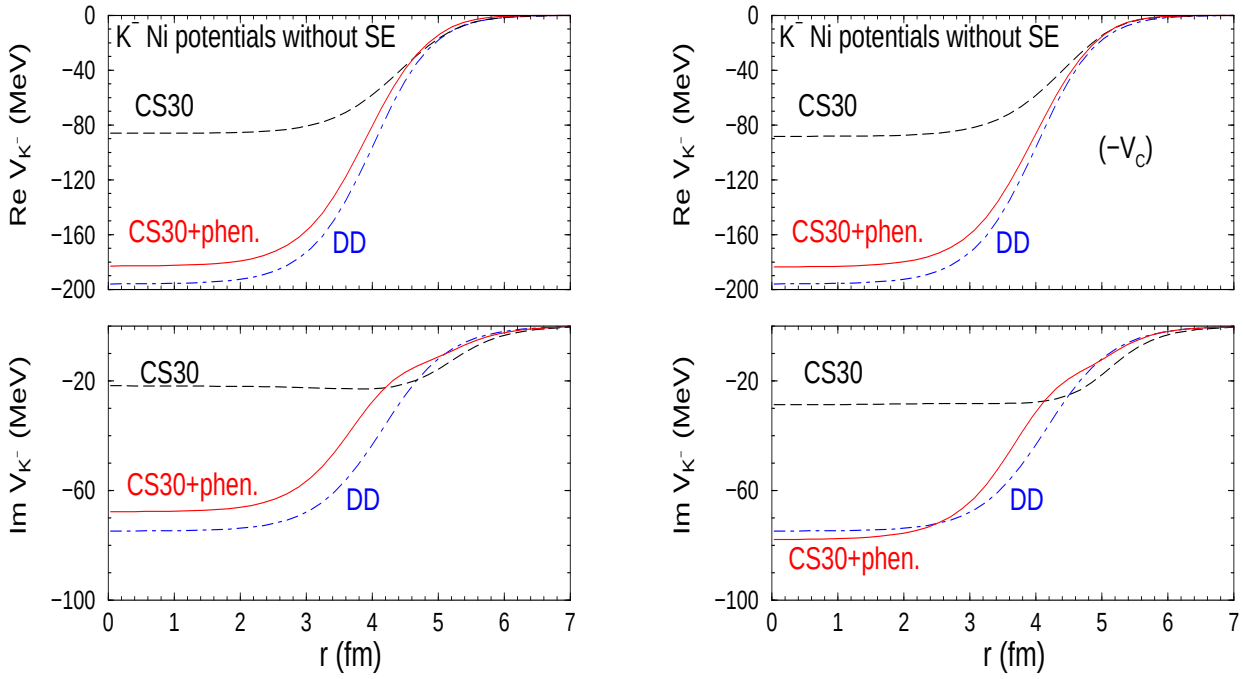

Figure 5: (Color online) Left: K^--nuclear potentials for K^- atoms of Ni. Dashed curves: derived self-consistently from in-medium CS30 amplitudes; solid curves: plus phenomenological terms from global fits; dot-dashed curves: purely phenomenological DD potentials from global fits. Right: the same as on the left, but with the substitution $\sqrt{s} \to \sqrt{s} - V_c$ in $\mathcal{F}^{\rm eff}_{K^-N}(\sqrt{s}, \rho)$.

nature of the CS30 amplitudes, where, as seen in Fig. 3 for the similar TW1 amplitude, the imaginary part practically vanishes around 80 MeV below threshold. We note that multi-nucleon absorption processes which become increasingly important at subthreshold energies are not included in the present approach. Since strong-interaction effects in kaonic atoms are dominated by the widths, the deficiency in the imaginary part of the amplitudes must be reflected when comparing predictions with experiment. This is indeed the case with χ^2 per point of about 10.

Figure 5 shows, as representative examples, several K^-–Ni potentials based on the CS30 'without SE' amplitudes, within the self consistent procedure described above. As a reference, the curves marked DD represent the best fit purely phenomenological density-dependent potentials [7] with $\chi^2 = 103$ for 65 data points. The potential marked CS30 is without any adjustable parameters and it differs substantially from the DD reference potential. Nevertheless its real part of -85 MeV is twice as deep as the shallow potential (not shown here) of Ref. [32] which results from *threshold* values $f_{K^-N}(E_{\rm th}, \rho)$, without

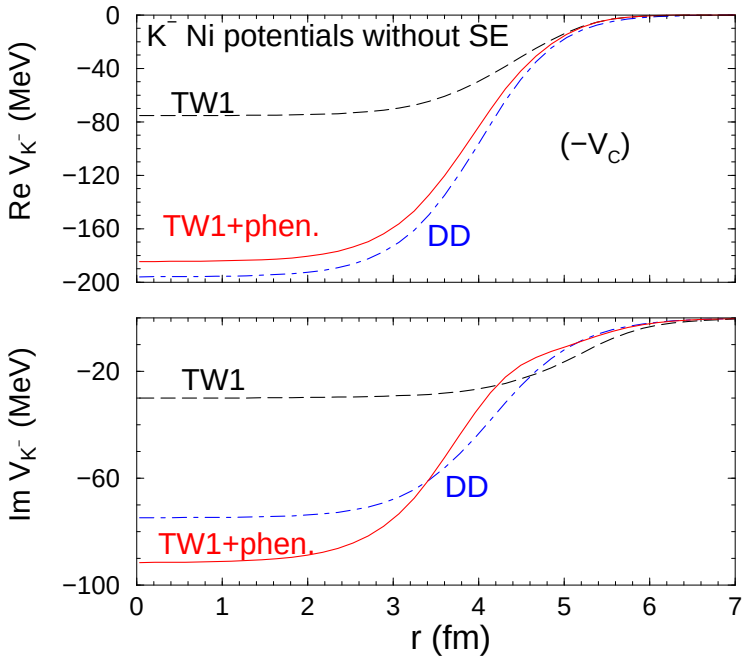

Figure 6: (Color online) K^- nuclear real and imaginary potentials for K^- atoms of Ni. Dashed curves: derived self-consistently from in-medium TW1 amplitudes; solid curves: plus phenomenological terms from global fits; dot-dashed curves: purely phenomenological DD potentials from global fits.

going subthreshold. Figure 5 also demonstrates the effect of adding adjustable ρ and ρ^2 terms to the CS30-based potentials, resulting in best-fit potentials $V_{K^-}^{\rm CS30+phen.}$ with χ^2 of around 130–140 for 65 points, very close to χ^2 values achieved with a fixed-t approach. It is seen that the resulting 'CS30+phen.' potentials are close to the DD ones and we note that the additional terms, both real and imaginary, are dominated by ρ^2 terms which are required by the fit procedure and which are likely to represent $\bar{K}NN$ absorptive and dispersive contributions, respectively. Similar results hold for in-medium TW1 amplitudes, such as shown in Fig. 3. The resulting TW1 K^- nuclear potentials are shown in Fig. 6, exhibiting remarkable similarity to the CS30 K^- nuclear potentials of Fig. 5. We note that the addition of phenomenological terms lowers the resulting χ^2 to as low a value as 124 for 65 data points.

On first sight the additional 'phen.' terms appear large in comparison with the one-nucleon based CS30 and TW1 potentials, particularly if one considers values of the potentials near the nuclear center. However, strong interaction effects in kaonic atoms are sensitive mostly to potential values near the nuclear surface [29], about 3.5 to 5 fm in the

examples shown. It is seen from the figures that over this range of radii the phenomenological part of the imaginary potential is of the order of 30% of the starting values, consistent with the fraction of multi-nucleon absorptions estimated from experiments in emulsion and bubble chambers [33]. By the same token one may safely conclude that the data imply real potentials of depths 80–90 MeV near the half-density radius. Finally a significant observation is that when the CS30 or the TW1 amplitudes are taken *at threshold*, then the additional phenomenological potential is no longer dominated by ρ^2 terms. In particular, *negative* imaginary ρ^2 terms are obtained, thus defying a two-nucleon absorption interpretation. The emerging phenomenology is similar to that for V_{π^-} in pionic atom studies where theoretically motivated single-nucleon contributions are augmented by phenomenological ρ^2 terms representing πNN processes [34]. More work is required to justify microscopically the size of the ρ^2 kaonic atom contributions suggested by successful $V_{K^-}^{\rm chiral+phen.}$ potentials.

4.3 Adding p waves

Next we turn to the question of whether kaonic atom data support contributions from a p-wave term in the K^-N interaction and, for reference, we first checked the effect of including such a phenomenological term in a $t\rho$ potential. A p-wave term was added to the simplest $t\rho$ s-wave potential as follows [10]:

$$2\mu V_{K^-N}(r) = q(r) + \vec{\nabla} \cdot \alpha(r) \vec{\nabla} \tag{17}$$

with $q(r)$ its s-wave part given by

$$q(r) = -4\pi(1 + \frac{\mu}{m_N}) b_0[\rho_n(r) + \rho_p(r)] \tag{18}$$

and the p-wave part given by

$$\alpha(r) = 4\pi(1 + \frac{\mu}{m_N})^{-1} c_0[\rho_n(r) + \rho_p(r)]. \tag{19}$$

Terms proportional to $\rho_n(r) - \rho_p(r)$ are neglected here.

Table 2: Results of $t\rho$ global fits to kaonic atoms data.

χ^2 (N=65)	Re b_0 (fm)	Im b_0 (fm)	Re c_0 (fm^3)	Im c_0 (fm^3)
132	0.60 ± 0.05	0.94 ± 0.05	–	–
110	0.73 ± 0.09	0.59 ± 0.09	−0.79 ± 0.32	0.75 ± 0.30

It is seen from Table 2 that an improved fit to the data is obtained with some of the absorption shifted from the s-wave term into the p-wave term which is repulsive and, thereby, the s-wave attraction required to fit the data is enhanced. However, this could also be just a numerical effect of the χ^2 fit process 'compressing' the real part of the otherwise s-wave $t\rho$ potential, as noted above.

The empirical p-wave term may be compared, for example, with the K^-p p-wave amplitude of Weise and Härtle [30] which is dominated by the $I = 1$ $\Sigma(1385)$ subthreshold resonance. Over the energy range between about 1385 MeV and the K^-N threshold at 1432 MeV the K^-p p-wave amplitude is approximated there by

$$c_{K^-p} = \frac{\sqrt{s}\ \gamma_1}{s_0 - s - \mathrm{i}\sqrt{s}\ \Gamma(\sqrt{s})} + d \tag{20}$$

with $\sqrt{s}_0$=1385 MeV, γ_1=0.42/m_K^3, $\Gamma(\sqrt{s}) \approx 40$ MeV and a background term d=0.06 fm^3. Considering that $c_{K^-n} = 2c_{K^-p}$ for an $I = 1$ dominated amplitude, then for $\rho_p \approx \rho_n$ and neglecting $\rho_n - \rho_p$ terms in the empirical potential, c_{K^-p} is to be multiplied by 3/2 in order to compare with the above c_0. Table 3 shows calculated values for a 'microscopic' $c_0^m = (3/2)c_{K^-p}$ obtained for $\sqrt{s}$ given by Eq. (7), here applied to Ni.

Table 3: Values of a 'microscopic' p-wave amplitude $c_0^m = (3/2)c_{K^-p}$ [see Eq. (20)] to be compared with the empirical c_0 of Table 2.

ρ/ρ_0	$\sqrt{s}$ (MeV)	Re c_0^m (fm^3)	Im c_0^m (fm^3)
0	1432	−0.09	0.08
0.25	1420	−0.12	0.12
0.50	1404	−0.16	0.25
0.75	1392	−0.06	0.44
1.00	1382	0.10	0.49

It is seen that at threshold the empirical c_0 is an order of magnitude too large compared to its 'microscopic' counterpart c_0^m. Averaging over subthreshold energies is unlikely to produce agreement between the two.

The natural next step was to include c_{K^-p} of Eq. (20) in the subthreshold evaluation of the s-wave potential to create also a K^-N-based p-wave potential. This was done at each radial point for the local density and the $\sqrt{s}$ obtained self-consistently for the dominant s-wave potential. Without any adjustable parameters it reduced the CS30-based χ^2 from $\approx$ 10 per point to about 6 per point. Including also two scaling factors, for the resonance part and for the background part of Eq. (20) and searching on these parameters, yielded a scaling

factor -0.025 ± 0.029 for the resonance and 3.5 ± 0.1 for the background, with $\chi^2 \approx 3$ per point. It means that within the subthreshold approach to the K^-N interaction a resonance term in the p-wave interaction is not required to fit the data. This is consistent with the first comprehensive phenomenological analysis of $\bar{K}N$–πY coupled channels by Kim [35], concluding that the $\Sigma(1385)$ is definitely not a p-wave $\bar{K}N$ bound state, but rather a $\pi\Lambda$ scattering resonance with very weak coupling to the $\bar{K}N$ channel. This conclusion was reinforced in a dispersion relation analysis by A.D. Martin [25] in which the $\bar{K}N$ channel coupled very weakly, compatible with zero coupling to the $\Sigma(1385)$ resonance. Finally, the p-wave amplitude c_{K^-p} of Eq. (20) was included in the 'CS30+phen.' fits, where ρ and ρ^2 terms were added to the CS30 potentials. Again the resonance term was found to vanish and only a small p-wave constant background term was acceptable. It is therefore concluded that fits to kaonic atom data do not require a resonant p-wave term within the subthreshold self consistent approach of the present work.

5 Calculations of K^- nuclear quasibound states

Quasibound K^- nuclear states in several nuclei across the periodic table were calculated in Refs. [9, 3] within the relativistic mean field (RMF) model for nucleons and antikaons. The energy independent K^- nuclear real potential $V_{K^-}^{\rm RMF}$ was supplemented in these calculations by a phenomenological '$t\rho$' imaginary potential Im V_{K^-} with energy dependence that accounted for the reduced phase space available for in-medium K^- absorption. Two-nucleon absorption terms were also included.

The present formulation differs fundamentally from these previous RMF calculations in that we use a K^- nuclear potential V_{K^-} given by Eq. (2) in terms of energy and density dependent in-medium K^-N scattering amplitudes $F_{K^-N}(\vec{p}, \sqrt{s}, \rho)$ generated from a well defined coupled-channel chiral model. The momentum dependence of F_{K^-N} was transformed into energy and density dependence using Eq. (6). The in-medium KG dispersion relation (14) leads to a bound-state KG equation satisfied by the K^- wavefunction which is written here in the form

$$\left[\nabla^2 + \omega_K^2 - m_K^2 + 4\pi \frac{\sqrt{s}}{m_N} F_{K^-N}(\sqrt{s}, \rho)\rho\right] \psi = 0, \tag{21}$$

where

$$\omega_K = m_K - \mathcal{B}_K - V_c \,, \tag{22}$$

$\mathcal{B}_K = B_K + \mathrm{i}\Gamma_K/2$ and $\sqrt{s}$ is given by Eq. (7) which now also includes the substitution $\sqrt{s} \to \sqrt{s} - V_c$:

$$\sqrt{s} \approx E_{\rm th} - B_N - \xi_N(B_K + V_c) - 15.1(\frac{\rho}{\rho_0})^{2/3} + \xi_K \mathrm{Re}\, V_{K^-}(\rho). \tag{23}$$

Equation (21) differs from the K^- atom equation (15) by A^{-1} correction terms. Since B_K and $V_{K^-}(\rho)$ appear through Eq. (23) in the argument $\sqrt{s}$ of F_{K^-N} (the latter is essentially V_{K^-}), it suggests a self consistency scheme in terms of *both* B_K and $V_{K^-}(\rho)$ for solving the KG equation (21). In order to study the effect of energy and density dependencies of the argument $\sqrt{s}$ of the chiral K^-N scattering amplitude F_{K^-N}, we first solved the KG equation in a static approximation, switching off the RMF self consistency cycle that accounts for the modification of the nuclear density by the strongly bound K^- meson and its effect on the binding energy B_K. Self consistency with respect to B_K and $V_{K^-}(\rho)$, however, remained operative in the static approximation. Realistic RMF density distributions $\rho(r)$ of the core nuclei were employed.

Table 4: Binding energies B_K and widths Γ_K (in MeV) of $1s$ K^- nuclear quasibound states in several nuclei, calculated using static RMF nuclear densities in Eq. (21) and TW1 chiral amplitudes with (i) $\sqrt{s} = E_{\rm th}$ and (ii) $\sqrt{s}$ from Eq. (23), in both in-medium versions 'no SE' and '+SE'. $K^-NN \to YN$ decay modes are excluded. Results of static RMF calculations of B_K, with a K^- nuclear interaction mediated by vector mesons only, are shown for comparison in the last row.

		^{12}C	^{16}O	^{40}Ca	^{90}Zr	^{208}Pb
$E_{\rm th}$, no SE	B_K	61.1	57.5	83.4	96.0	104.8
	Γ_K	149.1	135.9	150.7	151.2	143.9
$\sqrt{s}$, no SE	B_K	40.9	42.4	58.5	69.5	77.6
	Γ_K	29.4	30.8	23.6	22.4	22.0
$E_{\rm th}$, +SE	B_K	(-0.9)	6.4	25.0	39.0	53.4
	Γ_K	(137.6)	120.2	141.8	141.0	129.1
$\sqrt{s}$, +SE	B_K	42.4	44.9	58.8	68.9	76.3
	Γ_K	16.5	16.2	12.0	11.5	11.3
$V_{K^-}^{\rm RMF}$	B_K	49.1	47.7	60.5	69.6	76.8

In Table 4, we list binding energies B_K and widths Γ_K of $1s$ K^- nuclear quasibound states obtained by solving Eq. (21) self-consistently in several nuclei across the periodic table, using in-medium 'no SE' and '+SE' TW1 subthreshold amplitudes with argument

$\sqrt{s}$ given by Eq. (23) (denoted '$\sqrt{s}$' in the table). These values of B_K and Γ_K are compared to those calculated using threshold amplitudes without undergoing self consistency cycles (denoted '$E_{\rm th}$' in the table). The table illustrates the peculiar role of energy dependence of the $\bar{K}N$ scattering amplitudes. In the 'no SE' case, when the in-medium effects consist only of Pauli blocking, the self consistent calculations with subthreshold amplitudes yield lower B_K values compared to those calculated using threshold amplitudes. In contrast, in the '+SE' case, when hadron in-medium self energies are included, the self consistent calculations with subthreshold amplitudes yield considerably higher B_K values compared to those calculated using threshold amplitudes (in which case the $1s$ state in ^{12}C is even unbound). It is worth noting that the self consistent calculations of B_K give very similar results in the '+SE' version to those in the 'no SE' version, as could be anticipated from the deep-subthreshold portion of the scattering amplitudes shown in Fig. 1. These B_K values are also remarkably close to those calculated within a static RMF approach for nucleons and antikaons, when the K^- nucleus interaction is mediated exclusively by vector mesons with purely vector SU(3) F-type couplings, as shown in the last row of Table 4.

The calculated widths displayed in Table 4 represent only $K^-N \to \pi Y$ decays, accounted for by the coupled-channel chiral model. The widths are very large in both 'no SE' and '+SE' in-medium versions when using threshold amplitudes, and are considerably smaller in the self consistent calculations using subthreshold amplitudes owing to the proximity of the $\pi\Sigma$ thresholds. In this case the '+SE' widths are about half of the 'no SE' widths and approximately 10% of those calculated using threshold amplitudes.

The sensitivity of the calculated K^- binding energies and widths to the specific form of the in-medium subthreshold extrapolation of $\sqrt{s}$ is demonstrated in Fig. 7. Here, $1s$ states in several nuclei are calculated self-consistently in the 'no SE' version within the TW1 model for $\sqrt{s} = E_{\rm th} - B_K$ (dotted line), $\sqrt{s} = E_{\rm th} - B_K - V_c$ (dashed line), $\sqrt{s}$ of Eq. (23) (dot-dashed line), and for the latter $\sqrt{s}$ choice also in the 'SE' version (full line). To lead the eye, each of the four lines connects (B_K, Γ_K) values in different core nuclei using one of the above forms for $\sqrt{s}$. It is seen that the specific form chosen to extrapolate $\sqrt{s}$ has a relatively small effect on the binding energies B_K, which vary within 5 MeV for a particular nucleus. In contrast, the widths are reduced significantly from about 55 ± 10 MeV to 14 ± 3 MeV, when $\sqrt{s}$ is shifted further below threshold and the 'SE' version which incorporates in-medium hadron self energies is applied.

Figure 8 illustrates the model dependence of K^- nuclear quasibound state calculations by showing binding energies and widths of $1s$ states in several nuclei calculated

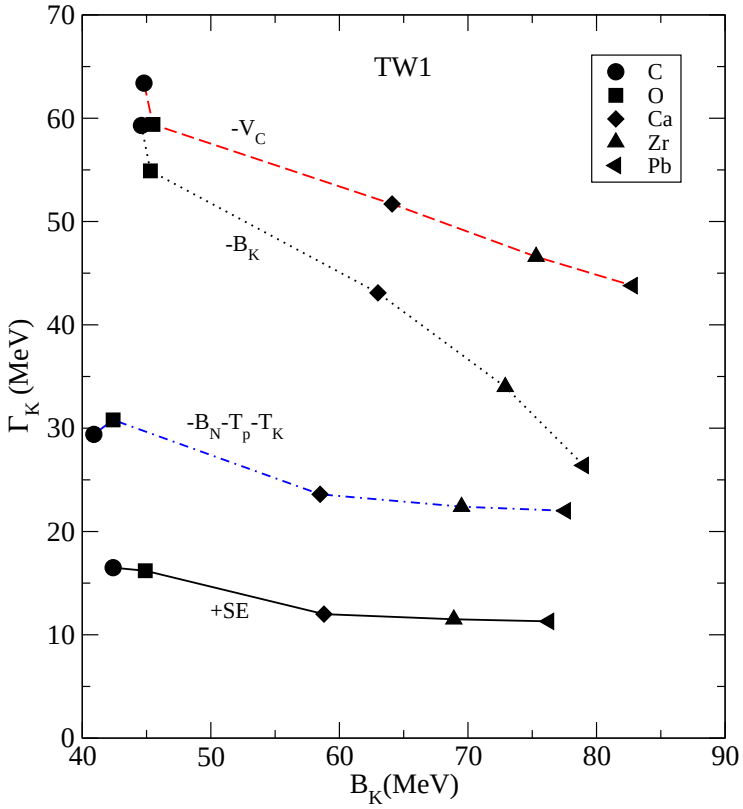

Figure 7: (Color online) Binding energies B_K and widths Γ_K (in MeV) of $1s$ K^- nuclear quasibound states, calculated by applying self-consistently several prescriptions of subthreshold $\sqrt{s}$ extrapolation with static RMF nuclear densities to in-medium TW1 amplitudes ('no SE' unless specified '+SE'). $K^-NN \to YN$ decay modes are excluded.

self-consistently by applying the subthreshold extrapolation $\sqrt{s} = E_{\rm th} - B_K - V_c$ [30] to the TW1 and CS30 in-medium 'no SE' amplitudes. It is seen that the K^- binding energies are more sensitive to the applied chiral model than to the form of subthreshold $\sqrt{s}$ extrapolation exhibited in Fig. 7. However, the difference in widths for a given nucleus is comparable to the differences due to the various forms of subthreshold $\sqrt{s}$ extrapolation shown there. The CS30 model produces higher binding energies and lower values of widths than in the TW1 model, with a difference of approximately 10 MeV. This systematics is explained by the stronger downward energy shift induced in CS30 with respect to TW1.

Effects of including a p-wave $\bar{K}N$ interaction assigned to the $\Sigma(1385)$ subthreshold resonance are demonstrated in Table 5 within the 'no SE' in-medium version of TW1 chiral amplitudes, for two subthreshold $\sqrt{s}$ extrapolations: [WH] denotes the form $\sqrt{s} = E_{\rm th} - B_K - V_c$ which was applied by Weise and Härtle [30] self-consistently to chiral $\bar{K}N$ amplitudes within a local density approximation to calculate K^- nuclear $1s$ quasibound

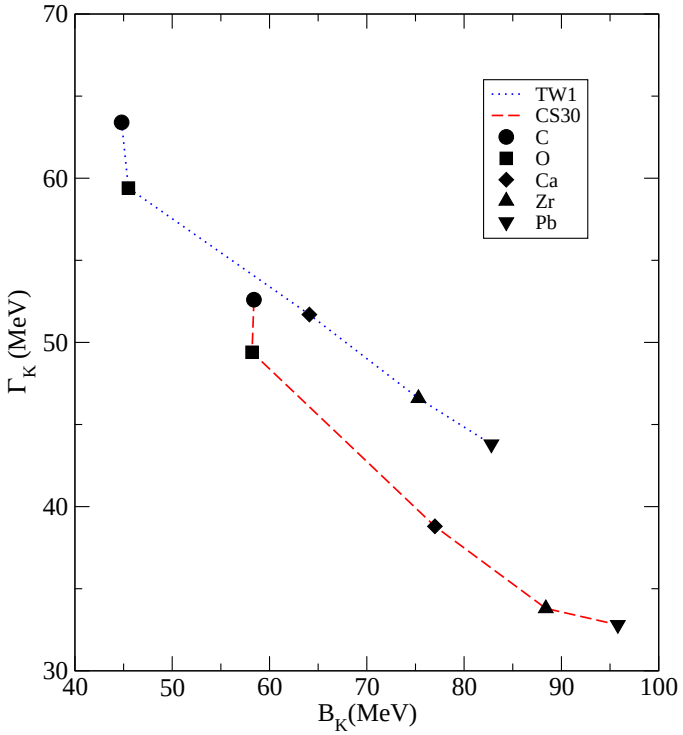

Figure 8: (Color online) Binding energies B_K and widths Γ_K (in MeV) of $1s$ K^- nuclear quasibound states, calculated by applying self-consistently the subthreshold extrapolation $\sqrt{s} = E_{\rm th} - B_K - V_c$ [30] with static RMF nuclear densities to the TW1 and CS30 in-medium 'no SE' amplitudes. $K^-NN \to YN$ decay modes are excluded.

states in ^{16}O and ^{208}Pb; and $\sqrt{s}$ corresponds to the energy argument of Eq. (23). For the p-wave amplitude we adopted the parametrization (20) from Ref. [30], used also in the previous section on kaonic atoms. The calculated binding energies and widths result from a delicate interplay between the energy dependent s-wave and p-wave amplitudes. The effect of p waves is more pronounced in light nuclei where surface contributions are relatively more important, and it decreases with increasing size of the nucleus. The p-wave interaction leads to larger (smaller) widths in the [WH] ($\sqrt{s}$) version and increases the K^- binding energies, with the exception of ^{12}C and ^{16}O in the [WH] subthreshold extrapolation where the substantially increased absorption acts repulsively to reduce B_K.

Table 6 presents binding energies and widths of $1s$ K^- nuclear quasibound states in several nuclei across the periodic table, calculated self-consistently within in-medium versions of CS30 chiral amplitudes. The first two sequences denoted [WH] and $\sqrt{s}$ illustrate the role of subthreshold $\sqrt{s}$ extrapolation which affects particularly the widths Γ_K, in a similar pattern to that already shown for the TW1 model in Table 5. The next three sequences

Table 5: Binding energies B_K and widths Γ_K (in MeV) of $1s$ K^- nuclear quasibound states in several nuclei, calculated self-consistently using static RMF nuclear densities and the in-medium 'no SE' version of TW1 chiral amplitudes with (i) $\sqrt{s} = E_{\rm th} - B_K - V_c$ and (ii) $\sqrt{s}$ from Eq. (23), without and with p-wave amplitudes. $K^-NN \to YN$ decay modes are excluded.

		^{12}C	^{16}O	^{40}Ca	^{90}Zr	^{208}Pb
[WH]	B_K	44.8	45.5	64.1	75.3	82.8
	Γ_K	63.4	59.4	51.7	46.6	43.8
[WH], $+p$ wave	B_K	39.7	43.7	69.1	79.9	87.2
	Γ_K	85.6	73.6	55.5	46.7	44.3
$\sqrt{s}$	B_K	40.9	42.4	58.5	69.5	77.6
	Γ_K	29.4	30.8	23.6	22.4	22.0
$\sqrt{s}$, $+p$ wave	B_K	46.0	46.0	60.8	71.5	79.4
	Γ_K	27.5	29.6	22.4	21.3	21.0

exhibit the effects of successively sophisticating the calculations: first, the in-medium 'no SE' amplitudes are dressed by self energies (denoted '+SE'), bringing the calculated widths further down (and marginally so the binding energies); then, the calculations are made dynamical (denoted '+dyn.') taking into account the polarization of the nuclear core by the strongly bound K^-, which produces higher binding energies B_K and smaller widths Γ_K; and last, energy dependent imaginary ρ^2 terms are added self consistently to simulate two-nucleon $K^-NN \to YN$ absorption modes (denoted '+2N abs.') and their available phase space [9, 3]. Whereas the binding energies decrease insignificantly, the resulting widths of order $\Gamma_K \sim 50$ MeV become comparable in light nuclei to the binding energies B_K.

6 Conclusion

In this work we have used several versions of in-medium $\bar{K}N$ scattering amplitudes constructed in a chirally motivated coupled channel separable potential model to derive self-consistently the K^- nuclear potential for several bound state applications. The $\bar{K}N$ scattering amplitudes exhibit, invariably, a strong energy and density dependence below threshold, which reflects the dominant effect of the $\Lambda(1405)$ subthreshold resonance. This is precisely the energy region relevant for the self consistent construction of V_{K^-} for kaonic atoms and for K^- nuclear quasibound state calculations. It was found that

Table 6: Binding energies B_K and widths Γ_K (in MeV) of $1s$ K^- nuclear quasibound states in several nuclei, calculated self-consistently using in-medium CS30 chiral amplitudes in the 'no SE' version (first two sequences) and in the '+SE' version (last three sequences) for various subthreshold $\sqrt{s}$ extrapolations marked as in Table 5. A combined nucleons+antikaon RMF scheme is applied dynamically in the last two sequences, and $K^-NN \to YN$ decay modes are included in the last sequence ('+2N abs.').

		^{12}C	^{16}O	^{40}Ca	^{90}Zr	^{208}Pb
[WH]	B_K	58.4	58.2	77.0	86.7	95.8
	Γ_K	52.6	49.8	33.8	33.8	32.8
$\sqrt{s}$	B_K	52.0	53.0	69.7	81.5	89.6
	Γ_K	19.6	21.6	14.4	13.6	14.0
+SE	B_K	50.7	52.5	68.2	79.3	86.6
	Γ_K	13.0	12.8	10.9	11.0	10.9
+dyn.	B_K	55.7	56.0	70.2	80.5	87.0
	Γ_K	12.3	12.1	10.8	10.9	10.8
+2N abs.	B_K	54.0	55.1	67.6	79.6	86.3
	Γ_K	44.9	53.3	65.3	48.7	47.3

kaonic atoms probe $\bar{K}N$ c.m. energies typically 30–50 MeV below threshold whereas K^- nuclear $1s$ quasibound states reach considerably lower $\bar{K}N$ subthreshold energies. Thus, the chiral model versions used in the present work produced potential depths in the range $-\mathrm{Re}\, V_{K^-}^{\mathrm{chiral}}(\rho_0) \sim$ 80–90 MeV in kaonic atoms, and somewhat deeper potentials of depths 100–110 MeV for K^- nuclear quasibound states. By comparing the size and shape of our subthreshold $\bar{K}N$ scattering amplitudes with those of other chiral models, as discussed for example in Ref. [28], we expect these results to hold generally in any coupled-channel chiral model constrained by low energy K^-p data once our self consistency construction is applied. The density dependence of the resulting kaonic atom potentials is such that by adding adjustable phenomenological terms to be determined by fits to the data, the real part of the potential becomes twice as deep and the imaginary part about three times as deep due to a ρ^2–dominated complex term which could represent $\bar{K}NN \to YN$ dispersive and absorptive modifications. These substantial modifications at full nuclear density represent extrapolations from the nuclear surface region to which kaonic atoms are mostly sensitive and where such modifications appear more modest. More work is needed to explain the origin and test the existence of the sizable ρ^2 term. Finally, the effects of a p-wave interaction generated by the $\Sigma(1385)$ subthreshold resonance are found secondary

to the effects of the s-wave interaction which is dominated by the $\Lambda(1405)$ subthreshold resonance.

Acknowledgments

Stimulating discussions with Wolfram Weise are gratefully acknowledged. This work was supported by the GACR Grant No. 202/09/1441, as well as by the EU initiative FP7, HadronPhysics2, under Project No. 227431.

Appendix: In-medium pole trajectories in model TW1

The observed properties of in-medium $\bar{K}N$ interaction may be related to the dynamics of the $\Lambda(1405)$ resonance in the nuclear medium. This is demonstrated for model TW1 in Fig. 9 which shows the motion in the complex energy plane of poles related to the $\pi\Sigma$ and $\bar{K}N$ channels upon increasing the nuclear density, including Pauli blocking but disregarding self energy insertions. The lower half of the energy plane, below the real axis, corresponds to the $[-,+]$ Riemann sheet standardly referred to as the second Riemann sheet and accessed from the physical region by crossing the real energy axis in between the $\pi\Sigma$ and $\bar{K}N$ thresholds. The upper half of the energy plane (above the real axis) shows the $[+,-]$ Riemann sheet, the third Riemann sheet, which does not allow for $\bar{K}N$ quasibound interpretation of poles located therein. The pole trajectories shown in the figure were calculated from the free-space pole positions (encircled dots) up to the pole positions at full nuclear density ρ_0. In addition to the two $I = 0$ poles listed and discussed in Table 1 of the main text, each of the decoupled $\pi\Sigma$ and $\bar{K}N$ channels also exhibits an $I = 1$ pole, the one related to $\bar{K}N$ developing into a resonance residing on the $[+,-]$ Riemann sheet and another one related to a $\pi\Sigma$ state residing on the $[-,+]$ Riemann sheet. While the $I = 1$ pole related to $\pi\Sigma$ lies too far from the real energy axis to affect any physical observable, the one related to $\bar{K}N$ is responsible for the peak structure in the real part of the K^-n amplitude near threshold. However, the Riemann sheet location of this pole denies it of any quasibound interpretation. The $I = 1$ poles persist also in the more involved NLO chiral models discussed in Ref. [20].

As expected, the nuclear medium has no significant impact on the position of poles related to the $\pi\Sigma$ channel. On the other hand, both poles related to the $\bar{K}N$ channel move to considerably higher energies as the density increases. The $I = 0$ $\bar{K}N$ pole that affects

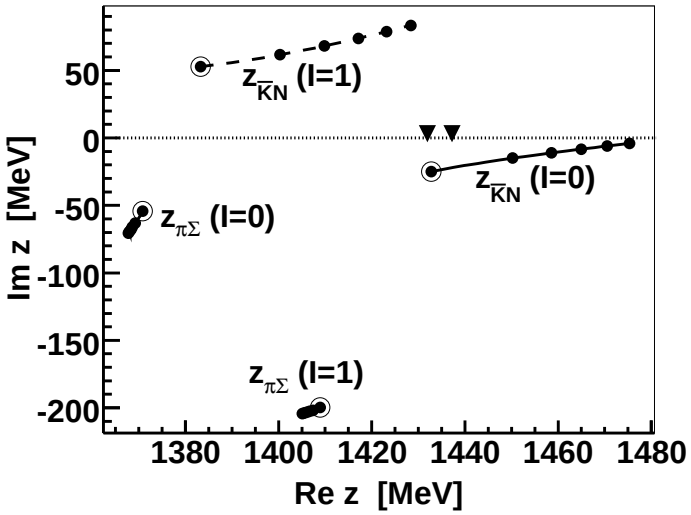

Figure 9: Pole movements on the complex energy manifold due to the increased effect of Pauli blocking in model TW1. $I = 0$ pole trajectories are marked by full lines, $I = 1$ pole trajectories by dashed lines. Pole positions in free space are encircled and the bullets mark pole positions for $\rho = x\rho_0$ for increments of x between 0 to 1, see text for more details. The solid triangles denote the K^-p and $\overline{K}^0 n$ thresholds.

most the $\bar{K}N$ scattering amplitude moves as high as about 1475 MeV, almost reaching the real energy axis. Since the pole is relatively far from the physical region due to the $\bar{K}N$ branch cut, the scattering amplitude exhibits a cusp instead of a proper resonance structure (see the dot-dashed line in Fig. 1 of the main text). When kaon self energy is implemented the pole moves back below the $\bar{K}N$ threshold, residing now in the $[+,-]$ Riemann sheet. Since it remains relatively far from the physical region, one again gets a cusp structure as exhibited by the solid line in Fig. 1.

References

[1] Contributions to *Recent advances in strangeness nuclear physics*, Eds. A. Gal and R.S. Hayano, Nucl. Phys. A **804** (2008) pp. 171-348.

[2] W. Weise, Nucl. Phys. A **835**, 51 (2010), and references therein.

[3] D. Gazda, E. Friedman, A. Gal, and J. Mareš, Phys. Rev. C **76**, 055204 (2007); **77**, 045206 (2008); **80**, 035205 (2009).

[4] J. Schaffner-Bielich, S. Schramm, and H. Stöcker, in *Proc. Int'l. School of Physics "Enrico Fermi", Course **CLXVII***, Eds. M. Anselmino, *et al.* (IOS Press, Amsterdam, 2008) pp. 119–144; F. Özel, G. Baym, and T. Güver, Phys. Rev. D **82**, 101301(R) (2010).

[5] Y. Tomozawa, Nuovo Cimento A **46**, 707 (1966); S. Weinberg, Phys. Rev. Lett. **17**, 616 (1966).

[6] T. Waas, N. Kaiser, and W. Weise, Phys. Lett. B **365**, 12 (1996); **379**, 34 (1996).

[7] E. Friedman, A. Gal, and C.J. Batty, Phys. Lett. B **308**, 6 (1993); Nucl. Phys. A **579**, 518 (1994).

[8] E. Friedman, A. Gal, J. Mareš, and A. Cieplý, Phys. Rev. C **60**, 024314 (1999).

[9] J. Mareš, E. Friedman, and A. Gal, Nucl. Phys. A **770**, 84 (2006).

[10] E. Friedman and A. Gal, Phys. Rep. **452**, 89 (2007).

[11] Y. Akaishi and T. Yamazaki, Phys. Rev. C **65**, 044005 (2002); T. Yamazaki and Y. Akaishi, Phys. Lett. B **535**, 70 (2002).

[12] M. Agnello *et al.* (FINUDA Collaboration), Phys. Rev. Lett. **94**, 212303 (2005).

[13] T. Yamazaki *et al.* (DISTO Experiment), Phys. Rev. Lett. **104**, 132502 (2010).

[14] A. Ramos and E. Oset, Nucl. Phys. A **671**, 481 (2000).

[15] A. Cieplý, E. Friedman, A. Gal, and J. Mareš, Nucl. Phys. A **696**, 173 (2001).

[16] A. Cieplý, E. Friedman, A. Gal, D. Gazda, and J. Mareš, Phys. Lett. B **702**, 402 (2011).

[17] S. Wycech, Nucl. Phys. B **28**, 541 (1971).

[18] W.A. Bardeen and E.W. Torigoe, Phys. Lett. B **38**, 135 (1972).

[19] J.R. Rook, Nucl. Phys. A **249**, 466 (1975).

[20] A. Cieplý and J. Smejkal, Eur. Phys. J. A **43**, 191 (2010).

[21] M. Bazzi *et al.* (SIDDHARTA Collaboration), Phys. Lett. B **704**, 113 (2011), and references therein to previous experiments.

[22] N. Kaiser, P.B. Siegel, and W. Weise, Nucl. Phys. A **594**, 325 (1995).

[23] E. Oset and A. Ramos, Nucl. Phys. A **635**, 99 (1998).

[24] M. Lutz, Phys. Lett. B **426**, 12 (1998).

[25] A.D. Martin, Nucl. Phys. B **179**, 33 (1981), and references therein.

[26] U.-G. Meissner, U. Raha, and A. Rusetsky, Eur. Phys. J. C **35**, 349 (2004).

[27] D. Jido, J.A. Oller, E. Oset, A. Ramos, and U.-G. Meißner, Nucl. Phys. A **725**, 181 (2003).

[28] T. Hyodo and W. Weise, Phys. Rev. C **77**, 035204 (2008).

[29] N. Barnea and E. Friedman, Phys. Rev. C **75**, 022202(R) (2007).

[30] W. Weise and R. Härtle, Nucl. Phys. A **804**, 173 (2008).

[31] A. Trzcińska, J. Jastrzębski, P. Lubiński, F.J. Hartmann, R. Schmidt, T. von Egidy, and B. Kłos, Phys. Rev. Lett. **87**, 082501 (2001).

[32] A. Baca, C. García-Recio, and J. Nieves, Nucl. Phys. A **673**, 335 (2000).

[33] C. Vander Velde-Wilquet, J. Sacton, J.H. Wickens, D.N. Tovee, and D.H. Davis, Nuovo Cimento **39** A, 538 (1977), and references therein.

[34] M. Ericson and T.E.O. Ericson, Ann. Phys. (NY) **36**, 323 (1966). For a recent review see Ref. [10].

[35] J.K. Kim, Phys. Rev. Lett. **19**, 1074 (1967).

Published in Nuclear Physics A 881 (2012) 159

Calculations of K^- nuclear quasi-bound states based on chiral meson-baryon amplitudes

Daniel Gazda and Jiří Mareš

Nuclear Physics Institute, 25068 Řež, Czech Republic

Abstract

In-medium $\bar{K}N$ scattering amplitudes developed within a new chirally motivated coupled-channel model due to Cieplý and Smejkal that fits the recent SIDDHARTA kaonic hydrogen $1s$ level shift and width are used to construct K^- nuclear potentials for calculations of K^- nuclear quasi-bound states. The strong energy and density dependence of scattering amplitudes at and near threshold leads to K^- potential depths $-\mathrm{Re}V_K \approx 80 - 120$ MeV. Self-consistent calculations of all K^- nuclear quasi-bound states, including excited states, are reported. Model dependence, polarization effects, the role of p-wave interactions, and two-nucleon $K^-NN \to YN$ absorption modes are discussed. The K^- absorption widths Γ_K are comparable or even larger than the corresponding binding energies B_K for *all* K^- nuclear quasi-bound states, exceeding considerably the level spacing. This discourages search for K^- nuclear quasi-bound states in any but lightest nuclear systems.

1 Introduction

The study of the interaction of antikaons with baryonic systems, such as kaonic atoms, K^- nuclear clusters or dense strange kaonic matter, is an interesting issue with far-reaching consequences, e.g. for heavy-ion collisions and astrophysics. The closely related problem of K^- nuclear quasi-bound states is far from being settled, despite much theoretical and experimental effort in the last decade [1, 2].

Our first studies of K^- quasi-bound states in nuclear many-body systems based on an extended relativistic mean field (RMF) model were focused on the widths expected for K^- quasi-bound states [3]. The subject of multi-K^- (hyper)nuclei was studied in Refs. [4, 5, 6] with the aim to explore whether kaon condensation could occur in strong-interaction self-bound baryonic matter. In the RMF formulation, the energy independent real K^- nuclear potential was supplemented by a phenomenological imaginary potential fitted to kaonic

atom data, with energy dependence that accounted for the reduced phase space available for in-medium K^- absorption, including 2-nucleon absorption modes.

Weise and Härtle performed calculations of K^- nuclear states in ^{16}O and ^{208}Pb using chiral-model $\bar{K}N$ amplitudes within a local density approximation [7].

This paper reports on our latest calculations of K^- nuclear quasi-bound states within a chirally motivated meson-baryon coupled-channel separable interaction model [8]. We apply a self-consistent scheme for constructing K^- nuclear potentials from subthreshold in-medium $\bar{K}N$ scattering amplitudes which was introduced in Refs. [9, 10]. This time, the $\bar{K}N$ amplitudes are constructed using a recent in-medium coupled channel model NLO30 [11] that reproduces all available low energy $\bar{K}N$ observables, including the latest $1s$ level shift and width in the K^- hydrogen atom from the SIDDHARTA experiment [12]. We demonstrate the crucial role of the strong energy and density dependencies of the K^-N scattering amplitudes, leading to deep K^- nuclear potentials for various considered versions of in-medium modifications of the scattering amplitudes. Using several versions of the chirally motivated coupled-channel model, we demonstrate the model dependence of our calculations. Moreover, we discuss the effects of p-wave interactions and the $K^-NN \to YN$ absorption modes. Finally, we present binding energies and widths of *all* K^- quasi-bound states – including excited states – in selected nuclei.

The paper is organized as follows. In Section 2, we briefly describe the model and underlying self-consistent scheme for constructing K^- nucleus potentials from in-medium subthreshold $\bar{K}N$ scattering amplitudes. In Section 3, we present results of our calculations of K^- quasi-bound states in various nuclei across the periodic table. Conclusions are summarized in section 4.

2 Model

In this section, we briefly outline the methodology which forms the framework of our calculations of K^- nuclear quasi-bound states. We concentrate only on basic ingrediences of the model since the details can be found in Refs. [9, 10, 11].

The K^- nuclear quasi-bound states are determined by self-consistent solution of the in-medium Klein–Gordon equation:

$$\left[\nabla^2 + \tilde{\omega}_K^2 - m_k^2 - \Pi_K(\omega_K, \vec{p}_K, \rho)\right] \phi = 0, \tag{1}$$

where $\tilde{\omega}_K$ is complex energy of antikaon containing the Coulomb interaction V_C introduced

by minimal substitution:

$$\tilde{\omega}_K = \omega_K - \mathrm{i}\Gamma_K/2 - V_C, \tag{2}$$

with Γ_K being the width of K^- nuclear state of energy $\omega_K = m_K - B_K$, where B_K is the binding energy of antikaon. The self-energy operator $\Pi_K = 2(\mathrm{Re}\,\omega_K)V_K$ is constructed in a "$t\rho$" form with the amplitude calculated in a chirally motivated coupled-channel approach:

$$\Pi_K(\omega_K, \vec{p}_K, \rho) = -4\pi\frac{\sqrt{s}}{m_N}\left[F_{K^-p}(\sqrt{s}, \vec{p}, \rho)\rho_p + F_{K^-n}(\sqrt{s}, \vec{p}, \rho)\rho_n\right], \tag{3}$$

where $F_{K^-p(n)}$ is the K^-–proton (neutron) in-medium scattering amplitude in a separable form, $\vec{p}$ is the relative K^-N momentum, and $\sqrt{s}$ is the K^-N total energy. The realistic proton ρ_p and neutron ρ_n density distributions in the core nuclei are taken from relativistic mean-field nuclear-structure calculations. The K^-N scattering amplitudes F_{K^-N} are constructed within a chirally motivated coupled-channel separable interaction model [8]. In this work, we applied the latest version NLO30 [11] which reproduces the recent K^- hydrogen $1s$ level shift and width from the SIDDHARTA experiment [12]. For the sake of comparison, we applied as well the TW1 model [10, 11] fitted also to the SIDDHARTA data, and the older CS30 model [8]. It is to be noted that in the TW1 (NLO30, CS30) model, the effective separable meson-baryon potentials are constructed to match the equivalent amplitudes derived from the chiral effective Lagrangian at leading (next-to-leading) order, respectively.

When the elementary K^-N system is embedded in the nuclear medium of density ρ, one has to consider in-medium modifications of the scattering amplitude, in particular Pauli blocking in the intermediate states (this in-medium version is marked 'no SE') [13]. The other version (marked '+SE') adds self-consistently meson and baryon self-energies generated by the interaction of hadrons with the nuclear medium [14, 15].

Figure 1 illustrates a typical resonance-shape energy dependence of the in-medium reduced [1] scattering amplitudes $f_{K^-N}(\sqrt{s}, \rho) = 1/2[f_{K^-p}(\sqrt{s}, \rho) + f_{K^-n}(\sqrt{s}, \rho)]$ for nuclear matter density $\rho_0 = 0.17$ fm^{-3}, corresponding to the interaction of the K^- meson with symmetric nuclear matter. The amplitudes were calculated within the TW1 and NLO30 models and for each of the models, two in-medium versions, 'no SE' and '+SE', are shown for comparison. The pronounced energy dependence of the scattering amplitude appears crucial in the self-consistent calculations of kaonic nuclear states. In particular, the real part of the '+SE' amplitudes in both models changes from weak attraction at and above

[1] $F_{K^-N} = g(p) f_{K^-N} g(p')$, see Ref. [10]

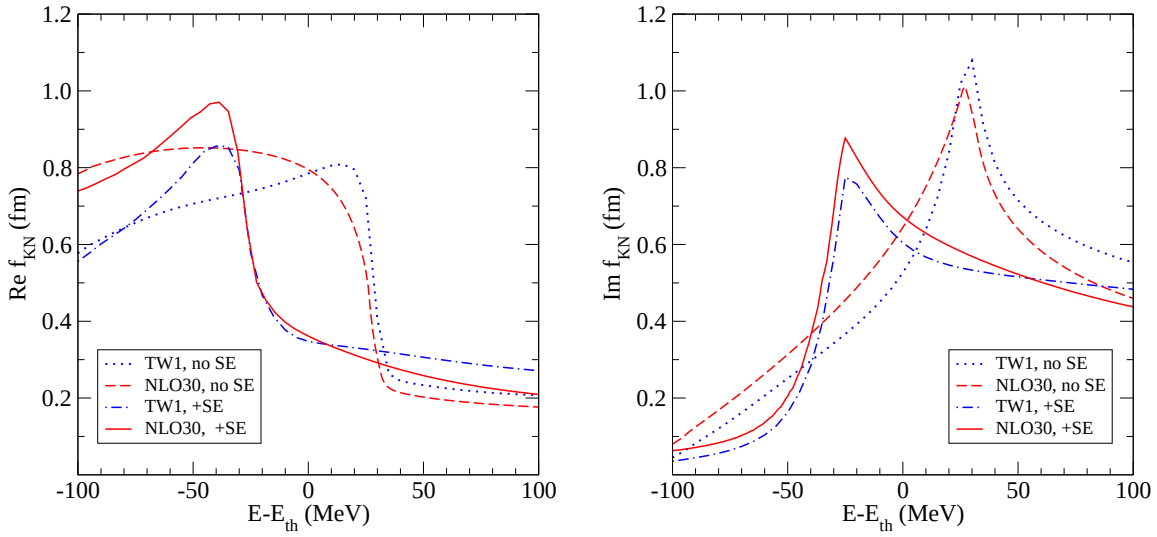

Figure 1: Energy dependence of the c.m. reduced amplitude f_{K^-N} in TW1 and NLO30 models (left: real part, right: imaginary part). Dotted and dashed lines: Pauli blocked amplitude ('no SE') for $\rho_0 = 0.17$ fm^{-3}; solid and dot-dashed lines: including also hadron self-energies ('+SE') at ρ_0.

threshold to strong attraction at $\sim$ 30 MeV below threshold. As a result, the '+SE' and 'no SE' amplitudes become close to each other at energies relevant for self-consistent calculations of kaonic nuclei. While both models give similar imaginary parts Imf_{K^-N} for each in-medium version, they differ considerably ($\approx 20\%$) in real parts of the scattering amplitudes below threshold. This indicates the extent of the model dependence of the calculations of K^- nuclear quasi-bound states.

The scattering amplitude F_{K^-N} in Eq. (3) is a function of K^-N c.m. energy $\sqrt{s}$ and relative momentum $\vec{p}$. For nuclear bound-state applications it is necessary to transform the two-body K^-N arguments into the $\bar{K}$–nuclear c.m. frame. For the relative momentum $\vec{p}$ we have

$$\vec{p} = \xi_N \vec{p}_K - \xi_K \vec{p}_N, \quad \xi_{N(K)} = m_N(K)/(m_N + m_K), \tag{4}$$

which upon averaging over angles yields p^2 of the form

$$p^2 = \xi_N \xi_K \left(2m_K \frac{p_N^2}{2m_N} + 2m_N \frac{p_K^2}{2m_K} \right). \tag{5}$$

Similarly, expanding near threshold energy $E_{\rm th} = m_K + m_p$, $\sqrt{s}$ assumes the form

$$\sqrt{s} \approx E_{\rm th} - B_K - V_C - B_N - \xi_N \frac{p_N^2}{2m_N} - \xi_K \frac{p_K^2}{2m_K}, \tag{6}$$

where B_N stands for the binding energy of nucleon, and the last two terms represent corrections due to the kinetic energies of nucleon and antikaon. The nucleon kinetic energy is approximated in the Fermi gas model $p_N^2/(2m_N) = 23(\rho/\rho_0)^{2/3}$ MeV and the kinetic energy of antikaon is obtained by means of local density approximation $p_K^2/(2m_N) = -B_K - {\rm Re}\,\mathcal{V}_K$, where $\mathcal{V}_K = V_K + V_C$. This finally leads to

$$p^2 \approx \quad \xi_N \xi_K \left[2m_K\, 23\, (\rho/\rho_0)^{2/3} - 2m_N (B_K + {\rm Re}\,\mathcal{V}_K(\rho)) \right] \quad \text{(in MeV)}, \tag{7}$$

$$\sqrt{s} \approx \quad E_{\rm th} - B_N - \xi_N B_K - 15.1 \left(\frac{\rho}{\rho_0} \right)^{2/3} + \xi_K {\rm Re}\mathcal{V}_K(\rho) \quad \text{(in MeV)}. \tag{8}$$

We note that the K^- potential V_K and the K^- binding energy B_K appear as arguments in the expression for $\sqrt{s}$, which in turn serves as an argument for the self-energy Π_K, and thus for V_K. This suggest a self-consistency scheme in terms of both V_K and B_K for solving the Klein-Gordon equation (1).

It is to be stressed that the present chiral model of K^-–nucleus interaction does not account for the absorption of K^- mesons in the nuclear medium through nonpionic conversion modes on two nucleons $K^-NN \to YN$ ($Y = \Lambda, \Sigma$). To estimate the contribution of two-nucleon absorption processes to the decay widths of K^- nuclear states we introduced phenomenological term into the K^- self-energy:

$${\rm Im}\,\Pi_K^{(2N)} = 0.2 f_{YN}(B_K) W_0 \rho^2, \tag{9}$$

where W_0 was fixed by kaonic atom data analysis and $f_{YN}(B_K)$ is kinematical suppression factor taking into account reduced phase space available for decay products of K^- nuclear bound states [3].

The present chiral model also does not address the p-wave part of the K^-–nucleus interaction. Since p-waves may play an important role for tightly bound K^- nuclear systems [16] we studied their contribution by adding the self-energy term:

$$\Pi_K^{(p)} = -4\pi \frac{m_N}{\sqrt{s}} \vec{\nabla} C_{K^-N}(\sqrt{s}) \rho \cdot \vec{\nabla}, \tag{10}$$

with C_{K^-N} p-wave amplitude constrained by the $\Sigma(1385)$ resonance phenomenology and

parametrized following Ref. [7].

3 Results and discussion

We adopted the above methodology to calculations of quasi-bound K^- states in selected nuclei across the periodic table. In most cases, we solved KG equation self-consistently in a static approximation. For the sake of comparison, we performed also fully dynamical calculations upon taking into account the polarization of the nuclear core by the strongly bound antikaon.

Figure 2 shows the K^- nuclear potentials for $1s$ state in Ca at threshold ('$E_{\rm th}$') and for $\sqrt{s}$ (Eq. (8)) calculated self-consistently with respect to ReV_K and B_K, for TW1 amplitudes (upper panels) and NLO30 amplitudes (lower panels). The relevant values of B_K in Ca and other nuclei are presented in the following figures. It is seen that the subthreshold extrapolation $\sqrt{s}$ is crucial for the depth of V_K, calculated using the TW1 amplitude in both 'no SE' and '+ SE' in-medium version. While at threshold the depth of ReV_K in the '+SE' case is about half of the depth in the 'no SE' case, for $\sqrt{s}$ both in-medium versions give a similar depth -Re$V_K(\rho_0) \approx 85 - 90$ MeV. In the case of the NLO30 model, the situation is rather different. While the self-consistent calculation is still important for the depth of ReV_K, evaluated using the '+SE' in-medium modification, in the 'no SE' case, the depths of ReV_K evaluated at threshold and at $\sqrt{s}$ are close to each other. This weak energy dependence of ReV_K has its origin in rather weak energy dependence of the 'no SE' NLO30 scattering amplitude below threshold, as shown in Fig. 1. The NLO30 model yields ~ 20 MeV deeper ReV_K than the TW1 model, as could be anticipated from Fig. 1. The imaginary parts of V_K and consequently the widths which represent only $K^-N \to YN$ decays, are considerably reduced in the self-consistent calculations of the subthreshold amplitudes owing to the proximity of the $\pi\Sigma$ threshold (see both right panels of Fig. 2).

The peculiar role of the energy dependence of the K^-N scattering amplitudes is illustrated for the TW1 model in Fig. 3. Binding energies B_K of $1s$ K^- nuclear quasi-bound states obtained by solving Eq. (1) self-consistently (denoted '$s^{1/2}$') for several nuclei are compared with B_K calculated using threshold amplitudes ($E_{\rm th}$). It is worth noting that the self-consistent calculations of B_K using 'no SE' and '+SE' in-medium amplitudes give very similar results. These B_K values are remarkably close to those calculated within a static RMF approach, when the K^--nucleus interaction is mediated exclusively by vector mesons with purely vector SU(3) F-type couplings (denoted 'RMF') [4]. For comparison,

we present also binding energies B_K calculated self-consistently using the NLO30 '+SE' amplitudes which are more than 10 MeV larger than the corresponding binding energies calculated using the TW1 amplitudes.

Figure 4 shows the effect of particular hadron self-energies in the intermediate states on the K^- binding energies B_K and widths Γ_K, calculated self-consistently within the NLO30 model. The widths Γ_K are plotted as function of B_K for various options of implementation

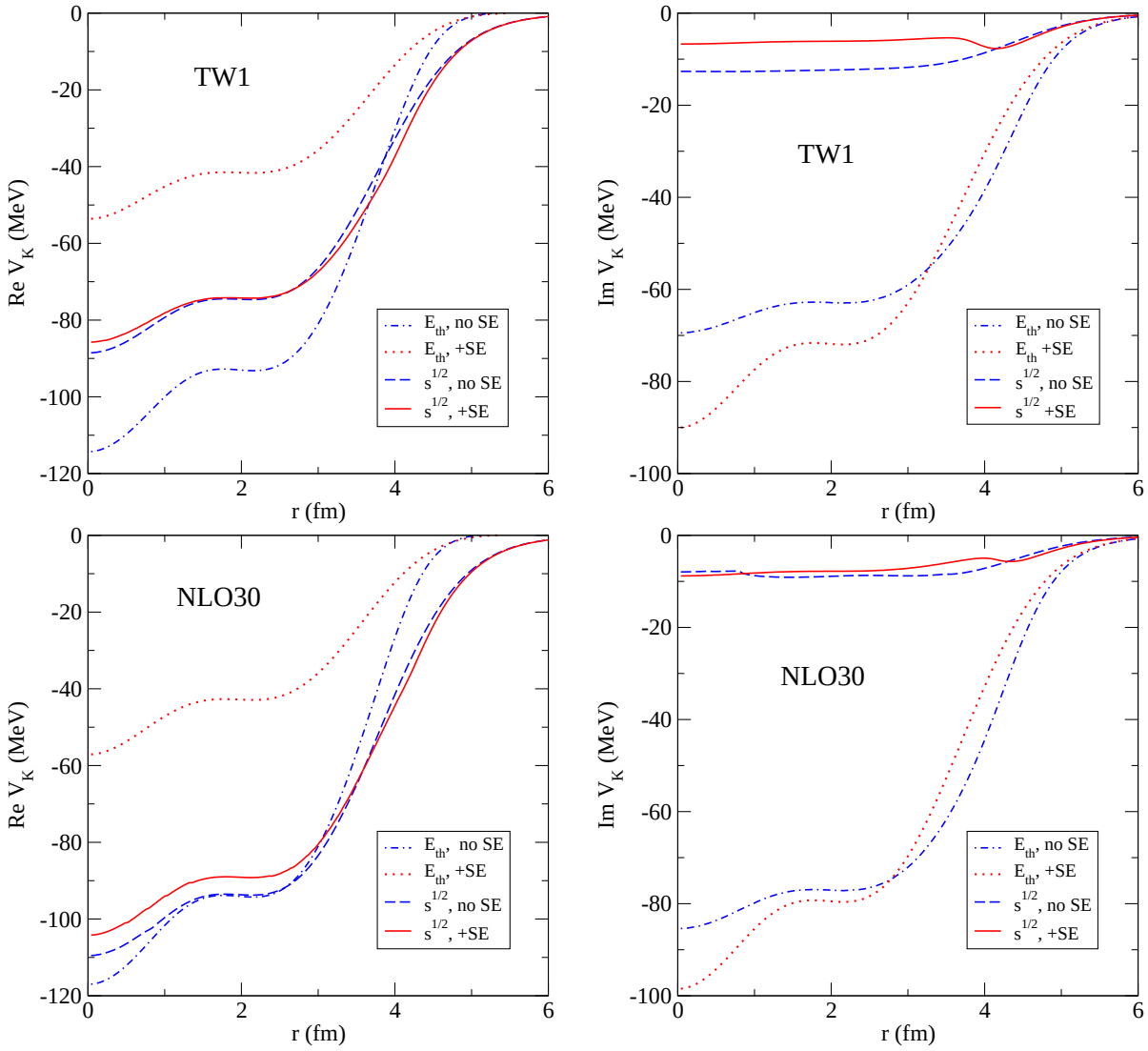

Figure 2: K^- nuclear potentials in Ca (left: real part, right: imaginary part), calculated with static RMF nuclear densities and chiral amplitudes (upper panels: TW1, lower panels: NLO30) at threshold ('$E_{\rm th}$') and with $\sqrt{s}$, in both in-medium versions: only Pauli blocking ('no SE') and including also hadron self-energies ('+SE').

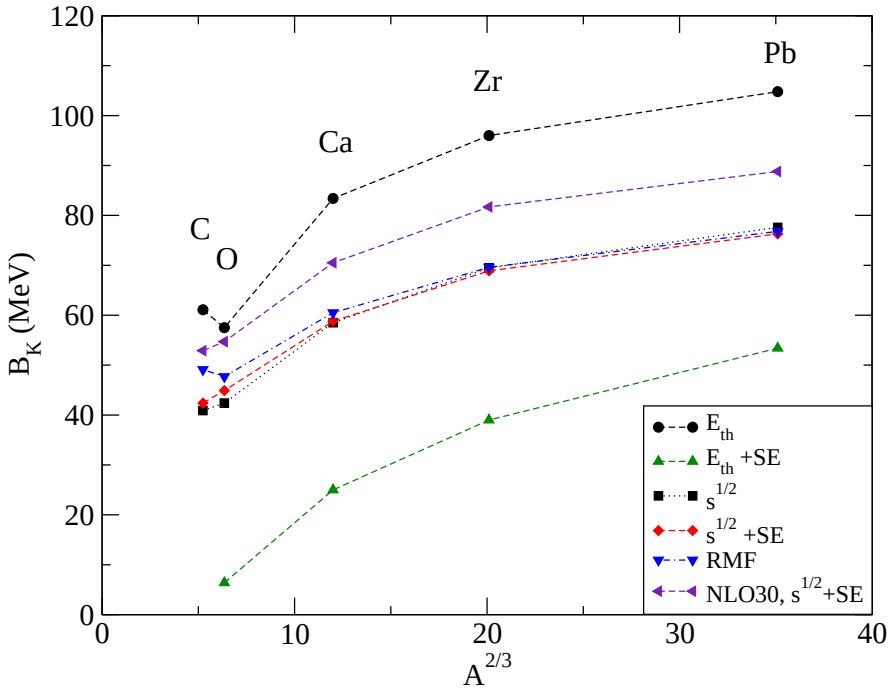

Figure 3: Binding energies B_K of $1s$ K^- nuclear quasi-bound states in several nuclei, calculated using static RMF nuclear densities and TW1 chiral amplitudes at threshold ('$E_{\rm th}$') and with $\sqrt{s}$, in both in-medium versions: only Pauli blocking ('no SE') and including also hadron self-energies ('+SE'). Results of static RMF calculations, with a K^- nuclear interaction mediated by vector mesons only, as well as for NLO30 chiral '+ SE' amplitudes are shown for comparison.

of the self-energies, as indicated in the legend of Fig. 4. The binding energies B_K in all nuclei under consideration differ in all cases by less than 5 MeV and the effect of self-energies seems to be A independent. Implementation of pion self-energies leads to a sizable reduction of the widths Γ_K in lighter nuclei (C, O). On the other hand, the role of hyperon self-energies seems to be marginal.

It is to be noted that the calculated widths shown in the figure represent only $K^-N \to \pi Y$ decays, accounted for by the coupled-channel chiral model. When phenomenological energy dependent imaginary ρ^2 terms are added self-consistently to simulate two-nucleon $K^-NN \to YN$ absorption modes and their available phase space [3], the resulting widths of order $\Gamma_K \approx 50$ MeV become comparable in light nuclei to the binding energies B_K.

Figure 5 illustrates the model dependence of the K^- nuclear state calculations by presenting B_K and Γ_K of $1s$ K^- states in selected nuclei calculated self-consistently using various chiral-model scattering amplitudes – TW1, CS30, and NLO30. The CS30 and

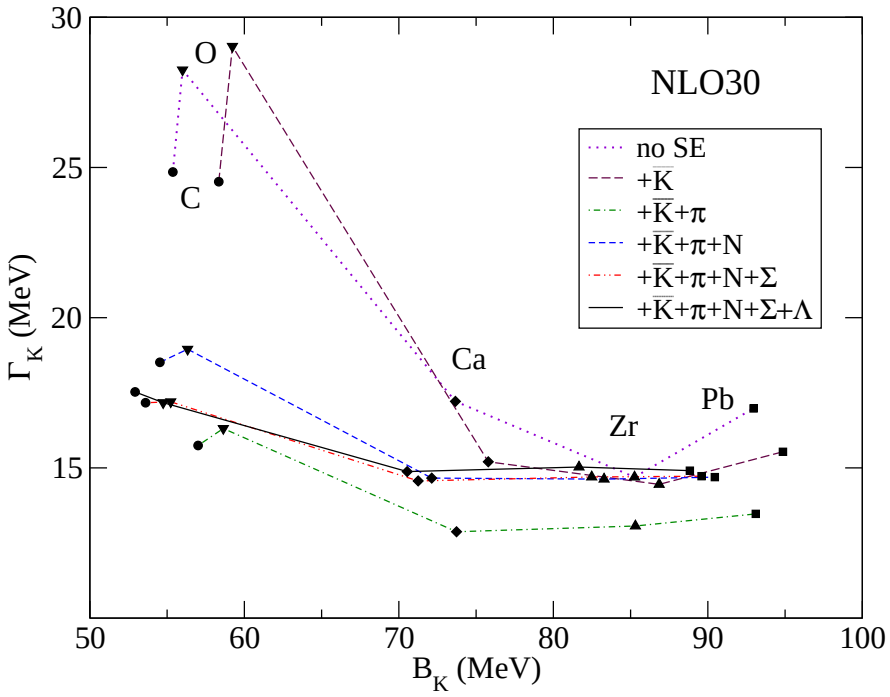

Figure 4: Binding energies B_K and widths Γ_K of $1s$ K^- nuclear quasi-bound states, calculated self-consistently with static RMF nuclear densities and in-medium NLO30 amplitudes with various hadron self-energies considered in intermediate states (see the legend). $K^-NN \to YN$ decay modes are not included.

NLO30 models yield larger binding energies and lower widths of the nuclear K^- quasi-bound states than the TW1 model. The differences between the chiral models are up to 20 MeV in the binding energies and up to 10 MeV in the widths. The model dependence of B_K and Γ_K is thus more pronounced than the effects of self-energies in the self-consistent calculations of kaonic nuclei.

Figure 6 shows binding energies and widths of K^- quasi-bound states – including excited states – in selected nuclei calculated by applying self-consistently the subthreshold extrapolations $\sqrt{s}$ of Eq. (8) to the NLO30 '+SE' amplitudes. Clearly, the widths of higher excited states are appreciable, exceeding the corresponding level spacing, even in the case when $2N$ absorption is not considered. This leads to considerable overlap of the K^- quasi-bound states even in the lightest nuclei (except Li, where only the $1s$ K^- quasi-bound state exists). It is to be stressed that the $2N$ absorption which was not considered here, adds additional sizable contribution to the widths, particularly of low lying states. Such large widths thus inevitably obscure experimental study of the K^- nuclear quasi-bound

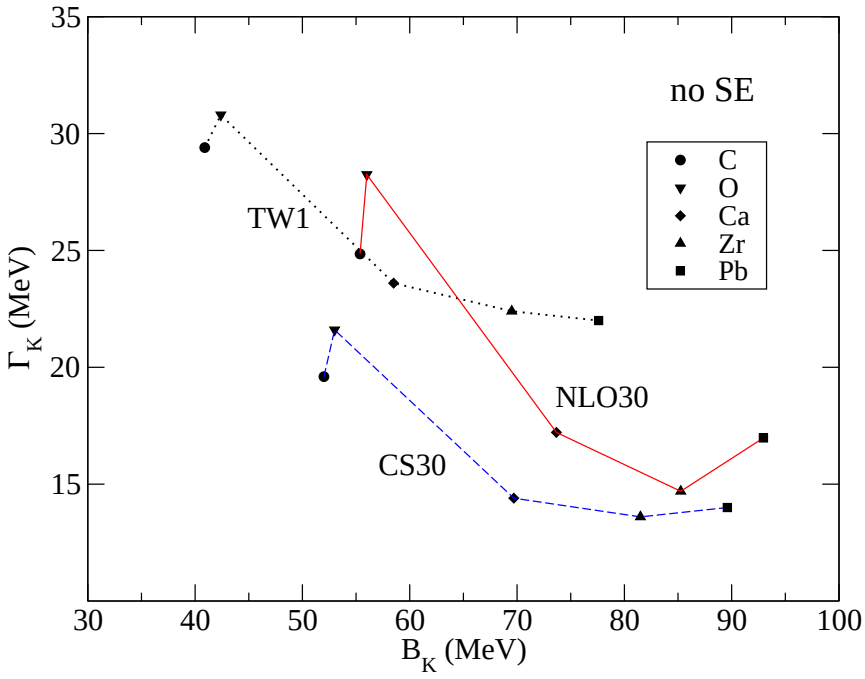

Figure 5: Binding energies B_K and widths Γ_K of $1s$ K^- nuclear quasi-bound states, calculated self-consistently with static RMF densities and the 'no SE' TW1, CS30 and NLO30 scattering amplitudes. $K^-NN \to YN$ decay modes are not included.

states in heavier nuclei.

Table 1 shows, as representative examples, binding energies B_K and widths Γ_K of K^- nuclear quasi-bound states in Ca, calculated self-consistently using the NLO30 '+SE'

Table 1: Binding energies B_K and widths Γ_K (in MeV) of the K^- nuclear quasi-bound states in Ca, calculated self-consistently using NLO30 '+SE' amplitudes. Dynamical and static RMF schemes are compared in the first two blocks. Results of a static RMF scheme including p-wave amplitudes is shown in the third block, and $K^-NN \to YN$ decay modes are included in the last block ('+2N abs.').

	dynamical		static		stat. + p wave		stat. + $2N$ abs.	
	B_K	Γ_K	B_K	Γ_K	B_K	Γ_K	B_K	Γ_K
$1s$	72.3	14.8	70.5	14.9	73.0	14.8	68.9	58.9
$1p$	52.8	17.7	50.6	18.0	53.1	17.9	49.2	53.6
$1d$	30.5	29.2	28.8	30.3	32.1	29.3	27.7	59.7
$2s$	24.6	30.9	23.9	33.8	26.3	34.2	21.6	67.1

scattering amplitudes. The results of fully dynamical RMF calculations which take into account the polarization of the nuclear core by the strongly bound K^- meson, are compared with the static RMF scheme in the first 2 blocks. The dynamical calculations give, in general, higher binding energies B_K and smaller widths Γ_K. As could be anticipated, the polarization effect is A dependent: while it increases B_K by $\sim$ 6 MeV in Li, it is less than 2 MeV in Ca (shown in Table 1), and in Pb the difference between static and dynamical calculations is less than 0.5 MeV. Effects of adding a p-wave K^-N interaction assigned to the $\Sigma(1385)$ resonance are demonstrated within the static RMF scheme in the third block of the table. The p-wave interaction increases the K^- binding energy only by few MeV, being more pronounced in light nuclei where surface effects are relatively more important. Nevertheless, even in Pb the p-wave interaction increases B_K by $\sim$ 2 MeV. Finally, phenomenological energy dependent imaginary ρ^2 terms are included to simulate $2N$ absorption processes $K^-NN \to YN$. Whereas the K^- binding energies B_K decrease only slightly, the absorption widths $\Gamma_K > 50$ MeV become comparable to the binding energies B_K or even much larger in the case of higher K^- nuclear quasi-bound states.

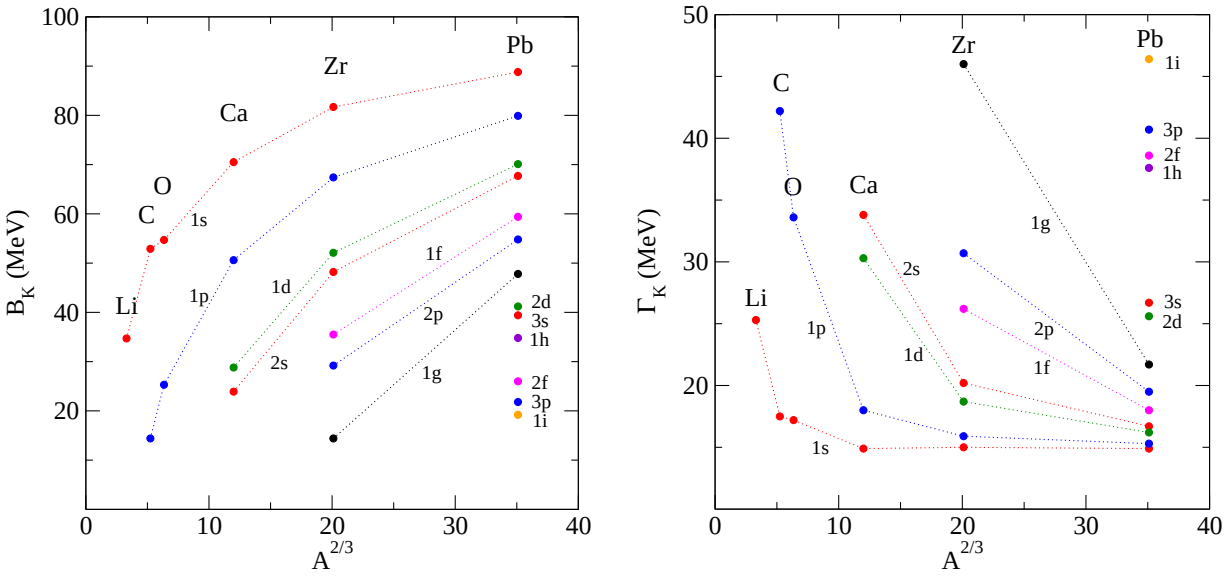

Figure 6: Binding energies B_K (left panel) and widths Γ_K (right panel) of K^- quasi-bound states in selected nuclei, calculated self-consistently with static RMF densities and the '+ SE' NLO30 scattering amplitudes. $K^-NN \to YN$ decay modes are not included.

4 Conclusions

We performed extensive study of the K^- nuclear quasi-bound states within a chirally motivated meson-baryon coupled-channel separable interaction model. We considered two in-medium versions of the K^-N scattering amplitudes: the 'no SE' version which takes into account only Pauli blocking in the intermediate states, and the '+SE' version which adds self-consistently hadron self-energies. In addition, we used several versions of the model to explore model dependence of our calculations. In this contribution, we demonstrate on few selected examples main results of the calculations with the aim to assess the role of various ingredients of the approach that influence binding energies and widths of the K^- nuclear states. Energy dependence of the in-medium scattering amplitudes, particularly in the K^-N subthreshold region, is the decisive mechanism that controls the self-consistent evaluation of corresponding K^- optical potentials. While the two in-medium versions of the K^-N scattering amplitudes yield considerably different potential depths $\mathrm{Re}V_K$ at threshold, they give similar depths in the self-consistent calculations with the subthreshold extrapolation of $\sqrt{s}$. The role of hadron self-energies in the self-consistent calculations of the K^- binding energies B_K is less pronounced than the model dependence of predicted B_K which amounts to $\Delta B_K \approx 15$ MeV. As for the calculated widths Γ_K, the model dependence and the effects due to the hadron self energies are comparable. The p-wave interaction generated by the $\Sigma(1385)$ subthreshold resonance was found to play only a marginal role.

The widths of low-lying K^- states due to $K^-N \to \pi Y$ conversions are substantially reduced in the self-consistent calculations, thus reflecting the proximity of the $\pi\Sigma$ threshold. On the contrary, the widths of higher excited K^- states are quite large even if only the pion conversion modes on a single nucleon are considered. After including 2 body $K^-NN \to YN$ absorption modes, the total decay widths Γ_K are comparable or even larger than the corresponding binding energies B_K for *all* K^- nuclear quasi-bound states, exceeding considerably the level spacing.

The above conclusions should discourage attempts to search for isolated peaks corresponding to K^- nuclear quasi-bound states in any but very light nuclear systems.

Acknowledgements

We wish to acknowledge a fruitful collaboration with Aleš Cieplý, Eli Friedman and Avraham Gal. This work was supported by the GACR grant No. 202/09/1441 and by the EU

inciative FP7, HadronPhysics2, under project No. 227431.

References

[1] See contributions in: A. Gal, R. S. Hayano (Eds.), *Recent Advances in Strangeness Nuclear Physics*, Nucl. Phys. A 804 (2008) 171-348.

[2] See contributions in: B. F. Gibson, K. Imai, T. Motoba, T. Nagae, A. Ohnishi (Eds.), *Proc. 10th Int. Conf. on Hypernuclear and Strange Particle Physics*, Tokai, 14-18 September 2009, Nucl. Phys. A 835 (2010) 1-469.

[3] J. Mareš, E. Friedman, A. Gal, Nucl. Phys. A 770 (2006) 84.

[4] D. Gazda, E. Friedman, A. Gal, J. Mareš, Phys. Rev. C 76 (2007) 055204.

[5] D. Gazda, E. Friedman, A. Gal, J. Mareš, Phys. Rev. C 77 (2008) 045206.

[6] D. Gazda, E. Friedman, A. Gal, J. Mareš, Phys. Rev. C 80 (2009) 035205.

[7] W. Weise, R. Härtle, Nucl. Phys. A 804 (2008) 173.

[8] A. Cieplý, J. Smejkal, Eur. Phys. J. A 43 (2010) 191.

[9] A. Cieplý, E. Friedman, A. Gal, D. Gazda, J. Mareš, Phys. Lett. B 702 (2011) 402.

[10] A. Cieplý, E. Friedman, A. Gal, D. Gazda, J. Mareš, Phys. Rev. C 84 (2011) 045206.

[11] A. Cieplý, J. Smejkal, Nucl. Phys. A 881 (2012) 115.

[12] M. Bazzi *et al.* (SIDDHARTA Collaboration), Phys. Lett. B 704 (2011) 113;
M. Bazzi *et al.* (SIDDHARTA Collaboration), Nucl. Phys. A 881 (2012) 88.

[13] T. Waas, N. Kaiser, W. Weise, Phys. Lett. B 365 (1996) 12;
T. Waas, N. Kaiser, W. Weise, Phys. Lett. B 379 (1996) 34.

[14] M. Lutz, Phys. Lett. B 426 (1998) 12.

[15] A. Ramos, E. Oset, Nucl. Phys. A 671 (2000) 481.

[16] S. Wycech, A. M. Green, Phys. Rev. C 79 (2009) 014001.